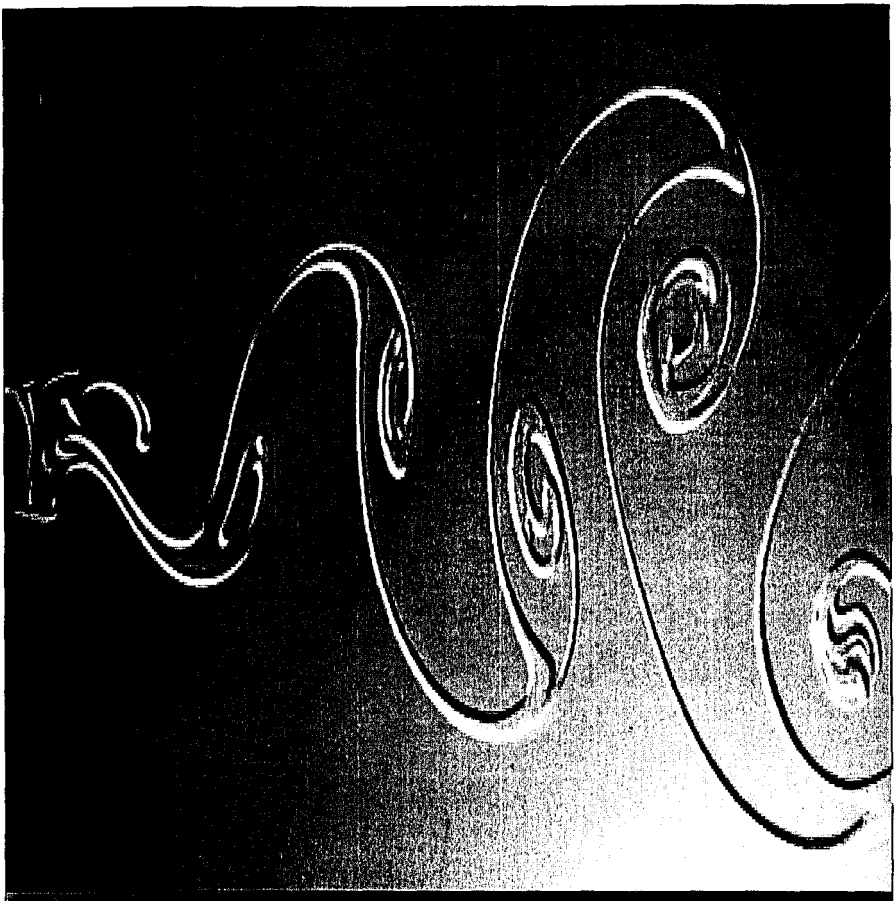

Transição e Turbulência

I Escola de Primavera ANAIS - Vol. I

Associação Brasileira de Ciências Mecânicas - ABCM

Instituto Alberto Luiz Coimbra de Pós-Graduação e
Pesquisa de Engenharia - COPPE/UFRJ
Instituto Militar de Engenharia - IME/RJ

21 a 25 de Setembro de 1998, Rio de Janeiro, Brasil.

Transição e Turbulência
I Escola de Primavera

Associação Brasileira de Ciências Mecânicas - ABCM

ABCM
Carlos Alberto de Almeida, Presidente
Hans Ingo Weber, Vice-Presidente
Paulo Batista Gonçalves, Secretário Geral
Felipe Bastos de F. Rachid, Diretor de Patrimônio
Nestor Alberto Zouain Pereira, Secretário

Comitê de Ciências Térmicas da ABCM
Antônio César P. Brasil Jr.
Leonardo Goldstein Jr.
José Alberto do Reis Parise
Jurandir Itizo Yanagihara
Atila P. Silva Freire
João Luís F. Azevedo
Sílvia Azucena Nebra de Perez

Conselho Científico da Escola de Primavera

Álvaro T. Prata	UFSC
Atila P. Silva Freire	COPPE/UFRJ
Daniel Onofre A. Cruz	UFPA
Leonardo Goldstein Jr.	UNICAMP
Luis Fernando A. Azevedo	PUC/RJ

Palestrantes Convidados Internacionais

Robert A. Antonia	University of Newcastle, Australia
Leslie J. S. Bradbury	Plymouth University, UK
Marcel Lesieur	Institut National Polytechnique, França
Michael Gaster	Queen Mary College, UK

Palestrantes Convidados Nacionais

Angela O. Nieckele	Pontificia Universidade Católica/RJ
Antônio César P. Brasil Jr.	Universidade de Brasília
Aristeu da Silveira Neto	Universidade Federal de Uberlândia
Atila P. Silva Freire	COPPE/UFRJ
Daniel Onofre A. Cruz	Universidade Federal do Pará
César J. Deschamps	Universidade Federal de Santa Catarina
Luis Fernando A. Azevedo	Pontificia Universidade Católica/RJ
Philippe Patrick M. Menut	COPPE/UFRJ

Editores

Atila P. Silva Freire	COPPE/UFRJ
Philippe Patrick M. Menut	COPPE/UFRJ
Su Jian	COPPE/UFRJ

Secretários

Mila R. Avelino	UERJ
Cláudio C. Pellegrini	FUNREI
Patricia Chedier	COPPE/UFRJ

AMBASSADE DE FRANCE
Service Culturel, Scientifique
et de Coopération

CAPES

Coordenação de Aperfeiçoamento
de Pessoal de Nível Superior

Fundação Universitária
José Bonifácio

Financiadora de Estudos e Projetos

A I Escola de Primavera em Transição e Turbulência é uma iniciativa do Comitê de Ciências Térmicas da Associação Brasileira de Ciências Mecânicas (ABCM). Sonho antigo da comunidade de mecânica dos fluidos, ela agora se torna realidade graças ao entusiasmo de alguns pesquisadores e o apoio generoso de certas entidades.

O Conselho Britânico, a Embaixada da França e a CAPES financiaram a vinda dos palestrantes internacionais. O apoio decisivo da Fundação José Bonifácio permitiu que os Anais com as contribuições técnicas e as notas dos mini-cursos estivessem disponíveis aos participantes em tempo hábil. A Reitoria da UFRJ e a COPPE/UFRJ garantiram a acomodação de todos os palestrantes convidados, nacionais e internacionais. A FADESP, Federação de Amparo ao Desenvolvimento do Estado do Pará, financiou a viagem de alguns palestrantes nacionais.

O CNPq, a FAPERJ e a FINEP colaboraram com a impressão do livro sobre Turbulência e de um volume especial da Revista Brasileira de Ciências Mecânicas dedicado ao evento, os quais deverão estar à disposição dos leitores a partir do começo do ano que vem.

O Instituto Militar de Engenharia cedeu graciosamente suas excelentes instalações para estagiar o evento. Seu corpo de professores e funcionários foi sempre muito solicito.

Finalmente, reitero o enorme apoio recebido da UFRJ, em todos os níveis, para o pleno sucesso da Escola de Primavera em Transição e Turbulência. Em tempos difíceis, de críticas contundentes e dilacerantes, é sempre um conforto ter a certeza de pertencer a uma instituição séria, com excelente quadro funcional, discente e docente.

APSF

Transição e Turbulência
I Escola de Primavera

Associação Brasileira de Ciências Mecânicas - ABCM

EFFECT OF DIFFERENT SURFACE ROUGHNESSES ON A TURBULENT BOUNDARY LAYER

R. A. Antonia* and P-Å. Krogstad+

*Department of Mechanical Engineering
University of Newcastle, N.S.W., 2308, Australia
+Department of Mechanics, Thermo and Fluid Dynamics
Norwegian University of Science & Technology, N-7034 Trondheim, Norway

ABSTRACT

The classical treatment of rough wall turbulent boundary layers consists in determining the effect the roughness has on the mean velocity profile. This effect is usually described in terms of the roughness function ΔU^+. The general implication is that different roughness geometries with the same ΔU^+ will have similar turbulence characteristics, at least at a sufficient distance from the roughness elements.

Measurements over two different surface geometries (a mesh roughness and spanwise circular rods regularly spaced in the streamwise direction) with nominally the same ΔU^+ indicate significant differences in the Reynolds stresses, especially those involving the wall-normal velocity fluctuation, over the outer region. The differences are such that the Reynolds stress anisotropy is smaller over the mesh roughness than the rod roughness. The Reynolds stress anisotropy is largest for a smooth wall.

The small-scale anisotropy and intermittency exhibit much smaller differences when the Taylor microscale Reynolds number and the Kolmogorov-normalized mean shear are nominally the same. There is nonetheless evidence that the small-scale structure over the three-dimensional mesh roughness conforms more closely with isotropy than that over the rod-roughened and smooth walls.

1 Introduction

The technological importance of wall-bounded turbulent flows is well accepted. In many situations, turbulent boundary layers develop over surfaces that are hydrodynamically rough over at least some part of their length. The major impact of surface roughness is to perturb the wall layer in such a way as to lead, in general, to an increase in the wall shear stress. This has obvious implications to both the shipbuilding and aviation industries (e.g. Schlichting, 1968). It also adversely affects the overall performance of turbines, compressors and other bladed turbomachinery (e.g. Acharya et al., 1986).

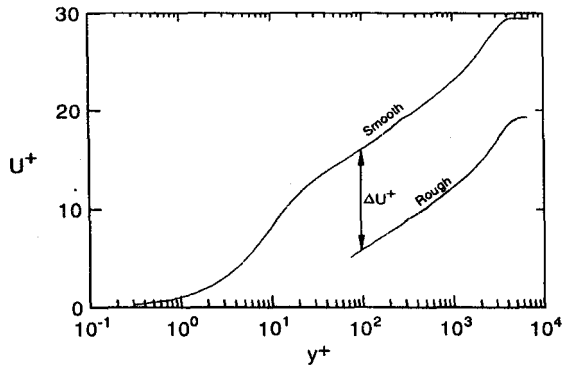

Figure 1: Typical mean velocity distributions, normalized using wall variables, over smooth and rough walls. The Clauser roughness function ΔU^+ is shown.

The increase in the wall shear stress is almost invariably accompanied by an increase in the wall heat or mass transfer rate. This has major implications in engineering, e.g. in terms of improving the efficiency of heat exchangers or in meteorology, in the context of the atmospheric surface layer over vegetated surfaces. Pimenta et al. (1979) mentioned a number of applications, including nose-tips on re-entry vehicles and transpiration-cooled turbine blades where there is heat transfer to or from pervious rough walls.

Clauser (1954,1956) presented a method of analysing the effects of surface roughness on the mean velocity distribution; the scheme has proved to be robust and continues to be used. He argued that the inner portion for rough walls must have a logarithmic region with the same slope as for a smooth surface. According to this now "classical" scheme, the sole effect of the roughness is to shift the log-law intercept C as a function of the roughness Reynolds number $k^+ \equiv U_\tau k/\nu$. With the exception of the "roughness sublayer", the inner mean velocity distribution on a rough wall is then described by

$$U^+ = \kappa^{-1} \ln y^+ + C - \Delta U^+ \tag{1}$$

where ΔU^+ represents the roughness-caused shift, as illustrated in Figure 1. (Note that the shift is generally downward although certain surfaces, e.g. longitudinal riblets, can, under certain conditions, produce a positive shift). The outer velocity, when expressed in defect form, viz.

$$U_1^+ - U^+ = f\left(\frac{y}{\delta}\right) \tag{2}$$

(δ is the boundary layer thickness) is identical for both smooth and rough walls. Although (1) and (2) have received widespread experimental verification, a few remarks are necessary, especially with respect to ΔU^+. The significance of this quantity cannot be overstated since, as Hama (1954) showed,

$$\Delta U^+ = \left(\frac{2}{c_f}\right)^{1/2}_{smooth} - \left(\frac{2}{c_f}\right)^{1/2}_{rough}$$

for the same magnitude of the Reynolds number $U_1\delta^*/\nu$ (δ^* is the displacement thickness). The magnitude of ΔU^+ is not uniquely determined by k, even for the so-called k-type roughness, for which

$$\Delta U^+ = \kappa^{-1} \ln k^+ + C_1 \ . \tag{3}$$

The additive constant C_1 depends, inter alia, on the roughness density, e.g. Dvorak (1969) and Raupach et al. (1991). The latter authors showed that (3) is very well supported by both laboratory and atmospheric surface layer data over an impressive range of k^+. A distinction has been made between k-type roughness and d-type roughness for which

$$\Delta U^+ = \kappa^{-1} \ln \delta^+ + C_2 \ . \tag{4}$$

However, experimental support for (4) is lacking, at least for a boundary layer. While there is mild support for a correlation based on ϵ^+ (ϵ is the error in surface origin), e.g. Perry et al. (1969), Wood and Antonia (1975), Osaka et al. (1984), Bandyopadhyay (1987), such a proposal is only tenable over a limited range of x (Raupach et al., 1991). Nonetheless, a surface comprising two-dimensional transverse bars with narrow cavities, which is generally associated with a "d-type" roughness, is of interest since it appears to satisfy the conditions for exact self-preservation, as set out by Rotta (1962), i.e. both U_τ/U_1 and $d\delta/dx$ are independent of x. Evidence in support of this was provided by Tani (1986,1987), Osaka et al. (1982), Osaka and Mochizuki (1988) and Djenidi and Antonia (1998). While this evidence is hard to refute, cogent physical reasons as to why this surface is closer to equilibrium than either a smooth wall or other rough walls have not been formulated; some work is being done in this direction (Djenidi and Antonia, 1998), especially in the context of self-sustaining energy production mechanisms. Although we subscribe to Raupach et al.'s assessment that there are difficulties with the division of roughness into k and (especially) d type classes, we see no reason why Clauser's proposal, encaptured by (1), (2) and (3), shoud not continue to be useful. We emphasise however that the scheme only addresses the mean velocity distribution. According to the Reynolds number similarity hypothesis (Townsend, 1976) or the wall similarity hypothesis (Perry and Abell, 1977), turbulent motions outside the roughness sublayer are independent of the wall roughness at sufficiently large Reynolds number. This is of course consistent with the universality of $f(y/\delta)$ in (2). The validity of this hypothesis has recently been challenged by Krogstad et al. (1992), also Krogstad and Antonia (1994). The experimental evidence presented in the last two papers indicates that the outer layer distributions of the wall-normal turbulence intensity and the Reynolds shear stress are markedly different between a mesh roughness and a smooth wall. There was also evidence of major differences in the characteristics of the large scale motion between the two surfaces.

One implication of these results is that the communication between the wall and the outer region is more important than has hitherto been thought. Another, possibly more serious, inference is that there may be a fundamental difference in the momentum-transport process contrary to what the equality of the log-law slope, Eq. (1), between smooth and rough surfaces may imply. As a consequence, classical mixing length

calculations, albeit allowing for a shift in origin, are unlikely to explain the differences in the Reynolds shear stress $-\langle uv \rangle$ (angular brackets denote time averaging), in the outer region of the layer.

This paper continues to examine possible differences between smooth and rough walls. A particular strategy we adopt is to consider different types of roughness geometries *but with the important requirement that* ΔU^+ *is kept constant.* We assess the influence of different surface conditions on the larger-scale (shear-stress carrying) as well as the smaller scale motions. Although the generally accepted wisdom is that the latter are less likely to be affected by the nature of the surface than the former, *especially if the Taylor microscale Reynolds number* R_λ *is kept constant*, the possibility that a reduced anisotropy of the large-scale motion (e.g. Krogstad and Antonia, 1994; Shafi and Antonia, 1995) could impact on the anisotropy of the small-scale motion should not be dismissed.

Following a brief description (Section 2) of the surfaces we consider, we address mainly the anisotropy of both the large scale (Sections 3 and 4) and the small scale motion (Section 5). We do not consider here the effect of the roughness on the heat transfer characteristics of the boundary layer nor do we treat the implications that the present observations may have on calculation methods. These topics merit to be addressed separately, at a future date.

2 Experimental Conditions

Two rough surfaces are considered. One is essentialy three-dimensional, consisting of a woven stainless steel mesh screen. The other is basically two-dimensional, consisting of circular rods placed in a spanwise direction at regular streamwise intervals. Dimensions for these two geometries are given in Table 1, where details on experimental conditions are also included. Both the screen and the rods were glued, in separate experiments, on to the aluminium wall of the wind tunnel working section (5.4 m long, inlet area $\equiv$ 0.9 m $\times$ 0.15 m). The ceiling of the working section was adjusted to set the pressure gradient to zero. The mesh screen covered a streamwise distance of 3.5 m; for the rods, the distance was 3.2 m. Further details for the mesh screen and rod roughness experiments can be found in Krogstad et al. (1992) and Krogstad and Antonia (1998) respectively. For reference, measurements were also made on a smooth wall, though in a different wind tunnel; only a few relevant experimental details are shown in Table 1. Whenever possible, the results obtained by Spalart (1988) for a smooth wall boundary layer direct numerical simulation are shown; only results at the highest value of R_θ (= 1410) have been used.

U was measured both with a Pitot tube (0.81 mm outer dia.) and single and X-hot wires (Pt-10% Rh). Most of the wires used has a diameter (d_w) 2.5 μm and a length ℓ_w of 0.5 mm; the measured frequency response was 12.5 kHz at U = 7 m/s. For the small-scale experiments, smaller diameter wires ($d_w = 1.2\mu$m and $\ell_w = 0.22$ mm) were used; the frequency response was about 23 kHz at U = 7 m/s. The X-wires had an included angle of 110°.

In-house constant temperature circuits were used to operate the hot wires. The output signals from the circuits were filtered (cut off frequency f_c) amplified to optimise the input range of the 12 bit (16 channel sample and hold) A/D converter and sampled (sampling frequency f_s). For most measurements, $f_c \simeq 5$ kHz, $f_s \simeq 10$ kHz and the record duration was about 30 s. For the small-scale measurements significantly larger values of f_c and f_s were used, with f_c set close to the Kolmogorov frequency f_K (e.g. Table 2); record durations up to 180 s were used.

Table 1. Characteristics of the Different Surfaces and Basic Experimental Conditions

Surface	k (mm)	$\lambda^\dagger$ (mm)	$x^\ddagger$ (m)	U_1 (m/s)	$\Pi^\S$	c_f ($\times 10^3$)	δ (mm)	ΔU^+	R_θ
mesh screen (wire dia. = 0.69 mm)	1.38	3.18	2.46	20	0.70	5.4	75	11.0	12800
circular rods (dia. = 1.60 mm)	1.60	6.40	2.03	7	0.83	6.3	74	11.4	4810
smooth	—	—	4.25	25	0.68	2.3	70	0	12570

$^\dagger\lambda$ is the streamwise wavelength for the mesh and the rods
‡refers to the measurement location
§Coles' wake function parameter

3 Mean Velocity and Velocity Fluctuation Moments

Mean velocity distributions are shown in Figure 2 for the three surfaces, with wall variable normalization. Both the present smooth wall results at $R_\theta = 12570$ and the DNS smooth wall results of Spalart (1988) for $R_\theta = 1410$ are shown. These two distributions overlap, in agreement with the law of the wall. The two rough wall distributions also overlap in the inner region indicating that nominally the same value of ΔU^+ (see Table 1) was indeed for each of the two rough surfaces and the experimental conditions chosen. As originally anticipated by Clauser [1954,1956; see Eq. (2)] and subsequently verified by many investigators, the velocity defect $(U_1^+ - U^+)$ [Figure 3], is the same for rough and smooth walls.

Reynolds stresses are plotted in Figures 4 ($\langle u^{+2} \rangle$), 5 ($\langle v^{+2} \rangle$) and 6 ($-\langle u^+ v^+ \rangle$) in terms of y/δ. If we focus our attention primarily on the outer layer, several salient observations can be made

1. There is much closer agreement between the different surfaces for $\langle u^{+2} \rangle$ than either $\langle v^{+2} \rangle$ or $-\langle u^+ v^+ \rangle$. Even in the case of $\langle u^{+2} \rangle$ (Figure 4), there are some differences between the three surfaces, $\langle u^{+2} \rangle$ tending to be larger over the rod

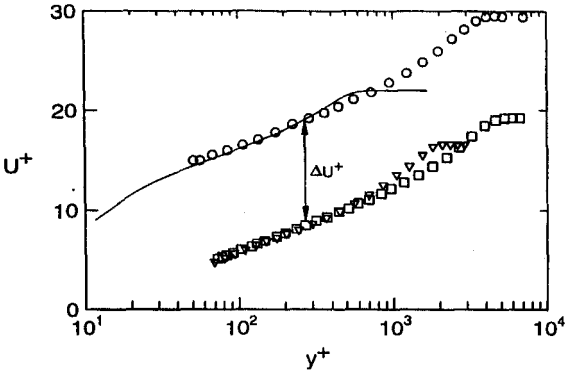

Figure 2: Mean velocity distributions normalized using wall variables. ○, smooth wall ($R_\theta = 12570$); □, mesh roughness ($R_\theta = 8000$); ▽, rod roughness ($R_\theta = 12000$); —, DNS smooth (Spalart, 1988; $R_\theta = 1410$). Unless noted, the same symbols are used in subsequent figures.

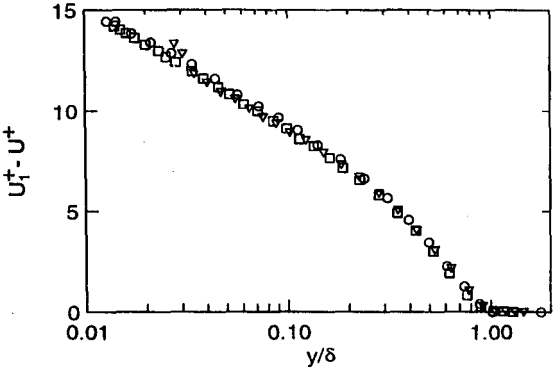

Figure 3: Mean velocity defect ($U_1^+ - U^+$) vs y/δ. Symbols are as in Figure 2.

roughness. The differences are believed to be genuine, since they fall outside the range of experimental uncertainty.

2. The most pronounced differences seem to occur on $\langle v^{+2} \rangle$ (Figure 5) and $-\langle u^+ v^+ \rangle$ (Figure 6), implying that the wall-normal motion is the most affected by the type of surface. Note that $\langle v^{+2} \rangle$ and $-\langle u^+ v^+ \rangle$ are also largest for the rod roughness, implying a much stronger momentum transport for this particular surface. Relative to the smooth surface, there is clearly much more activity associated with the wall-normal velocity fluctuation over the rough surface.

3. Although ΔU^+ is the same for the two roughnesses, the Reynolds stress distributions are different. This alone considerably limits the generality of ΔU^+ as a descriptor of the effect that different surface conditions have on the momentum transport.

Outer layer differences for the turbulent kinetic energy $k^+ \equiv \frac{1}{2}(\langle u^+ \rangle^2 + \langle v^+ \rangle^2 + \langle w^+ \rangle^2)$

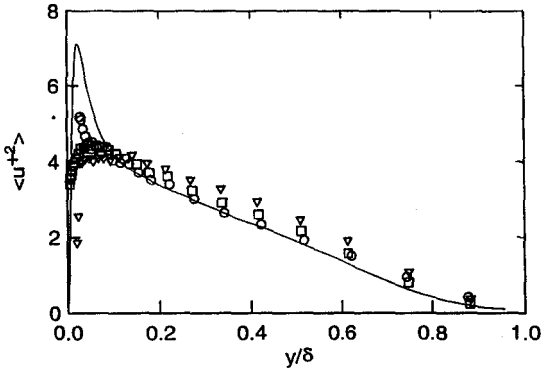

Figure 4: $\langle u^{+2} \rangle$ vs y/δ. Symbols as in Figure 2.

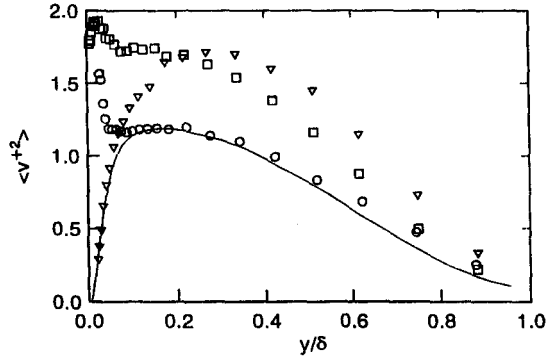

Figure 5: $\langle v^{+2} \rangle$ vs y/δ. Symbols as in Figure 2.

[Figure 7] between the rough surfaces are less pronounced than those for $\langle v^{+2} \rangle$ or $-\langle u^+ v^+ \rangle$, reflecting the dominant contribution from $\langle u^{+2} \rangle$ to $\langle k^+ \rangle$. Both rough wall distributions lie significantly above the smooth wall distribution.

A comment with regard to the smooth wall DNS distribution shown in this and previous figures seems appropriate. The agreement between the DNS distribution at $R_\theta = 1410$ and the present smoth wall measurements at $R_\theta = 12570$ is generally quite good in the outer region, implying that the moderately low R_θ DNS results of Spalart can serve as a reliable smooth wall reference against which the effect of the rough wall can be assessed.

Velocity triple products are expected to be a more sensitive indicator of the effect of surface condition than second-order moments. Andreopoulos and Bradshaw (1981) noted that triple products were spectacularly altered for a distance up to 10 roughness heights above a surface covered with floor-sanding paper. Bandyopadhyay and Watson (1988) reported that instantaneous motions involved in the shear stress flux near the

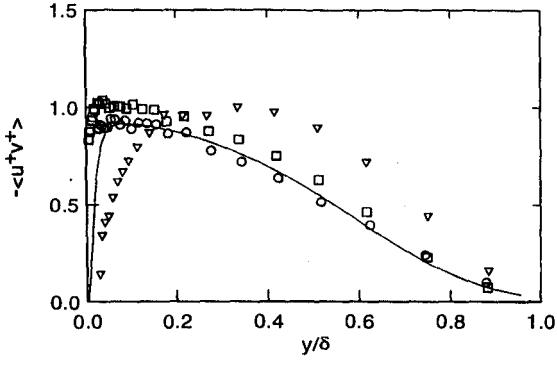

Figure 6: $-\langle u^+v^+\rangle$ vs y/δ. Symbols as in Figure 2.

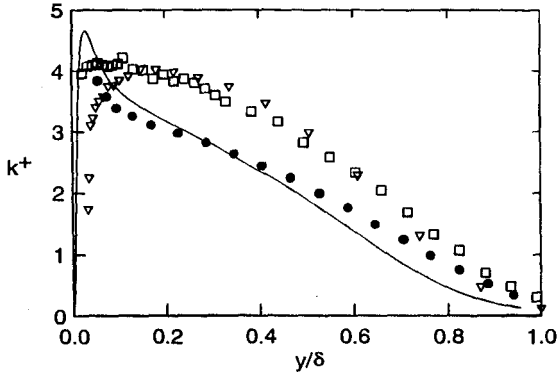

Figure 7: Turbulent kinetic energy, normalized by U_τ^2, vs y/δ. Symbols as in Figure 2. ●, $R_\theta = 2788$ (Erm, 1988).

wall in smooth and transversely grooved surfaces are opposite in sign to those over a three-dimensional roughness. Distributions of $\langle u^{+2}v^+\rangle$ and $\langle v^{+3}\rangle$ are shown in Figures 8a and 8b respectively. There are major differences both for $\langle u^{+2}v^+\rangle$ and $\langle v^{+3}\rangle$ between the two types of roughness in the region $y/\delta \lesssim 0.5$. In particular, both triple products change sign above the rod-roughened wall. For the mesh roughness, only $\langle u^{+2}v^+\rangle$ changes sign but negative values $\langle u^{+2}v^+\rangle$ occur only very near the surface ($y/\delta \lesssim 0.03$). Contrary to what happens over the mesh-screen roughness (or indeed the sandgrain roughness investigated by Andreopoulos and Bradshaw, 1981), there is an important transport of u^2 and v^2 *towards* the wall over the rods. Although distributions of $\langle w^{+2}v^+\rangle$ and $\langle u^+v^{+2}\rangle$ are not shown here, the transport of turbulent energy and momentum flux *towards* the wall over the two-dimensional roughness contrasts with a transport *away* from the wall for the three-dimensional roughness. The y-derivatives of $\langle u^{+2}v^+\rangle$ and $\langle v^{+3}\rangle$ contribute to the term which represents the turbulent energy diffusion associated with v. Although not shown here, the term is negative over the

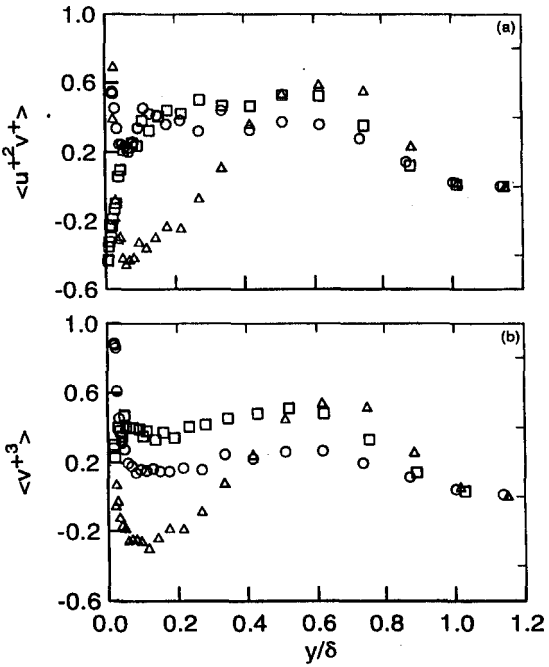

Figure 8: Third-order moments of velocity fluctuations, normalized by U_τ^3, vs y/δ. (a) $\langle u^{+2}v^+\rangle$; (b) $\langle v^{+3}\rangle$. Symbols as in Figure 2.

rods — thus representing a *gain* of turbulent energy — but positive over the mesh screen.

The skewness ($S_\alpha \equiv \langle\alpha^3\rangle/\langle\alpha^2\rangle^{3/2}$) and flatness factor ($F_\alpha \equiv \langle\alpha^4\rangle/\langle\alpha^2\rangle^2$) of u and v are shown in Figures 9 and 10 respectively. While S_u changes sign, irrespectively of the type of surface, near the wall, S_v changes sign only over the rods. In contrast to S_v, F_v is, like F_u, practically unaffected by the surface up to $y/\delta \simeq 0.6$. There are nevertheless differences between the three surfaces in both F_u and F_v as the edge of the turbulent/non-turbulent interface is approached.

4 Anisotropy of Reynolds Stresses

Ratios such as $\langle v^2\rangle/\langle u^2\rangle$, $\langle v^2\rangle/\langle w^2\rangle$ or $-\langle uv\rangle/\langle v^2\rangle$ provide a rough indication of the departure of the Reynolds stresses from isotropy. Figure 11a shows that, while there may not be large differences in $\langle v^2\rangle/\langle u^2\rangle$ between the two rough surfaces, the magnitude of this ratio is significantly smaller for a smooth wall (the DNS data of Spalart, 1988, is used here and in subsequent figures). The inference is that the anisotropy — at least for the Reynolds normal stresses — is reduced over a rough wall. Note that $\langle v^2\rangle/\langle u^2\rangle$

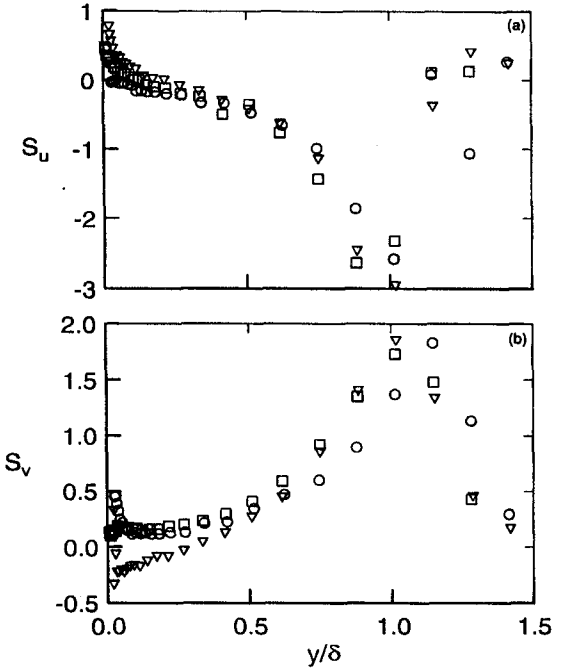

Figure 9: Skewnesses of u and v. (a) u; (b) v. Symbols as in Figure 2.

is somewhat larger, in the region $y/\delta < 0.4$, for the mesh than for the rod roughness. This closer tendency towards isotropy for the mesh roughness is better illustrated by the ratio $\langle v^2\rangle/\langle w^2\rangle$ in Figure 11b over a significant fraction of the layer. The ratio $-\langle uv\rangle/\langle v^2\rangle$, Figure 11c, is also smaller for the mesh than the rods. The smooth wall values of $-\langle uv\rangle/\langle v^2\rangle$ are largest, reflecting the greater anisotropy for this surface.

A better measure of the anisotropy of the Reynolds stresses is provided by the second (II) and third (III) invariants of the Reynolds stress anisotropy tensor b_{ij} defined by

$$b_{ij} = \frac{\langle u_i u_j\rangle}{\langle u_i u_i\rangle} - \frac{\delta_{ij}}{3}$$

where $\langle u_i u_i\rangle \equiv \langle q^2\rangle$ is the mean turbulent energy and δ_{ij} is the Kronecker delta tensor. The states that characterise b_{ij} can be identified on a plot of $-II$ ($\equiv b_{ij}b_{ji}$) vs III ($1/3b_{ij}b_{jk}b_{ki}$), as originally proposed by Lumley and Newman (1976). The limiting values of the invariants delineate an anisotropy invariant map or partially curvilinear triangle as shown in Figure 12. The upper linear boundary of the triangle characterises 2-component turbulence, such as might be expected in the vicinity of a smooth wall; the DNS boundary layer data of Spalart (1988) shown in the figure and the DNS channel flow data of Kim et al. (1987), shown in Antonia et al. (1991), confirm this behaviour.

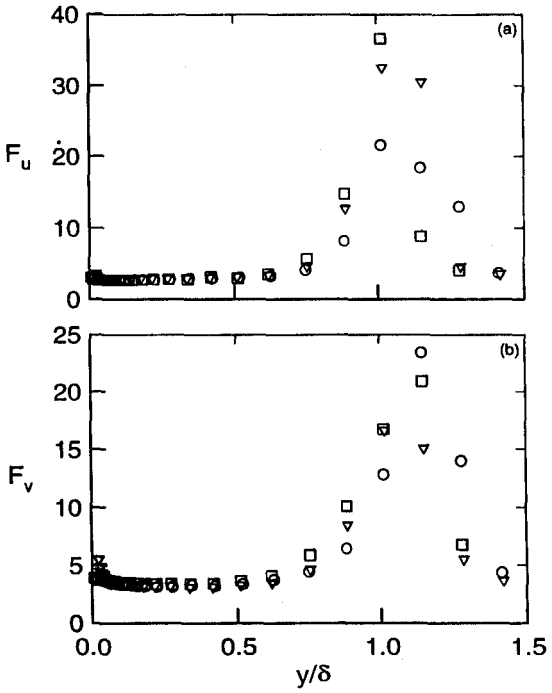

Figure 10: Flatness factors of u and v. (a) u; (b) v. Symbols as in Figure 2.

Figure 12 clearly highlights the greater tendency towards isotropy of the rough wall layers relative to the smooth wall layer. The majority of the rough wall data are much closer to the bottom cusp (i.e. isotropy) of the triangle. In particular, this behaviour is better approximated (inset in Figure 12) by the mesh data than the rod data, thus corroborating previous inferences from Figure 11. A few data points lie just outside the right axisymmetric boundary of the triangle; this is most likely due to the uncertainties in measuring the Reynolds stresses. The information in Figure 12, which is presented solely in terms of invariants, is, unlike that in Figure 11, independent of the choice of coordinate axes. This feature of Figure 12 would be worth exploiting when better quality data — for example with adequately resolved LDV — become available in the vicinity of different rough surfaces.

A further measure of the anisotropy of the Reynolds stresses is provided by the parameter F ($\equiv 1 + 27III + 9II$) which is proportional to the product of the three eigen values of $\langle u_i u_j \rangle / \langle u_i u_i \rangle$. F is bounded between 0 and 1. It is zero along the linear boundary of the triangle, which describes a 2-component state of turbulence. It is 1 when both II and III are zero, i.e. for isotropic turbulence. Figure 13 clearly shows that, almost everywhere in the layer, F is largest for the mesh roughness and smallest for the smooth wall.

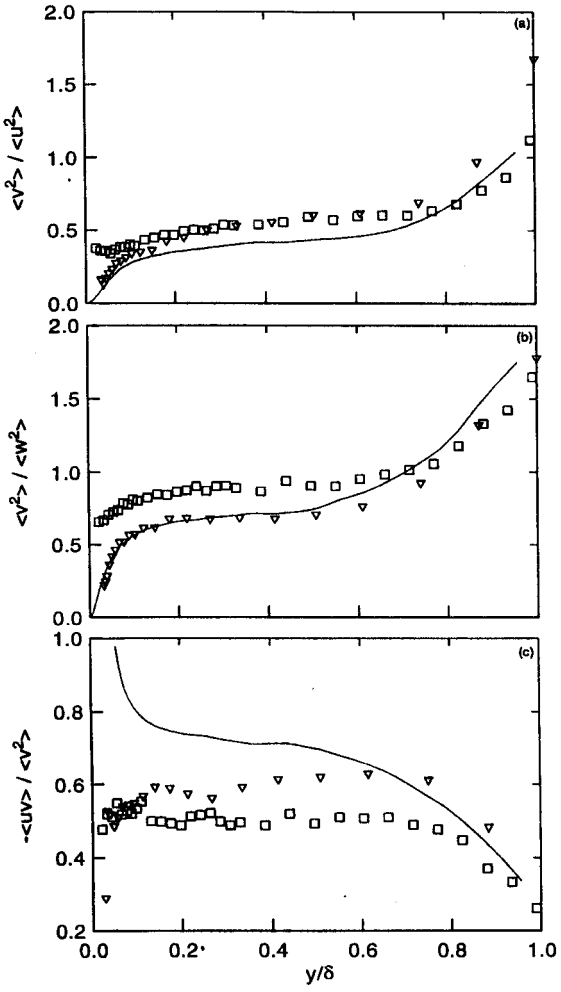

Figure 11: Reynolds stress ratios. (a) $\langle v^2 \rangle / \langle u^2 \rangle$; (b) $\langle v^2 \rangle / \langle w^2 \rangle$; (c) $-\langle uv \rangle / \langle v^2 \rangle$. Symbols as in Figure 2.

5 Small-Scale Anisotropy and Intermittency

Ideally, the anisotropy of the small scale-motion should be quantified by evaluating the anisotropy invariants of the energy dissipation rate tensor, in similar manner to the way the Reynolds stress invariants were obtained in the previous section. Anisotropy invariants of ϵ_{ij} require all velocity derivatives to be known. This is not yet feasible

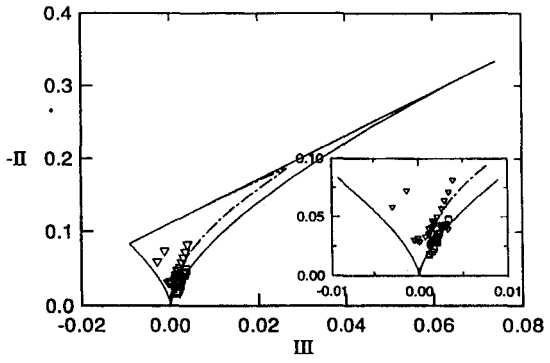

Figure 12: Invariant map for the Reynolds stress anisotropy tensor. Symbols as in Figure 2.

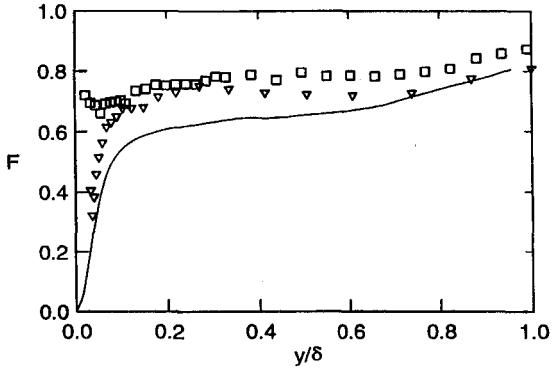

Figure 13: Invariant function F. Symbols as in Figure 2.

experimentally (it is possible from direct numerical simulations, e.g. Kim and Antonia, 1993, but these have yet to be performed for surface geometries of comparable complexity to those considered here). We therefore limit ourselves here to considering relatively simple measures of small-scale anisotropy, as provided for example by the ratios $\langle(\delta v)^2\rangle^c/\langle(\delta v)^2)\rangle^m$ and $\phi_v^c(k_1)/\phi_v^m(k_1)$, where the superscripts c and m denoted calculated (using isotropy) and measured values. As noted in the introduction, the small-scale anisotropy is expected to depend on a number of factors, such as R_λ, the mean shear, the proximity to the wall or the presence of a turbulent/non-turbulent interface. Here we consider data at $y/\delta \simeq 0.2$, a location where the influence of the last two factors should not be significant. Experimental conditions were chosen so that the magnitude of R_λ is about the same for the three surfaces considered. Also, the magnitude of $S^* \equiv S(\nu/\langle\epsilon\rangle)^{1/2}$, where $S \equiv \partial\langle U\rangle/\partial y$ is the mean shear, is nominally the same for the three surfaces. The experimental conditions are summarised in Table 2.

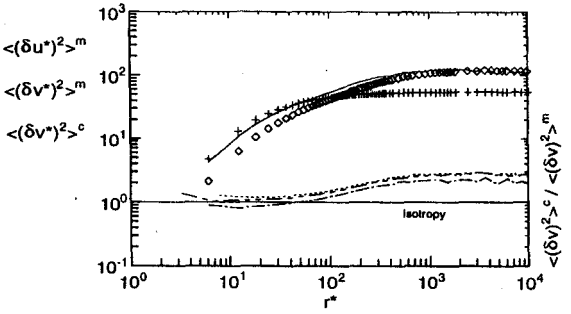

Figure 14: Second-order moments of longitudinal and transverse velocity increments. The normalization is by Kolmogorov variables. Also shown is the ratio $\langle(\delta v)^2\rangle^c / \langle(\delta v)^2\rangle^m$, where the superscripts c and m refer to calculated (using isotropy) and measured values. Rod roughness : $\diamond$, $\langle(\delta u^*)^2\rangle^m$; +, $\langle(\delta v^*)^2\rangle^m$; —, $\langle(\delta v^*)^2\rangle^c$. $\langle(\delta v)^2\rangle^c / \langle(\delta v)^2\rangle^m$: – –, smooth wall; — · · —, mesh roughness; — · —, rod roughness.

Table 2. Experimental Conditions for Different Surfaces Yielding Approximately the Same R_λ at $y/\delta \simeq 0.2$

Surface	y/δ	U_∞ (m/s)	$\langle U\rangle$ (m/s)	$\frac{\langle v^2\rangle}{\langle u^2\rangle}$	R_θ	R_λ	$\eta^\dagger$ (mm)	$f_K^\ddagger$ (kHz)	S^*
Mesh	0.22	10	6.66	0.49	8000	240	0.126	8.41	0.09
Rods	0.20	10	5.34	0.43	12000	248	0.109	7.90	0.11
Smooth	0.19	23	18.4	0.35	12570	230	0.077	38.1	0.12

$^\dagger\eta$ is the Kolmogorov length scale $\nu^{3/4}/\langle\epsilon\rangle^{1/4}$
$^\ddagger f_K$ is the Kolmogorov frequency $U/2\pi\eta$

Distributions of $\langle(\delta u^*)^2\rangle^m$, $\langle(\delta v^*)^2\rangle^m$ and $\langle(\delta v^*)^2\rangle^c$ are shown in Figure 14 for the rod roughness. The values of $\langle(\delta v^*)^2\rangle^c$ were calculated using the isotropic relation

$$\langle(\delta v)^2\rangle = \left(1 + \frac{r}{2}\frac{\partial}{\partial r}\right)\langle(\delta u)^2\rangle \ . \tag{5}$$

As expected, the ratio $\langle(\delta v^*)^2\rangle^c / \langle(\delta v^*)^2\rangle^m$, also shown in the figure for the other two surfaces, is close to 1 at small r^* and increases as r^* increases. As $r^* \to \infty$ (or, to a reasonable approximation $r^* \gtrsim L^*$, where L is the integral length scale), $\langle(\delta u^*)^2\rangle \to 2\langle u^{*2}\rangle$ and $\langle(\delta v^*)^2\rangle = 2\langle v^{*2}\rangle$. Since $\langle(\delta u^*)^2\rangle^m$ was used as input in Eq. (5), $\langle(\delta v^*)^2\rangle^c = \langle(\delta u^*)^2\rangle^m$ when r^* is large enough for $\partial\langle(\delta u^*)^2\rangle^m/\partial r^*$ to be zero. The different levels of the ratio $\langle(\delta v)^2\rangle^c / \langle(\delta v)^2\rangle^m$ in Figure 14 reflect the different values of the ratio $\langle v^2\rangle^m / \langle u^2\rangle^m$ for the three different surfaces (Table 2).

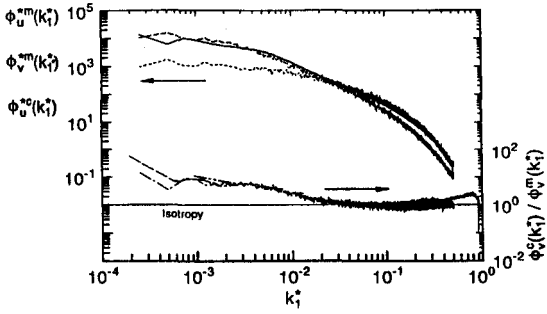

Figure 15: Kolmogorov-normalized spectra of u and v. The ratio ϕ_u^c/ϕ_u^m is also shown. The superscripts c and m refer to calculated (using isotropy) and measured distributions. Rod roughness : – –, $\phi_u^{*m}(k_1^*)$; - - -, $\phi_v^{*m}(k_1^*)$;; —, $\phi_v^{*c}(k_1^*)$. $\phi_v^c(k_1)/\phi_v^m(k_1)$: – –, smooth wall; — - - —, mesh roughness; — - —, rod roughness.

Distributions of $\phi_u^{*m}(k_1^*)$, $\phi_v^{*m}(k_1^*)$ and $\phi_v^{*c}(k_1^*)$ are shown in Figure 15 as a function of k_1^*, where k_1 is the one-dimensional wavenumber. $\phi_v^{*c}(k_1^*)$ was evaluated from the isotropic relation

$$\phi_v(k_1) = \frac{1}{2}\left(1 - k_1\frac{\partial}{\partial k_1}\right)\phi_u(k_1)$$

with $\phi_u^m(k_1)$ as input. The departures of $\phi_v^c(k_1)/\phi_v^m(k_1)$ from 1 at high wavenumbers of course reflects that of $\langle(\delta v)^2\rangle^c/\langle(\delta v)^2\rangle^m$ from 1 at small separations (Figure 14).

It is difficult to select unambiguously, from ratios in Figures 14 and 15, a surface for which the anisotropy is smallest. One could conclude that all three surfaces satisfy isotropy equally well to a rough approximation. Alternately, it may be argued that isotropy is somewhat better satisfied, especially in terms of the extent of the range — in either r^* or k_1^* — for the mesh roughness. A more detailed examination of the small-scale structure for this roughness supports this argument, in particular, transverse vorticity spectra were found (Antonia and Shafi, 1998) to satisfy isotropy at least as well as the boundary layer measurements (Ong and Wallace, 1995) in the NASA-Ames wind tunnel at $R_\lambda \simeq 1400$. Speculatively, the small-scale structure over three-dimensional surfaces such as the mesh screen may satisfy isotropy more closely than that over two-dimensional roughnesses such as the rods. Although more work is needed, for example, vorticity measurements have yet to be made over the rods or, for that matter, over the present smooth wall, the experimental conditions (in particular the magnitudes of η and f_k) in Table 2 clearly indicate that small-scale statistics should be measured more accurately over rough surfaces than smooth walls.

A measure of small-scale intermittency is provided by the departure of the IR exponents $\zeta_u(p)$ where

$$\langle(\delta u)^p\rangle \sim r^{\zeta_u(p)}$$

from the corresponding Kolmogorov (1941) values. According to Kolmogorov (1941),

$$\langle(\delta u)^p\rangle \sim r^{p/3}$$

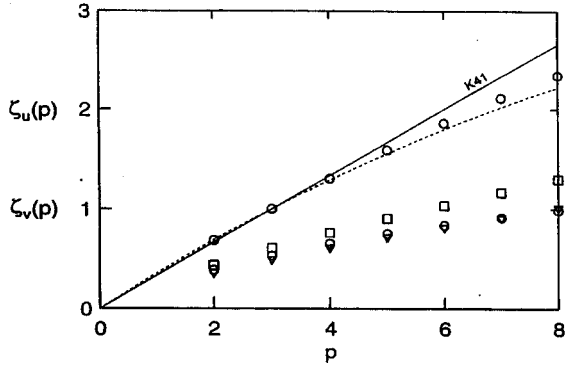

Figure 16: Scaling range exponents for $\langle|\delta u|^p\rangle$ and $\langle|\delta v|^p\rangle$ at nominally the same R_λ ($\simeq$ 240) and y/δ ($\simeq$ 0.2). $\zeta_u(p)$: O, smooth wall; □, mesh roughness; ▽, rod roughness. $\zeta_v(p)$: O, smooth wall; □, mesh roughness; ▽, rod roughness.

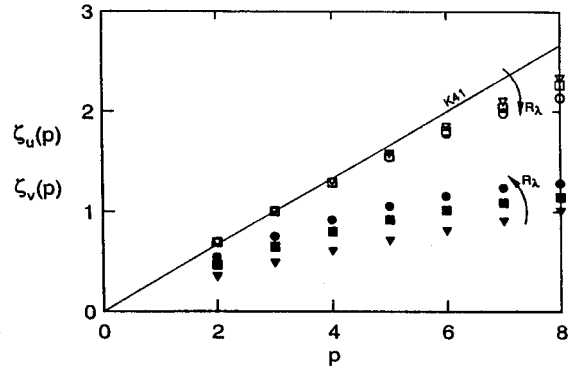

Figure 17: Scaling range exponents for $\langle|\delta u|^p\rangle$ and $\langle|\delta v|^p\rangle$ at different R_λ but the same y/δ ($\simeq$ 0.2). Open and solid symbols represent $\zeta_u(p)$ and $\zeta_v(p)$ respectively. ▽, $R_\lambda = 240$; □, 330; O, 375.

when r lies within the IR. This departure, which is usually described as the "anomalous scaling", increases as p increases (e.g. Anselmet et al., 1984) but is detectable even for small values of p (e.g. Stolovitzky and Sreenivasan, 1993).

The magnitude of $\zeta_u(p)$ was estimated using the extended self-similarity (ESS) method of Benzi et al. (1993); the scaling range was however restricted to that over which $\langle|\delta u|^3\rangle r^{*-1}$ was approximately constant (this range is loosely identified here with the IR). For consistency, the same range was used to determine $\zeta_v(p)$, the IR exponent of $\langle|\delta v|^p\rangle$, viz.

$$\langle|\delta v|^p\rangle \sim r^{\zeta_v(p)} \quad .$$

It is worth emphasising that ESS only yields *relative*, rather than *absolute*, estimates of $\zeta_u(p)$ and $\zeta_v(p)$. The distributions of $\zeta_u(p)$ over the three different surfaces at $y/\delta \simeq 0.2$ (Figure 16) are nearly the same, implying that the intermittency affects each flow in similar fashion. For comparison, the prediction of the lognormal model (Kolmogorov,

1962), viz.

$$\zeta(p) = \frac{p}{3} - \frac{\mu p(p-3)}{18}$$

where μ ($\simeq 0.2$) is the intermittency factor, has been included in Figure 16. While it is in reasonable agreement with the experimental estimates of $\zeta_u(p)$, it does not differentiate between $\zeta_u(p)$ and $\zeta_v(p)$. The experimental magnitudes of $\zeta_v(p)$ are significantly smaller than those of $\zeta_u(p)$, possibly suggesting that transverse velocity fluctuations are more intermittent than longitudinal velocity fluctuations. Another possibility may be that v is more sensitive to anisotropy than u. In this context, we note that $\zeta_v(p)$ is generally bigger for the mesh roughness than the other two surfaces, in support of the earlier suggestion that the small-scale turbulence over three-dimensional surfaces satisfies isotropy more closely than that over either a smooth wall or a two-dimensional surface roughness.

As the Reynolds number (R_θ or R_λ) increases, the anisotropy is expected to decrease, thus bringing $\zeta_v(p)$ into closer alignment with $\zeta_u(p)$. This tendency is illustrated in Figure 17 for the rod-roughness. Note that $\zeta_u(p)$ is hardly affected by the increase in R_λ. It should be mentioned that the increase in $\zeta_v(p)$ with R_λ in Figure 17 and the difference between the three $\zeta_v(p)$ distributions in Figure 16 are statistically significant, allowing for experimental uncertainty in estimating $\zeta_v(p)$.

6 Conclusions

The Clauser roughness function ΔU^+ is a useful descriptor of the effect that the surface roughness has on the mean velocity distribution in the inner region of a boundary layer. Also, the mean velocity distribution in the outer region is, to a good approximation, unaffected by the roughness. However, there is as yet no adequate scheme which describes the effect the roughness has on the Reynolds stresses in the outer region of the boundary layer. In particular, we have noted that for two different roughness geometries for which ΔU^+ is approximately the same, the outer layer distributions of the Reynolds stresses, especially those involving the wall-normal velocity distribution, are discernibly different. They also differ with respect to the smooth wall. The Reynolds stress differences are such that the Reynolds stress anisotropy is smallest over the mesh screen and largest for the smooth wall.

We have also shown that when R_λ and a Kolmogorov-normalized value of the mean shear are kept constant, the differences in the small scale anisotropy are only small. Nonetheless, there is evidence indicating that, for the three-dimensional roughness, the small scales are more closely isotropic than for either the two-dimensional roughness or the smooth wall. Consistently, the difference between IR power-law exponents of longitudinal and transverse velocity structure functions appears to be smallest for the mesh screen roughness. A useful feature of rough walls is that a particular value of R_λ can be attained at a particular value of y/δ for a significant smaller free stream velocity relative to a smooth wall. There are consequently less severe experimental constraints in rough wall layers in the context of adequately resolving the small-scale motion.

Acknowledgements

RAA acknowledges the continued support from the Australian Research Council. We would like to acknowledge the contribution from Mr. R. Smalley to the rod roughness experiment and many useful discussions with Dr L. Djenidi in the context of a turbulent boundary layer over the so-called "d-type" surface.

References

ACHARYA, M., BORNSTEIN, J. and ESCUDIER, M. P. 1986. Turbulent boundary layers on rough surfaces, *Expts. in Fluids*, **4**, 33-47.

ANDREOPOULOS, J. and BRADSHAW, P. 1981. Measurements of turbulence structure in the boundary layer on a rough surface, *Boundary-Layer Meteorol.*, **20**, 201-213.

ANSELMET, F., GAGNE, Y., HOPFINGER, E. J. and ANTONIA, R. A. 1984. High order velocity structure functions in turbulent shear flows, *J. Fluid Mech.*, **140**, 63-89.

ANTONIA, R. A., BROWNE, L. W. B. and KIM, J. 1991. Some characteristics of small scale turbulence in a turbulent duct flow, *J. Fluid Mech.*, **233**, 369-388.

ANTONIA, R. A. and SHAFI, H. S. 1998. Small scale intermittency in a rough wall lturbulent boundary layer, *Expts. in Fluids* (to appear)

BANDYOPADHYAY, P. R. 1987. Rough-wall turbulent boundary layers in the transition regime, *J. Fluid Mech.*, **180**, 231-266.

BANDYOPADHYAY, P. R. and WATSON, R. D. 1988. Structure of rough-wall turbulent boundary layers, *Phys. Fluids*, **31**, 1877-1883.

BENZI, R., CILIBERTO, S., TRIPICCIONE, R., BAUDET, C., MASSAIOLI, F. and SUCCI, S. 1993. Extended self-similarity in turbulent flows, *Phys. Rev. E*, **48**, R29-R32.

CLAUSER, F. H. 1954. Turbulent boundary layers in adverse pressure gradient, *J. Aeronaut. Sci.*, **21**, 91-108.

CLAUSER, F. H. 1956. Turbulent boundary layer, *Adv. Appl. Mech.*, **4**, 1-51.

DJENIDI, L. and ANTONIA, R. A. 1997. Reynolds stress producing motions in smooth and rough wall turbulent boundary layer, in R. Panton (ed.) *Self-Sustaining Mechanisms of Wall Turbulence*, Southampton, Computational Mech. Pubs., 181-199.

DVORAK, F. A. 1969. Calculation of turbulent boundary layers on rough surfaces in pressure gradient, *AIAA Jnl.*, **7**, 1752-1759.

ERM, L. 1988. Low Reynolds number turbulent boundary layers, Ph.D. Thesis, University of Melbourne.

HAMA, F. R. 1954. Boundary layer characteristics for smooth and rough surfaces, *Trans. Soc. Naval Arch. Marine Engrs.*, **62**, 333-358.

KIM, J. and ANTONIA, R. A. 1993. Isotropy of the small scales of turbulence at low Reynolds number, *J. Fluid Mech.*, **251**, 219-238.

KIM, J., MOIN, P. and MOSER, R. D. 1987. Turbulence statistics in fully developed channel flow at low Reynolds number, *J. Fluid Mech.*, **177**, 133-166.

KOLMOGOROV, A. N. 1941. Energy dissipation in locally isotropic turbulence, *Dokl. Akad. Nauk. SSSR*, **32**, 19-21.

KOLMOGOROV, A. N. 1962. A refinement of previous hypothesis concerning the local structure of turbulence in a viscous incompressible fluid at high Reynolds number, *J. Fluid Mech.*, **13**, 82-85.

KROGSTAD, P.-Å. and ANTONIA, R. A. 1994. Structure of turbulent boundary layers on smooth and rough walls, *J. Fluid Mech.*, **277**, 1-21.

KROGSTAD, P.-Å. and ANTONIA, R. A. 1998. Surface roughnes effects in turbulent boundary layers (in preparation)

KROGSTAD, P.-Å., ANTONIA, R. A. and BROWNE, L. W. B. 1992. Comparison between rough- and smooth-wall turbulent boundary layers, *J. Fluid Mech.*, **245**, 599-617.

LUMLEY, J. L. and NEWMAN, G. R. 1976. The return to isotropy of homogeneous turbulence, *J. Fluid Mech.*, **82**, 161-178.

ONG, L. and WALLACE, J. M. 1995. Local isotropy of the vorticity field in a boundary layer at high Reynolds number, in R. Benzi (ed.) *Advances in Turbulence V*, Dordrecht, Kluwer Academic Pub., 392-397.

OSAKA, H. and MOCHIZUKI, S. 1988. Coherent structure of a d-type rough wall boundary layer, in M. Hirata and N. Kasagi (eds.) *Transport Phenomena in Turbulent Flows : Theory, Experiment and Numerical Simulation*, New York, Hemisphere, 199-211.

OSAKA, H., NAKAMURA, I. and KAGEYAMA, Y. 1984. Time averaged properties of a turbulent boundary layer over a d-type rough surface, *Trans. Japan Soc. Mech. Eng.*, **50**, 2299-2306

OSAKA, H., NISHINO, T., OYAMA, S. and KAGEYAMA, Y. 1982. Self-preservation for a turbulent boundary layer over a d-type rough surface, *Memoirs of the Faculty of Engineering, Yamaguchi University*, **33**, 9-16.

PERRY, A. E. and ABELL, C. J. 1977. Asymptotic similarity of turbulence structures in smooth- and rough-walled pipes, *J. Fluid Mech.*, **79**, 785-799.

PERRY, A. E., SCHOFIELD, W. H. and JOUBERT, P. N. 1969. Rough-wall turbulent boundary layers, *J. Fluid Mech.*, **37**, 383-413.

PIMENTA, M. M., MOFFAT, R. J. and KAYS, W. M. 1979. The structure of a boundary layer on a rough wall with blowing and heat transfer, *J. Heat Transfer*, **101**, 193-198.

RAUPACH, M. R., ANTONIA, R. A. and RAJAGOPALAN, S. 1991. Rough-wall turbulent boundary layers, *Appl. Mech. Rev.*, **44**, 1-25.

ROTTA, J. C. 1962. Turbulent boundary layers in incompressible flow, in A. Feric, D. Kucheman and L. H. G. Stone (eds.) *Progress in Aeronautical Science*, Oxford, Pergamon, 1-220.

SCHLICHTING, H. 1968. *Boundary Layer Theory*, 6th ed., New YUork, McGraw-Hill.

SHAFI, H.S. and ANTONIA, R. A. 1995. Anisotropy of the Reynolds stresses in a turbulent boundary layer on a rough wall, *Expts. in Fluids*, **18**, 213-215.

SPALART, P. R. 1988. Direct simulation of a turbulent boundary layer up to R_θ = 1410, *J. Fluid Mech.*, **187**, 61-98.

STOLOVITZKY, G. and SREENIVASAN, K. R. 1993. Scaling of structure functions, *Phys. Rev. E*, **48**, R33-R36.

TANI, I. 1986. Some equilibrium turbulent obundary layers, *Fluid Dyn. Res.*, **1**, 49-58.

TANI, I. 1987. Equilibrium, or nonequilibrium, of turbulent boundary layer flows, *Proc. Japan Academy*, **63**, 96-100.

TOWNSEND, A. A. 1976. *The Structure of Turbulent Shear Flow*, CUP.

WOOD, D. H. and ANTONIA, R. A. 1975. Measurements of a turbulent boundary layer over a d-type surface roughness, *J. Appl. Mech.*, **42**, 591-597.

MODELING OF TURBULENT FLOW THROUGH RADIAL DIFFUSER

César J. DESCHAMPS

Departamento de Engenharia Mecânica
Universidade Federal de Santa Catarina
88040–900 Florianópolis – SC, Brazil
e-mail: deschamps@emc.ufsc.br

MODELING OF TURBULENT FLOW THROUGH RADIAL DIFFUSER

Keywords: Radial Diffuser, Renormalization Group k-ε Model

ABSTRACT

The work considers the modeling of turbulent flow in radial diffuser with axial feeding. The flow through the diffuser is characterized by the Reynolds number Re based on the feeding orifice diameter d. Due to its claimed capability to predict flow including features such as recirculation region, curvature and adverse pressure gradient (all of them existing in the flow considered here), the RNG k-ε model of Orzag et al. (1993) has been applied in the present numerical analysis. The governing equations are numerically solved using the finite volume methodology, and the approximation of convective transport was performed using the higher-order accurate QUICK scheme. Experimental results for different values of displacement between the disks and Reynolds number when compared to the numerical solution showed that the RNG k-ε model can provide a good prediction of the flow.

NOMENCLATURE

A_d	Entrance cross sectional area of the diffuser, $[= \pi ds]$
A_f	Cross sectional area of the feeding orifice, $[= \pi d^2 / 4]$
d	Orifice diameter
D	Front disk diameter
I	Turbulence intensity, $[= \sqrt{\overline{uu}} / U_{in}]$
e	Orifice length
$\dot{m}$	Mass flow rate
p	Pressure, also step height in Fig. 1
p^*	Dimensionless pressure, $[= 2p / \rho \overline{U}_{in}^2]$
p_{atm}	Atmospheric pressure
r,x	Cylindrical coordinates
Re	Reynolds number based on the orifice diameter, $[= \rho \overline{U}_{in} d / \mu]$
s	Displacement between the disks
t	Step width
u,v	Velocity components
$\overline{U}_{in}$	Average velocity in the orifice
y+	Dimensionless distance from the wall, $[= \rho u^* y / \mu]$
u^*	Wall-friction velocity $[= \sqrt{\tau_w / \rho}]$

Greek Symbols

μ	Air absolute viscosity
ρ	Air density
ψ^*	Dimensionless stream-function $[= \psi / \dot{m}]$

INTRODUCTION

A three dimensional schematic view of a radial diffuser and the geometric parameters that govern the flow, including a backward facing radial step (not shown in the 3-D view), are shown in Figs. 1a and 1b, respectively. The fluid enters the diffuser flowing axially through the feeding orifice, hits the front disk, and after being deflected by it a radial flow is established. The impact of the flow on the front disk produces a bell-shape pressure distribution and, depending on the gap between the disks and on the flow Reynolds number, negative pressure regions can occur.

The radial diffuser geometry of Fig. 1 represents a basic configuration for many engineering flows. Examples include reed type valves of reciprocating compressors (Prata and Ferreira, 1990), aerostatic bearings (Hamrock, 1994), vertical take off and landing aircrafts with centrally-located downward pointing jets (Moller, 1963), electro-discharge machining (Osenbruggen, 1969), aerosol impactors used as inertial separation device for collecting air borne particles (Marple et al. 1974), injection molds used for polymer processing (Pearson, 1966), pilot valves employed in hydraulic and pneumatic components (Hayashi et al., 1975), and prosthetic valves used to replace diseased natural heart valves in humans (Mazumdar and Thalassoudis, 1983).

Despite the numerous works related to laminar radial flows, very little attention has been given to

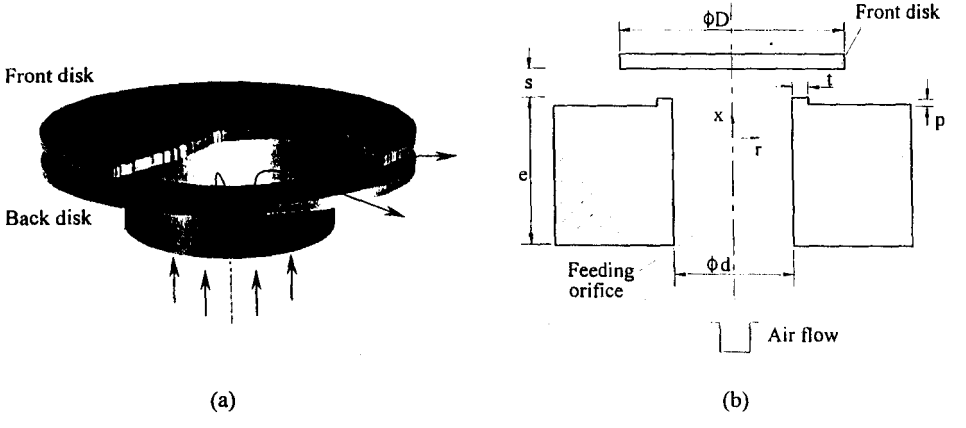

Figure 1 - Geometry of radial diffuser with axial feeding.

turbulent flows. For references on laminar radial flow the interested reader is referred to Hayashi et al. (1975), Wark and Foss (1984), Ferreira et al. (1989), Gasche et al. (1992) Prata et al. (1995), Possamai et al. (1996), and the literature cited therein.

The few works dealing with radial turbulent flow focused on pure radial flow between parallel disks without considering the inlet (Ervin et al., 1989 and Tabatabai and Pollard, 1987). Apparently, the first attempt to solve the turbulent flow in axially feeding radial diffusers was made by Deschamps et al. (1988). There it was found that the high Reynolds number k-ε model used to close the averaged Navier-Stokes equations was unable to predict the flow, even with the inclusion of correction terms to take into account effects such as flow curvature. The poor quality of the numerical solution was attributed to the wall-functions needed in the model. This was confirmed later when a low Reynolds number k-ε model, which does not use wall-functions, produced better flow predictions (Deschamps et al. 1989). Nevertheless, even for this model there were significant differences between experiments and computations. In reality, the k-ε model is known to produce excessive turbulence in the presence of adverse pressure gradient, as is the case at the entrance of the radial diffuser. This leads to an overprediction of turbulence intensity and to delay, or even suppress, any eventual flow separation hinted at by the laboratory measurements.

The main goal of the present paper is to perform a numerical simulation with experimental validation of the turbulent flow through the geometry depicted in Fig. 1. Due to the claimed capability to predict flows that include features such as stagnation and recirculation regions, curvature and adverse pressure gradients (all of them present in the flow considered here) the RNG k-ε model of Orzag et al. (1993) was adopted in this work.

EXPERIMENTAL SETUP AND PROCEDURE

A careful experimental setup was built to measure the pressure distribution on the front disk as a function of the Reynolds number, Re, and the displacement between the disks, s. Of paramount importance in the experiments was the correct adjustment of the displacement to the desired value

due to the strong influence of this parameter on the flow field. The uncertainty associated to the experimental data is less than 5%. A description of both the experimental setup and procedure will not be presented here due to space limitations, but can be found in Possamai et al. (1995).

TURBULENCE MODELING

The foundation of most turbulence models is the time/ensemble averaging of the flow transport equations, where the turbulent component of any property is defined as the departure from its time/ensemble averaged value. For an isothermal and incompressible flow under the effect of no body force the equations of motion (here written in Cartesian tensor notation) are:

Mass conservation,

$$\frac{\partial U_i}{\partial x_i} = 0 \quad , \tag{1}$$

Momentum conservation for the U_i component of velocity,

$$U_i \frac{\partial U_j}{\partial x_i} = -\frac{1}{\rho}\left(\frac{\partial P}{\partial x_j}\right) + \frac{\partial}{\partial x_i}\left[\nu \frac{\partial U_j}{\partial x_i} - \overline{u_i u_j}\right] \quad . \tag{2}$$

The term $\overline{u_i u_j}$ appearing in the above equation is the Reynolds stress tensor and is never negligible in any turbulent flow. Equations (1) and (2) can only be solved if the Reynolds stresses are known, a problem referred to as the 'closure problem' since the number of unknowns is greater than the number of equations. A brief account of some common techniques used to close Eq. (2) is given below. A good review of several other methods is provided by Markatos (1986).

Reynolds Stress Models

By manipulating the Navier-Stokes equation for instantaneous velocity it is possible to obtain a transport equation for the Reynolds stress $\overline{u_i u_j}$. However, the resulting set of equations is not closed since they include higher order correlations, such as the third order moments $\overline{u_i u_j u_k}$, as well as correlations between fluctuating velocities and pressure. Any attempt to provide transport equations for these higher order correlations leads to the appearance of even higher correlations and, consequently, to a dramatic increase in the computing time required to calculate flows. For this reason, most works using this level of modeling have used transport equations for second order correlations and simple algebraic expressions to approximate the triple-moments and the correlations between fluctuating velocities and pressure. Models for closing the Reynolds stress transport equations, following the aforementioned procedure, were proposed quite early (see for instance Rotta, 1951).

A considerable obstacle for the use of Second Moment closures is the modeling of the near-wall region and, despite much effort have been directed to the solution of the problem, progress has not reached the point for the full benefit of flow in complex geometries as the one considered here. On the other hand, the employment of wall-functions, to bridge the whole of the near-wall sublayer where viscous effects are significant, is unsuitable for the present flow situation, as hinted at by previous works (Deschamps et al., 1989). This is mainly related to the numerical aspect and caused by the condition of minimum turbulence level that must be observed when using wall-functions (for practical reasons usually fixed as $y^+ \approx 11.6$). Naturally, in flows where important features occur close to the walls it is quite difficult to balance the needed grid resolution against the minimum value for y^+. Given the foregoing reasons and in order to predict the flow in radial diffusers it seems to be essential to avoid the use of wall-functions and to include the near-wall region in the calculations.

Eddy Viscosity Models

The assumption that turbulence is proportional to the velocity gradient, acting like the viscous stresses, was first made by Boussinesq, who introduced the concept of a 'turbulent' or 'eddy' viscosity ν_t. A generalized form of the Boussinesq's hypothesis, proposed by Kolmogorov, is as follows:

$$\overline{u_i u_j} = -\nu_t \left[\frac{\partial U_i}{\partial x_j} + \frac{\partial U_j}{\partial x_i} \right] + \frac{2}{3}\delta_{ij} k \quad , \tag{3}$$

where δ_{ij} is the Kronecker delta and the kinetic energy of the turbulent motion, k, is defined as $k = (\overline{u_i u_i})/2$. Substitution of Eq. (3) into Eq. (2) results in the averaged Navier-Stokes equations with the Reynolds stresses modeled via the viscosity concept:

$$U_j \frac{\partial U_i}{\partial x_j} = -\frac{1}{\rho}\frac{\partial}{\partial x_i}\left(p + \frac{2}{3}\rho k \right) + \frac{\partial}{\partial x_j}\left[\nu_{eff} \left(\frac{\partial U_i}{\partial x_j} + \frac{\partial U_j}{\partial x_i} \right) \right] \tag{4}$$

where $\nu_{eff} = \nu + \nu_t$. By far the most common choice for calculating of ν_t has been that in terms of the turbulence kinetic energy k and its rate of dissipation, ε, i.e.

$$\nu_t = C_\mu \frac{k^2}{\varepsilon} \quad . \tag{5}$$

Models of this kind were originally proposed by Harlow and Nakayama (1968) and subsequently refined by Launder and Spalding (1972). Later, Jones and Launder (1972) included low-Reynolds-number effects into the k-ε model (by making certain coefficients dependent on the turbulent

Reynolds number) so that it can be used to compute near-wall flows as well as those where wall effects are not present.

Due to its robustness, economy and acceptable results for a considerable amount of flows the k-ε model has been the most used model for numerical predictions of industrial flows. However, it is known to have deficiencies in some situations involving streamline curvature, acceleration and separation; all of them are present in the case of flow through radial diffusers. For instance, turbulence is very sensitive to small amounts of curvature of the streamlines; see Bradshaw(1973). The effects of curvature tend to increase the magnitude of the turbulence shear stress where the angular momentum of the flow decreases in the direction of the radius of curvature, and to decrease when the angular momentum increases with the radius. Hence, for example, on a typical turbomachine blade the skin friction may be reduced by the curvature on the convex surface by as much as 20 % and increased on the concave surface by a comparable amount. Such effects cannot be accounted for in turbulence models based on the simple eddy-viscosity hypothesis unless some ad hoc extra terms be introduced into the equations (it is opportune to state that the Reynolds stress equations, in the case of curved streamline flows, contain in exact form extra-strain production terms that account for the curvature). Moreover, in the presence of adverse pressure gradient regions, the equation for ε is known not to be capable of responding to the surge of kinetic energy, returning an excessive level of turbulence that can lead to a delay of an eventual flow separation or even to a total suppression of it, as pointed out by Rodi and Scheuerer (1986). Finally, in the case of separated flows Simpson et al. (1981) found that the Reynolds shearing stresses must be modelled by relating them to the turbulence structure and not to the local mean velocity gradients.

A new form of k-ε model has been proposed by Orzag et al. (1993) and was derived from the original governing equations for the fluid motion using Renormalization Group (RNG) methods. The novelty of the so called RNG k-ε model, compared to the standard k-ε model, is that constants and functions are evaluated by the theory and not by empiricism and that the model can be applied to the near-wall region without recourse to wall-functions or ad-hoc function in the transport

equations of the turbulence quantities. Due to this mathematical foundation, compared to the semi-empirical approaches adopted in the standard k-ε, Orzag and his colleagues argue that the RNG k-ε model offers a wider range of applicability. Some examples of flows where the RNG k-ε model has been seen to return better predictions than the standard k-ε are those including flow separation, streamline curvature and flow stagnation. As pointed out before, all these flow features are present in the case of radial diffusers and, therefore, it seemed natural to adopt the RNG k-ε model in the present work.

The effective viscosity in the RNG k-ε model is given by

$$\nu_{eff} = \nu\left[1+\sqrt{\frac{C_\mu}{\nu}}\frac{k}{\sqrt{\varepsilon}}\right]^2 \quad , \tag{6}$$

which is valid across the full range of flow conditions from low to high Reynolds numbers. The turbulence kinetic energy k and its dissipation ε appearing in Eq. (3) are obtained from the following transport equations:

$$U_j\frac{\partial k}{\partial x_j} = \frac{\partial}{\partial x_j}\left[\alpha\nu_{eff}\frac{\partial k}{\partial x_j}\right] + \nu_t S^2 - \varepsilon \quad , \tag{7}$$

$$U_j\frac{\partial \varepsilon}{\partial x_j} = \frac{\partial}{\partial x_j}\left[\alpha\nu_{eff}\frac{\partial \varepsilon}{\partial x_j}\right] + C_{\varepsilon 1}\frac{\varepsilon}{k}\nu_t S^2 - C_{\varepsilon 2}\frac{\varepsilon^2}{k} - R \quad , \tag{8}$$

where the values of $C_{\varepsilon 1}$ e $C_{\varepsilon 2}$ are equal to 1.42 and 1.68; respectively. The inverse Prandtl number α for turbulent transport is given by the following relationship:

$$\left|\frac{\alpha-1.3929}{\alpha_o-1.3929}\right|^{0.6321}\left|\frac{\alpha+2.3929}{\alpha_o+2.3929}\right|^{0.3679}=\frac{\nu}{\nu_{eff}}\quad , \tag{9}$$

with $\alpha_o = 1.0$. The rate of strain term, R, is given by

$$R=\frac{C_\mu\eta^3(1-\eta/\eta_0)}{1+\beta\eta^3}\frac{\varepsilon^2}{k}\quad , \tag{10}$$

where $\eta = Sk/\varepsilon$, $\eta_o \approx 4.38$, $\beta = 0.012$ and $S^2 = 2S_{ij}S_{ij}$ in which S_{ij} is the rate of strain tensor. In regions of small strain rate, the term R has a trend to increase ν_{eff} somewhat, but even in this case ν_{eff} still is typically smaller than its value returned by the standard k-ε model. In regions of elevated strain rate the sign of R becomes negative and ν_{eff} is considerably reduced. This feature of the RNG k-ε is responsible for substantial improvements verified in the prediction of large separation flow regions.

Also the reduced value of $C_{\varepsilon 2}$ in the RNG theory , compared to the value of 1.9 used in the standard k-ε turbulence model, acts to decrease the rate of dissipation of ε, leading to smaller values of ν_{eff}.

Boundary conditions

Boundary conditions at inlet, walls, axis of symmetry and outlet are required to solve Eqs. (4),(6) and (7). For the inlet boundary it was recognized by Ferreira et al. (1989) that, as the flows exits the feeding orifice of area A_f and enters the diffuser of area A_d , the strong reduction of the passage area given by the ratio $A_d / A_f = 4s/d$ brings about a strong flow acceleration next to the orifice wall for small values of s/d. Due to this phenomenon the inflow velocity profile at the feeding orifice plays no role in the solution of the flow field in the diffuser; therefore, the inlet boundary condition

was specified as $U=U_{in}$ and $V=0$. Although no information is available for the turbulence kinetic energy, numerical tests indicated that when the level of the turbulence intensity was increased from 3% to 6% no significant change was observed in the predicted flow. Therefore, a value of 3% of turbulence intensity was used in the calculation of all results shown in this work. Finally, the distribution of the dissipation rate was estimated based on the assumption of equilibrium boundary layer, that is

$$\varepsilon = C_\mu^{3/4} k^{3/2} / \ell_m \quad , \tag{11}$$

where C_μ=0.09, and the mixing length was calculated using an empirical coefficient for turbulent pipe flow, that is, $\ell_m = 0.07d/2$.

At the solid boundaries the condition of no-slip and impermeable wall boundary condition were imposed for the velocity components, that is, U=V=0, with calculations being extended up to the walls across the viscous sublayer. For the turbulence quantities k and ε rather than prescribing a condition at the walls, they were calculated in the control volume adjacent to the wall following a two-layer based non-equilibrium wall-function. In the plane of symmetry, the normal velocity and the normal gradients of all other quantities were set to zero.

At the outlet boundary two different procedures had to be adopted. For D/d = 3 the diffuser exit is far enough downstream and a condition of parabolic flow can be assumed. Yet, for the much smaller ratio, D/d = 1.45, this is not possible and, therefore, the solution domain had to be extended well beyond the diffuser exit and the atmospheric pressure verified in the experiment was set to the outlet. The boundary condition for k in this case was fixed according to a turbulence intensity of 3% whereas the dissipation rate was estimated based on the same assumption of equilibrium boundary layer used at the orifice inlet, Eq. (11). Given the wall jet characteristic of the flow exiting the diffuser it is expected that any eventual inaccuracy of the above outlet conditions will not have a significant impact on the numerical solution.

NUMERICAL METHODOLOGY

The numerical solution of the governing equations was performed using the commercial computational fluid dynamics code FLUENT, version 4.2 (1993). In this code the conservation equations for mass, momentum and turbulence quantities are solved using the finite volume discretization method (Patankar, 1981). For this practice the solution domain is divided in small control volumes, using a non-staggered grid scheme, and the governing differential equations are integrated over each control volume with use of Gauss' theorem. The resulting system of algebraic equations is solved using the Gauss-Seidel method and the SIMPLE algorithm.

In the finite volume method, interpolation at the control volume faces of properties transported by convection can be of primary importance on the accuracy of the numerical results. The classical approach of first order accurate upwind differencing usually suffers from severe inaccuracies in complex flow situations originated by truncation errors and streamline-to-grid skewness. A consequence of the first is that the only truncation-error-free problems are those whose solutions vary almost linearly with the grid index in the streamwise direction. The second source of error occurs where the vector velocity is not aligned with the grid lines (as in recirculating flow regions), and usually is referred to as false diffusion. Recirculating regions of course are a common feature in radial diffusers and, therefore, such flow situations are susceptible to this sort of error. An effective approach to reduce truncation error, while still maintaining the grid size within computational resource limits, is the introduction of a more accurate differencing scheme into the numerical analysis. In the present work, the QUICK scheme was adopted in the solution of the momentum equations, yielding a second order accuracy for the interpolated values. Yet, for the transport equations of turbulence quantities the Power Law Differencing Scheme (PLDS) of Patankar (1980) was adopted since the unboundedness of the QUICK scheme usually introduces serious numerical instabilities, causing calculations to diverge. Nevertheless, there is some evidence (Craft, 1991) that in the case of these equations the source terms are dominant, with the convective terms playing secondary role.

Two grid levels (70x80 and 100x140, axial x radial) were used to assess the numerical truncation error. The refinement was mainly promoted in the entrance of the diffuser, where flow property gradients are steeper. Of great help to this test was some evidence of the discretization needed for the analysis and made available by Deschamps et al. (1989) and Possamai et al. (1995).

Because of the strong non-linearity of the equations, under relaxation coefficients were required. For the velocity components these coefficients were 0.15, for pressure 0.25 and for the turbulence quantities 0.2. At the very first interaction of the numerical procedure the sum of the residual of all algebraic equations (all five variables included) was on the order of one; convergence was stopped when this sum was less than $5x10^{-4}$.

RESULTS AND DISCUSSIONS

The flow through the radial diffuser in Fig. 1 was investigated for three displacements, s/d (=0.05, 0.07 and 0.10), three Reynolds number, Re (=10,000; 20,000 and 40,000), and two diameter ratios, D/d (=1.45 and 3). Additionally, for D/d=1.45, the effect of a backward facing radial step in the back disk was also considered (p/d=0.039 and t/d=0.138, according to Fig. 1).

Numerical Solution Validation

The numerical solution was validated by means of sensitivity tests of the results with respect to grid refinement and boundary conditions. The numerical solution is expected to represent thus a pure prediction of the flow through the turbulence model, for which an assessment was possible by a comparison between numerical results and experimental data. The numerical validation and the turbulence model assessment were conducted with reference to results of pressure distribution on the front disk.

Figure 2 shows the result emerging from the sensitivity tests. In Fig. 2a results of radial pressure distribution on the disk surface yielded by two different levels of grid refinement (70x80 and 100x140) are compared for the flow situation D/d=3 and Re=20,100. It is clear that both results are virtually the same, and hence, in order to reduce computing times the less refined grid will be used in the remaining calculations. Another source of uncertainty that had to be investigated is related to the inlet boundary condition for turbulence at the entrance of the feeding orifice since the experimental setup used in this work cannot provide such information. Because the flow upstream of the test section follows a straight smooth pipe, it was assumed that levels of turbulence are moderate and therefore the levels of turbulence intensity I tested were 0.03 and 0.06. The result of the test (Fig. 2b) shows that the pressure distribution on the disk surface was not significantly affected by the variation in the level of turbulence intensity. A value of I = 0.03 will be adopted for the remaining calculations.

Assessment of the Turbulence Model

Figures 3 to 5 show the radial pressure distribution along the front disk surface obtained from the experiments and computations for a variety of flow geometries. In all situations the pressure profile exhibits a plateau on the central part of the curve ($r/d < 0.5$), as previously verified for the laminar

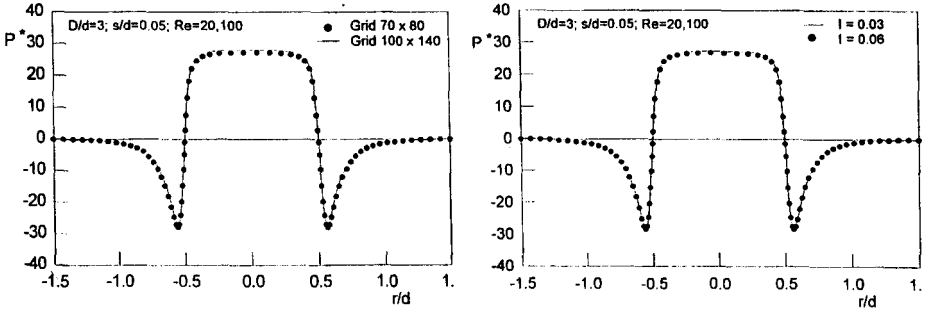

(a) Computational mesh refinement (b) Turbulence intensity at the inlet

Figure 2 – Sensitivity of results for pressure distribution to numerical parameters.

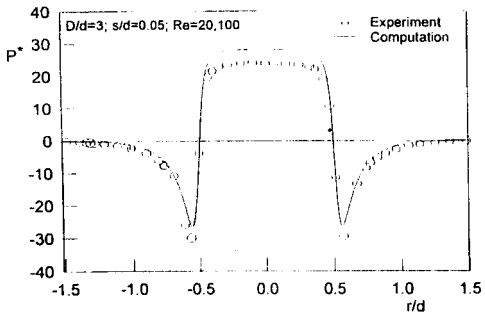

(a)

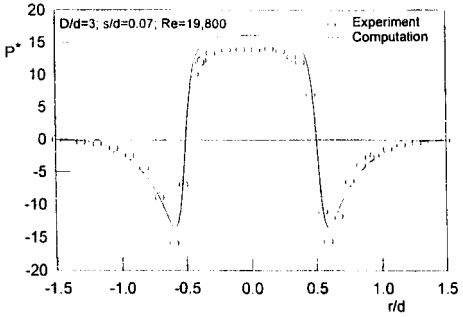

(b)

Figure 3 - Numerical and experimental results for pressure distribution; D/d=3.

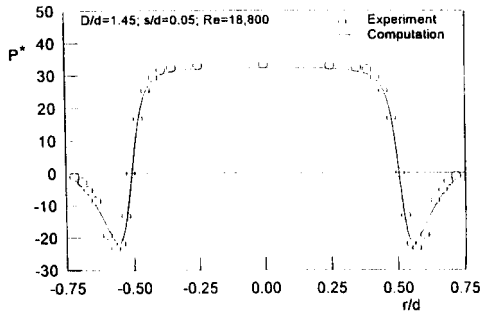

(a)

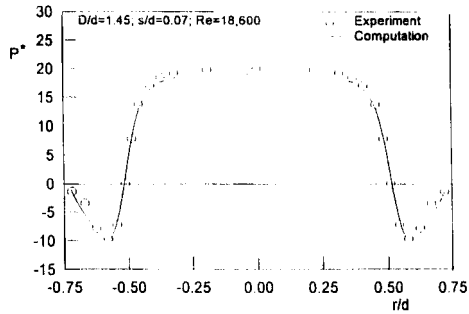

(b)

Figure 4 - Numerical and experimental results for pressure distribution; D/d=1.45.

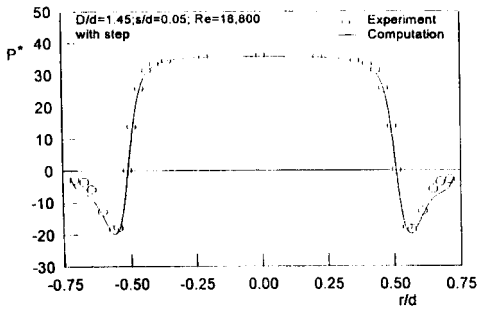

(a)

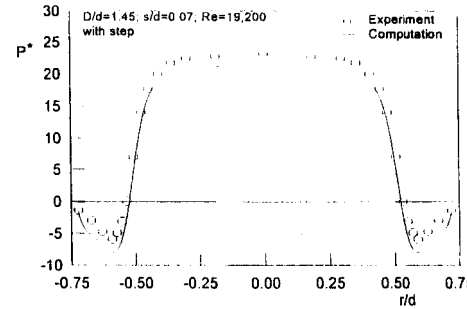

(b)

Figure 5 - Numerical and experimental results for pressure distribution; D/d=1.45; with step.

flow by Ferreira and Driessen (1986) and Ferreira et al. (1989). Also similar to the laminar flow is the sharp pressure drop at the radial position r/d ≈ 0.5, which is due to the change in the flow direction. For the outer part of the curve (r/d>0.5) the pressure level never recovers a positive value, a situation which is also verified in the laminar flow for combinations of both large displacement and high Reynolds number.

For the diameter ratio D/d=3 (Figs. 3a and b) the pressure level goes to almost zero for regions r/d > 1.25. This is not the case for the smaller diameter ratio D/d=1.45 where the pressure even at the exit of the diffuser is seen not to reach the atmospheric condition, but still remains negative. The reason for this being that in the latter case the diffuser does not have sufficient length to allow for complete pressure recovery, which does not defy expectation. The effect on the flow of the backward facing radial step is explored in Figs. 4 (without step) and 5 (with step). For the situations investigated here, the influence of the step is small. However, a careful examination of Figs. 4 and 5 suggests as a consequence of the step, a small increase in the pressure values for r/d>0.5.

The good agreement between experiments and computations seen in Figs. 3 to 5 provided confidence in the turbulence model. Thus, the next step in the analysis was to generate numerical simulations for flow situations not included in the experimental investigation. The computations were then conducted for D/d=1.45 without the backward facing radial step, considering three displacements (s/d=0.05, 0.07 and 0.10) and two Reynolds numbers (Re=10,000 and 40,000). The results plotted in Figs. 6a and b at first sight show no significant difference between the pressure distributions on the valve surface for the two Reynolds numbers explored. However, a first distinction between the curves is that for increasing Re values, the magnitude of the negative pressure profiles decreases. To support the explanation for this feature Fig. 7 was prepared. In this figure dimensionless stream-function contours are plotted at the entrance of the diffuser for s/d=0.05 and 0.10 at two flow rate conditions (Re=10,000 and 40,000). For the smaller value of s/d the flow is seen to separate at r/d ≈ 0.5 and to reattach downwards inside the diffuser. As the gap

between the disks is increased to 0.10, and the flow inertia becomes stronger, the separation region is increased and the recirculating zone moves into the diffuser exit. Since the negative pressure values are dictated by the flow passage area in the diffuser, the rise in those values with increasing values of Re is a direct consequence of the growth of the separated flow region in the diffuser.

Another important detail of Fig. 6 is disclosed with the help of Fig. 8. There the pressure distributions for Re = 10,000 and 40,000, normalized by the pressure value at the center of the front disk (r/d=0), are presented for s/d =0.05 and 0.10. The figure shows that the pressure drop at r/d ≈ 0.5 is more pronounced for smaller displacements. This is an expected result since as the gap between the disks increases, the change in the flow direction at r/d ≈ 0.5 becomes less stiff. Additionally, for s/d=0.05 an increase in the Reynolds number brings about a considerable enhancement of the negative region in the pressure distribution, whereas, for s/d=0.10, the Reynolds number effect in the shape of the pressure distribution is much less prominent. This feature is related to the size of the separated flow region in the diffuser, as can be noticed from Fig. 7.

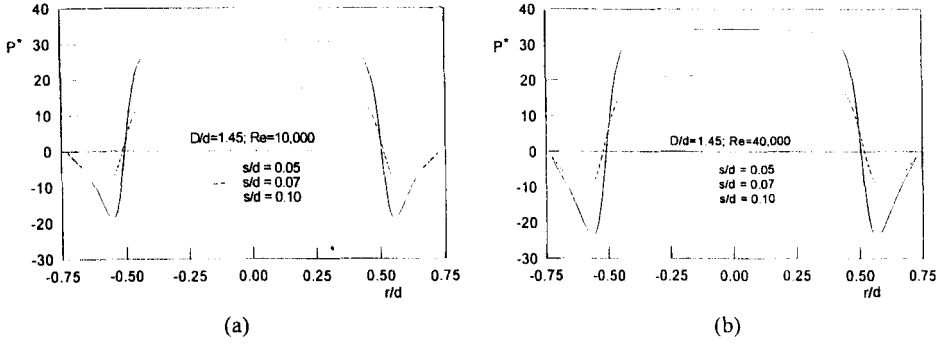

Figure 6 - Numerical results for pressure distribution on valve reed; D/d=1.45.

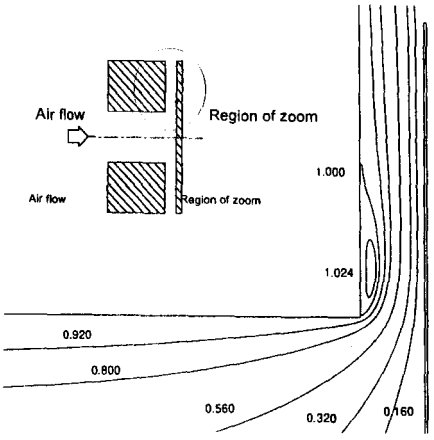

(a) s/d=0.05; Re=10,000

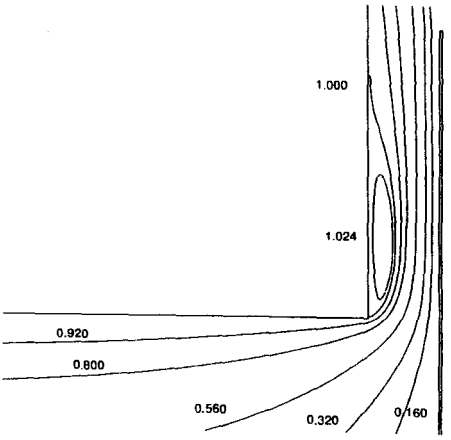

(b) s/d=0.05; Re=40,000

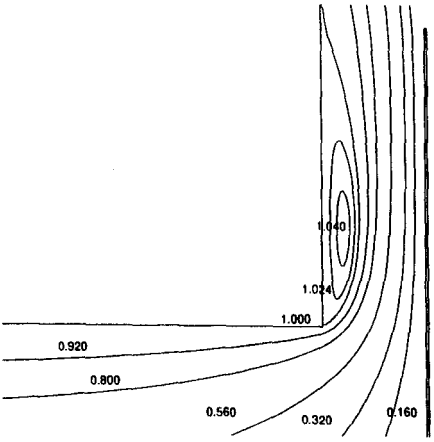

(c) s/d=0.10; Re=10,000

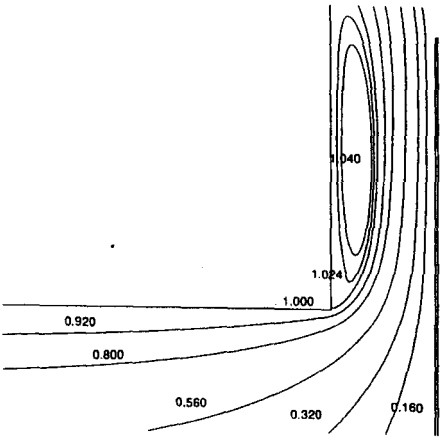

(d) s/d=0.10; Re=40,000

Figure 7 - Stream-function contours at the diffuser entrance, D/d=1.45.

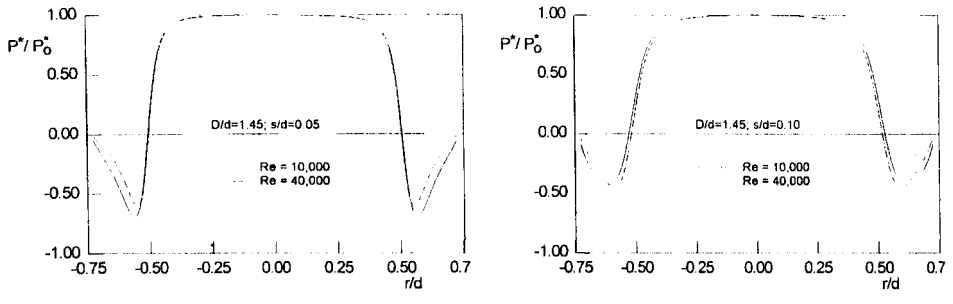

Figure 8 - Results of normalized pressure distributions on valve reed; D/d=1.45.

CONCLUSIONS

The present work has presented a numerical and experimental investigation of the incompressible turbulent and isothermal flow in a radial diffuser. This is the basic flow problem associated with several engineering flows, such as automatic valve reeds of reciprocating compressors, aerostatic bearings and aerosol impactors. The flow was analyzed for different parameters such as Reynolds number, diameter ratios and gap between the disks.

The RNG k-ε turbulence model used to predict the flow was found to reproduce well the experimental results. It should be mentioned though that a complete assessment of the turbulence model would require comparisons between numerical results and experimental data of turbulence quantities, such as Reynolds stresses. This could not be addressed in the present work due to limitations of the experimental setup.

One of the main features observed in all flow situations is the presence of a separated flow region in the diffuser. This contributes greatly to the negative pressure region observed along the entire diffuser on the front disk surface. For the cases investigated here, it seems that as the gap between the disks is increased the shape of the pressure distribution on the disk surface becomes less and less dependent on the Reynolds number and the gap itself.

REFERENCES

Bradshaw, P., 1973, "Effects of streamline curvature on turbulent flow", NATO, AGARD monograph No. 169.

Craft, T. J., 1991, "Second-moment modeling of turbulent scalar transport", Ph.D. Thesis, UMIST, England.

Deschamps, C.J., Ferreira, R.T.S and Prata, A.T. 1988, "Application of the k-ε Model to Turbulent Flow in Compressor Valves", Proc. 2nd Brazilian Thermal Science Meeting, São Paulo, pp. 259-262 (in Portuguese).

Deschamps, C.J., Prata, A.T. and Ferreira, R.T.S., 1989, "Turbulent Flow Modeling in Presence of Stagnation, Recirculation, Acceleration and Adverse Pressure Gradient", Proc. X Brazilian Congress of Mechanical Engineering, Rio de Janeiro, Vol. I, pp. 57-60 (in Portuguese).

Ervin, J. S., Suryanarayana, N. V. and Ng, H. C., 1989, "Radial, Turbulent Flow of a Fluid Between Two Coaxial Disks", ASME J. Fluids Eng., Vol. 111, pp. 378-383.

Ferreira, R. T. S. and Driessen, J. L., 1986, "Analysis of the Influence of Valve Geometric Parameters on the Effective Flow and Force Areas", Proc. 9th Purdue Int. Compressors Technology Conference, West Lafayette, USA, pp. 632-646.

Ferreira, R. T. S., Deschamps, C. J. and Prata, A. T., 1989, "Pressure Distribution Along Valve Reeds of Hermetic Compressors", Experimental Thermal and Fluid Sciences, Vol. 2, pp. 201-207.

Gasche, J. L., Ferreira, R. T. S. and Prata, A. T., 1992, "Pressure Distributions Along Eccentric Circular Valve Reeds of Hermetic Compressors", Proceedings of the International Compressor Engineering Conference at Purdue, West Lafayette, USA, Vol. IV, pp. 1189-1198.

Hamrock, B. J., 1994, "Fundamentals of Fluid Film Lubrication", McGraw-Hill.

Harlow, F. H. and Nakayama, P. I. 1968, "Transport of Turbulence Energy Decay Rate", Rep. LA 3854, Los Alamos Sci. Lab.

Hayashi, S., Matsui, T. and Ito, T., 1975, "Study of Flow and Thrust in Nozzle-Flapper Valves", ASME J. Fluids Eng., Vol. 97, pp. 39-50.

Jones, W. P. and Launder, B. E., 1972, "The Calculation of Low-Reynolds-Number Phenomena with a Two-Equation Model of Turbulence", J. Heat Mass Transfer, Vol. 16, pp. 1119-1130.

FLUENT, 1993, Fluent Inc., Centerra Resource Park, 10 Cavendish Court, Lebanon, NH 03766.

Launder, B. E. and Spalding, D. B., 1972, "Lectures in Mathematical Models of Turbulence", Academic Press.

Markatos, N. C., 1986, "The Mathematical Modelling of Turbulent Flows", Appl. Math. Modelling, Vol.10, pp.190-220.

Marple, V. A., Liu, B. Y. H. and Whitby, K. T., "Fluid Mechanics of the Laminar Flow Aerosol-Impactors", Aerosol Science, Vol. 5, pp. 1-16.

Mazumdar, J. and Thalassoudis, K., 1983, "A Mathematical Model for the Study of Flow Through Disc-Type Prosthetic Heart Valves", Medical and Biological Engineering, Vol. 21, pp. 400-409.

Moller, P. S., 1963, "Radial Flow Without Swirl Between Parallel Discs", The Aeronautical Quartely, May, pp. 163-186.

Orzag, S. A., Yakhot, V. Flannery, W. S., Boysan, F., Choudhury, D. Marusewski, J., Patel, B. 1993, "Renormalization Group Modeling and Turbulence Simulations", So, R. M. C., Speziale, C. G. and Launder, B. E. (eds.), Near-wall turbulent flows. Elsevier Science Publisher,

Osenbruggen, C. V., 1969, "High Precision Spark Machining", Philips Technical Review, Vol. 30, pp. 195-208.

Pearson J. R. A., 1966, "Mechanical Principles of Polymer Melt Processing", Oxford, Pergamon Press.

Patankar, S. V., 1980, "Numerical Heat Transfer and Fluid Flow", Washington D. C., Hemisphere Publ. Corp.

Possamai, F. C., Ferreira, R. T. S. and Prata, A. T.,1995, "Pressure Distribution in Laminar Radial Flow Through Inclined Valve Reeds", ASME International Mechanical Engineering

Congress, Heat Pump and Refrigeration Systems Design, Analysis and Applications, AES Vol.34, pp. 107-119.

Prata, A. T. and Ferreira, R. T. S, 1990, "Heat Transfer and Fluid Flow Considerations in Automatic Valves of Reciprocating Compressors", Proceedings of the 1990 International Compressor Engineering Conference, West Lafayette, USA, Vol. I, pp. 512-521.

Prata, A. T., Pilichi, C. D. M. and Ferreira, R. T. S., 1995, "Local Heat Transfer in Axially Feeding Radial Flow Between Parallel Disks", ASME J. of Heat Transfer, Vol.117, pp. 47-53.

Rodi, W. and Scheuerer, G., 1986, "Scrutinizing the k-ε Turbulence Model under Adverse Pressure Gradient Conditions", ASME J. Fluids Engng., Vol. 108, pp. 174--179.

Rotta, J. A 1951, "Statistische theorie nichthomogener turbulenz", Z. Phys., Vol. 129, pp. 547.

Simpson, R.L., Chew, Y-T and Shivaprasad, B.G., 1981, "The Structure of a Separating Turbulent Boundary Layer. Part 1. Mean Flow and Reynolds Stresses", J. Fluid Mechanics, Vol. 113, pp. 23-51.

Tabatabai, M. and Pollard, A., 1987, "Turbulence in Radial Flow Between Parallel Disks at Medium and Low Reynolds Numbers", J. Fluid Mechanics, Vol. 185, pp. 483-502.

Wark, C. E. and Foss, J. F., 1984, "Forces Caused by the Radial Outflow Between Parallel Disks", ASME J. Fluids Eng., Vol. 106, pp. 292 - 297.

TRANSITION TO TURBULENCE OF LOW AMPLITUDE THREE-DIMENSIONAL DISTURBANCES IN FLAT PLATE BOUNDARY LAYERS

Marcello A. F. de MEDEIROS

Departamento de Engenharia Mecânica
Pontifícia Universidade católica de Minas Gerais
Av. Dom José Gaspar, 500
30535–610 Belo Horizonte – MG, Brazil
e-mail: marcello@mea.pucminas.br

TRANSITION TO TURBULENCE OF LOW AMPLITUDE THREE-DIMENSIONAL DISTURBANCES IN FLAT PLATE BOUNDARY LAYERS

Departamento de Engenharia Mecânica
Pontifícia Universidade Católica de Minas Gerais
Av. Dom José Gaspar, 500, Belo Horizonte, 30535-610 - MG - Brazil
e-mail: marcello@mea.pucminas.br

SUMMARY

This paper presents results of an experimental study of the nonlinear evolution of a three-dimensional Tollmien-Schlichting wavetrain excited by a harmonic point source in a flat plate boundary layer. The three-dimensional wavetrains behaved very differently from two-dimensional ones. In particular, the first sign of nonlinearity to appear was not a subharmonic mode, but a mean flow distortion. This distortion had a spanwise structure consisting of regions of positive and negative mean distortion distributed like longitudinal streaks, which became more complex as the nonlinearity developed. The observations suggest that the early stages of the nonlinear interaction may be explained by a weakly nonlinear mechanism. The subsequent stages seem to involve mechanisms that are as yet not known.

1 Introduction

Owing to its importance in fundamental and applied fluid mechanics, the laminar turbulent transition has attracted the attention of many researchers. Over the years many aspects of the phenomenon have been understood, but there are still important areas where further research is needed. Among the less researched areas is the so called natural transition. This area is concerned with the transition process that originates from randon disturbances that are always present in natural conditions. Recent studies (Gaster 1978, Shaikh 1997, Medeiros & Gaster 1997, Medeiros & Gaster 1998) have shown that the transition that is observed in such environments display some features that are not observed when the most commonly studied case of periodic plane disturbances are used to drive the process.

It apears that the streamwise modulation and the three-dimensionality that characterise the natural transition give rise to nonlinear inteactions that dp not occur for regular plane wavetrains. The cited previous works have studied either wavepackets or white noise which display the combined effects of streamwise modulation and three-dimensionality. The complexity of the nonlinear interaction observed has made it difficult to interpret the results.

At first it appeared that the important ingredient was the streamwise modulation, rather than the spanwise modulation, that is, the three-dimensionality (Gaster 1984, Medeiros & Gaster 1994, Medeiros & Gaster 1995). However numerical simulations of two-dimensional wavepackets by Medeiros (1996) have shown that spanwise modulation is essential to the process. The current paper focuses on the effect of three-dimensionality alone by investigating the nonlinear evolution of a wavetrain emanating from a point source. Preliminary results of this investigation have been presented by Medeiros (1996, 1997, 1998)

Investigations of three-dimensional wavetrains in shear layers have also been carried out by other researchers (Kachanov 1985, Mack 1985, Seifert 1990, Seifert & Wygnanski 1991, Wiegand, Bestek, Wagner & Fasel 1995), but these were restricted to the linear regime.

2 Experimental Results

The current experiments were conducted in the low turbulence wind tunnel of the University of Cambridge, Cambridge, UK [1]. Details of the experiemental set-up and precedures can be found in Medeiros (1996, 1997, 1998)

In experiments with wavetrains the flow is usually disturbed by a continuous harmonic source. In the current series of experiments a long but finite 200Hz wavetrain is excited from a point source. The linear evolution of a two-dimensional mode with frequency 200Hz is shown by the straight line on the instability diagram, figure 1. The excitation was introduced at R_δ about 800 and measurements were taken up to R_δ^* 2100, as indicated by the dashed lines in the figure. One can see that the excitation was introduced upstream of branch I of the neutral curve and that measurements were taken beyond branch II, after which the Tollmien-Schlichting waves decay. The waves cross branch II at R_δ^* around 1700.

The evolution of the disturbances observed experimentally along the centreline is shown in figure 2. The measurements were taken at a nondimensional distance of $0.52\delta^*$. Using finite wavetrains, the flow is disturbed by an event that can be repeated. Therefore ensemble averages can be taken in order to get a clearer signal. The records displayed here, as well as those shown in other figures, were obtained from 64 ensembles. The first important observation is that wave amplitudes grow up to R_δ^* about 1700 and thereafter decay, consistent with the linear theory, figure 1. A mean flow distortion that is not predicted by the linear theory is also observed . Initially the distortion is negative, but further downstream

[1] This tunnel is now located at Queen Mary and Westfield College, London University, London, UK

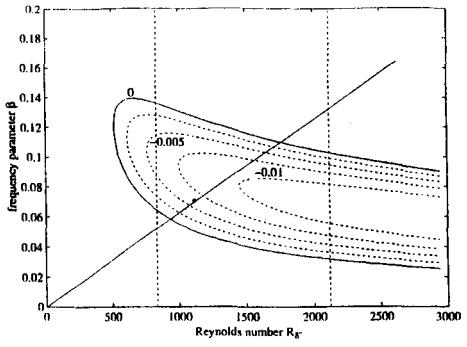

Figure 1: The instability diagram showing the path of the 200Hz Tollmien Schlichting wave.

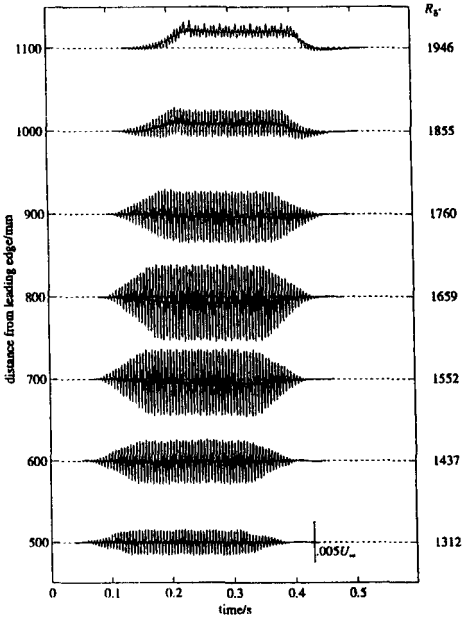

Figure 2: The evolution of the 200Hz three-dimensional wavetrain along the centerline of the plate at a distance of $0.52\delta^*$ from the wall.

switches to positive. It is remarkable that the change in the trend of the mean flow distortion occurs close to where the disturbance crosses branch II. The mean flow distortion is made very clear by the use of finite length wavetrains. It could have remained undetected if a continuous wavetrains were used. It is possible that the use of continuous wavetrains have prevented these mean flow distortions from being observed in previous experiments with three-dimensional wavetrains.

Measurements were also taken off the centerline of the flow to provide a three-dimensional view of the mean flow distortion. Velocity records were taken at different spanwise locations 10mm apart from each other covering the entire width of the disturbance field. To make the streaks clearer the oscillating part of the signal was digitally filtered. Details of the signal processing can be found in Medeiros (1997, 1998). A picture of the evolution of the streak structure as it evolves downstream is shown in figure 3. Initially there is a central region

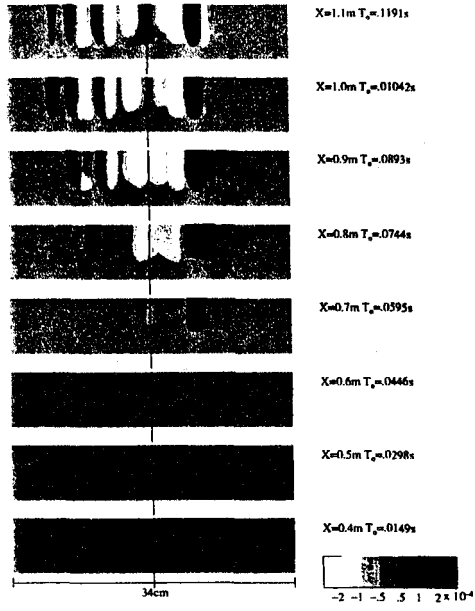

Figure 3: Downstream evolution of the streaks

of negative mean flow distortion together with two lateral regions of positive mean flow distortion. This structure suggests the existence of a pair of counter-rotating concentrations of vorticity which would push down high momentum fluid in the lateral regions and lift up low momentum fluid in the central region. However, it is as yet unclear whether these mechanisms are actually taking place. The concentrations of vorticity are probably too weak to be considered vortices and perhaps the lift up/push down effect is too small to affect the flow. As the waves evolve, the structure becomes more complex. At x=1000mm the appearence of a region of positive mean flow distortion right at the center of the wavetrain is observed. This corresponds to the change in the sign of the mean flow distortion shown in figure 2. From station x=1000mm onwards the structure does not display remarkable changes, apart from the broadening of the central positive mean flow distortion.

It is interesting to look at the evolution in the frequency domain. This has been carried out by Medeiros (1997). However, the spanwise resolution of the experiment is relatively low. The results became difficult to interpret because alias effects could not be ruled out. Therefore, care should be taken in analyzing those results. What is clear is that initially the nonlinear mechanism generates only two region of positive mean flow distortion and one central region where the distortion is negative, while further downstream the spanwise wavenumbers become significantly larger.

Also important is to investigate the structure of the mean flow distortion in the direction normal to the wall. Figures 4 and 5 show contour plots of the mean flow distortion on planes perpendicular to the flow direction at 900mm and 1100mm from the leading edge. The

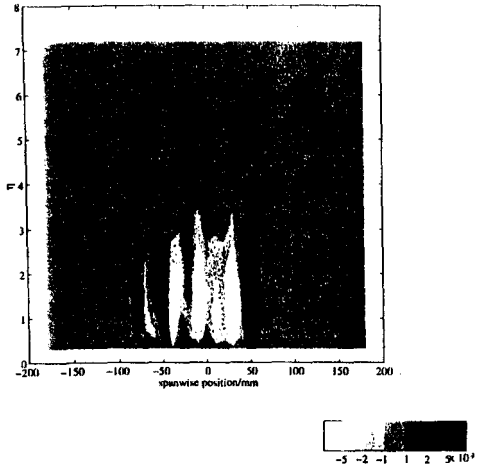

Figure 4: The mean flow distortion distribution on a plane perpendicular to the flow direction 900mm from the leading edge.

mean flow distortion is concentrated inside the boundary layer. In the external part of the flow no sign of the mean flow distortion is observed. At x=900mm the structure is basically composed of two regions of positive mean flow distortion and a central region of negative mean flow distortion. Whereas the positive lumps are fairly concentrated the negative region spreads over a larger portion. Moreover, the negative region appears to be composed of several lumps. The profiles resemble that of the Klebanoff modes with a single maximum inside the boundary layer, particularly for the positive streaks. The maximum is located between $\eta(= y\sqrt{\frac{U_\infty}{\nu x}})$ 1 and 2, which is also consitent with Klebanoff modes. At x=1100mm the negative central region splits into a number of regions and lumps of positive mean flow distortion arise. At this stage the central part of the disturbance field is too complex for any definite conclusion concerning the location of the maxima.

The evolution of the profile along the streamwise direction may be more meaningful than the analysis of the signal at a particular streamwise station, figure 6.

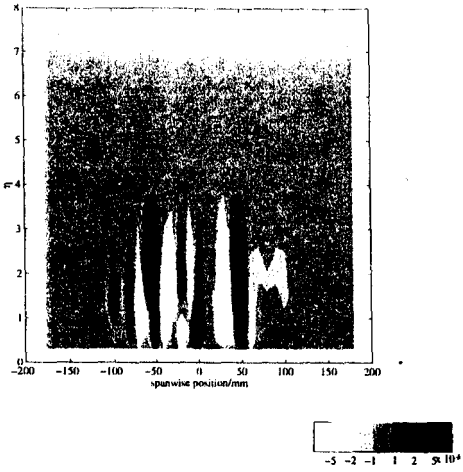

Figure 5: The mean flow distortion distribution on a plane perpendicular to the flow direction 1100mm from the leading edge.

The figure shows how the disturbance field slowly evolves

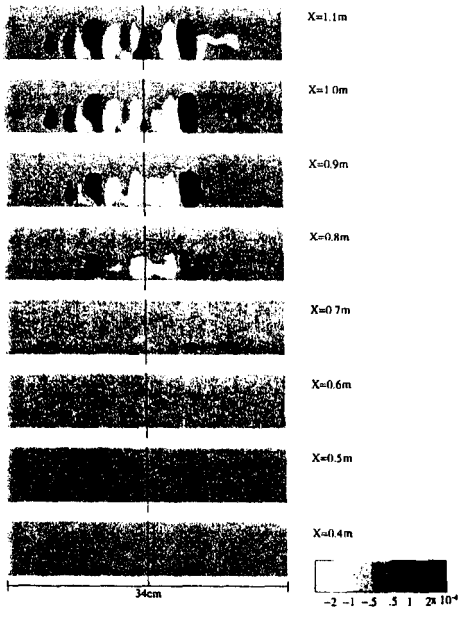

Figure 6: Evolution of the mean flow distortion.

from a relatively simple structure at x=800mm into a much more complex one at x=1100mm.

An overall view of the transfer of momentum from

the low velocity streaks to the high velocity streaks is given by the distribution of the displacement thickness variation over the entire disturbance field, figure 7. In

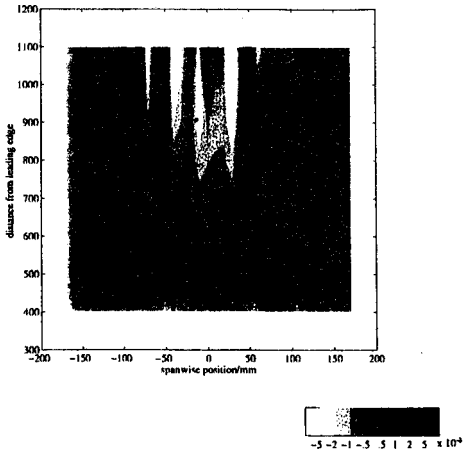

Figure 7: The displacement thickness variation over the plate relative to displacement thickness of the Blasius profile.

this picture the details of the complex distribution in the direction perpendicular to the wall are lost, and an averaged view of the distortions is obtained. The figure shows a somewhat more symmetric pictures of the flow than that of figure 3. For the positive lateral regions the displacement thickness distribution indicates a structure similar to that suggested by figure 3. The central region, on the other hand, indicated that the central negative region splits into three regions separeted by two newly generated positive regions.

3 Some Theoretical Considerations

The standard procedure used to analyse the stability of flows involves the decomposition of the velocity field and the pressure field into a base part $\mathbf{V}, P$, which is a solution of the equations of motion, and a small disturbance part $\mathbf{v}, p$. For analysing nonlinear interactions of the disturbance field it is assumed further that the velocity and pressure disturbances can be written as

$$\mathbf{v} = \epsilon \mathbf{v}_0 + \epsilon^2 \mathbf{v}_1 + \epsilon^3 \mathbf{v}_2 \ldots$$

$$p = \epsilon p_0 + \epsilon^2 p_1 + \epsilon^3 p_2 \ldots$$

Substituting into the Navier-Stokes equations, subtracting out the base flow and collecting terms of order ϵ one arrives at a linear system of equations describing the disturbance field:

$$\frac{\partial}{\partial t}\mathbf{v}_0 + (\mathbf{V}\cdot\nabla)\mathbf{v}_0 + (\mathbf{v}_0\cdot\nabla)\mathbf{V} = -\nabla p_0 + \frac{1}{R}\nabla^2\mathbf{v}_0 \quad (1)$$

$$\nabla\cdot\mathbf{v}_0 = 0. \quad (2)$$

The parameter ϵ characterizes the amplitude of the disturbance and since it is small it is natural to attempt to expand the solution of the perturbed problem in powers of ϵ. However, we note that it is not clear that it is legitimate to do that, because there is no guarantee that such series will converge. Therefore in practice it is necessary to verify whether the solution found is really a good approximation to the flow.

The coefficients of equation 1 are given by the base flow solution. For the boundary layer the equations of motion are non-dimensionalized by the free-stream velocity U_∞ and the displacement thickness δ^*, therefore $R = \frac{U_\infty \delta^*}{\nu}$, where ν is the kinematic viscosity. With the additional assumption that the base flow is parallel, that is, $\mathbf{V} = (U, 0, 0)$, the system of equations (1–2) permits the normal modes solution

$$\begin{bmatrix} u_0 \\ v_0 \\ w_0 \\ p_0 \end{bmatrix} = \begin{bmatrix} \hat{u}_0(y) \\ \hat{v}_0(y) \\ \hat{\omega}_0(y) \\ \hat{p}_0(y) \end{bmatrix} e^{i(\alpha_x x + \alpha_z z - \beta t)}, \quad (3)$$

where u, v, w represent the velocity components in the streamwise, normal to the wall and spanwise directions (x, y, z), respectively. In the expression β is the non-dimensional frequency, and α_x and α_z are the non-dimensional streamwise and spanwise wavenumbers. These quantities are in general complex, but for the flat plate boundary layer α_x is the only complex exponent and accounts for the amplification or decay of the waves in the streamwise direction (Gaster 1962, Gaster 1965). The functions $\hat{u}(y), \hat{v}(y), \hat{w}(y), \hat{p}(y)$ are also complex and give the structure of the mode across the boundary layer.

Substituting (3) together with $\mathbf{V} = (U, 0, 0)$ in (1) and (2) the equations of motion for a three-dimensional disturbances reduce to a pair of ordinary differential equations (Squire 1933, Mack 1984, Cohen, Breuer & Haritonidis 1991)

$$\left\{\frac{d^4}{dy^4} - 2k^2\frac{d^2}{dy^2} + k^4 - iR\alpha_x\left[(U-c)\left(\frac{d^2}{dy^2} - k^2\right) - \frac{d^2U}{dy^2}\right]\right\}\hat{v}_0 = 0 \quad (4)$$

$$\left[\frac{d^2}{dy^2} - k^2 - iR\alpha_x(U-c)\right]\hat{\eta} = i\alpha_z R\frac{dU}{dy}\hat{v}_0 \quad (5)$$

with boundary conditions

$$\begin{array}{llll} \text{at} & y = 0 & \hat{v}_0(y) = 0, & \frac{\partial}{\partial y}\hat{v}_0(y) = 0, \quad \hat{\eta}(y) = 0 \\ \text{at} & y \to \infty & \hat{v}_0(y) \to 0, & \frac{\partial}{\partial y}\hat{v}_0(y) \to 0, \quad \hat{\eta}(y) \to 0 \end{array} \quad (6)$$

where $k^2 = \alpha_x^2 + \alpha_z^2$ and $c = \frac{\beta}{\alpha_x}$ is the phase velocity of the mode.

Equation (4) is the Orr-Sommerfeld equation (OSE) which governs the linear stability the flow. The OSE together with the associated homogeneous boundary conditions, constitutes an eigenvalue problem. Nontrivial solutions, or modes, have to satisfy a dispersion relation

$$F(\alpha_x, \alpha_z, \beta, R) = 0. \quad (7)$$

The dispersion relation for two-dimensional modes ($\alpha_z = 0$) in a flat plate boundary layer is represented in figure 1. The solid curve represents neutral modes. Modes

ouside the loop are stable whereas those inside the loop are unstable.

If now the terms of order ϵ^2 are collected from equantion 1 and 2 one arives at an OSE for the $\hat{v}_1$ with a non homogeneous term which is a function of v_0 and p_0. Owing to the quadratic nature of the nonlinear terms neglected at order (ϵ) the non homogeneous terms of order (ϵ^2) have the form

$$e^{i[\pm(\alpha_x x+\alpha_{z_p} z-\beta t)\pm(\alpha_x x+\alpha_{z_q} z-\beta t)]}. \quad (8)$$

For a harmonic point source there is only one α_x and one β, but a number of three-dimensional modes (α_z).

Therefore, the quadratic interaction produces modes with streamwise wavenumbers 0 or $2\alpha_x$. The experimental observations show the appearance of modes with streamwise wavenumber 0, the mean flow distortions, but no sign of harmonics ($2\alpha_x$) is observed. It is important to remember that the boundary layer will respod differently for these two types of forcing. For instance it is possible that the harmonics are more linearly dumped than the mean distortion which would be consistent with the observations.

Analysis of the spanwise wavenumber is not so straighforward because the system involves a large number of spanwise modes. However, because the boundary layer responds differently to the modes, the amplitude of the different three-dimensional modes will not be identical. Moreover one expects the nonlinear interaction to be stronger for the larger modes. It turns out that in some circumstances the largest three-dimensional mode has α_z different from 0 (Wiegand et al. 1995), say $\alpha_{z_{max}}$. This mode would then generate nonlinear modes with spanwise wavenumner 0 and $2\alpha_{z_{max}}$. It is possible that selective linear dumping would result in one nonlinear mode being larger than the other.

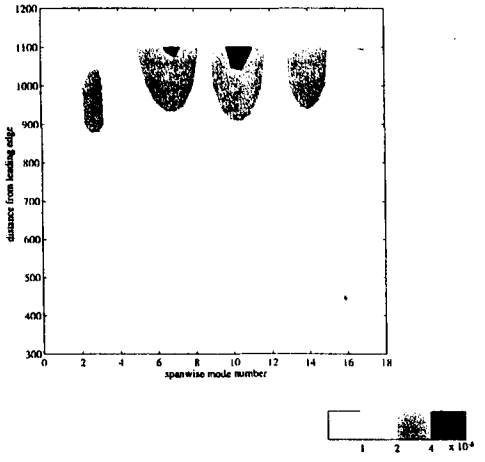

Figure 8: Spanwise Fourier transformation of figure 7.

Figure 8 shows the spanwise Fourier transformation of figure 7. It is observed that the first sign of nonlinearity corresponds to the appearance of a mode with non zero spanwise wavenumber. This mode reaches a maximum of amplitude between 900 and 1000mm from the leading edge. The fundamental waves also reach a maximum within the experimental domain, figure 2, which is consistent with the amplitude dependence of the nonlinear interaction discussed above.

At x=1000mm modes of higher spanwise wavenumber are also present. Care should be taken in analysing these results because the spanwise resolution is relatively poor and alias effects can not be ruled out. It is tempting to think that these modes originate from a second generation of the nonlinear interaction discussed above, but this time including the first nonlinearly generated mode. However, the observations show that these modes continue to grow even after the first nonlinear mode has decayed. Other results, not shown here, indicate that these modes do not decay within the experimental domain, x$\leq$1300mm. This observation is not consistent with the nonlinear interaction described, and it appears that the higher spanwise number modes arise from a mechanism as yet not identified.

4 Conclusion and Discussion

This work studies the nonlinear evolution of wavetrains emanating from a point source in a flat plate boundary layer. The first interesting result was that the first indication of nonlinear behaviour was not a subharmonic signal, as would be expected for plane wavetrains, but a mean flow distortion that formed longitudinal streaks. Initially the mean flow distortion displayed a relativelly simple spanwise structure with a central region of negative mean flow distortion and two lateral regions of positive mean flow distortion.

This initial mean flow distortion may have arisen from self interaction of the modes via the Reynolds stresses term. Analysis of the spectra of the displacement thickness variation cause by the disturbance over the plate is consistent with this idea. It appeared that the strength of the nonlinear interaction at this stage was stronger off the centerline of the flow. This might be linked to the fact that for some frequencies the three-dimensional wavetrains also display amplitude maxima off the centerline in the linear regime (Wiegand et al. 1995).

The structure of these distortions in the direction perpendicular to the wall was also investigated. Initially they resemble Klebanoff modes with one amplitude peak at a position η between 1 and 2.

The relatively simple structure gives rise to a fairly complicated flow field further downstream which appears to originate at a position close to the second branch. The more complicated structure arises in the central portion of the wavetrain, where the initial negative mean flow distortion was formed. There, regions of positive mean flow distortion arises and the profiles of the mean flow distortions no longer display the Klebanoff mode shape. Despite the complexity, an overall view shown by the displacement thickness variation over the plate, suggests that the central negative region splits into three. The positive mean flow distortion regions do not change considerably along the process, except in amplitude.

Streaks have also been observed in by pass transition. However, there the streaks tend to keep their spanwise spacing, as oppose to what is observed in the current experiment. Longitudinal streaks have been observed in turbulent flow. In some cases they appear to be

a key ingredient of the mechanism of production of turbulence. It has also been shown that modulated waves give rise to transition at smaller amplitudes in comprison with plane wavetrains. It is possible that the modulation of the waves provide a short cut between the early wavelike behaviour and the vortical structures observed in turbulent flows. These conjecture is currently being investigated. The possibility that the initial mean flow distortion be generated from the self interaction of waves is also being further inyestigated.

References

Cohen, J., Breuer, K. S. & Haritonidis, J. H. (1991), 'On the evolution of a wave packet in a laminar boundary layer', *J. Fluid Mech.* **225**, 575–606.

Gaster, M. (1962), 'A note on the relation between temporally-increasing and spatially-increasing disturbances in hydrodynamic instability', *J. Fluid Mech.* **14**, 222–224.

Gaster, M. (1965), 'On the generation of spatially growing waves in a boundary layer', *J. Fluid Mech.* **22**, 433–441.

Gaster, M. (1978), The physical process causing breakdown to turbulence, *in* '12th Naval Hydrodynamics Symposium', Washington.

Gaster, M. (1984), A non-linear transfer function description of wave growth in a boundary layer, *in* V. V. Kozlov, ed., 'Laminar-turbulent transition', IUTAM Symposium, IUTAM, Springer-Verlag, pp. 107–114.

Kachanov, Y. S. (1985), Development of spatial wave packets in boundary layer, *in* V. V. Kozlov, ed., 'Laminar-turbulent transition', springer-Verlag, pp. 115–123.

Mack, L. M. (1984), Boundary-layer linear stability theory, *in* 'Special course on stability and transition of laminar flow', AGARD Rep. No 709.

Mack, L. M. (1985), Instability wave patterns from harmonic point sources and line sources in laminar boundary layers, *in* V. V. Kozlov, ed., 'Laminar-turbulent transition', springer-Verlag, pp. 125–132.

Medeiros, M. A. F. (1996), The nonlinear behaviour of modulated Tollmien-Schlichting waves, PhD thesis, Cambridge University - UK.

Medeiros, M. A. F. (1997), Laminar-turbulent transition: the nonlinear evolution of three-dimensional wavetrains in a laminar boundary layer, *in* 'Proc. of the XIV Brazilian Congress of Mechanical Engineering', Bauru. (in CD-ROM).

Medeiros, M. A. F. (1998), nonlinear evolution of a three-dimensional wavetrain in a flat plate boundary layer, *in* '21th Congress of the International Council do the Aeronautical Sciences', Melbourne. (to be published).

Medeiros, M. A. F. & Gaster, M. (1994), The nonlinear behaviour of modulated Tollmien-Schlichting waves: experiments and computations, *in* 'Second EUROMEC Conference', Warsaw – Poland.

Medeiros, M. A. F. & Gaster, M. (1995), The nonlinear behaviour of modulated Tollmien-Schlichting waves, *in* 'IUTAM Conference on nonlinear instability and transition in tri-dimensional boundary layers', Manchester, pp. 197–206.

Medeiros, M. A. F. & Gaster, M. (1997), 'The nonlinear evolution of wavepackets in a laminar boundary layers: Part I'. (submitted to the *J. Fluid Mech.*).

Medeiros, M. A. F. & Gaster, M. (1998), 'The nonlinear evolution of wavepackets in a laminar boundary layers: Part II', *J. Fluid Mech.* (to be published).

Seifert, A. (1990), On the interaction of small amplitude disturbances emanating from discrete points in a Blasius boundary layer, PhD thesis, Tel-Aviv University.

Seifert, A. & Wygnanski, I. (1991), On the interaction of wave trains emanating from point sources in a Blasius boundary layer, *in* 'Proc. Conf. on Boundary Layer Transition and Control', The Royal Aeronautical Society, Cambridge, pp. 7.1–7.13.

Shaikh, F. N. (1997), 'Investigation of transition to turbulence using white noise excitation and local analysis techniques', *J. Fluid Mech.* **348**, 29–83.

Squire, H. B. (1933), 'On the stability of three-dimensional distribution of viscous fluid between parallel walls', *Proc. Roy. Soc. London A* **142**, 621–628.

Wiegand, T., Bestek, H., Wagner, S. & Fasel, H. (1995), Experiments on a wave train emanating from a point source in a laminar boundary layer, *in* '26th AIAA Fluid Dynamics Conference', San Diego, CA.

UMA FORMULAÇÃO DE PAREDE PARA ESCOAMENTOS TURBULENTOS COM RECIRCULAÇÃO

D.O.A. CRUZ & F.N. BATISTA
Grupo de Turbomáquinas / Departamento de Engenharia Mecânica/ CT-UFPA
66075-900 Belém-PA-Brasil – gtdem@amazon.com.br

M. BORTOLUS
Universidade Federal de Minas Gerais – Departamento de Engenharia Mecânica
31270-901 Belo Horizonte-MG-Brasil – borta@vesper.demec.ufmg.br

Abstract

This work presents a new wall law formulation for recirculating turbulent flows. An alternative expression for the internal lenght which can be applied in the separated region is also presented. The formulation was implemented in a numerical code which solves the k-ε model using the finite volume method. The solution is then compared with an experimental case existing in the literature and describes the phisics of the problem more accurately than the standard k-ε model.

Palavras-chave

Turbulência, recirculação, modelo k-ε, lei da parede

1. INTRODUÇÃO

O modelo k-ε tem se tornado ao longo dos anos um dos mais populares modelos de turbulência sendo utilizado em inúmeras aplicações práticas. Essa popularidade se deve principalmente a uma composição de uma relativa simplicidade de implementação com uma certa generalidade de aplicação. Apesar dessas vantagens o modelo k-ε ainda apresenta algumas dificuldades, principalmente na descrição dos escoamento próximo a superfícies sólidas.

Com o objetivo de contornar essa dificuldade várias soluções foram propostas as quais se dividem basicamente em dois grupos. O primeiro chamado de modelo de alto número de Reynolds turbulento que utiliza as chamadas Lei de Parede Logarítmica (CHIENG, C.C. & LAUNDER, B.E.,(1980) CIOFALO,H. & COLLINS, M.W., (1989)) e requer uma malha pouco refinada junto à parede, o segundo grupo é conhecido como modelos de baixo número de Reynolds turbulento e utiliza uma malha bastante refinada junto à parede (PATEL, V.C., RODI, W. & SHEUERER, G.,(1985)). Ambos os grupos apresentam características distintas,

sendo que o primeiro possui uma maior robustez e facilidade de convergência, embora não descreva adequadamente o escoamento em muitos casos como nas regiões onde ocorre recirculação, por exemplo. O segundo grupo, embora consiga retratar melhor o escoamento, é computacionalmente mais dispendioso, além de, em alguns casos, apresentar uma certa dificuldade de convergência. Grande parte da dificuldade dos modelos do primeiro grupo em descrever certos tipos de escoamento está concentrada na utilização da lei da parede logarítmica clássica a qual foi deduzida para escoamento sobre uma placa plana e não se aplica a escoamentos onde ocorra separação e recirculação.

No presente trabalho será apresentado uma versão da lei da parede logarítmica a qual pode ser empregada ao longo de todo o escoamento, inclusive nas regiões de separação e escoamento reverso. Uma definição alternativa do comprimento característico da região interna do escoamento será utilizado (CRUZ, D.O.A. & SILVA FREIRE, A.P., (1995)). Essa formulação será implementada em um código numérico o qual utiliza o método dos volumes finitos, e os resultados obtidos para o escoamento em torno de um degrau descendente *(figura 1)* serão comparados com resultados experimentais assim como com a formulação do modelo k-ε de Spalding e Launder *(1974)*.

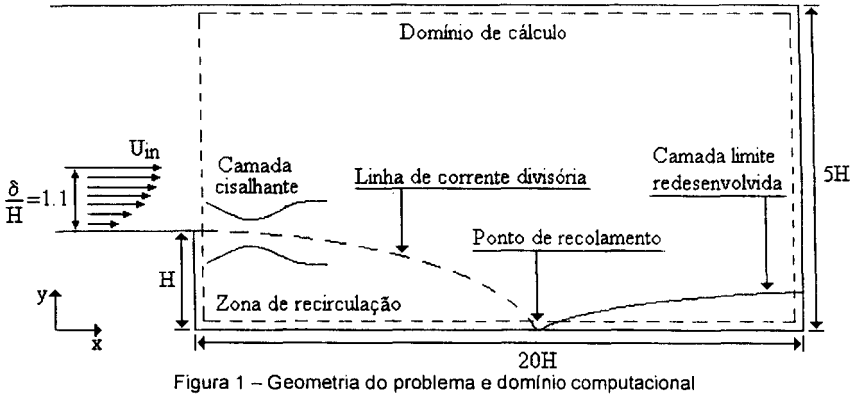

Figura 1 – Geometria do problema e domínio computacional

2. AS EQUAÇÕES GOVERNANTES

Na análise do escoamento foram utilizadas as equações médias de Reynolds para o caso incompressível, juntamente com as equações da energia cinética turbulenta (k) e da dissipação (ε) as quais são mostradas abaixo:

$$\frac{Dk}{Dt} = \frac{\partial}{\partial x_i}\left[\frac{\nu_T}{\sigma_K}\frac{\partial k}{\partial x_i}\right] + \nu_T\left[\frac{\partial U_i}{\partial x_j} + \frac{\partial U_j}{\partial x_i}\right]\frac{\partial U}{\partial x_j} - \varepsilon \qquad (1)$$

$$\frac{D\varepsilon}{Dt} = \frac{\partial}{\partial x_i}\left[\frac{\nu_T}{\sigma_t}\frac{\partial \varepsilon}{\partial x_i}\right] + C_1 \frac{\varepsilon}{k}\nu_T\left[\frac{\partial U_i}{\partial x_j} + \frac{\partial U_j}{\partial x_i}\right]\frac{\partial U}{\partial x_j} - C_2\frac{\varepsilon^2}{k} \qquad (2)$$

Onde $\nu_T = C_\mu \frac{\varepsilon^2}{k}$; C_μ=0,09, C_1=1,44;C_2=1,92; σ_t=1,3; σ_K=1

3. A FORMULAÇÃO DE PAREDE

Na região próxima à parede onde os termos de inércia são pequenos a equação da conservação da quantidade de movimento pode ser aproximada pela seguinte relação(CRUZ, D.O.A. & SILVA FREIRE, A.P., (1995)):

$$\nu\frac{\partial u}{\partial x} + \overline{u'v'} = \frac{\tau_w}{\rho} + \frac{1}{\rho}\frac{dp}{dx}y \qquad (3)$$

onde ν é a viscosidade cinemática, τ_w é a tensão na parede e p é a pressão, $\overline{u'v'}$ representa a tensão de cisalhamento turbulenta e ρ é a massa específica do fluido. Na equação acima, o lado esquerdo representa a tensão cisalhante total a qual é dada pela soma do termo laminar e do termo turbulento como descrito abaixo:

$$\nu\frac{\partial u}{\partial x} + \overline{u'v'} = \tau \qquad (4)$$

No cálculo da tensão na parede será utilizada aqui uma versão simplificada da lei da parede proposta por Cruz e Silva Freire (1995), além de uma equação alternativa para o cálculo do comprimento característico da região interna do escoamento. Ambas as relações são mostradas abaixo:

$$u = \frac{\tau_w}{|\tau_w|}\frac{2}{\bar{k}}\sqrt{\frac{\tau_w}{\rho} + \frac{1}{\rho}\frac{dp}{dx}y} + \frac{\tau_w}{|\tau_w|}\frac{u_\tau}{\bar{k}}\ln\left(\frac{y}{L_C}\right) \qquad (5)$$

$$L_C = \frac{-\frac{\tau_w}{\rho} + \sqrt{\left(\frac{\tau_w}{\rho}\right)^2 + 2\nu\frac{dp}{dx}u_R}}{\frac{1}{\rho}\frac{dp}{dx}} \qquad (6)$$

onde $\bar{k}$ é a constante de Vón Karmán=0.41, $u_T=\sqrt{\frac{\tau_w}{\rho}}$ é a velocidade de fricção e u_R é descrito pela seguinte equação:

$$u_R=\sqrt{\tau} \tag{7}$$

As equações (5) e (6) representam uma generalização da Lei da Parede Logarítmica clássica que pode ser aplicada em várias regiões do escoamento . Na região longe do ponto de descolamento na de a tensão na parede é positiva e dP/dx y <<τw temos que as equações (5) e (6) assumem a seguinte forma:

$$u=\frac{2}{\bar{k}}u_T+\frac{u_T}{\bar{k}}\ln\left(\frac{y}{L_C}\right) \tag{8}$$

$$L_C=\nu/u_T \tag{9}$$

ou seja , a Lei Logarítmica clássica . Próximo ao ponto de descolamento onde τw =0 a equação fica sendo dada por :

$$u=\frac{2}{\bar{k}}\sqrt{y\frac{dP}{\rho dx}} \tag{10}$$

A equação (9) é semelhante à expressão proposta por Stratford (1959) a qual descreve o perfil de velocidade dos escoamentos turbulentos próximo à parede na região de separação onde a tensão de cizalhamento na parede tende à zero.

Na região de recirculação onde dP/dx y >>τw as relações (5) e (6) pode ser rescritas da seguinte forma:

$$u=-\frac{2}{\bar{k}}u_T-\frac{u_T}{\bar{k}}\ln\left(\frac{y}{L_C}\right) \tag{11}$$

$$L_C=2\left|\tau_w/\frac{dp}{dx}\right| \tag{12}$$

A principal diferença enter as equações (9) e (8) e as equações (11) e (12) além do sinal negativo na expressão que descreve a velocidade está na definição do comprimento característico do escoamento próximo à parede (equação (12)) o qual difere do comprimento característico clássico dado pela equação (9).

Com o objetivo de evitar um procedimento iterativo adicional o qual poderia dificultar a convergência do esquema numérico o seguinte conjunto de equações foi adotado no cálculo da tensão na parede:

$$\tau = C_{\mu}^{1/2} k + \nu \frac{\partial u}{\partial y} \tag{13}$$

$$\tau_{wo} = \frac{u \sqrt{\tau} \rho \bar{k}}{\ln\left(Ey \frac{\sqrt{\tau}}{\nu} \right)} C_{\mu}^{1/2} \tag{14}$$

$$\frac{1}{\rho} \frac{dp}{dx} = \frac{\tau - \tau_w}{y} \tag{15}$$

$$L_C = \frac{-\frac{\tau_{wo}}{\rho} + \sqrt{\left(\frac{\tau_{wo}}{\rho} \right)^2 + 2\nu \frac{dp}{dx} u_R}}{\frac{1}{\rho} \frac{dp}{dx}} \tag{16}$$

$$\tau_w = \frac{u \sqrt{\tau} \rho \bar{k}}{\left[2 \sqrt{\left| \frac{\tau}{\tau_{wo}} \right|} + \ln\left(\frac{y}{L_C} \right) \right]} \tag{17}$$

onde E=9.8

O conjunto de equações acima representa uma linearização no procedimento de obtenção da tensão na parede, o que torna o cálculo mais robusto além de acelerar a convergência do código numérico.

A dissipação é então descrita pela seguinte relação:

$$\varepsilon = C_{\mu}^{1/2} k \left[\frac{\sqrt{\tau}}{ky} + \frac{\frac{1}{\rho} \frac{dp}{dx}}{k \sqrt{\tau}} \right] \tag{18}$$

4. ANÁLISE DOS RESULTADOS

A formulação aqui apresentada foi utilizada no cálculo do escoamento em torno de um degrau descendente sendo os resultados comparados com os experimentos de Vogel e Eaton (1985) as equações governantes na sua formulação conservativa são discretizadas utilizando a formulação de volumes finitos acoplada com um esquema híbrido para o tratamento dos termos convectivos e difusivos simultaneamente. O conjunto de equações diferenciais foi resolvido iterativamente utilizando uma versão robusta e extensivamente testada do código numérico TEACH-2E (Teaching Eliptic Axi-Symmetrical Caracteristic Heuristically) o qual incorpora o algoritmo SIMPLE específico para acoplamento pressão-velocidade em escoamentos incompressíveis. A melhor relação entre precisão e tempo de CPU foi conseguida utilizando-se uma malha de 146x102 pontos.

Nas figuras abaixo são mostrados os perfis de velocidade na região próxima à parede para várias estações do escoamento. Uma comparação entre os resultados obtidos pela presente formulação com o modelo k-ε padrão de Launder e Spalding (1974) e com os resultados experimentais de Vogel e Eaton (1985) é feito. Os resultados obtidos com a formulação aqui proposta se mostram superiores aos da formulação padrão, descrevendo melhor o perfil de velocidade, principalmente próximo à parede, sem nenhum acréscimo no tempo de computação. Na verdade o cálculo numérico feito com o modelo padrão necessita de mais iterações para convergir (1200), que o modelo aqui apresentado (1100) para uma precisão da ordem de 5E-3. Vale ressaltar que o procedimento proposto retrata a pequena zona de recirculação secundária presente no escoamento próximo ao degrau *(figura 5)*. Outras formulações os quais também empregam a lei logarítmica clássica nas equações do modelo k-ε original (CHIENG, C.C. & LAUNDER, B.E.,(1980) CIOFALO,H. & COLLINS, M.W., (1989)) dividindo o escoamento próximo à parede em várias camadas, fornecem melhores resultados que a formulação padrão, essas formulações, contudo, não reproduzem a zona de recirculação secundária (BORTOLUS, M. & GIOVANNINI, A (1995))

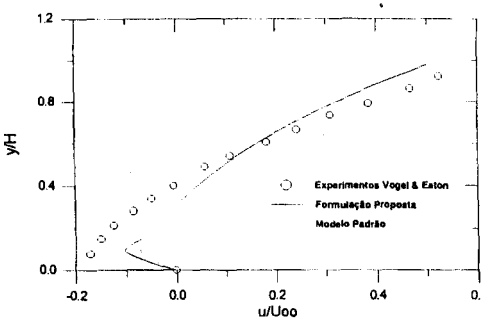

Figura 2- Comparação do Perfil de Velocidade Junto à Parede (x-Xr)/Xr=0.33

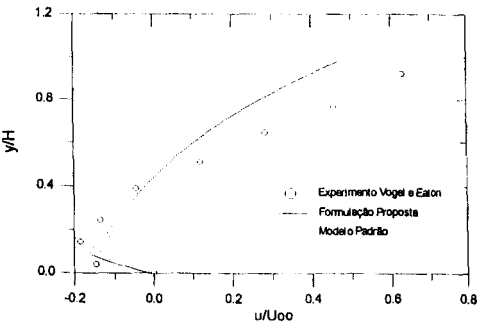

Figura 3- Comparação do Perfil de Velocidade Junto à Parede (x-Xr)/Xr=0.44

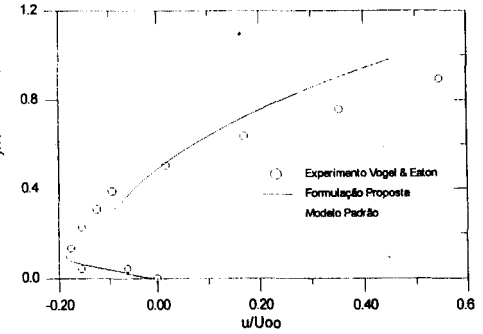

Figura 4- Comparação do Perfil de Velocidade Junto à Parede (x-Xr)/Xr=-0.55

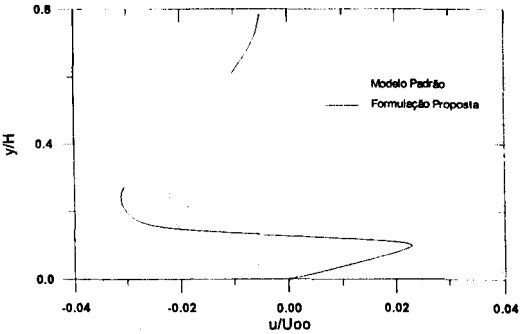

Figura 5- Comparação do Perfil de Velocidade Junto à Parede Próximo ao Degrau

Nas figuras acima Xr representa a posição do ponto de recolamento.

Na figura abaixo é mostrada uma comparação entre o fator de atrito na parede *(Cf)* fornecido pelo procedimento aqui desenvolvido com os resultados do modelo k-ε padrão e com os dados experimentais. Novamente os resultados aqui obtidos reproduzem melhor o experimento que a formulação padrão tanto antes quanto depois do ponto de descolamento. Pode-se observar na região próximo ao degrau ($x/H \cong 0$) que a tensão na parede (Cf) é positiva, atestando a presença da pequena zona de recirculação secundária como já havia sido mencionado. A predição do descolamento secundário constitui um importante teste para a capacidade do modelo k-ε de descrever os escoamentos próximo à superfícies sólidas.

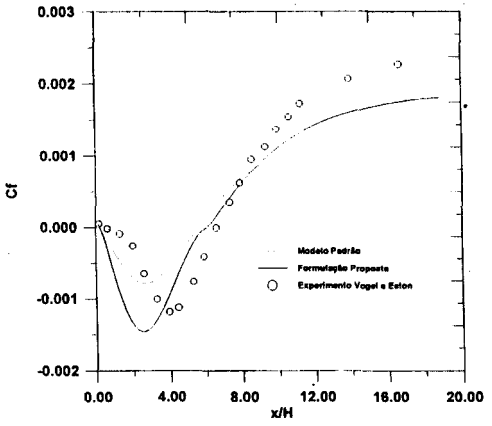

Figura 6 – Comparação do coeficiente de fricção (Cf) para os diversos casos

Na tabela 1, aparecem os valores do ponto de recolamento fornecido pelas duas teorias juntamente com o valor obtido experimentalmente. O cálculo feito com a teoria proposta fornece um comprimento da zona de recirculação mais próximo do valor experimental quando comparado com o valor obtido pelo modelo k-ε padrão. Isto ocorre porque a equação (18) fornece valores maiores para a taxa de dissipação junto à parede causando uma diminuição da viscosidade turbulenta nessa região o que causa um aumento da zona de recirculação.

CÁLCULO DO PONTO DE RECOLAMENTO	X/H
EXPERIMENTAL	6.6
PRESENTE FORMULAÇÃO	6.0
MODELO PADRÃO	5.5

Tabela 1 – Pontos de recolamento calculados e experimental

5. CONCLUSÃO

No presente trabalho uma nova formulação para a descrição dos escoamentos turbulentos próximo a superfícies sólidas foi apresentado. Essa formulação foi implementada em num código numérico o qual resolve as equações médias de Reynolds juntamente com as equações clássicas do modelo k-ε de turbulência através do método dos volumes finitos. Foi mostrado que a formulação proposta reproduz melhor os experimentos de Vogel e Eaton que a formulação de Launder e Spalding com um custo computacional equivalente.

Os resultados obtidos sugerem que a capacidade de descrição dos escoamentos das equações do modelo k-ε clássico, podem ser melhorados através da utilização adequada de uma formulação de parede, este incremento na precisão do modelo ocorre sem que haja alguma perda de sua robustez ou algum acréscimo de custo computacional, características estas de grande importância na solução de problemas práticos de engenharia.

6. REFERÊNCIAS BIBLIOGRÁFICAS

1. BORTOLUS, M. & GIOVANNINI, A., "Numerical Prediction of Wall Heat Transfer in Complex Turbulent Flows" - Turbulence-Heat and Mass Transfer 1, pp.228-232, BEGELL HOUSE, 1995.

2. CHIENG, C.C. & LAUNDER, B.E., "On the Calculation of Turbulent Transport Downstream for an Abrupt pipe expansion", Numerical Heat Transfer, Vol.3, pp189-207, 1980.

3. CIOFALO,H. & COLLINS, M.W., "k-ε Predictions of Heat Transfer in Turbulent Recirculating Flows Using na Improved Wall Treatment", Numerical Heat Transfer, Part B, Vol.15, pp21-47, 1989.

4. CRUZ, D.O.A. & SILVA FREIRE, A.P., "The Assimptotic Structure of the Thermal Boundary Layer Near a Separation Point" - Turbulence-Heat and Mass Transfer 1, pp.57-62, BEGELL HOUSE, 1995.

5. LAUNDER, B.E. & SPALDING, D.B., "The Numerical Computation of Turbulent Flows", Computer Methods in Applied Mechanics, Vol.3, pp269-289, 1974.

6. PATEL, V.C., RODI, W. & SHEUERER, G., "Turbulence Models for Near Wall and Low-Reynolds Number Flows: a Review", AIAA Journal, Vol.23, n.9, pp1308-1319, Sept. 1985.

7. STRATFORD,B.S., "A n Experimental Flow With Zero Skin Friction Throughout its Region of Pressure Rise ", Journal of Fluid Mechanics, Vol.5, n.17, . 1959.

8. VOGEL, J.C. & EATON, J.K., "Combined Heat Transfer and Fluid Dynamic Measurements Downstream of a Backward Facing Step", Journal of Heat Transfer Transactions of ASME vol.107, pp 922-929, 1985.

Mass Injection in a Wake of a Fixed and Rotating Cylinder

José Antonio G. Croce, MSc Student
Fernando Martini Catalano, Ph.D. MRAeS, MAIAA
Universidade de São Paulo – USP
Escola de Engenharia de São Carlos – EESC
Departamento de Engenharia Mecânica
Laboratório de Aeronaves
Av. Dr. Carlos Botelho, 1465
CEP 13560-250 – São Carlos – SP – Brasil
e-mail – croce@sc.usp.br

Abstract

An experimental work was carried out in order to measure the effect of a mass injection in a wake of a fixed and a rotating two-dimensional cylinder. A jet made the injection of mass from a small cylinder located just behind the main cylinder. The jet position could be changed in order to assure that the blowing was direct into the wake. A very low turbulence wind tunnel was used for flow visualization of both fixed and rotating cylinder. The velocity distribution behind de cylinder was measured by a constant temperature hot wire anemometer in a grid of 100 points and at two downstream positions. A small open circuit wind was used for drag and lift measurements through a special two component balance. Results showed that small jet flows could reduce significantly the wake of both fixed and rotating cylinder with the inherent reduction of the base drag. A significant increase on the lift to drag ratio could be achieved on the rotating cylinder due to the reduction of drag. The jet and wake mixing measured in detail with a fine grid at the downstream positions showed that the jet mixing layer immediately smoothes out the velocity gradient between jet and wake. As the jet is blowing outside the main cylinder this system could be used to control the vortex shedding of structures such as bridges, chimney and towers.

1. Introdução

Qualquer método que possibilite uma redução significativa na força de arrasto de um corpo sujeito à ação de ventos além do caráter cientifico, produz avanços nas mais diversas áreas da engenharia. Estruturas altas como

edifícios, chaminés, ou pontes estão a todo tempo sujeitas a ação de escoamentos atmosféricos os quais produzem o aparecimento de forças de arrasto devido tanto ao atrito do ar com as paredes destas estruturas quanto, e na maioria dos casos principalmente, ao surgimento de esteiras de baixa pressão na parte traseira destes corpos, tomando-se como referência o sentido do escoamento.

Além das forças de arrasto podem surgirem outras, como por exemplo forças de sustentação devido à diferença de pressão entre duas superfícies. Um exemplo clássico de indução de sustentação é o cilindro de efeito Magnus. Um cilindro rodando e imerso em um escoamento, gera altos valores de força de sustentação no entanto possui o inconveniente pertinente a todos corpos rombudos de apresentar uma alta força de arrasto. O efeito Magnus foi bastante estudado e utilizado como no caso do uso de cilindros com rotação na embarcação conhecida como "Backau", um navio construído nos anos trinta por FLETTNER (1925), o qual usava no lugar de velas dois cilindros girando. Outra aplicação apresenta uma aeronave com cilindros rotativos no lugar de asas desenvolvida também na década de trinta. Várias outras aplicações foram testadas; como uso de cilindros rotativos para a confecção de bombas hidráulicas e turbinas eólicas, estudados por CAMARGO VIERA (1965); em dirigíveis em forma de uma grande esfera, a qual girava lentamente enquanto em voo para gerar sustentação pelo efeito Magnus, desenvolvidos pelos INSTITUTOS CANADENSE DE PESQUISA AERONÁUTICA (1988).

Métodos para a redução de arrasto de perfil em corpos rombudos abrangem um grande número de possibilidades. Dentre eles pode-se citar a sucção da camada limite com a intenção de atrasar a separação e consequentemente reduzir o tamanho da esteira, PRANDTL (1927). Outros processos visam aumentar a intensidade da turbulência do escoamento através do posicionamento de pequenos cilindros à frente do corpo para provocar a diminuição do arrasto. Recentemente, IGARASHI (1997) obteve bons resultados de redução de arrasto em prismas quadrados através do posicionamento a frente do modelo de um pequeno cilindro. Ainda pode-se citar o uso de rugosidade na superfície de corpos imersos em escoamento, para induzirem a transição da camada limite mais cedo, atrasando o ponto de separação com conseqüente redução da força de arrasto.

Com o método aqui proposto pretende-se determinar as características aerodinâmicas de um processo de redução do arrasto em cilindros parados e rotativos. Este método consiste em se colocar na esteira dos modelos um pequeno cilindro contendo uma série de furos no sentido do escoamento. Isto é feito com a intenção de se injetar massa na esteira e desta forma reduzir seu tamanho e alterar também seu comportamento. Sendo o equipamento de injeção de massa montado externamente a estes corpos, o processo em quase nada altera a forma destes. Isto é vantajoso pois permite adaptações ao contrário de modificações estruturais. Para determinar as características do escoamento foram realizados uma seqüência de ensaios de visualização, anemometria a fio quente dos perfis de velocidade da esteira, e de medidas das forças de arrasto geradas.

2. Descrição do Experimento

2.1. Experimento de Visualização

O experimento de visualização com fumaça foi montado em um túnel de vento de circuito aberto, de baixa velocidade, e com características de baixo indicie de turbulência. O modelo utilizado consistia de um cilindro de diâmetro igual a 0,059 metros montado, através de um eixo interno, em um mancal de rolamento fixado na parede da câmara de ensaio. Ao redor do mancal foi montado um anel onde foi fixada uma placa circular que continha o pequeno cilindro para o jato. O cilindro de jato é composto de pequenos furos, com diâmetro igual a 0,0016 metros, em todo seu comprimento para a injeção de massa. Para o caso do cilindro rotativo, um sistema composto de motor elétrico de corrente continua e todo o cinematismo necessário foi montado na parte traseira da câmara de ensaio. A Figura 1 detalha melhor o aparato usado.

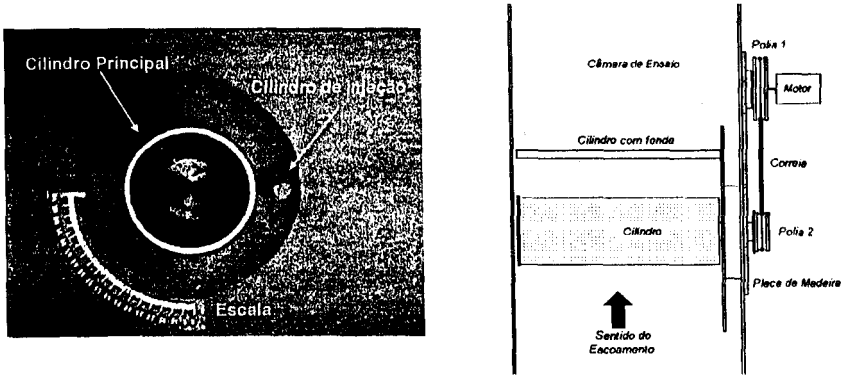

Figura 1 – Experimento de visualização.

2.2. Anemometria a fio quente.

O levantamento dos perfis de velocidade da esteira do cilindro rodando e parado foi montado em outro túnel de vento de circuito aberto, com maiores velocidades de escoamento. O modelo tinha mesmo diâmetro, igual a 0,059 metros, mas com a diferença de ter dois eixos em suas extremidades para a fixação nos mancais de rolamentos (Figura 2). As características do cilindro de injeção de massa e a placa foram mantidas iguais ao do modelo usado na visualização. Para as medidas dos perfis de velocidades usou-se um anemômetro de fio quente de temperatura constante. Foram levantadas curvas dos perfis de velocidades , tanto para o cilindro fixo quanto para o girando, a distância constante à montante em um 'grid' de 100 estações.

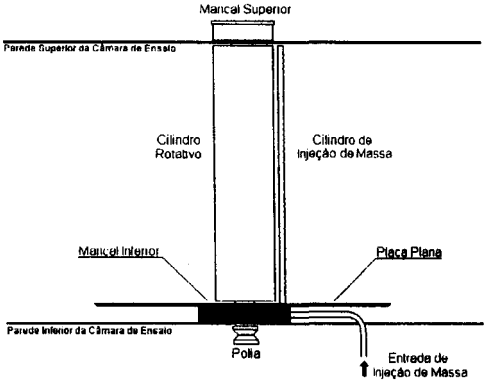

Figura 2 – Experimento de Anemometria.

3.3. Medidas de Forças Aerodinâmicas.

Para as medidas das forças aerodinâmicas foi utilizada uma balança aerodinâmica de dois graus de liberdade para a medição da força arrasto. Esta balança foi projetada e construída exclusivamente para este fim. O modelo foi o mesmo utilizado nos ensaios de anemometria montado em um suporte em forma de "U" conectado à balança aerodinâmica. A leitura dos valores de arrasto foi medido por um amplificador instrumental de precisão e lido em um microcomputador PC através de um aplicativo capaz de ler pequenas variações de força da ordem de 0,001 N. Desta

forma obteve-se alta precisão para pequenas variações de força de arrasto. A Figura 3 apresenta uma vista geral da balança sem o modelo no suporte.

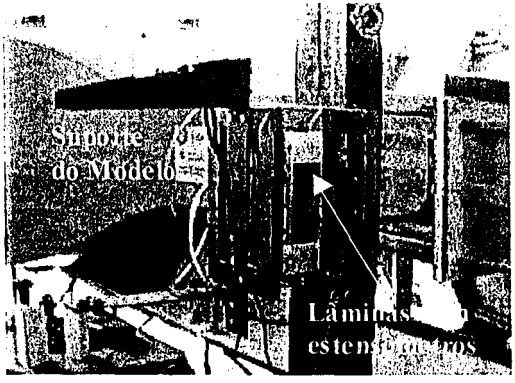

Figura 3 - Vista Geral da Balança Aerodinâmica.

3. Resultados

3.1. Visualização do Escoamento

Os resultados obtidos a partir dos ensaios de visualização são apresentados a seguir. São apresentados as curvas dos perfis de velocidade da esteira básica e de duas esteiras com injeção de massa tanto para o cilindro parado quanto para o rodando. A velocidade do escoamento foi mantida constante no valor de 1,4 metros por segundo, resultando em um número de Reynolds de 5506,7 baseado no diâmetro do cilindro. São apresentados duas situações de injeção de massa com o jato 1 e jato 2 com valores de quantidade de movimento iguais a 0,0129 N e 0,0395 N respectivamente.

O escoamento ao redor do cilindro parado e rodando pode ser visto na Figura 4. Os dois modelos encontram-se nas mesmas condições de escoamento, e o cilindro rotativo está girando a uma rotação constante de 950 rpm. Pode-se notar, como esperado, a esteira do cilindro parado maior do que a do cilindro rotativo.

Como pode ser visto na Figura 5, o efeito do jato na esteira do cilindro parado é bastante significativo quanto à redução de seu tamanho. Pode-se também constatar que a esteira não apresenta de forma evidente a formação de

grandes vórtices descolados e periódicos. Isto pode ser tomado como a evidência da influência da injeção massa na alteração da formação do 'Vortex Shedding'. Na Figura 6 observa-se também a diminuição do tamanho da esteira do cilindro parado. No entanto agora é possível observar também uma redução da esteira do cilindro com rotação.

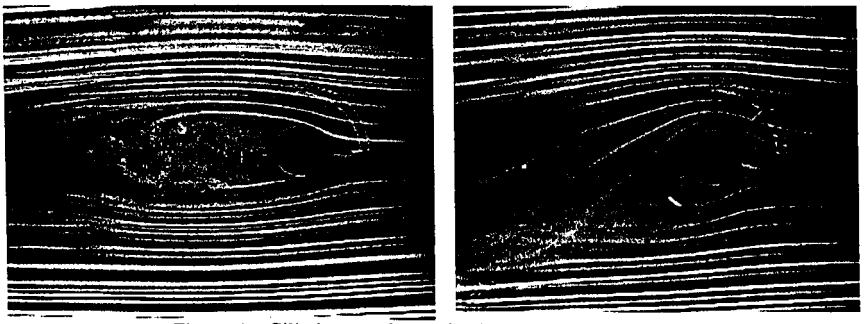

Figura 4 – Cilindro parado e rodando sem a injeção de massa.

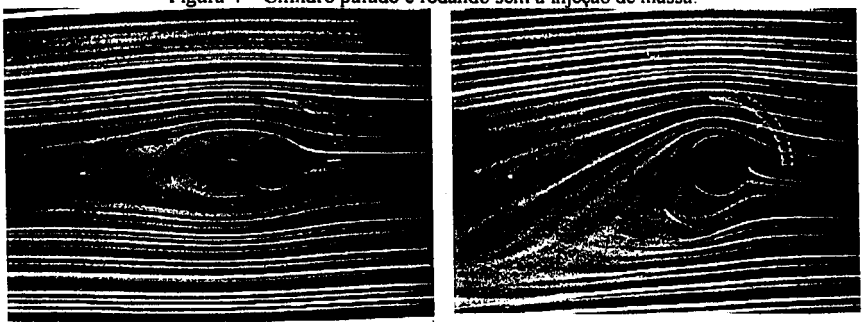

Figura 5 – Cilindro parado e rodando com jato 1

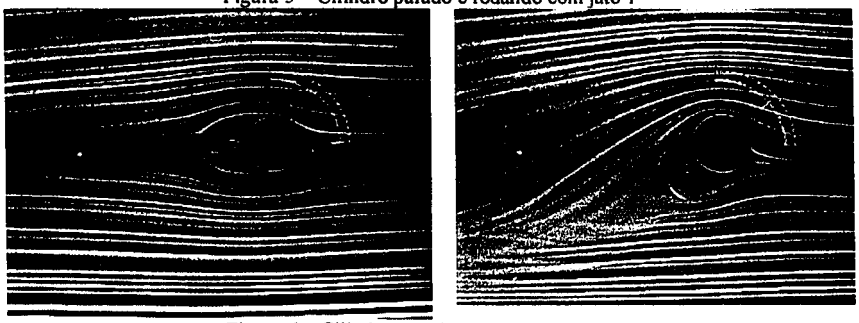

Figura 6 – Cilindro parado e rodando com jato 3

3.2. Levantamento dos perfis de velocidade.

A seguir é apresentado os resultados dos levantamentos dos perfis de velocidades da esteira do cilindro para e rodando. Estes levantamentos foram feitos à uma velocidade média na câmara de ensaio de 2,3 metros por segundo. Manteve-se a velocidade relativamente baixa devido ao fato de que nestas condições o efeito dos jatos na redução da esteira foi mais pronunciado. Isto não impede de extrapolar os resultados para outras condições de escoamento, devido principalmente a similaridade de perfis garantir o comportamento básico igual em um vasta faixa de condições de escoamento.

Nas figuras 8 e 9 pode ser visto que a redução da esteira é significativa com o aumento do valor da injeção de massa. A figura 7 apresenta os jatos que foram utilizados nesta parte do experimento. A Figura 8 apresenta os resultados para a esteira de um cilindro parado sem jato e com uma série de jatos. A Figura 9 apresenta os mesmos resultados mas para o cilindro rotativo. A seguir é mostrado a relação dos jatos usados com seu valor de quantidade de movimento.

Jato 40 - 0,02041 N

Jato 60 - 0,0547 N

Jato 80 - 0,08715 N

Jato 100 - 0,15475 N

Jato 120 - 0,19794 N

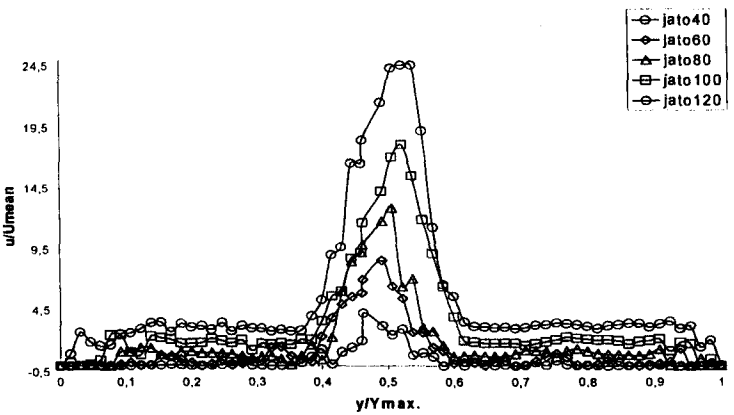

Figura 7 – Perfis de velocidade dos jatos usados.

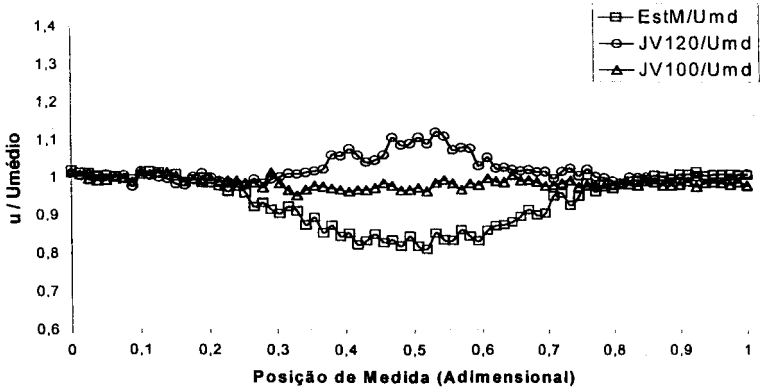

Figura 8 – Perfis de velocidade das esteiras sem e com jatos (Cilindro Parado).

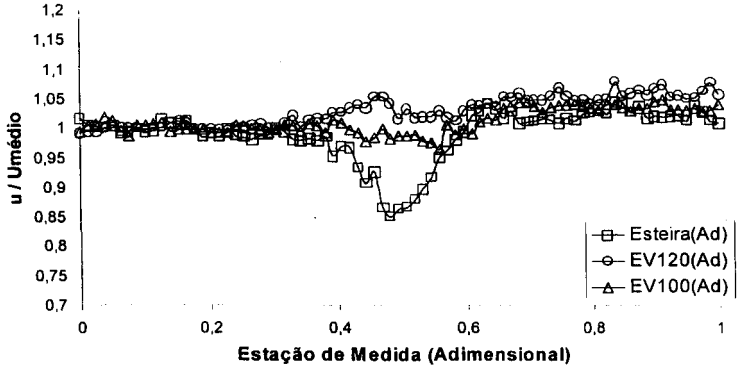

Figura 9 - Perfis de velocidade das esteiras sem e com jatos (Cilindro Rodando).

3.3. Medidas de Força

A seguir são apresentados os resultados das medidas de força utilizando a balança aerodinâmica. Foram, até o momento, realizados apenas as medidas com o cilindro parado, isto devido a complicações técnicas nas medições com o cilindro rodando. As velocidades usadas variaram entre 5 e 20 metros por segundo. Foi usada esta faixa de

velocidades pois foi a melhor que se adequou as condições de medição da balança e limitada pela velocidade máxima controlável do túnel de vento.

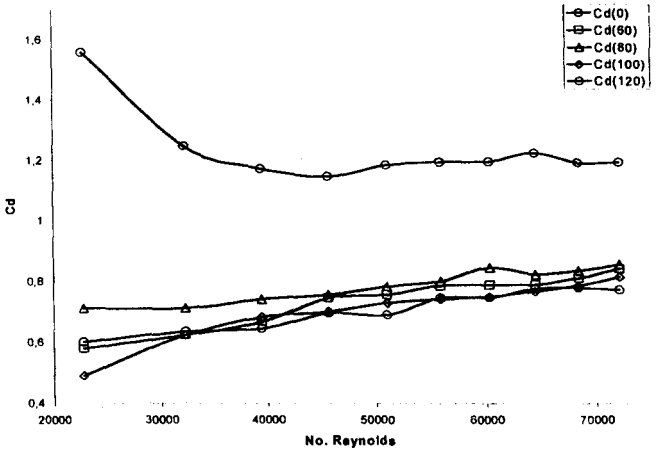

Figura 10 – Curvas de Cd pelo número de Reynolds para vários tipos jatos.

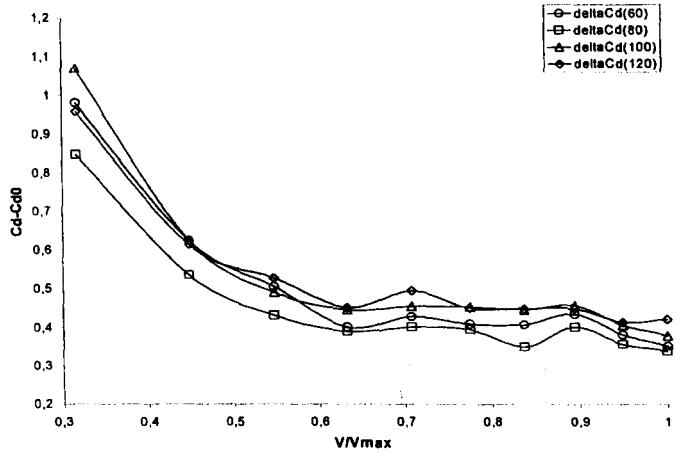

Figura 11 – Diferença entre Cd provocado por cada jato e Cd da esteira básica.

4. Discussão

4.1. Visualização do escoamento

Através das imagens obtidas pelo ensaio de visualização, fica claro que a redução do tamanho da esteira tanto para o cilindro parado quanto para o rodando é bastante grande. Na Figura 4 pode-se ver a esteira formada pelos dois cilindros, fixo e rodando. Logo após na Figura 5 a esteira tem suas características modificadas pela injeção de massa. O mais notável aqui é a aparente eliminação dos vórtices periódicos no cilindro fixo. Apenas uma pequena modificação no comportamento do cilindro rodando é notada. No entanto assim que o valor da vazão do jato é aumentada, uma notável diminuição no tamanho da esteira para ambos cilindros é observada. Pode-se aqui concluir que a injeção de massa provoca uma diminuição na pressão estática no escoamento à montante, fazendo com que o gradiente de pressão na superfície dos cilindros fique menos adverso.

4.2. Levantamento dos perfis de velocidade

De acordo com o que pode ser visto pelos resultados da anemometria, fica claro que a idéia de reduzir a distribuição de velocidades em esteiras através da injeção de massa, é um objetivo realizado. Os resultados apresentados na Figura 8, para o cilindro parado e na Figura 9 para o cilindro rodando, comprovam que a injeção de massa a uma determinada velocidade, a esteira sofre uma grande modificação. Esta modificação pode ser uma redução em seu tamanho como pode levar até a uma esteira invertida com acréscimo de velocidade e não de perda. Isto pode significar o surgimento de uma força de empuxo.

4.3. Medidas de Força

Os resultados das medidas de força de arrasto apresentados nas Figura 10 e 11 mostram que o fenômeno de redução da esteira pela injeção de massa não comporta-se forma seqüencial. Em outras palavras fica claro que uma grande redução no valor do arrasto é obtido. No entanto esta redução não é muito mais aumentada mesmo com o acréscimo na injeção de massa. Isto, aparentemente, leva à uma conclusão de que o fenômeno está mais relacionado com a injeção de um alto nível de turbulência no escoamento. Assim sendo, a camada limite na superfície do modelo

tende a transicionar mais cedo do que o esperado, eliminado a separação que é em alguns casos laminar para uma separação, bem mais a frente, turbulenta. Isto representa uma grande diminuição na força de arrasto entre os números de Reynolds 20000 a 30000 e tendendo á um patamar logo após.

5. Conclusões

Foram observados uma serie de provas experimentais que caracterizam a injeção de massa em uma esteira como sendo um método eficiente na redução do arrasto em corpos rombudos. Tanto os experimentos de visualização quanto o de medição dos perfis de velocidades mostraram uma redução grande nas dimensões da esteira e uma mudança de suas características. No entanto o experimento de medida das forças de arrasto mostrou que o fenômeno para certos números de Reynolds ser inerente à camada limite do que a esteira. Para os casos de separação laminar o efeito mais significativo para a redução do arrasto está na transição prematura da camada limite, devido ao aumento do índice de turbulência provocada pela presença do jato. Isto leva a um atraso na separação da camada limite com a conseqüente redução do arrasto de perfil. Mas todos estes resultados comprovam que houve de fato uma redução no valor do arrasto de perfil atrás dos modelos estudados.

Este método é, do ponto de vista de montagem, muito aconselhável para o uso em aplicações práticas. Dentre elas pode-se citar a redução do arrasto e o controle do 'Vortex Shedding' de pontes, torres altas, chaminés e demais estruturas sujeitas a ação de ventos. Outra aplicação é a implementação do sistema de injeção de massa para a redução do arrasto em aparelhos que pretendem o uso de cilindros rodando, efeito Magnus, melhorando assim a performance atualmente prejudicada pelo alto valor da força de arrasto encontrada nestes casos. Todas estas aplicações práticas irão necessitar de pouca adaptação para a montagem do sistema estudado.

Referências

BATCHELOR, G. K. (1967). *An Introduction to Fluid Dynamics*. Cambridge University Press, Londres.

BIRKHOFF, G. , ZARANTONELLO, E. H. (1957). *Jets, Wakes, and Cavities*. Academic Press Inc, Nova Iorque.

CAMARGO VIEIRA, R. C. (1964). *Contribuição ao estudo das aplicações dos cilindros rotativos*. São Carlos. 82p. Tese (Livre Docência) – Escola de Engenharia de São Carlos, Universidade de São Paulo.

DEPARTMENT OF EXTERNAL AFFAIRS (1988). *Tecnologia dos transportes: A experiência Canadense*. Ottawa. Ontario. Canadá. */folder/*

FLETTNER, A. (1925). The Flettner Rotor Ship. *Engieering*. P. 117-20, jan.

IGARASHI, T. (1997). Drag reduction of a square prism by flow control using a small rod. *Journal of Wind Engineering and Industrial Aerodynamics*. 69-71,p.141-53.

JOHNSON, W. (1986). The Magnus effect – Early investigations and a question of priority. *International Journal of Mechanics Sciences*. V. 28, n. 12, p.859-72.

PRANDTL, L. (1927). The generation of vortices in fluids of small viscosity. *Aeronautical Reprints*, n.20.

SCHLICHTING, H. (1968). *Boundary Layer Theory*. McGraw-Hill Book Company, Nova Iorque, 6ª Edição.

SWANSON, W. M. (1961). The Magnus Effect: A Summary of Investigations to Date. *Journal of Basics Engineering*. ASME 830, p. 461-70, set.

TOLLMIEN, W. (1945). Berechnung turbulenter Ausbreitungsvorgänge. *NACA TM 1085.*

APPLICATION OF A NON ISOTROPIC TURBULENCE MODEL TO STABLE ATMOSPHERIC FLOWS AND DISPERSION OVER 3D TOPOGRAPHY

Fernando T. BOÇON, Clóvis R. MALISKA

Departamento de Engenharia Mecânica
Universidade Federal do Paraná
C.P. 19011
81531-990 Curitiba – PR, Brazil
e-mail: bocon@demec.ufpr.br

APPLICATION OF A NON ISOTROPIC TURBULENCE MODEL TO STABLE ATMOSPHERIC FLOWS AND DISPERSION OVER 3D TOPOGRAPHY

ABSTRACT

A non isotropic turbulence model is extended and applied to three dimensional stably stratified flows and dispersion calculations. The model is derived from the algebraic stress model (including wall proximity effects), but it retains the simplicity of the "eddy viscosity" concept of first order models. The "modified k-ε" is implemented in a three dimensional numerical code. Once the flow is resolved, the predicted velocity and turbulence fields are interpolated into a second grid and used to solve the concentration equation. To evaluate the model, various steady state numerical solutions are compared with small scale dispersion experiments which were conducted at the wind tunnel of Mitsubishi Heavy Industries, in Japan. Stably stratified flows and plume dispersion over three distinct idealized complex topographies (flat and hilly terrain) are studied. Vertical profiles of velocity and pollutant concentration are shown and discussed. Also, comparisons are made against the results obtained with the standard k-ε model.

***Keywords**: Atmospheric dispersion, flow over hills, anisotropic k-ε, numerical simulation*

INTRODUCTION

Atmospheric boundary layer flows are object of intense study over the last years. A more comprehensive understanding of the complex phenomena involved in this particular type of flow is being sought, aiming the analysis of structural implications due to strong winds (neutral atmosphere), the pollutant dispersion under neutral or stable conditions and also for meteorological purposes. The

phenomenal increase in computer power over the last two decades has led to the possibility of computing such flows by the integration of the (modeled, time-averaged) Navier-Stokes equations.

Raithby *et al* (1987) employed the k-ε model (with modification in the C_μ value) to calculate the neutrally buoyant flow over the Askervein hill, and compared their numerical results with the experiment made over the real terrain in Scotland. Dawson *et al* (1991) also used the k-ε model (with some modification in the constants of the dissipation equation) to simulate the flow and dispersion over Steptoe Butte (Washington, USA) under neutrally and stably stratified atmosphere. Their results were favorably compared with experimental data, indicating that mathematical models using the eddy viscosity assumption in the turbulence closure could be used to predict the flow and pollutant dispersion over complex terrain. In Brazil, Dihlmann (1989) studied numerically the thermal discharge (from chimneys) into neutral and stable stratified environments. Santos *et al* (1992) applied the standard k-ε model to simulate the discharge of a chimney and the correspondent plume dispersion over a flat terrain. Queiroz *et al* (1994) applied the standard k-ε model to study (in two dimensions) the effect of heat islands in the atmospheric diffusive capacity.

Koo (1993) developed a non isotropic modified k-ε to account for different eddy diffusivities in the lateral and vertical directions in the atmosphere. His model is derived from the algebraic stress model and was applied in one dimensional problems to predict the vertical profiles of velocity, potential temperature and turbulence variables for the horizontal flow in a homogeneous atmospheric boundary layer. Also, the model was applied in two dimensional problems to simulate the sea breeze circulation and the manipulation of the atmospheric boundary-layer by a thermal fence. Koo's model is similar to the level 2.5 model of Mellor and Yamada (1982). Recently, Castro and Apsley (1997) compared numerical (using a "dissipation modification" k-ε model, as named by the authors) and laboratory data for two dimensional flow and dispersion over topography. Also, Boçon and Maliska (1997a, 1997b) extended the non isotropic k-ε model of Koo (1993) to numerically simulate the flow and pollutant dispersion over complex idealized topography, under neutral stratification.

Computational results were compared with experimental data obtained from a wind tunnel simulation.

More sophisticated models, like the Reynolds stress model, were also applied to predict environmental flows and pollutant dispersion, for instance the work of Andrén (1990). Sykes and Henn (1992) applied the Large Eddy Simulation technique to simulate plume dispersion. Our view is that for the time being, because of limitations in computer resources, those more complex turbulence models (like Reynolds stress and LES) are not suitable for most engineering problems, due to large CPU time and memory required.

In the present work we extend the application of Koo's modified k-ε model to predict three dimensional stably stratified flows and pollutant dispersion over complex terrain. The prediction of the plume dispersion downwind from a pollutant source is obtained from the solution of the concentration equation. To do so, it's necessary firstly to calculate the velocity field and eddy viscosities in the region of interest. Thus, convection and turbulent diffusion of the plume may be calculated.

MATHEMATICAL MODEL

The task of computing the concentration field downstream from a pollutant source is divided into two decoupled steps. Firstly we calculate the flow (velocity, temperature and turbulence variables) in the region of interest. Secondly, we use the computed velocity field and eddy diffusivities to solve the concentration equation. This separation can be done as we consider that the pollutant release does not disturb the flow. In fact, in the wind tunnel experiment, against which we compare our results, the tracer gas was released with practically no momentum nor buoyancy force.

Flow and Dispersion Modelling

The governing equations for the stratified flow are the conservation of mass, momentum and energy, written below in the usual tensor notation. Dispersion of a pollutant is computed from the concentration equation, after the flow is resolved.

$$\frac{\partial u_i}{\partial x_i} = 0 \tag{1}$$

$$\frac{\partial u_i}{\partial t} + u_j \frac{\partial u_i}{\partial x_j} = -\frac{1}{\rho}\frac{\partial p}{\partial x_i} + \nu \frac{\partial^2 u}{\partial x_j \partial x_j} + \frac{\partial}{\partial x_j}\left(-\overline{u_i' u_j'}\right) \tag{2}$$

$$\frac{\partial T}{\partial t} + u_j \frac{\partial T}{\partial x_j} = \frac{\partial}{\partial x_j}\left(-\overline{u_j' T'}\right) \tag{3}$$

$$\frac{\partial c}{\partial t} + u_j \frac{\partial c}{\partial x_j} = \frac{\partial}{\partial x_j}\left(-\overline{u_i' c'}\right) \tag{4}$$

where p is the pressure deviation with respect to the hydrostatic pressure. Primed variables denote turbulent fluctuations. As we are simulating wind tunnel flows, the Coriolis effect is neglected. Modelling of fluctuation terms are described in the next section.

Turbulence Modelling

In environmental flows the non isotropic character of turbulence is notable, specially in the case of dispersion of a scalar (pollutant) in the flow. For the case of stably stratified flows, for instance, vertical fluctuations are much inhibited due to buoyancy forces (arising from the positive vertical temperature gradient), while horizontal fluctuations are not. Even neutrally stratified flows feature some anisotropy. So, it is not expected that isotropic turbulence models may well reproduce the non isotropic turbulent diffusion. However, standard k-ε is successfully applied for environmental flows calculation where horizontal gradients (of velocity, temperature and turbulence variables) are smaller than the vertical gradients. In these situations, turbulent diffusion is significant only in the vertical direction, and an isotropic model can handle it appropriately. On the contrary, in the problem

of pollutant dispersion from a point source, both vertical and horizontal concentration gradients are significant, so are the corresponding turbulent diffusion. For this situations, a better description of the anisotropy in turbulent exchanges is necessary.

In his Ph.D. thesis, Koo (1993) proposed a modification on the classic k-ε model, through use of algebraic stress model including wall proximity effects. The resulting model was compared to data and higher order (turbulence closure) simulations for one and two dimensional atmospheric flows. The modified k-ε reproduced well the observed behaviors.

In our work we extend the application of the Koo's modified k-ε model to three dimensional flow and to dispersion problems. A description of the turbulence model is given below. Detailed description of derivation of the model can be seen in Koo (1993). Following the Boussinesq's eddy viscosity concept, Reynolds stresses are related to the gradient of the velocity components as

$$-\overline{u_i' u'}_j = K_m^j \left(\frac{\partial u_i}{\partial x_j} + \frac{\partial u_j}{\partial x_i} \right) - \frac{2}{3} k \delta_{ij} \qquad (5)$$

where K_m^j is the turbulent eddy viscosity in the j direction. Analogously, turbulent heat exchange and mass dispersion are expressed, respectively, by

$$-\overline{u_j' T'} = K_h^j \frac{\partial T}{\partial x_j} \qquad (6)$$

$$-\overline{u_j' c'} = K_c^j \frac{\partial c}{\partial x_j} \qquad (7)$$

where K_h^j and K_c^j are the eddy diffusivity in the j direction, respectively for heat and concentration. Eddy viscosities (for momentum) and eddy diffusivities (for energy and concentration) are expressed as functions of turbulent kinetic energy and its dissipation rate. For the vertical direction:

$$K_m^z = C_m \frac{k^2}{\varepsilon} \qquad (8)$$

$$K_h^z = C_h \frac{k^2}{\varepsilon} \tag{9}$$

$$K_c^z = C_c \frac{k^2}{\varepsilon} \tag{10}$$

And for the horizontal directions:

$$K_m^x = K_m^y = C_\mu \frac{k^2}{\varepsilon} \tag{11}$$

$$K_h^x = K_h^y = \frac{K_m^x}{Pr_t} \tag{12}$$

$$K_c^x = K_c^y = \frac{K_m^x}{Sc_t} \tag{13}$$

C_m is the proportionality coefficient for eddy viscosity in the vertical direction. C_h and C_c are the proportionality coefficients for eddy diffusivities in the vertical direction, respectively, for heat and mass concentration. These three coefficient are defined by functions of flow structure (from the algebraic stress model). Pr_t is the turbulent Prandlt number (=0.5) and Sc_t (=0.5) is the turbulent Schmidt number.

$$C_m = \frac{2}{3} \frac{(c_1 - 1)(E_7 - A G_H)}{E_4 + \frac{E_4 E_8}{C_{1T}} G_H - E_5 E_7 G_M + E_5 A G_H G_M} \tag{14}$$

$$C_h = C_c = \frac{2}{3} \frac{(c_1 - 1) + E_5 G_M C_m}{\left(c_{1T} + c'_{1T} f\right) E_4 + \left(\frac{2E_4 E_9}{E_{10}} + E_6\right) G_H} \tag{15}$$

$$f = \frac{l}{k_v z} = \frac{C_\varepsilon k^{3/2}}{k_v z \varepsilon} \tag{16}$$

Except for G_M, G_H and f, the coefficients in equations (14) and (15) are model constants, which can be found in Koo (1993). f is the wall function which reflects the effect of the ground

proximity on the Reynolds stresses and turbulent heat and mass fluxes, l is the turbulence length scale, k_v is the von Karman constant (=0.4), z is the distance from the ground and $C_\varepsilon = 0.13$.

The C_m, C_h and C_ε proportionality coefficients are functions of G_M, the production of turbulent kinetic energy by mean velocity shear, and G_H, the production (or destruction) of turbulent kinetic energy by buoyancy effects

$$G_M = \left(\frac{k}{\varepsilon}\right)^2 \left[\left(\frac{\partial u}{\partial z}\right)^2 + \left(\frac{\partial v}{\partial z}\right)^2\right] \tag{17}$$

$$G_H = g\beta\left(\frac{k}{\varepsilon}\right)^2 \frac{\partial \theta}{\partial z} \tag{18}$$

Turbulent kinetic energy and its dissipation rate are computed from their well known prognostic equations:

$$\frac{\partial k}{\partial t} + u_j \frac{\partial k}{\partial x_j} = \frac{\partial}{\partial x_j}\left(\frac{K_m^j}{\sigma_k}\frac{\partial k}{\partial x_j}\right) + P + G - \varepsilon \tag{19}$$

$$\frac{\partial \varepsilon}{\partial t} + u_j \frac{\partial \varepsilon}{\partial x_j} = \frac{\partial}{\partial x_j}\left(\frac{K_m^j}{\sigma_\varepsilon}\frac{\partial \varepsilon}{\partial x_j}\right) + C_{\varepsilon 1}(P+G)\frac{\varepsilon}{k} - C_{\varepsilon 2}\frac{\varepsilon^2}{k} \tag{20}$$

P is the production term due to mean velocity gradients

$$P = -\overline{u_i' u_j'}\frac{\partial u_i}{\partial x_j} = K_m^j\left(\frac{\partial u_i}{\partial x_j} + \frac{\partial u_j}{\partial x_i}\right)\frac{\partial u_i}{\partial x_j} \tag{21}$$

G is the production (or destruction) term due to buoyancy

$$G = g\beta\,\overline{w'T'} = -g\beta K_h^z \frac{\partial T}{\partial z} \tag{22}$$

Constants in equations (11), (19) and (20) are those from the standard k-ε model, and can be seen in table 1.

C_{μ}	σ_k	σ_ε	$C_{\varepsilon 1}$	$C_{\varepsilon 2}$
0.09	1.0	1.3	1.44	1.92

Table 1 - Constants of the turbulence model

NUMERICAL METHOD

The finite volume method is employed to solve the governing equations, in a non orthogonal, generalized curvilinear coordinate system. Co-located arrangement is used for variables storage in the grid, and the QUICK interpolation scheme with source deferred correction term Lien (1994) is applied on the convection terms, except for turbulence variables where a hybrid scheme (WUDS of Raithby and Torrance, 1967) is adopted. Our own codes NAVIER (1991) and SMOKE (1997) are used to solve the governing equations, respectively, for the flow and concentration.

As the grid used for computing the flow is not adequate for the concentration calculation, a second grid (refined near the source) is used for the last purpose. Velocities and eddy diffusivities obtained from the flow solution are interpolated into the second grid for the concentration calculation. Also, in order to verify grid dependent errors, the computations are made in a coarse and in a fine grid. Figures 1 and 2 illustrate some of the coarse grids used for flow and concentration (inflow boundary at left). Fine grids are 95x41x41 and 128x64x64 for flow and concentration, respectively. Coarse grids have half the number of volumes in each direction, with respect to the fine grids. Only half domain is resolved, because of symmetry.

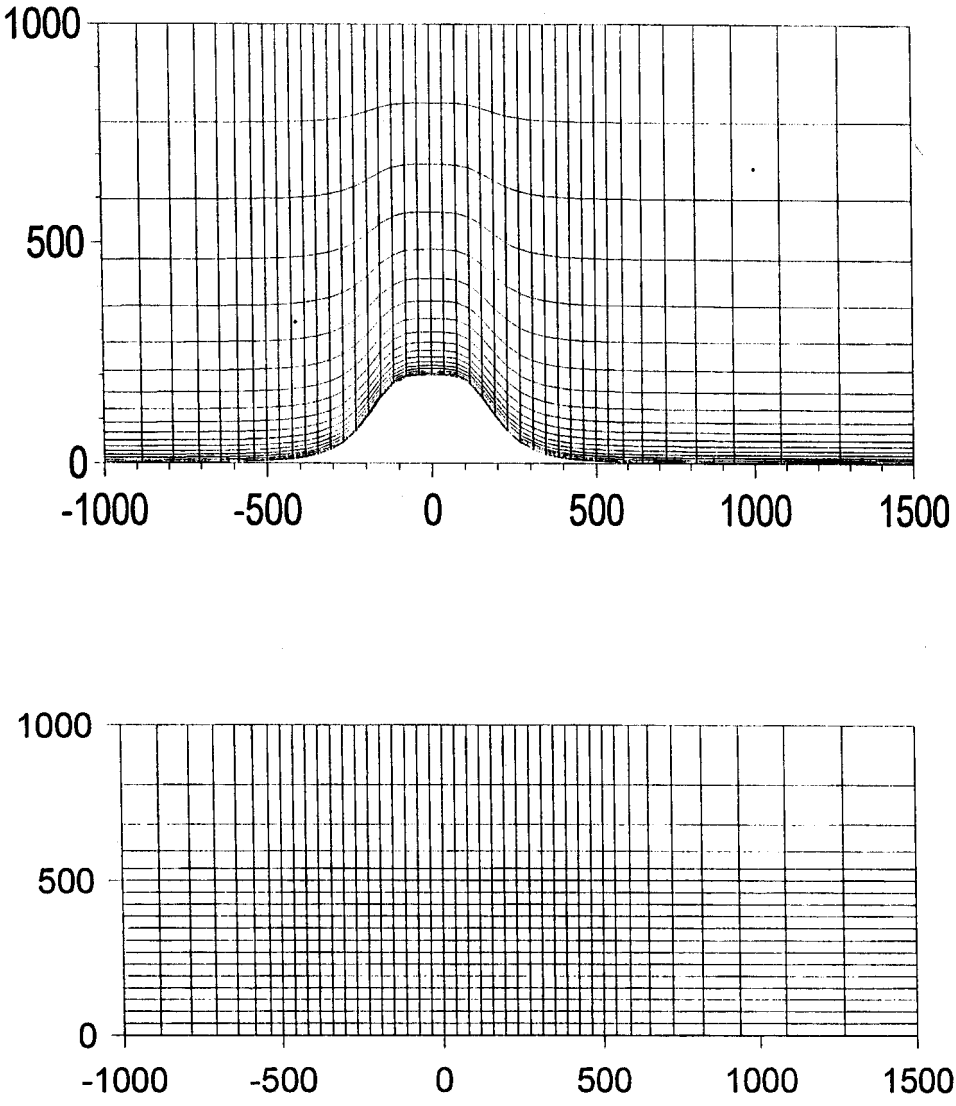

Figure 1 - Vertical (at the xz symmetry plane, above) and horizontal (below) views of the coarse grid for hill height 200mm (42x18x18 volumes) - vertical dimensions (z direction) exaggerated

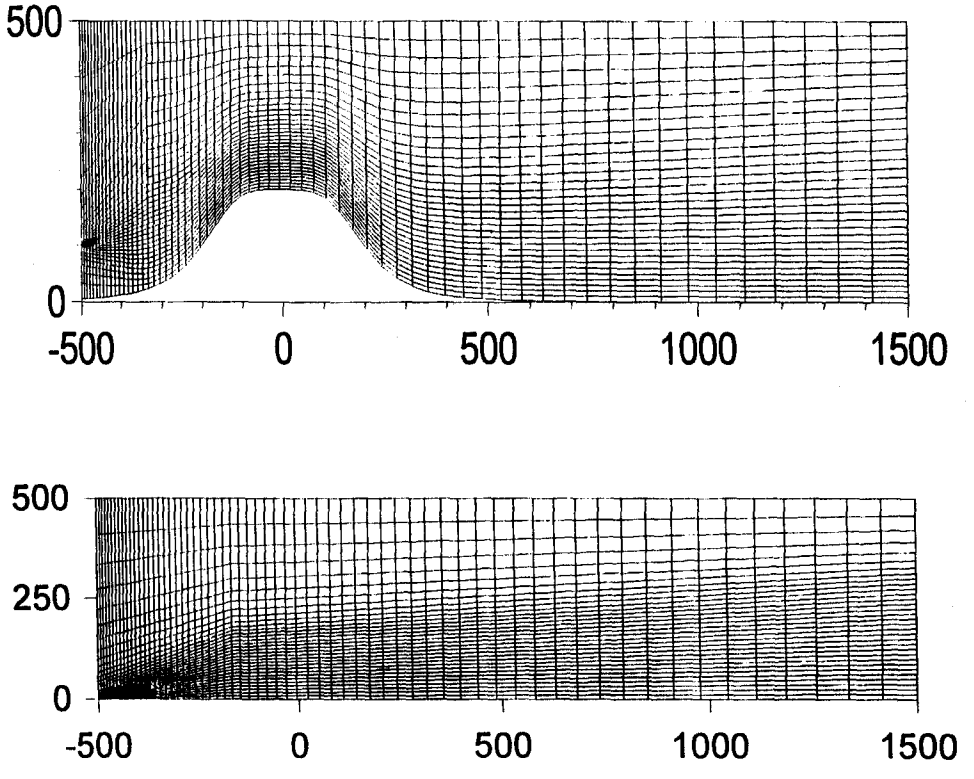

Figure 2 - Vertical (at the xz symmetry plane, above) and horizontal (below) views of the coarse grid for hill height 200mm (64x32x32 volumes) - vertical dimensions (z direction) exaggerated

To verify the model performance, in a first step, the above described modified k-ε is applied to simulate wind tunnel experiments.

THE WIND TUNNEL EXPERIMENT

Pollutant dispersion wind tunnel experiments were conducted at the Mitsubishi Heavy Industries, in Nagasaki, Japan, 1991. A report containing the results was obtained directly from that company. Wind tunnel test section is 2.5m wide, 1m high and 10m long. Axisymetric hills of different heights (0, 100 and 200mm), were positioned with the top located at (x,y)=(0,0). Hill shape

can be seen in figures 1 and 2. Streamwise direction is x, lateral is y and vertical is z. Source of tracer gas was positioned at (x, y, z)=(-500 mm, 0, 50mm) for hill heights 0 and 100mm, and at (x, y, z) = (-500mm, 0, 100mm) for hill height 200mm. Cases of neutral (ΔT=0, Pasquill class D) and stable atmosphere (ΔT=20°C , Pasquill class E) were performed. Streamwise velocity, velocity fluctuations, temperature and concentration were measured at various locations.

NUMERICAL EXPERIMENTS AND BOUNDARY CONDITIONS

Three different wind tunnel experiments were computationally simulated. They are designated with a letter - indicating stability class - followed by a number indicating hill height in mm. Hill heights of 0, 100 and 200mm were simulated. Neutral flows (Pasquill class D) and pollutant dispersion over these topographies were already numerically studied by Boçon and Maliska (1997a, 1997b). At this time, stably stratified flows (Pasquill class E) are considered. At the inflow boundary, velocity, temperature and turbulent kinetic energy are specified according to experimental measured values. As the dissipation rate of turbulent kinetic energy was not measured during the experiment, its inflow profile is calculated according to a prescribed turbulence length scale. For neutral boundary layer atmospheric flows, this length scale increases linearly with the distance from the wall (height above the surface, in the present problems). However, in the case of stably stratified flows the turbulence length scale does not increase linearly with the height, but it is limited to a maximum value (Castro and Apsley, 1997).

$$l = \frac{k_v z}{1 + \frac{k_v z}{0.085 L}} \qquad (23)$$

where z is the distance from the ground, k_v is the von Karman constant (=0.4) and L is the Monin-Obukhov length (=0.13m), which was calculated from the experimental values of velocity and temperature near the ground.

Outflow conditions are that of zero gradient for all variables. For velocity, lateral and upper boundaries are impermeable, with zero tangential stresses. For all other variables, lateral and upper boundary conditions are of null fluxes. Wall functions are invoked to apply boundary conditions appropriate to a rough wall (z_0 = 1.5e-4m) at the ground. Symmetry conditions are applied at the boundary coincident with the plane of symmetry ($y = 0$).

TREATMENT OF NEAR SOURCE DIFFUSIVITY

After applying the modified model and computing concentrations, we constated that, for all the cases studied (neutral and stable stratification), there was a large unrealistic plume spread near the source and, consequently, low concentrations everywhere in the domain (specially up to 500mm downstream the source). Taking a look at the turbulence length scale near the source, we noticed that it is larger than the plume dimensions. It means that the turbulent eddy sizes present in the flow are bigger than the plume, and could not promote such a observed diffusion in the numerical simulations. Therefore, we speculate that the length scale to be applied in the eddy diffusivities for the concentration should be appropriately reduced for the initial stages of plume spread, according to local plume dimensions. Based on a Gaussian plume distribution near the source, as a first investigation, we decide to reduce linearly the eddy diffusivities computed from the flow solution, to be applied in the concentration calculations. Using this simple procedure, the quality of the results improved considerably. Reduction of eddy diffusivity near the source is made taking its value (at the source location), obtained from the flow solution, and applying it in the Gaussian model for diffusion from a point source, to calculate how far from the emission point the plume width is about five times the local turbulence length scale. This value (five) was empirically determined from the analysis of the results. It was found, however, that the value is roughly the same for all the cases studied. At a given distance from the source, plume width is defined as the distance from the plume center line to the point where the concentration is 10% of its peak value. Indeed, further work is needed to better

model the initial stages of plume spread, where its dimensions are smaller than the characteristic turbulence length scale of the flow.

RESULTS AND DISCUSSION

In this section, some results of the flow and concentration calculations are presented, for the three stably stratified cases which were computationaly simulated. Figures 3, 4 and 5 show vertical profiles of concentration on the symmetry plane (y=0) for the cases E0, E100 and E200. The graphs in each figure refer to different positions downstream the source. In figure 3, for the case of flat terrain (E0), it can be seen a good agreement between numerical and experimental values. At the position x=200mm (third graph in fig. 3), we believe that there possibly was a mistake with respect to the report of the experimental results, which are inconsistently underestimated (as it can be noticed by comparison between the two peak concentration values corresponding to the positions x=0 and x=500mm).

Figures 4 and 5 show, respectively, the concentration profiles for the cases of hilly terrain E100 and E200 (hill heights 100 and 200 mm). From the view of a numerical analist, these are the most critical cases, due to the characteristics of stable flow and complex topography. Although the peak concentration values are fair well predicted, their locations are not. For the problem of pollutant dispersion over complex terrain, the plume path is dictated by the deviations in the mean flow caused by the irregular topography. A correct description of the plume path requires a sufficiently accurate prediction of the flow field (which "drives" the plume).

Figures 6 and 7 show vertical profiles of the streamwise component (u) of velocity on the symmetry plane (y = 0) for the cases E100 and E200. For both cases, the modified and the standard k-ε model produced nearly the same velocity profiles, and the recirculation zone in the lee side of the hill was underestimated. Different inflow turbulent length scales were tested at the inflow to verify a

possible influence, but it was noticed that the flow after the hill top is essentially determined by local conditions. A possible explanation for this model defect would be that the pronounced velocity gradients in this region, due to the three dimensional open recirculation zone (see figure 8), increase the production of turbulent kinetic energy and consequently enhance the eddy viscosities there, thus diminishing the size of the recirculation. However, a comparison between numerical and wind tunnel measured values did not reveal that the turbulent kinetic energy level has been overestimated by the mathematical model. Thus, regarding to the above cited problem of high eddy viscosities in the recirculation zone, the model drawback should be attributed to the dissipation equation, which is underestimating ε, and not to an overestimation of the production of turbulent kinetic energy (P).

The underestimation in the size of the open recirculating three dimensional zone by the flow model leads to an incorrect determination of the plume path. As the numerical model foresees a smaller recirculation, the flow, after passing over the hill top, brings (convectively) the plume down to the ground. Thus, in the numerical simulation, the center line of the plume (the place of the peak concentration values along the plume path) is nearer the ground than the experimental plume, and the ground level concentration numerical values result higher than the measured ones.

For the case E200, figure 5 also shows the concentration results produced by the standard k-ε model (isotropic), which clearly are more diffusive than those from the modified model. In this sense, it is demonstrated that the non isotropic character of the turbulent diffusion under stably stratified flow conditions is relevant, and that the modified k-$\dot{\varepsilon}$ has better ability to predict the dispersion of a plume in such conditions.

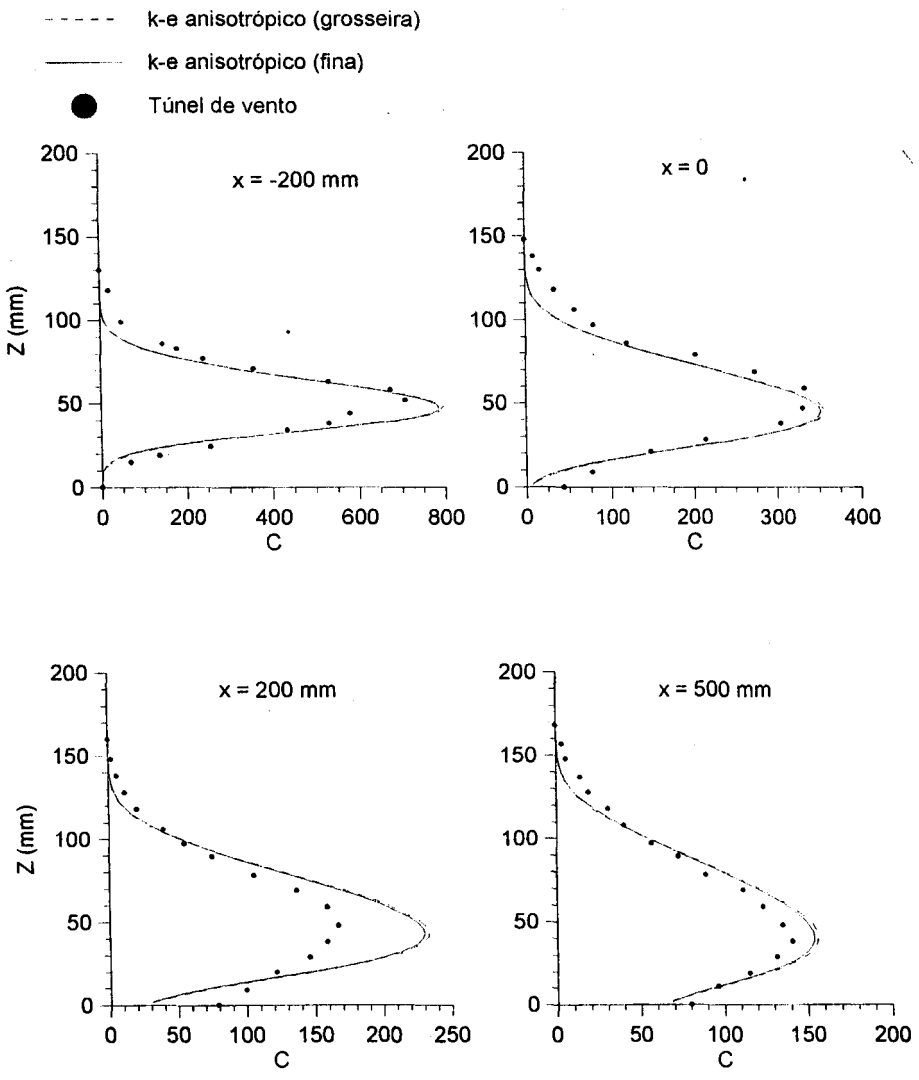

Fig. 3 - Case E0 - Concentration at the symmetry plane - flat terrain

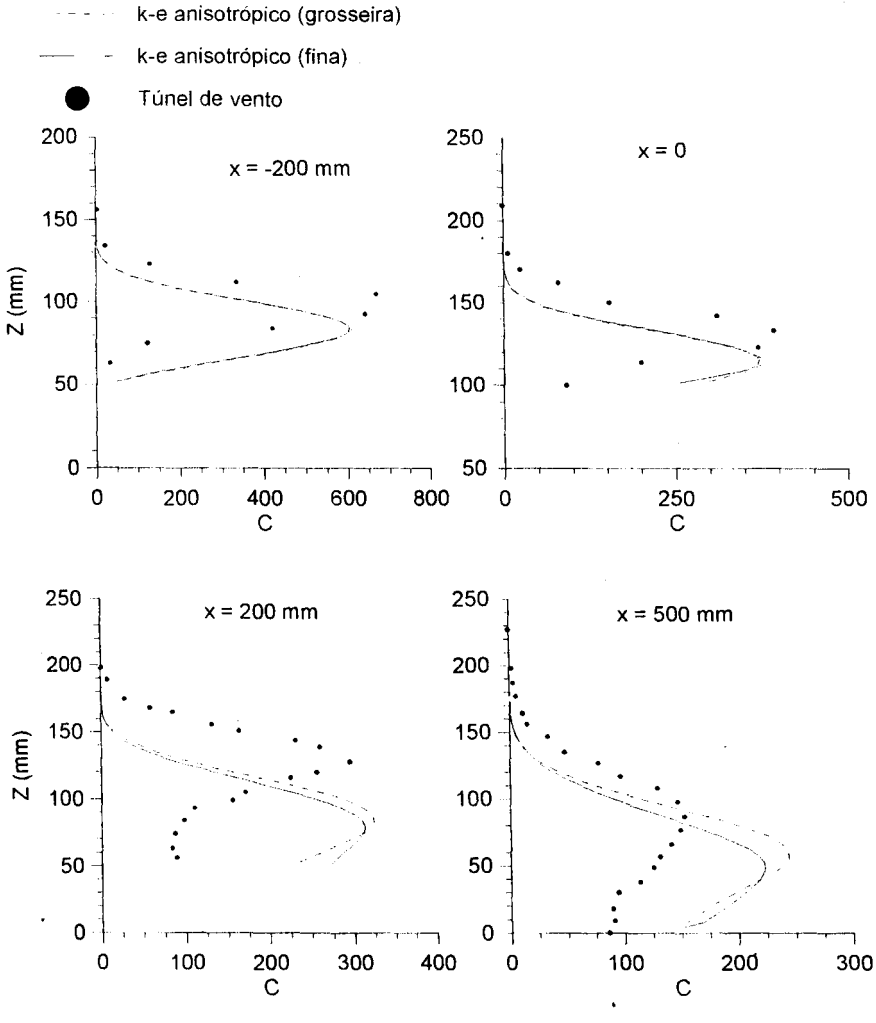

Fig. 4 - Case E100 - Concentration at the symmetry plane - hill height 100 mm

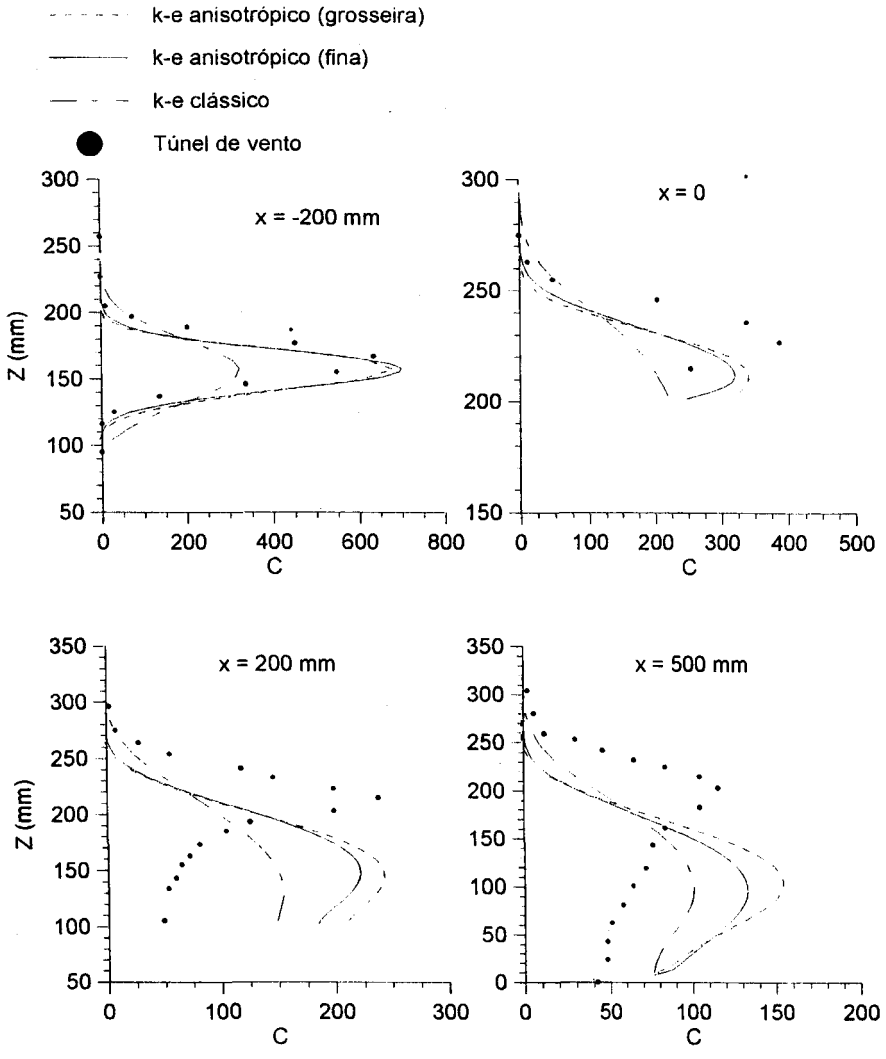

Fig. 5 - Case E200 - Concentration at the symmetry plane - hill height 200mm

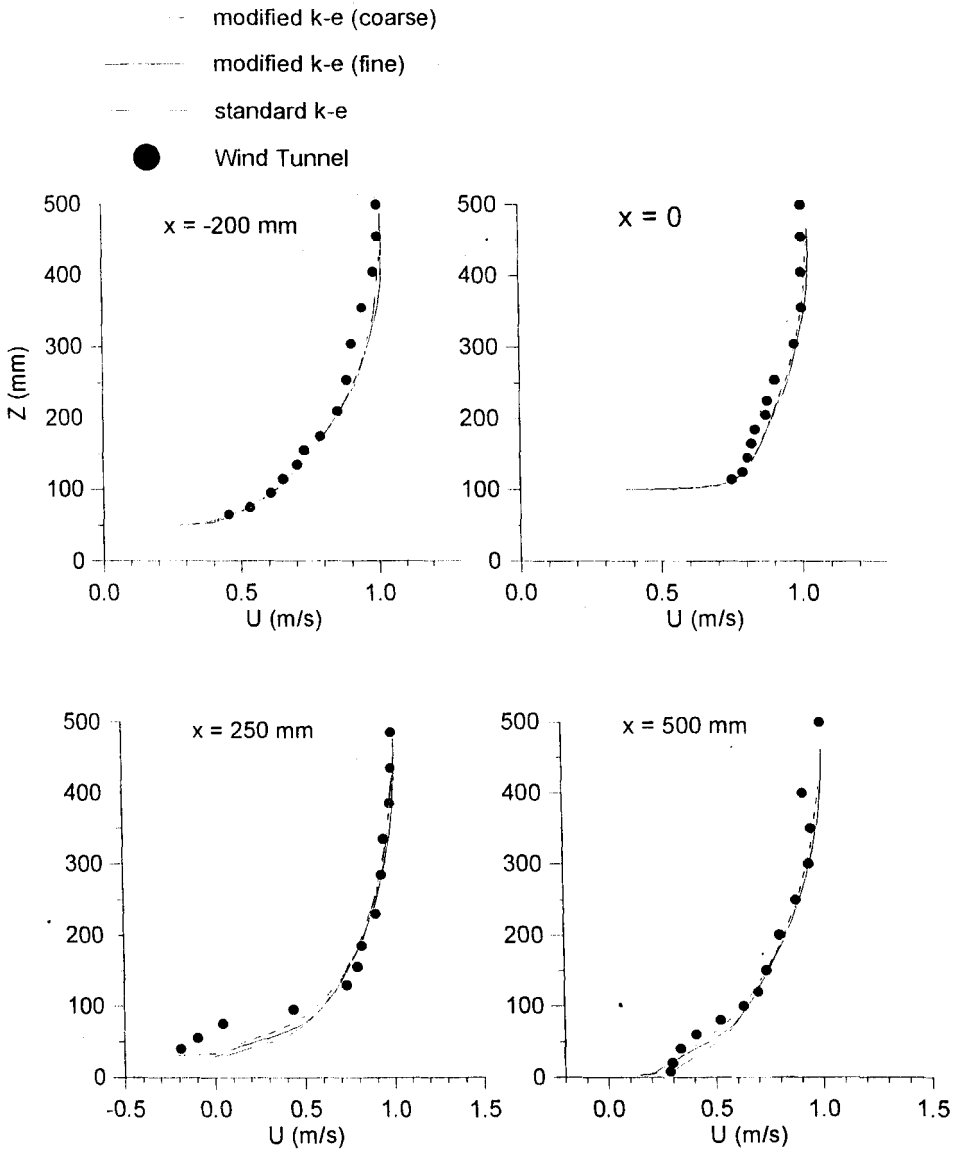

Figure 6 - Case E100 - vertical profiles of streamwise component of velocity (u) at the symmetry plane (y = 0) for different positions upstream and downstream the hill top (x = 0)

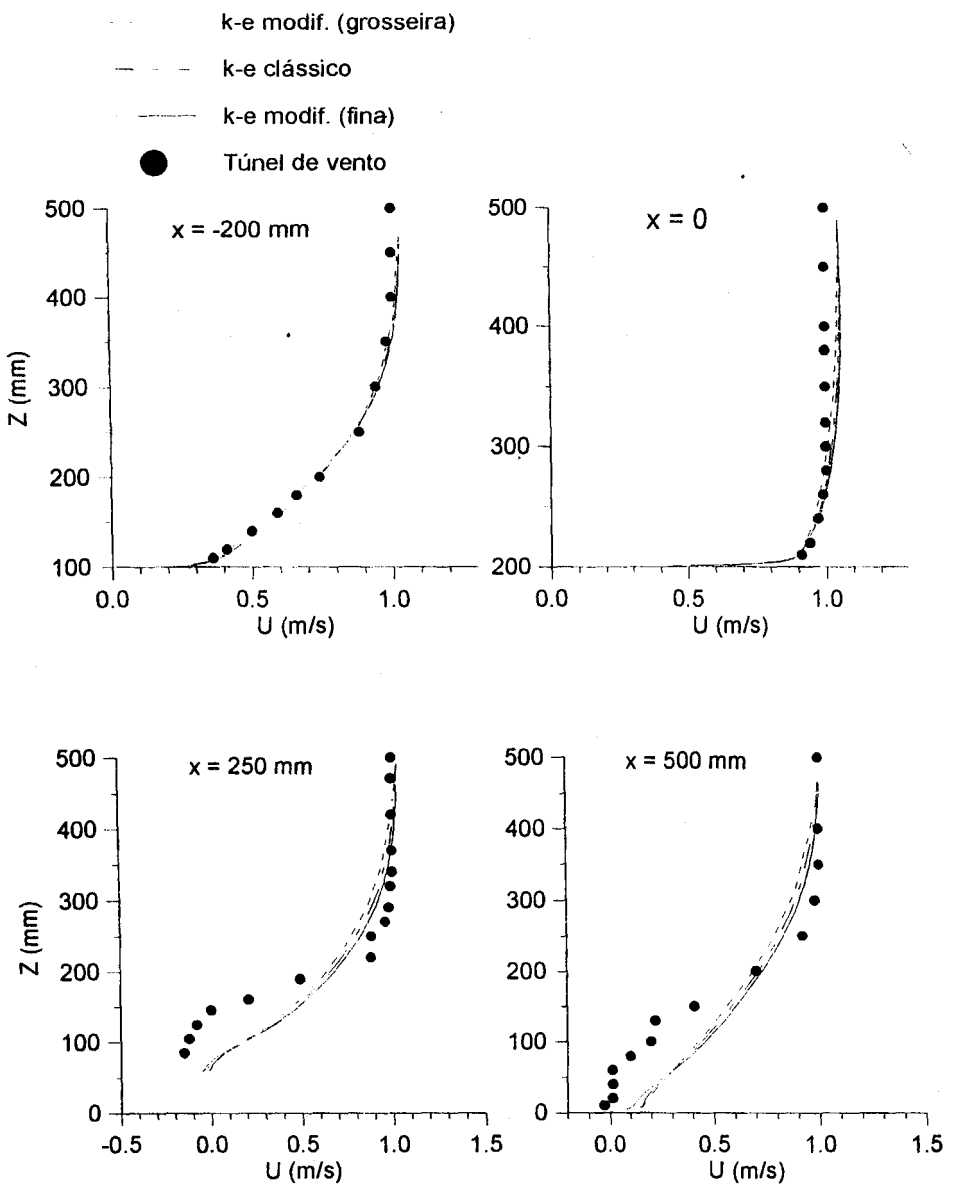

Figure 7 - Case E200 - vertical profiles of streamwise component of velocity (u) at the symmetry plane (y = 0) for different positions upstream and downstream the hill top (x = 0)

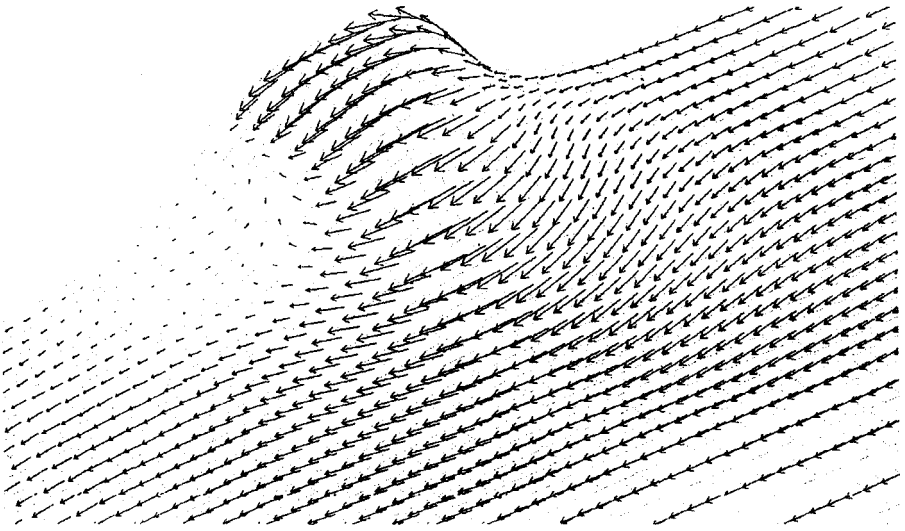

Figure 8 - Top view of velocity vectors 10 mm above the ground - case E200

CONCLUSIONS

A modified non isotropic k-ε model is applied to simulate three dimensional stably stratified atmospheric flows (Pasquill class E) and dispersion over an idealized complex terrain. The results for the velocity field are similar to those obtained with the standard model, because the vertical gradients of flow variables are not great (when compared with the concentration field), resulting nearly the same turbulent diffusion for both the standard (isotropic) and the modified (non isotropic) k-ε models. However, for the concentration results, the differences between the numerical solutions obtained with the standard and the modified k-ε models are quite distinct. The agreement of the concentration values - against the wind tunnel results - is very satisfactory for the case of flat terrain. Over hilly terrain, the concentration peak values are fair well predicted, but their locations (height above the ground) are not. The problem is attributed to a model fault in predicting the open recirculating three dimensional zone, which occurs in the lee side of the hills. In the recirculation

zones, the eddy viscosities are overestimated and thus the size of the recirculation is underpredicted. Consequently, the plume path over the top and the lee side of the hill is not well predicted, with respect to its height above the ground, which is underestimated. Despite of these drawbacks, the modified non isotropic k-ε produces better results than the conventional isotropic model.

ACKNOWLEDGMENTS

We are grateful for the financial support provided by CNPq and CAPES.

REFERENCES

Andrén, A., 1990, "A Meso-Scale Plume Dispersion Model. Preliminary Evaluation in a Heterogeneous Area", Atmospheric Environment, v. 24A, n. 4, p. 883-896.

Boçon, F. T. and Maliska, C. R., 1997a, "Numerical Modelling of Flow Over Complex Terrain", Proceedings, XVIII Iberian Latin American Congress on Computational Methods in Engineering, Brasília - DF, published in CD-ROM.

Boçon, F. T. and Maliska, C. R., 1997b, "Numerical Modelling of Flow and Dispersion Over Complex Terrain", Proceedings, XIV Brazilian Congress of Mechanical Engineering, ABCM, Bauru-SP, p. 211-218.

Castro, I.P. and Apsley, D.D., 1997, "Flow and Dispersion Over Topography: A Comparison Between Numerical and Laboratory Data for Two-Dimensional Flows", Atmospheric Environment, vol. 31, no 6, pp. 839-850.

Dawson, D., Stock, D.E. and Lamb, B., 1991, "The Numerical Simulation of Airflow and Dispersion in Three-Dimensional Atmospheric Recirculation Zones", J. Applied Meteorology, vol. 30, pp. 1005-1024.

Dihlmann, A., Maliska, C. R., Silva, A. F. C., 1989, "Solução Numérica da Descarga de Jatos Poluentes em Meio Estratificado", Anais do X Congresso Brasileiro de Engenharia Mecânica, ABCM, Rio de Janeiro-RJ, p. 101-104.

Koo, Y.S., 1993, "Pollutant Transport in Buoyancy Driven Atmospheric Flows", Ph.D. Thesis, The Louisiana State University and Agricultural and Mechanical Col.

Lien, F.S. and Leschziner, M.A., 1993, "Upstream Monotonic Interpolation for Scalar Transport With Application to Complex Turbulent Flows", Int. J. For Numerical Methods in Fluids, vol. 19, pp. 527-548.

Mellor, G.L. and Yamada, T., 1982, "Development of a Turbulence Closure Model for Geophysical Fluid Problems", Reviews of Geophysics and Space Physics, vol. 20, no 4, pp. 851-875.

NAVIER, 1991, "Desenvolvimento de Códigos Computacionais para Solução de Problemas de Escoamentos de Alta Velocidade", Relatório preparado para o Instituto de Atividades Espaciais do Centro Técnico Aeroespacial - UFSC - Dep. Eng. Mecânica - Parte VII.

Panofsky, H. A., Dutton, J. A., 1984, "Atmospheric Turbulence - Models and Methods for Engineering Applications", John Wiley & Sons, New York.

Raithby, G.D. and Torrance, K.E., 1967, "Upstream-Weighted Differencing Schemes and Their Application to Elliptic Problems Involving Fluid Flow", Computer and Fluids, vol. 2, pp. 12-26.

Raithby, G. D., Stubley, G. D., and Taylor, P. A., 1987, "The Askervein Hill Project: A Finite Control Volume Prediction of Three-Dimensional Flows over the Hill", Boundary-Layer Meteorology, v. 39.

SMOKE, 1997, "Código Computacional para a Solução da Dispersão de Escalares em Geometrias Tridimensionais", Laboratório de Simulação Numérica em Mecânica dos Fluidos e Transferência de Calor do Departamento de Engenharia Mecânica da Universidade Federal de Santa Catarina - SINMEC.

Explorando o Não-fechamento no Equacionamento da Turbulência

Exploring the Nonclosure Question in Turbulence Equations

Harry Edmar Schulz
Laboratório de Hidráulica Ambiental-CRHEA
Departamento de Hidráulica e Saneamento
Escola de Engenharia de São Carlos-Universidade de São Paulo
C.P.359, 13560-270, São Carlos, S.P., Brasil
(Trabalho desenvolvido no Institut für Hydromechanics, Universität Karlsruhe, Alemanha)

Abstract

In this study it is shown that the use of the turbulent kinetic energy dissipation rate as a relevant parameter in the search of a closure equation for turbulence evokes the concept of entropy generation. The Gouy-Stodola theorem is used to show this connection. Further, an alternative formulation for turbulence is presented here. This formulation is very similar to the entropy equation for thermal radiation. It is shown that simple relations exist between the parameters defined in this formulation and the entropy generation rate.
***Keywords**: entropy generation rate, Gouy-Stodola theorem, nonclosure in turbulence, turbulence equations.*

Resumo

Uma discussão é conduzida no sentido de mostrar que o uso da taxa de dissipação de energia cinética turbulenta, como variável relevante na busca de uma equação de fechamento para o problema de turbulência, evoca o conceito de geração de entropia. Isto é feito recordando o teorema de Gouy-Stodola. Posteriormente, um equacionamento alternativo para turbulência é explorado visando verificar a identidade possível entre variáveis deste equacionamento e a taxa de geração de entropia. Este equacionamento possui uma semelhança formal muito forte com a equação de entropia em radiação térmica.
***Palavras-chave**: taxa de geração de entropia, teorema de Gouy-Stodola, não-fechamento em turbulência, equações de turbulência.*

Introdução

No estudo da turbulência com bastante frequência nos concentramos no conjunto de equações que governam o movimento de fluidos newtonianos, isto é, fluidos que, se admitidos como compondo um contínuo, seguem uma proporcionalidade entre tensão e gradiente de velocidade. Neste caso, as equações de Navier-Stokes e a equação da continuidade compõem um conjunto fechado e representam convenientemente a segunda lei de Newton e o princípio de conservação de massa. Entretanto, utilizar essas equações para representar parâmetros flutuantes, ainda submetidas

ao operador de média, acrescenta a dificuldade de ser necessário estabelecer equações adicionais para exprimir as funções de correlação entre flutuações de velocidades, ou de outras grandezas, que decorrem dos procedimentos tradicionalmente aceitos para efetuar as médias. Surge, portanto, o problema do fechamento, no qual se impõe que sejam introduzidas equações complementares com informações novas acerca do fenômeno, porém sem introduzir variáveis novas.

O problema é antigo e tem conduzido a diferentes aproximações. A experiência acumulada ao longo deste século conduziu gradativamente ao uso da taxa de dissipação de energia (ε) como um parâmetro relevante na modelação da equação faltante. Um exemplo de sucesso bastante expressivo é o modelo k-ε, que liga a taxa de dissipação de energia ao conceito de viscosidade turbulenta, este último uma simplificação conveniente para calcular escoamentos turbulentos. Neste modelo, são utilizadas as equações de Reynolds (segunda lei de Newton), da continuidade (conservação de massa) e da energia (transporte da energia cinética turbulenta). Nesta última surge a taxa de dissipação de energia e, na busca de maiores informações, gera-se uma nova equação para esta taxa (a qual geralmente é apresentada desvinculada, de forma mais evidente, de um princípio físico aparente) e, finalmente, conecta-se esta variável à viscosidade turbulenta já mencionada.

O sucesso em utilizar a taxa de dissipação de energia como variável relevante induz à pergunta elementar: se já foi utilizado o conceito de conservação de energia, no qual parte é dissipada e no qual se define a taxa de dissipação, como justificar uma nova equação para esta dissipação sem evidenciar um conceito físico adicional? Evidentemente o desenvolvimento da equação adicional fundamenta-se na própria física dos escoamentos turbulentos, na qual o princípio utilizado está imbutido. Mas podemos ainda caminhar no sentido de explorar as possibilidades decorrentes do uso da taxa de dissipação de energia e indicar os conceitos que podem estar sendo evocados ao fornecermos uma aproximação adicional para a mesma.

Os Princípios Físicos Usuais em Turbulência

Como em qualquer problema em Mecânica dos Fluidos, a formulação em turbulência utiliza, conforme já foi mencionado, os seguintes princípios:

- Conservação de massa.
- Conservação (transporte) da quantidade de movimento.

O uso das equações de Navier-Stokes para descrever o escoamento de fluidos em condições especiais de proporcionalidade entre tensão e taxa de deformação gerou uma comunidade de especialistas neste tipo de escoamento e permitiu o avanço no cálculo de soluções numéricas explícitas para estas equações. O estudo da turbulência se enquadra nesta comunidade, uma vez que as equações utilizadas são uma aplicação das equações de Navier-Stokes.

- Conservação (transporte) de energia.

Em turbulência utiliza-se a "energia cinética turbulenta", que é desenvolvida também a partir das equações de Navier-Stokes. O uso das flutuações de velocidade garante a interpretação que vincula esta energia apenas à parcela turbulenta do escoamento. A equação de conservação ou transporte resultante apresenta todos os termos deste tipo de equacionamento, ou seja, de forma resumida: variação temporal, advecção, difusão, produção e dissipação.

Os princípios mencionados, que conduzem cada um à sua própria equação, são de fácil assimilação. A "equação adicional", que deve possibilitar o fechamento do problema de turbulência, tem dispendido um esforço razoável por parte dos pesquisadores, os quais apontam para o uso de uma equação que envolva a taxa de dissipação de energia, ou que a descreva. Isto nao implica em dizer que a taxa de dissipação de energia represente o único problema a ser resolvido no fechamento das equações. Entretanto, os termos desconhecidos são representados, comumente, como dependentes da taxa de dissipação de energia.

Como exemplo de uso da taxa de dissipação de energia para obter uma solução particular podemos mencionar a solução de Kolmogoroff para a distribuição da energia sobre os diferentes números de ondas. A lei dos 5/3 que recebe o seu nome é desenvolvida no contexto da turbulência isotrópica, utilizando análise dimensional, na qual um procedimento de "inclusão-exclusão de variável relevante" é utilizado para a viscosidade cinemática (Schulz, 1997). Este procedimento, embora conduza ao resultado correto, mostra que talvez a melhor forma de analisar o problema ainda não foi atingida. Na análise dimensional efetuada, a taxa de dissipação de energia permite obter a forma do espectro, bem como definir escalas de velocidade e comprimento características para os maiores números de ondas.

No sentido de obter um equacionamento mais geral, o uso das equações de Navier-Stokes para gerar uma equação de transporte (conservação) da vorticidade e, conseqüentemente, uma equação de transporte (conservação) da taxa de dissipação da energia para altos números de Reynolds, é talvez o procedimento reconhecido como aquele mais vinculado à própria física do escoamento. Este procedimento também inclui uma nova variável, a vorticidade, para a qual se propõe a sua própria lei de variação. Em uma primeira análise, portanto, conseguiu-se associar uma nova equação a um novo conceito (vorticidade). Contudo, esta nova relação traz consigo os problemas já mencionados decorrentes do uso constante das equações de Navier-Stokes para a geração de novas equações de conservação ou transporte: parcelas componentes apenas estao definidas na própria equação e não possuem comportamento determinado por outras relações conhecidas. Assim, essas parcelas necessitam ser determinadas a partir de novas considerações. Conseqüentemente, a conservação (transporte) da vorticidade, embora tenha permitido estabelecer uma relação para a taxa de dissipação de energia, transfere o problema do fechamento para outras equações adicionais e, evidentemente, para outros princípios físicos.

Tendo em vista este aspecto, comenta-se, no presente trabalho, uma abordagem que conduz o problema da taxa de dissipação de energia para um ponto de vista no qual a taxa de geração de entropia é evidenciada. Não se pretende, evidentemente, resolver o problema do fechamento, mas mostrar as possibilidades decorrentes deste ponto de vista.

Taxa de Dissipação de Energia e o Teorema de Gouy-Stodola

Uma verificação da possibilidade de vínculo entre a taxa de dissipação de energia e outros conceitos não aventados na abordagem tradicional de turbulência é interessante. A entropia é um princípio físico de uso corrente, ainda não utilizado na formulação até o momento apresentada. Uma forma possível de abordagem pode talvez ser melhor analisada a partir de um exemplo ilustrativo. Se se considerar um agitador qualquer que mantém um fluido em um estado de turbulência estacionária, podemos dizer que estamos continuamente alterando a ordem deste sistema (fluido), ou continuamente gerando entropia no mesmo. Assim, está-se utilizando o estado turbulento como um gerador de entropia. Como conseqüência, o equacionamento de entropia deve ser convenientemente adaptado para representar a geração da mesma. Note-se ainda que a manutenção de um estado turbulento também exige um fornecimento contínuo de energia, que é dissipada, o que indica que uma relação entre as duas grandezas deve ser possível. Esta relação já está estabelecida pelo teorema de Gouy-Stodola (ver Bejan, 1982, ou Schulz, 1997) O seu desenvolvimento, embora tradicional na literatura, é pouco utilizado no desenvolvimento de soluções para os escoamentos turbulentos, motivo pelo qual é incluído no presente texto. Uma breve apresentação do teorema de Gouy-Stodola é aqui feita, onde inicialmente são colocadas as equações básicas com as quais se trabalha. O desenvolvimento na forma integral aqui apresentada é conveniente para a rápida assimilação do conteúdo do teorema.

1 - Equação de Conservação de Massa, na sua forma integral usual:

$$\frac{\partial}{\partial t}\int_{VC}\rho\, dVol = -\int_{SC}\rho\,\vec{V}.d\vec{A} \tag{1}$$

Ou:

$$\frac{\partial M}{\partial t} = \sum_{Sai}\dot{m} - \sum_{Entra}\dot{m} \tag{2}$$

ρ é a massa específica do fluido, *Vol* é o volume de controle, $\vec{V}$ é a velocidade, A é a área, M é a massa e $\dot{m}$ representa o fluxo de massa através das paredes do volume de controle.

2 - Primeira Lei da Termodinâmica, na sua forma integral usual:

$$\dot{Q} - \dot{W} = \frac{\partial}{\partial t}\int_{VC} e\rho\, dVol + \int_{SC}\left(e + \frac{p}{\rho}\right)\rho\,\vec{V}.d\vec{A} \tag{3}$$

$$E = \int_{VC} e\rho\, dVol \qquad e = \frac{V^2}{2} + gz + u \qquad h = u + \frac{p}{\rho} \tag{4}$$

$$\frac{\partial E}{\partial t} = \sum_{Entra}\dot{m}\left(h + \frac{V^2}{2} + gz\right) - \sum_{Sai}\dot{m}\left(h + \frac{V^2}{2} + gz\right) + \dot{Q} - \dot{W} \tag{5}$$

$\dot{Q}$ é a potência térmica, $\dot{W}$ é a taxa de trabalho, e é a energia específica, p é a pressão, g é a aceleração da gravidade e z é a cota.

3 - Segunda Lei da Termodinâmica, na sua forma integral usual:

$$\frac{\partial}{\partial t}\int_{VC} s\rho\, dVol + \int_{SC} s\rho\,\vec{V}.d\vec{A} \geq \int_{SC}\frac{1}{T}\left(\frac{\delta\dot{Q}}{A}\right)dA \tag{6}$$

s é a entropia por unidade de massa. Define-se a entropia S como:

$$S = \int_{VC} s\rho\, dVol \tag{7}$$

Tem-se, então:

$$\frac{\partial S}{\partial t} \geq \sum_{Entra}\dot{m}s - \sum_{Sai}\dot{m}s + \frac{\dot{Q}}{T} \tag{8}$$

Portanto, verificando-se sempre a desiguladade 8, define-se a entropia gerada como sendo:

$$\dot{S}_{Ger} = \frac{\partial S}{\partial t} - \sum_{Entra}\dot{m}s + \sum_{Sai}\dot{m}s - \frac{\dot{Q}}{T} \geq 0 \tag{9}$$

4 - Teorema de Gouy-Stodola:

Da equação 5 e da desigualdade 8 resulta:

$$\dot{W} \leq \sum_{Entra} \dot{m}\left(h + \frac{V^2}{2} + gz - T_0 S\right) - \sum_{Sai} \dot{m}\left(h + \frac{V^2}{2} + gz - T_0 S\right) - \frac{\partial}{\partial t}\left(E - T_0 S\right) \tag{10}$$

T_0 é a temperatura do ambiente onde está imersa a parte do volume de controle por onde atravessa o calor, sendo também a temperatura daquela parte da superfície de controle. Alterações de temperatura são consideradas ocorrerem no interior do volume. A desigualdade 10 mostra que a potência utilizável do sistema possui um limite superior, quando se adota a igualdade. A diferença entre este limite superior e a potência utilizável é a potência utilizável perdida (potência dissipada).

$$\dot{U} = \dot{W}_{max} - \dot{W} \tag{11}$$

Utilizando as relações 5, 10 e 11, obtém-se:

$$\dot{U} = T_0\left(\frac{\partial S}{\partial t} - \sum_{Entra} \dot{m}s + \sum_{Sai} \dot{m}s - \frac{\dot{Q}}{T_0}\right) \tag{12}$$

Das equações 9 e 12 tem-se, imediatamente:

$$\dot{U} = T_0 \dot{S}_{Ger} \tag{13}$$

Esta é uma forma conveniente de apresentação do teorema de Gouy-Stodola para a Mecânica dos Fluidos (Bejan, 1982). Nota-se que a taxa de dissipação de energia (potência dissipada) no volume de controle é diretamente proporcional à taxa de geração de entropia neste mesmo volume. A equação 13 não permite encaminhar no momento qualquer proposta de fechamento, mas mostra que ao buscarmos soluções que envolvem a taxa de dissipação de energia nos problemas de turbulência, estamos apenas seguindo o caminho natural que evoca o conceito de entropia. Assim, o equacionamento em turbulência envolve de fato os conceitos de massa, quantidade de movimento, energia e entropia.

A identidade imediata entre as duas grandezas sugere que a questão da taxa de dissipação de energia deva ser observada a partir do ponto de vista da taxa de geração de entropia.

Uma Formulação que Usa a Analogia com Equações de Entropia

O uso de analogias com formulações de Entropia na área de Fenômenos de Transporte, vinculados ou não a escoamentos turbulentos, é bastante marginal, havendo poucos textos específicos, como Bejan (1982). Como a entropia tem as suas raízes históricas no desenvolvimento da termodinâmica, as equações de radiação térmica, que envolvem freqüentemente a entropia, passam desapercebidas pelo estudioso em mecânica dos fluidos. Entretanto há um potencial de analogia que deve ser explorado, tendo em vista a gama de resultados positivos que a área de radiação térmica gerou e tem gerado ao longo de sua existência.

Um exemplo de analogia com equacionamento de entropia vinculado à radiação térmica é detalhadamente discutido em Schulz (1997), de onde foi adaptada a tabela 1, utilizando a simbologia do presente texto. Este equacionamento foi estudado no âmbito do tratamento conjunto de

resultados esparsos em turbulência. Esses resultados esparsos foram coletados não da aplicação numérica da teoria estatística da turbulência, mas dos estudos fenomenológicos da área, ou seja, daqueles estudos que originaram soluções independentes a partir de pontos de vista independentes e fundamentados na experimentação. A proposta básica é oferecer uma formulação que contenha uma raiz comum para os diferentes resultados obtidos. A busca dessa raiz comum é motivada pela crença de que fenômenos decorrentes da ação turbulenta dos fluidos possam ser descritos por uma "mecânica da turbulência", conforme já sugerido em Mɑnin e Yaglom (1979, 1981). Os resultados explorados nesta formulação são as equações de velocidade de escoamentos (Chézy e equação universal de perda de carga), equações de transferência de grandezas escalares (coeficiente de transferência proporcional à taxa de dissipação de energia elevada ao expoente ¼), a definição da taxa de dissipação de energia como proporcional à razão entre a velocidade característica ao cubo e a escala do turbilhão, a definição do número de Reynolds com as grandezas usuais de turbulência, as relações para escalas de velocidade e comprimento, os resultados clássicos de escoamentos a jusante de grelhas e a lei dos 5/3 de de Kolmogoroff. Note-se que esses são resultados bem conhecidos e comprovados, porém possuem diferentes formas de abordagem para a sua justificativa teórica. Alguns se fundamentam no uso de análises dimensionais convenientemente conduzidas, porém sem relações aparentes entre elas. Uma caracterísitica adicional desta formulação é que a mesma se ocupa com resultados vinculados a grandezas "macroscópicas" do escoamento, como o volume de um turbilhão, a sua velocidade característica, a taxa de dissipação de energia e coeficientes de transferência. A discussão acerca da aplicação desta formulação direciona-a para a tubulência isotrópica. Detalhes referentes à estrutura da turbulência (distribuições espectrais, por exemplo) não aparecem como variáveis do equacionamento apresentado.

Embora a tabela 1 mostre uma forte identidade entre a formulação aqui discutida e a equação para radiação térmica, esta identidade é casual. Ela foi verificada em um estágio mais avançado do desenvolvimento da formulação, tendo servido como apoio para indicar o valor do expoente da grandeza x (Schulz, 1997).

Tabela 1: Semelhança formal entre os equacionamentos de Radiação Térmica e de Turbulência

Equacionamento de Radiação Térmica	**Equacionamento Alternativo de Turbulência**
$dS = \frac{4u}{3T} dVol + \frac{Vol}{T} du$	$d\phi = \frac{4\dot{u}}{3x} dVol + \frac{Vol}{x} d\dot{u}$
S	ϕ
u	$\dot{u}$
T	x
$u = \alpha T^4$	$\dot{u} = \alpha x^4$

Na primeira coluna tem-se que S é a entropia, u é a densidade de energia e T é a temperatura absoluta. Na segunda coluna ϕ é uma forma de representar o número de Reynolds do turbilhão, $\dot{u}$ é densidade de potência e x é uma variável vinculada à transferência de propriedades físicas. Nos trabalhos iniciais de Schulz (1990), x representou o coeficiente de transferência de massa. Verificou-se, ainda, que para situações nas quais ϕ é constante (iso-ϕ), x representa a escala de velocidade turbulenta. Vale lembrar que a densidade de potência e a taxa de dissipação de energia por unidade de massa estão simplesmente relacionadas através da massa específica. Assim:

$$\varepsilon = \frac{\dot{u}}{\rho} \tag{14}$$

Em outras palavras, as relações obtidas envolvendo a densidade de potência podem igualmente ser utilizadas com a taxa de dissipação de energia. A identidade verificada na tabela 1 ainda pode ser mais valorizada, considerando as seguintes equações:

Para a entropia:

$$dS = \frac{dQ}{T} \tag{15}$$

Para o equacionamento alternativo:

$$d\phi = \frac{\dot{U}\, d\left(\ln \int_{Vol} V^3 dVol\right)}{x} \qquad \dot{U} = \dot{u}\, Vol \tag{16}$$

Q é a quantidade de calor transferida, $\dot{U}$ é a potência total dissipada em um volume de fluido Vol e V é a velocidade característica neste volume. As equações 15 e 16 mostram formas semelhantes e relacionam S e ϕ com outras grandezas expressas na forma diferencial.

Do equacionamento alternativo, vê-se que a variação da grandeza ϕ está relacionada com a taxa de dissipação de energia e, conseqüentemente, com a taxa de geração de entropia. Porém uma relação direta entre as duas variáveis ainda não está fornecida. A formulação permite, todavia, estabelecer esta relação, de modo bastante simples. Alguns resultados parciais, entretanto, necessitam ser demonstrados. Nos procedimentos que seguem, D é a escala dos turbilhões.

1 - Coeficiente de transferência de grandeza escalar:

Partindo da equação proposta na tabela 1, do fato conhecido de que $x = x(\dot{u})$, e reconhecendo a regra da cadeia (expressa por vezes como derivar em relação a uma variável enquanto a outra é mantida constante), obtém-se:

$$\frac{\partial \phi}{\partial Vol} = \left.\frac{4\dot{u}}{3x}\right|_{\dot{u}}$$
$$\frac{\partial \phi}{\partial \dot{u}} = \left.\frac{Vol}{x}\right|_{Vol} \tag{17}$$

Efetuando a derivada segunda com a variável faltante:

$$\frac{\partial^2 \phi}{\partial Vol\, \partial \dot{u}} = \frac{4}{3x} - \frac{4\dot{u}}{3x^2}\frac{dx}{d\dot{u}}$$
$$\frac{\partial^2 \phi}{\partial \dot{u}\, \partial Vol} = \frac{1}{x} \tag{18}$$

Lembrando da igualdade de Schwarz (derivadas segundas iguais) e rearranjando, tem-se:

$$\frac{dx}{x} = \frac{1}{4}\frac{d\dot{u}}{\dot{u}} \tag{19}$$

A integração produz:

$$x = \alpha_1 \dot{u}^{1/4} \qquad \text{ou} \qquad x = \alpha_1' \varepsilon^{1/4} \tag{20}$$

α_1 e α_1' são constantes de integração (possuem dimensões). Assim, obtém-se o resultado de que o coeficiente de transferência de grandezas escalares é proporcional à taxa de dissipação de energia elevada ao expoente ¼. Para situações iso-ϕ, Schulz (1997) mostra que x representa a escala de velocidade característica do turbilhão, valendo para esta escala a mesma relação de dependência mostrada nas equações 20.

2 - Número de Reynolds associado ao turbilhão

Igualando a equação da tabela 1 e a equação 16, tem-se:

$$d\left(\ln \int_{Vol} V^3 \, dVol\right) = \frac{4}{3}\frac{dVol}{Vol} + \frac{d\dot{u}}{\dot{u}} \tag{21}$$

Exprimindo o diferencial do logaritmo de forma extensa e introduzindo a viscosidade cinemática (constante):

$$\frac{d\left(\int_{Vol} \frac{V^3 \, dVol}{\nu^3}\right)}{\left(\int_{Vol} \frac{V^3 \, dVol}{\nu^3}\right)} = \frac{4}{3}\frac{dVol}{Vol} + \frac{d\dot{u}}{\dot{u}} \tag{22}$$

Integrando, para velocidade característica constante no turbilhão:

$$\frac{V^3 Vol}{\nu^3} = \alpha_2 Vol^{4/3} \dot{u} \tag{23}$$

Reconhecendo, em turbulência isotrópica, a proporcionalidade entre o volume do turbilhão e sua escala de comprimento (D) elevada ao cubo, e que o primeiro membro da equação 23 representa uma potência do número de Reynolds, tem-se:

$$\mathrm{Re} = \alpha_3 D^{4/3} \dot{u}^{1/3} \qquad \text{ou} \qquad \mathrm{Re} = \alpha_3' D^{4/3} \varepsilon^{1/3} \tag{24}$$

α_2, α_3 e α_3' são constantes (com dimensão e que podem conter a viscosidade cinemática) e Re é o número de Reynolds do turbilhão. A equação 24 é utilizada em diferentes abordagens, na literatura (ver Monin e Yaglom, 1979, por exemplo), sempre fundamentada em argumentos dimensionais. Na presente abordagem esta relação surge de operações elementares efetuadas com o equacionamento alternativo apresentado.

3 - Relação entre ϕ e o número de Reynolds associado ao turbilhão

Utilizando a equação 16 e seguindo uma argumentação semelhante àquela conduzida para obter uma expressão para o número de Reynolds do turbilhão, tem-se:

$$d\phi = \frac{\dot{U}}{x}\frac{d\,\mathrm{Re}^3}{\mathrm{Re}^3} \tag{25}$$

Utilizando a definição de $\dot{U}$ apresentada na equação 16 e o resultado geral da equação 20, tem-se:

$$d\phi = \alpha_4\, \dot{u}^{3/4} D^3 \frac{d\,\mathrm{Re}}{\mathrm{Re}} \tag{26}$$

Considerando, agora, o resultado geral da equação 24, resulta:

$$d\phi = \alpha_5\, \mathrm{Re}^{5/4}\, d\,\mathrm{Re} \tag{27}$$

A integração desta equação produz:

$$\phi = \alpha_5'\, \mathrm{Re}^{9/4} + \alpha_5'' \tag{28}$$

α_4, α_5, α_5' e α_5'' são constantes (com dimensões). Vê-se que ϕ é uma forma de representação do número de Reynolds do turbilhão. Para grandes números de Reynolds, a equação 28 é simplificada para:

$$\phi = \alpha_5'\, \mathrm{Re}^{9/4} \tag{29}$$

4 - Relação entre ϕ e a taxa de geração de entropia

Os resultados intermediários apresentados anteriormente são agora utilizados para exprimir a relação entre ϕ e $\dot{S}_{Ger}$.

Do teorema de Gouy-Stodola, expresso na equação 13, e da definição de $\dot{U}$ apresentada na equação 16, define-se a taxa de geração de entropia por unidade de volume, $\dot{s}_{Ger}$:

$$\dot{u} = T_0\, \dot{s}_{Ger} \tag{30}$$

Assim, todos os resultados envolvendo a densidade de potência podem ser expressos como função da taxa de geração de entropia por unidade de volume.

Das equações 24 e 30 tem-se:

$$\dot{s}_{Ger} = \frac{1}{\left(\alpha_3^3 T_0\right)}\frac{\mathrm{Re}^3}{D^4} \tag{31}$$

Este resultado mostra que a taxa de geração de entropia cresce em aumentando o número de Reynolds do turbilhão. O número de Reynolds e a taxa de geração de entropia, portanto, tem uma forte identidade entre si, havendo ainda, na relação entre as duas grandezas, um fator multiplicativo encvolvendo uma potência do volume considerado.

Unindo a equação 29 (para grandes números de Reynolds) e a equação 31 resulta:

$$\dot{s}_{Ger}^{3/4} = \frac{1}{\left(\alpha_3^3\, \alpha_5'^{4/3}\, T_0\right)^{3/4}}\left(\frac{\phi}{D^3}\right) \tag{32}$$

Reconhecendo que o volume do turbilhão é proporcional à sua escala ao cubo, resulta, finalmente:

$$\dot{s}_{Ger}^{3/4} = \alpha_6 f \qquad (33)$$

α_6 é uma constante e f representa a a grandeza ϕ por unidade de volume. Obteve-se, portanto, uma lei de potência simples entre as duas variáveis, podendo-se dizer, portanto, que f (ou ϕ / Vol) é uma forma conveniente de representar a taxa de geração de entropia por unidade de volume (na situação de grandes números de Reynolds).

Assim, demonstra-se que o equacionamento alternativo de turbulência apresentado na tabela 1 envolve, como grandeza relevante, a taxa de geração de entropia. A discussão conduzida por Schulz (1997) mostra a busca deste vínculo e apresenta sugestões que apontam para a necessidade de maiores estudos, visando verificar as reais possibilidades desta opção de abordagem do problema da turbulência e localizar as suas limitações. O campo de trabalho, todavia, é aberto, uma vez que as equações que governam os movimentos turbulentos continuam não-fechadas. No ítem seguinte é apresentada uma aplicação para a obtenção da equação de Chézy, que mostra a forma direta como alguns resultados estão agregados a esta formulação.

Equação de Chézy a partir da Formulação Alternativa Apresentada

Em termos de equacionamento de escoamentos turbulentos, pode-se dizer que qualquer expressão empírica para avaliar a vazão desses escoamentos é uma equação para turbulência. O problema prático desta avaliação com certeza acompanha o homem desde os seus primórdios. Talvez, na história das civilizações, o exemplo mais ilustrativo seja os sistemas hidráulicos elaborados pelos engenheiros romanos. Aquedutos extensos foram construídos para suprir cidades, com suas termas e fontes. Alguns desses aquedutos representam soluções arquitetônicas e de engenharia altamente criativas, considerando os recursos da época. Muito provavelmente não se empreendia uma consturção desse porte sem haver alguma avaliação, pelo menos empírica, da vazão a ser transportada para suprir as necessidades previstas. A literatura, entretanto, não faz menção de equações que tivessem sido utilizadas por esses engenheiros. Talvez o primeiro equacionamento empírico que produziu alguma repercussão tenha sido a equação de Chézy, proposta em 1775 (citado em Netto, 1977), que relaciona velocidade média do escoamento, o raio hidráulico da seção trasnversal e a declividade da linha de energia (em escoamentos livres, adotada como sendo a declividade do canal). Nota-se que a equação de Chézy é anterior a qualquer questionamento acerca das equações de Navier-Stokes ou acerca de turbulência. Entretanto, a sua simplicidade, associada ao fato de envolver variáveis de fácil medida (sem a introdução de conceitos físicos novos) garantiram o seu sucesso.

No caso da determinação da velocidade média em um duto ou canal, convém utilizar uma escala de comprimento associada à seção transversal do mesmo. No presente estudo considera-se o diâmetro equivalente da seção considerada. Na figura 1 mostra-se um esquema desta situação de estudo. O volume na figura 1 é dado pela expressão:

$$Vol = A.D \qquad A = \frac{\pi D^2}{4} \qquad (34)$$

Assim verfica-se que se mantém a proporcionalidade entre o volume e a escala de comprimento ao cubo. Partindo da equação apresentada na tabela 1 e da equação 16 tem-se:

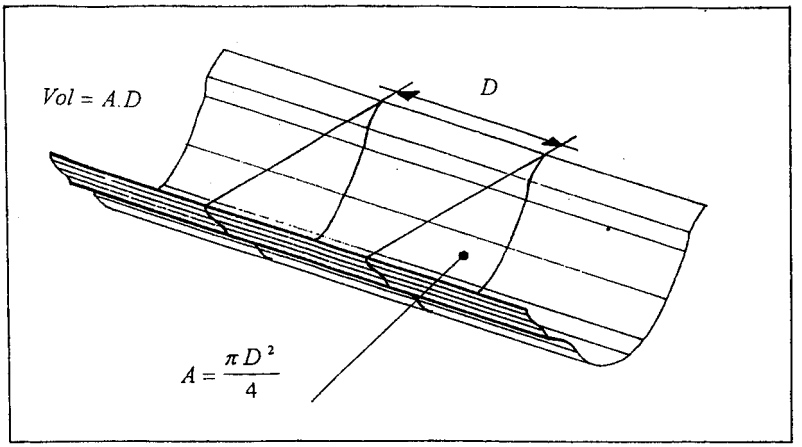

Figura 1: Volume considerado para a análise efetuada. A escala de comprimento D representa o diâmetro equivalente da seção transversal

$$d\left(\ln \int_{AD} V^3 \, d(AD)\right) = \frac{4}{3}\frac{d\,AD}{AD} + \frac{d\,\dot{u}}{\dot{u}} \tag{35}$$

Como se procura uma relação para a velocidade média no volume considerado (portanto constante neste volume), tem-se, após a integração da equação 35:

$$V^3\,AD = \alpha_7\,(AD)^{4/3}\,\dot{u} \tag{36}$$

α_7 é uma constante de integração. A equação 3 permite obter a segunda expressão que envolve a potência dissipada no escoamento, necessária para a resolução do problema, ou seja:

$$\dot{U} = \gamma\,Q\,h_p \tag{37}$$

Q é a vazão e h_p é a perda de carga no escoamento. A união das equações 36 e 37, lembrando que $Q=VA$, produz:

$$V = (\alpha_7)^{1/2}\,J^{1/2}\,(AD)^{1/6} \qquad J = h_p / D \tag{38}$$

J é a declividade da linha de energia. Considerando dutos de seção circular, tem-se:

$$V = (\alpha_7)^{1/2}\left(\frac{\pi}{4}\right)^{1/6} J^{1/2} D^{1/2} \tag{39}$$

Ou, representando a equação 39 de forma mais simplificada, resulta:

$$V = \alpha_8 \sqrt{JD} \tag{40}$$

O diâmetro utilizado representa também o diâmetro hidráulico, uma vez que a constante multiplicativa necessária pode ser inserida sem problemas na constante de proporcionalidade α_8. A equação 40 é a equação de Chézy, que surge, nesta análise, como decorrente da aplicação da formulação alternativa para turbulência. É interessante observar que a equação de Chézy aparece aqui como resultado de uma abordagem que visa tratar o problema específico da turbulência, no sentido de unificar diferentes resultados. Entretanto, em 1775 este problema não estava colocado. As equações consideradas como aquelas que governam os fenômenos ligados à turbulência não eram conhecidas e talvez apenas homens como Leonardo da Vinci pudessem ter observado e levantado questões associadas ao movimento turbulento da água (recordando o seu célebre desenho dos turbilhões a jusante do despejo provindo de um duto de água). Boussinesq e Reynolds passariam a se interessar pela questão apenas no século seguinte. A motivação de Chézy muito provavelmente foi aplicativa, mas as variáveis envolvidas e os expoentes então sugeridos mostram uma sensibilidade aguda na observação e explicação da realidade. Embora sem procurar vincular o resultado final obtido com a motivação original de Chézy, pode-se dizer que o seu equacionamento constitui de fato um primeiro modelo para escoamentos turbulentos, quando apenas as grandezas médias são consideradas.

Conclusões

Neste trabalho desenvolveu-se, inicialmente, uma discussão visando mostrar que os esforços para buscar uma equação adicional para a turbulência conduzem ao conceito de taxa de geração de entropia. Esta conclusão se baseia na concentração de resultados envolvendo a taxa de dissipação de energia e no teorema de Gouy-Stodola. Um desenvolvimento resumido do teorema de Gouy-Stodola foi inserido no texto, visando demonstrar a sua simplicidade e a conveniência de se falar em entropia no equacionamento de turbulência. Embora não se tenha tentado fornecer uma equação de fechamento para o problema de turbulência, conseguiu-se demonstrar que a entropia é o conceito evocado quando se utilizam equações empíricas e semi-empíricas para a taxa de dissipação de energia. Vale lembrar que problemas complexos que concentram a sua resolução no uso de uma variável, como é o caso dos escoamentos turbulentos e da taxa de dissipação de energia, podem conduzir à situação de se utilizar inadvertidamente o mesmo princípio de forma múltipla, ora rigorosamente, ora de forma simplificada (o que pode ocorrer através das informações empíricas). Isto pode gerar um desafio conceitual e confusões sobre a validade das aproximações feitas. A inserção da taxa de geração de entropia, com sua identidade imediata com a taxa de dissipação de energia, deve permitir redirecionar as discussões e oferecer um campo mais amplo para a apresentação de novas aproximações para o problema de turbulência.

Adicionalmente à discussão acima mencionada, foi apresentada uma formulação alternativa para turbulência (extraída de Schulz, 1997), cuja característica mais marcante é a forte semelhança existente com a equação de entropia para radiação térmica. Esta semelhança induziu à busca de uma identidade entre as grandezas utilizadas nesta formulação e a entropia, mostrando-se que há uma lei de potência relacionando a grandeza ϕ da formulação mencionada e a taxa de geração de entropia, ambas por unidade de volume. A utilidade deste equacionamento alternativo é demonstrada a partir de um exemplo no qual se obtém a equação de Chézy para escoamentos em dutos ou canais. A

generalidade da validade deste tipo de formulação, ou as suas restrições de aplicação, não foram discutidas, uma vez que o objetivo do trabalho foi o de valorizar o ponto de vista da utilização da taxa de geração de entropia nos problemas de turbulência.

Agradecimentos

O autor agradece à FAPESP, pelo apoio obtido através do processo 1997/11743-0 para execução de pesquisa no exterior, na qual o presente trabalho se insere, e ao Prof. Gerhard Jirka, anfitrião no Institut für Hydromechanik, Universität Karlsruhe, Alemanha.

Referências Bibliográficas

Bejan, A., 1982, "Entropy Generation Through Heat and Fluid Flow", A Willey-Interscience Publication, John Willey & Sons, New York.

Monin, A.S. e Yaglom, A.M., 1979, "Statistical Fluid Mechanics-Mechanics of Turbulence", Vol 1, the MIT Press, Massachussets.

Monin, A.S. e Yaglom, A.M., 1981, "Statistical Fluid Mechanics-Mechanics of Turbulence", Vol 2, the MIT Press, Massachussets.

Netto, J.M.A.,1977, "Manual de Hidráulica", 3a. reimpressão da 6a. edição, Volumes 1 e 2, Editora Edgard Blücher Ltda, São Paulo.

Schulz, H.E., 1990, "Investigação do Mecanismo de Reoxigenação da Água em Escoamento e sua Correlação com o Nível de Turbulência Junto à Superfície", Tese apresentada à Escola de Engenharia de São Carlos, Universidade de São Paulo, 896 p.

Schulz, H.E., 1997, "Teste de uma Formulação Alternativa em Turbulência", Tese apresentada à Escola de Engenharia de São Carlos, Universidade de São Paulo, 86 p.

LAMINAR-TURBULENT TRANSITION: THE NONLINEAR EVOLUTION OF THREE-DIMENSIONAL WAVETRAINS IN A LAMINAR BOUNDARY LAYER [1]

MARCELLO A. FARACO DE MEDEIROS [2]
Departamento de Engenharia Mecânica
Escola de Engenhariade São Carlos - Universidade de São Paulo
Rua Dr. Carlos Botelho, 1465, São Carlos, 13560-250 - SP - Brazil

Abstract

This paper presents results of an experimental study of the transition in boundary layers. The experiments were conducted in a low-turbulence wind tunnel. The process was triggered by a three-dimensional Tollmien-Schlichting wavetrain excited by a harmonic point source in the plate. Hot-wire anemometry was used to measure the signal and investigate the nonlinear regime of these waves. It was observed that the three-dimensional wavetrain behaved very differently from two-dimensional ones. In particular, it did not involve the growth of subharmonics or higher harmonics. The first nonlinear signal to appear was a mean flow distortion. This had a spanwise structure consisting of regions of positive and negative mean distortion distributed like streaks, which became more complex as the nonlinearity developed. Elsewhere studies have revealed the existence of streak-structures in turbulent flow. It is conjectured that the current experiments may provide a link between early wave-like instabilities and some coherent structures of turbulent boundary layers.

1 Introduction

Laminar-turbulent transition in boundary layers is a subject in fluid mechanics that has gained increasing interest in recent years. It is known that the process usually involves waves of small amplitude, the so called Tollmien-Schlichting (TS) waves, which amplify as they travel downstream. These waves are excited by disturbances in the flow such as wall vibrations, acoustic waves, free-stream turbulence or wall roughness. When the waves reach some finite size they cause the breakdown of the laminar flow structure creating a turbulent flow. For small enough amplitudes the evolution of these waves can be described by a linear version of the Navier-Stokes equation, the Orr-Sommerfeld equation (Lin 1955). However, experiments show that prior to transition the TS waves behave nonlinearly (Klebanoff, Tidstrom & Sargent 1962). Moreover, the amplification rates are often considerably larger in the nonlinear regime and therefore the transition point is ultimately determined by this stage. However, scientists

[1] This paper has been published in the proceedings of the 14th Brazilian Congress of Mechanical Engineering, in CD-Rom

[2] Current Address: Departamento de Engenharia Mecânica - Pontifícia Universidade Católica de Minas Gerais - Av. Dom José Gaspar, 500, Belo Horizonte, 30535-610 - MG - Brazil. E-mail:marcello@mea.pucminas.br

have not been able to explain entirely the nonlinear regime of the TS waves, and this remains a very active field of research.

Most of the research on nonlinear TS waves has concentrated on the evolution of plane two-dimensional wavetrains. This effort has been able to established that when a two-dimensional TS wave reaches some threshold amplitude a secondary instability sets is causing strong amplification of three-dimensional modes (Kachanov 1987, Herbert 1988, Corke & Mangano 1989). The mechanism is of a parametric resonant nature and saturates in the form of a staggered pattern of λ vortices that, for some yet unclear reason, breakdown into turbulence. If the primary TS wave is very large, the process involves the generation of harmonics producing an aligned arrangement of λ vortices (Kachanov 1994).

The situation of more practical interest, however, involves highly three-dimensional modulated waves. Moreover, experiments have shown that these waves cause transition in a way that is remarkably different from that of two-dimensional regular wavetrains, and often the appearance of turbulence spots is observed (Shaikh 1997). As an example of this more generic type of waves, three-dimensional wavepackets have been studied a number of times (Gaster & Grant 1975, Gaster 1975, Cohen, Breuer & Haritonidis 1991, Konzelmann 1990, Medeiros & Gaster 1995, Medeiros 1996, Medeiros & Gaster 1997, Medeiros & Gaster 1998). These studies however have not been able to explain the complicated nonlinear behaviour observed. Research is now concentrating on a simpler three-dimensional wave, namely the three-dimensional wavetrain (Mack 1985, Kachanov 1985, Seifert 1990, Seifert & Wygnanski 1991, Wiegand, Bestek, Wagner & Fasel 1995) in the hope that this could bring some insight into the more complex cases. These works were mainly concentrated on the linear evolution. The work by Wiegand included the nonlinear regime, but the investigation was restricted to flow visualization. The objective of our current work is to investigate the nonlinear regime of these waves in a more detailed and quantitative way. This paper presents some preliminary findings.

2 Experimental set-up

Experiments on transition in boundary layers are usually carried out in wind tunnels in which the levels of disturbances of the flow are kept to a minimum. This in turn excites very small amplitude TS waves which take a long downstream distance to reach the amplitudes that cause breakdown to turbulence. It is then possible to disturb the flow with some controlled wavemaker and excite TS waves artificially. If the artificially excited waves are substantially larger than the naturally arising ones, the transition process can be controlled and repeated to a considerable degree even at the highly nonlinear stages. This provides a fundamental tool for research in this subject.

The experiments here presented were carried out in a 0.9m x 0.9m low-turbulence wind tunnel in which the free-stream velocity was 16.7m/s. The RMS free-stream turbulence level was of about .008%. The boundary layer studied developed on a 2m long elliptic nosed plate placed vertically at the centre of the tunnel. The plate was slightly inclined to the tunnel wall on the working side in order to compensate for the boundary layer growth so as to ensure a constant pressure in the streamwise direction. Fine adjustment of the pressure gradient was achieved by flaps at the trailing edge of the plate. The artificial excitations were produced by a loudspeaker embedded in the plate and coupled to the flow via a .3mm hole located on the centre line of the plate 203mm from the leading edge. A more detailed description of the set up is given by Medeiros (1996). First the loudspeaker was driven continuously by a 200Hz sine wave and the disturbance flow field was studied. The streamwise velocity fluctuations were detected by a constant temperature hot-wire anemometer. The anti-aliases filter was adjusted at 600Hz. Measurements were taken at a constant nondimensional distance from the wall, namely $y/\delta^* = .58$ (δ^* = displacement thickness), which is close to the inner peak of the

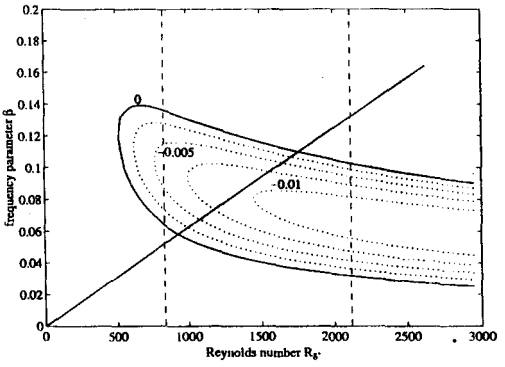

Figure 1: The instability diagram showing the path of the 200Hz TS wave.

streamwise velocity eigenfunction. Figure 2 shows velocity records taken along the centreline of the flow at different distances from the leading edge of the plate. These results can best be interpreted with the help of figure 1. This figure shows the stability diagram of the flat plate boundary layer obtained by solving the Orr-Sommerfeld equation. It indicates in a Reynolds number(R)×nondimensional frequency ($\beta = 2\pi f \delta^*/U_\infty$) plane the region of flow instability. The curve indicates the neutrally unstable waves and separate the unstable region (the inner part) from the stable region. The picture also displays, inside the loop, curves of constant amplification rates. Waves traveling downstream in the boundary layer follow straight lines that irradiate from the origin of the coordinate system. The line displayed in figure 1 corresponds to the wave in figure 2. It is observed that the first measuring station ($R = 1312$) is located within the unstable region. This is confirmed by the observation that the wave amplifies from station x=500 to x=600mm. From stations x=800 to 900mm the signal starts to decays. That corresponds to the region where the waves cross the upper part of the neutral curve and return to the stable region.

3 The nonlinear three-dimensional wavetrain

A more detailed study of the linear evolution the wavetrain was carried out, but this paper focuses on the more interesting nonlinear regime. Previous studies have used a continuous wavetrain to excite the flow. Here the excitation used to study the nonlinear regime was a finite wavetrain. However, the finite wavetrain was made long enough so as to behave like a continuous one. Also, care was taken that the ends of the wavetrain were very smooth in order that the modulation did not affect the results. In this way, the hot-wire records obtained were composed of two parts, a disturbed part and an undisturbed one, figure 3. The background noise in the experiment was very low, but the random part of the signal was further reduced by ensemble averaging a set of 64 records generated by identical excitations. Analysis of the signals revealed no sign of subharmonic or higher harmonic. In fact, the first sign of nonlinearity was clearly a mean flow distortion also indicated in the picture.

A somewhat surprising behaviour was that the mean flow distortion changed from negative to positive somewhere along the evolution. Under this experimental conditions, the positive mean flow distortion occurred after the disturbances had crossedthe second branch of the instability loop. Although the fundamental disturbances were decaying in this region, the positive mean flow distortion was larger then the negative one. To shed more light into the phenomenon,

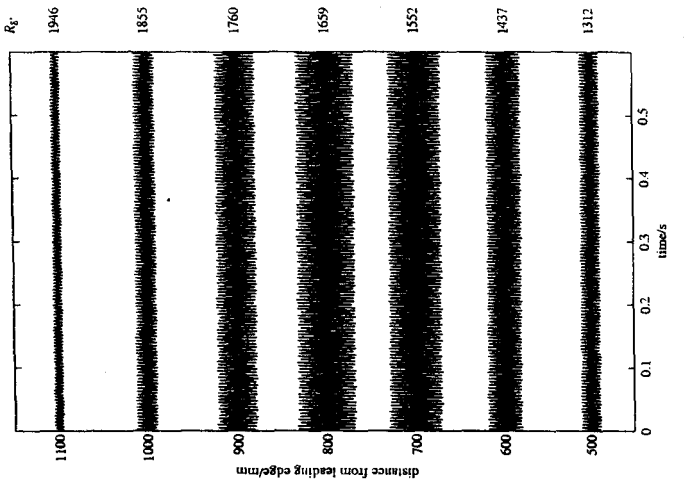

Figure 2: Centreline linear evolution of a continuous wavetrain excited by a point source.

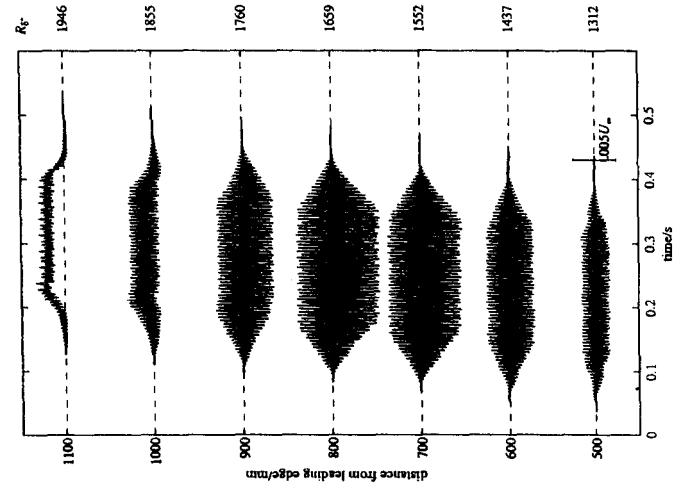

Figure 3: Centreline nonlinear evolution of a wavetrain excited by a point source.

the experiments were extended to include measurements off the centreline of the flow, in order to produce a three-dimensional view of the disturbance field. Figure 4 shows contour plots of the wave field as it passes a downstream station, namely x=1100mm. It is important to note that this view was constructed from 41 spanwise equally spaced time series measured by hot-wire anemometer and it should not be taken as a snap-shot of the flow at a particular time. Figure 4 shows some streak structures which developed nonlinearly in the flow. A clearer view of streak structures is obtained by filtering out the oscillating part of the signal, figure 5.

Figure 6 shows the streamwise evolution of the nonlinearly generated mean flow distortion. At x=.7m the mean flow distortion is already apparent. It is observed that the distortion is

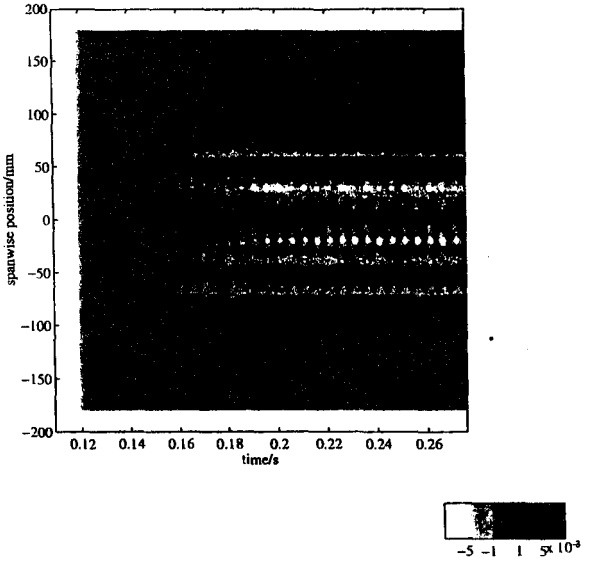

Figure 4: Spanwise distribution of the disturbance field at x=1100mm.

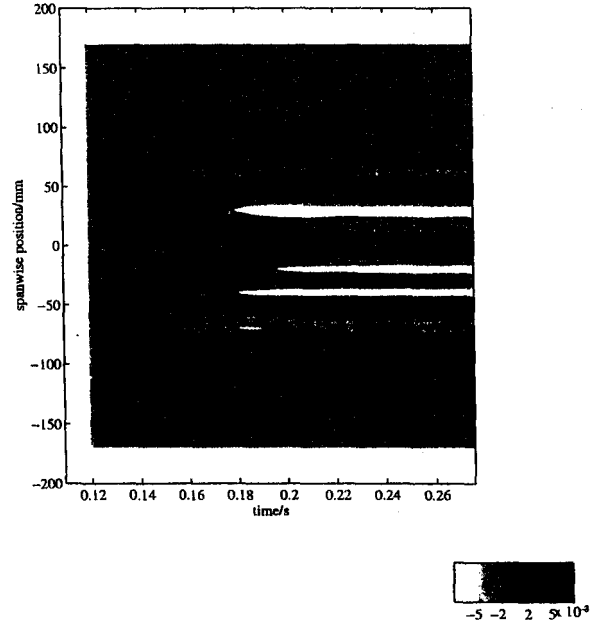

Figure 5: Spanwise distribution of the mean flow distortion caused by the disturbance field at x=1100mm.

not negative everywhere, but has some spanwise structure. At x=.8m the distortion is larger, but remains similar in structure. At x=.9m a more complex structure is forming. It is very difficult to obtain spanwise symmetry in experiments at so large streamwise distances, and this affects the interpretation of the results. However, the picture conveys the idea that the positive lumps of mean distortion on the edge of the disturbance field are splitting. At x=1.0m the central lump of negative distortion is split in two by a localized positive mean distortion. It is remarkable that the phenomenon occurs exactly at the centreline of the flow, although the disturbance field appears to be asymmetrical. After x=1.0m the spanwise distribution of the streak structures remains essentially the same with a widening of the positive distortion generated at the centre of the wave field.

From figure 6 it appeared that the spanwise wavelength at station x=1.3m is approximately half of that at x=.7m. To try and gain more insight into the phenomenon the signals were also studied in Fourier space. Two dimensional discrete Fourier transforms of the signals were taken mapping the spectra onto a nondimensional frequency ($F = 10^4\beta/R$)×spanwise wavenumber (α_z)plane, figure 7. In the figure the frequency coordinate was stretched and only the frequencies close to zero were shown. Initially the mean flow distortion appears as a double peak of symmetrical spanwise wavenumbers. As the nonlinearity developed the spanwise distribution became more complex and more peaks appear in the spectra. The change of sign of the mean flow distortion on the centreline at x=1.0m manifests itself in the appearance of spanwise modes of even higher wavenumbers.

4 Discussion and conclusions

The current experiments have shown that the nonlinear evolution of three-dimensional wave-trains does not seem to be linked with the appearance of sub or higher harmonics as occurs with two-dimensional ones. In fact, the first nonlinear signal to appear was a mean flow distortion. The experiment was not designed for a detailed investigation of the origin of this distortion, but some conjectures can be made. It is possible that the nonlinearity arises from the Reynolds stresses terms ($u'v'$) that are neglected in the linear approximation. It is known that this terms can produce both harmonics and mean flow distortion (Stuart 1960). In a three-dimensional case this mechanism would produce both spanwise and time harmonics, but it is possible that the time harmonics have been highly dumped because of their high frequency and only the mean distortion remained. The appearance of the higher spanwise wavenumber number modes might be connect with a secondary Reynolds stress interaction which would produce even higher harmonics. A similar mechanism has been found in the so called oblique transition (Elofsson & Alfredsson 1997). Our experiment, however, did not have enough spanwise resolution for a definitive conclusion. In any case, the results appear to provide a link between the early wave-like instability and streak structures which seem to be a key ingredient of boundary layer transition (Monkewitz 1997).

References

Cohen, J., Breuer, K. S. & Haritonidis, J. H. (1991), 'On the evolution of a wave packet in a laminar boundary layer', *J. Fluid Mech.* **225**, 575–606.

Corke, T. C. & Mangano, R. A. (1989), 'Resonant growth of three-dimensional modes in transitioning Blasius boundary layers', *J. Fluid Mech.* **209**, 93–150.

Elofsson, P. A. & Alfredsson, P. H. (1997), 'An experimental study of oblique transition in plane poiseuille flow'. (submitted to the J. Fluid Mech.).

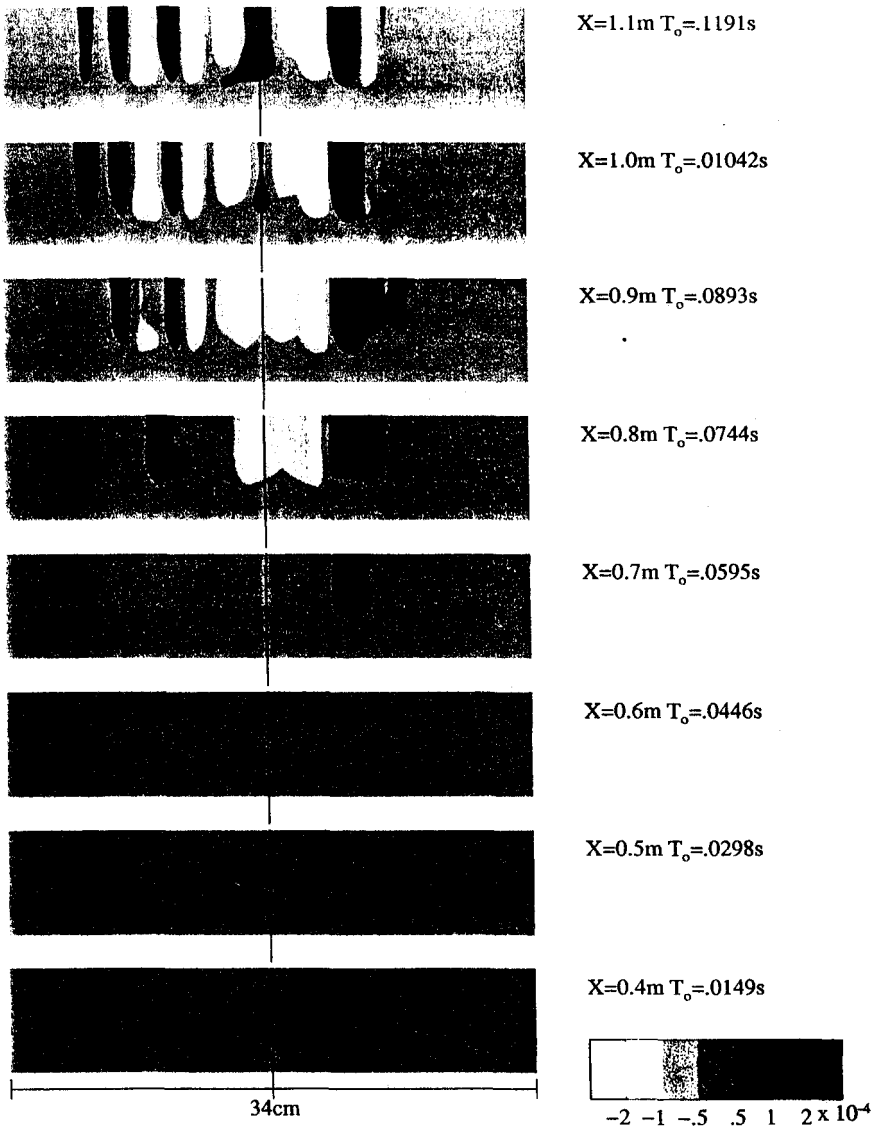

Figure 6: Evolution of the mean flow distortion.

Gaster, M. (1975), 'A theoretical model of a wave packet in the boundary layer on a flat plate', *Proc. R. Soc. London A* **347**, 271–289.

Gaster, M. & Grant, I. (1975), 'An experimental investigation of the formation and development of a wavepacket in a laminar boundary layer', *Proc. Royal Soc. of London A* **347**, 253–269.

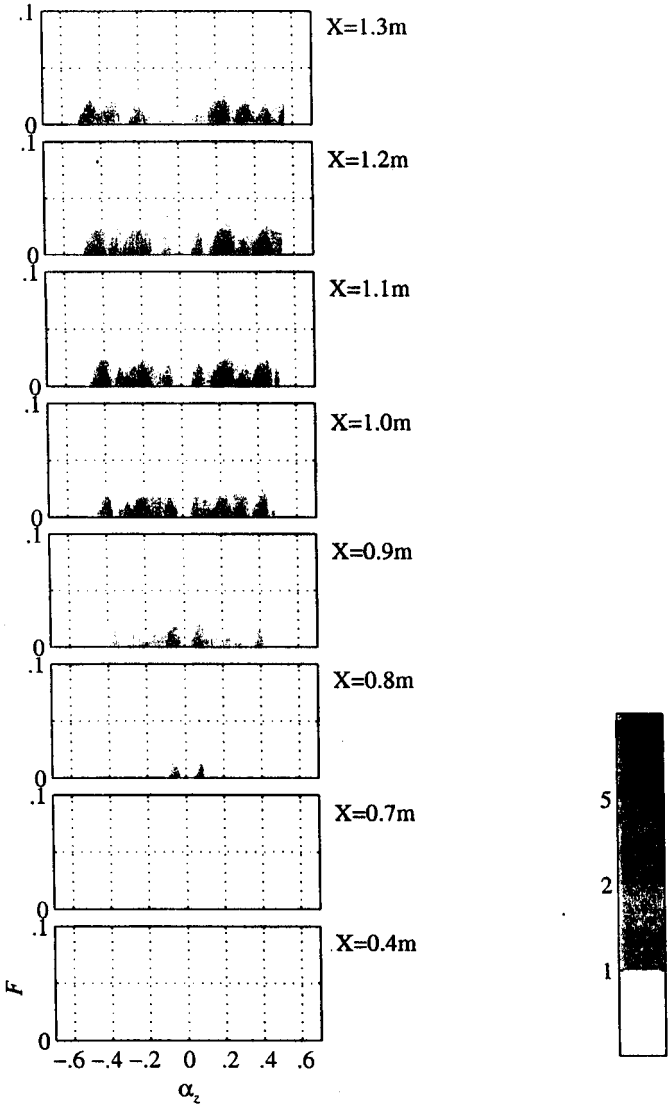

Figure 7: Evolution of the mean flow distortion in Fourier space.

Herbert, T. (1988), 'Secondary instability of boundary layers', *Ann. Rev. Fluid Mech.* **20**, 487–526.

Kachanov, Y. S. (1985), Development of spatial wave packets in boundary layer, *in* V. V. Kozlov, ed., 'Laminar-turbulent transition', springer-Verlag, pp. 115–123.

Kachanov, Y. S. (1987), 'On the resonant nature of the breakdown of a laminar boundary layer', *J. Fluid Mech.* **184**, 43–74.

Kachanov, Y. S. (1994), 'Physical mechanisms of laminar boundary layer transition', *Ann. Rev. Fluid Mech.* **26**, 411–482.

Klebanoff, P. S., Tidstrom, K. D. & Sargent, L. M. (1962), 'The three-dimensional nature of boundary layer instability', *J. Fluid Mech.* **12**, 1–34.

Konzelmann, U. (1990), Numerische Untersuchungen zur räumlichen Entwicklung dreidimensionaler Wellenpakete in einer Plattengrenzschichtströmung, PhD thesis, Universität Stuttgart.

Lin, C. C. (1955), *The Theory of Hydrodynamic stability*, Cambridge University Press.

Mack, L. M. (1985), Instability wave patterns from harmonic point sources and line sources in laminar boundary layers, *in* V. V. Kozlov, ed., 'Laminar-turbulent transition', springer-Verlag, pp. 125–132.

Medeiros, M. A. F. (1996), The nonlinear behaviour of modulated Tollmien-Schlichting waves, PhD thesis, Cambridge University - UK.

Medeiros, M. A. F. & Gaster, M. (1995), The nonlinear behaviour of modulated Tollmien-Schlichting waves, *in* 'IUTAM Conference on nonlinear instability and transition in tridimensional boundary layers', Manchester, pp. 197–206.

Medeiros, M. A. F. & Gaster, M. (1997), 'The nonlinear evolution of wavepackets in a laminar boundary layers: Part I'. (submitted to the *J. Fluid Mech.*).

Medeiros, M. A. F. & Gaster, M. (1998), 'The nonlinear evolution of wavepackets in a laminar boundary layers: Part II', *J. Fluid Mech.* (to be published).

Monkewitz, P. (1997), personal communication.

Seifert, A. (1990), On the interaction of small amplitude disturbances emanating from discrete points in a Blasius boundary layer, PhD thesis, Tel-Aviv University.

Seifert, A. & Wygnanski, I. (1991), On the interaction of wave trains emanating from point sources in a Blasius boundary layer, *in* 'Proc. Conf. on Boundary Layer Transition and Control', The Royal Aeronautical Society, Cambridge, pp. 7.1–7.13.

Shaikh, F. N. (1997), 'Investigation of transition to turbulence using white noise excitation and local analysis techniques', *J. Fluid Mech.* **348**, 29–83.

Stuart, J. T. (1960), 'On the nonlinear mechanisms of wave disturbances in stable and unstable parallel flows', *J. Fluid Mech.* **9**, 1–21.

Wiegand, T., Bestek, H., Wagner, S. & Fasel, H. (1995), Experiments on a wave train emanating from a point source in a laminar boundary layer, *in* '26th AIAA Fluid Dynamics Conference', San Diego, CA.

Investigação Experimental da Transição de Escoamentos num Sistema Pulverizador Jato-Placa

Marcelo Bacci da Silva, Leonardo Machado Amorim e Aristeu da Silveira Neto

Departamento de Engenharia Mecânica da Universidade Federal

de Uberlândia - 38400-206 - Uberlândia - M. G.

Neste artigo apresenta-se os resultados obtidos com uma técnica de fotografia a alta velocidade, que serve para congelar fenômenos dinâmicos de altas frequências envolvidos no problema de geração de gotas por meio de um sistema pulverizador jato-placa. Foram analisadas as instabilidades que caracterizam a transição do jato e observou-se importantes fenômenos físicos, como por exemplo as instabilidades dinâmicas e os buracos formados sobre o filme de líquido após a placa aspersora.

Introdução

Foi conduzida uma investigação experimental dos mecanismos físicos envolvidos na transição de escoamento de um sistema pulverizador jato-placa. O princípio deste tipo de pulverizador é comumente usado para sistemas de irrigação na agricultura, mas encontra-se também aplicação em outras áreas, como na injeção de combustível nos equipamentos de combustão interna e nos sistemas de proteção contra incêndios. A investigação experimental contribui para a compreensão dos mecanismos de transferência de massa, momento e energia em escoamentos com duas fases dispersas.

O sistema montado para a investigação experimental é composto de um bico injetor que projeta um jato de água contra uma placa cônica. O jato é concêntrico com a placa, como ilustra a figura1. Um filme de líquido se forma após a placa. A espessura deste filme diminui devido à abertura radial. As forças de tensões viscosas atuantes provocam uma diminuição da quantidade de movimento do fluido e ele se expande para fora da placa cônica causando uma redução adicional na sua espessura. O filme escoa na direção radial para fora da placa, e se quebra em gotas. Para um alto número de Reynolds, a interação do filme com o ar gera ondas tridimensionais de grande amplitude, e com o aumento dessas amplitudes, perfurações surgem ao longo do filme de líquido.

Trabalhos Preliminares

Um número de trabalhos importantes tem sido direcionado para este problema. O interesse primário de tais trabalhos é o entendimento dos mecanismos físicos que aumentam as taxas de transporte de calor e massa envolvendo jatos livres: Stevens e Webb (1992), Buyevich e Ustinov (1994), Elison e Webb (1994) e Mansour e Chigier (1994).

Uma revisão bibliográfica mais detalhada sobre os mecanismos de formação de gotas foi desenvolvido por Kolev (1993). Um primeiro modelo para a transformação de um filme líquido em gotas foi proposto por Dombrowski e Jones (1963). Eles acreditam que as instabilidades que aparecem sobre o filme líquido favorece a aceleração do processo de formação das gotas. Um modelo físico similar foi proposto por Chin *et al.* (1991), usando um formalismo de entropia máxima. Spielbauer e Aidum (1994) propuseram que a quebra em

gotas é devida a perfurações localizadas do filme líquido. Este fenômeno é claramente apontado no presente trabalho.

Aparato Experimental

O equipamento experimental usado para investigação dos mecanismos físicos envolvidos na transição do escoamento de um sistema pulverizador jato-placa é apresentado na figura 1. A seção de testes é constituída de uma caixa coletora a qual é equipada com três janelas de vidro (W). O equipamento é composto por 1 bomba (P), um reservatório de água (R), três rotâmetros (FM) que controlam o fluxo de água, tubos PVC de 25 mm de diâmetro, um bico de injeção e uma placa cônica (NP). A pressão de operação foi monitorada por um manômetro de Bourdon (M) localizado antes do bico de injeção.

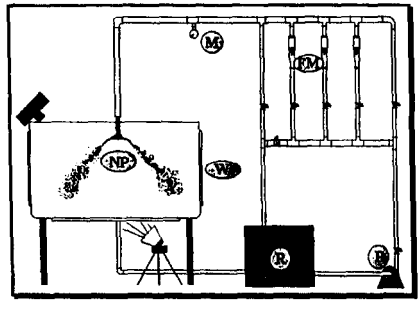

Figura 1. Esquema da Montagem Experimental.

As fotografias foram tiradas usando uma câmera Pentax 35 mm e uma lâmpada estroboscópica de alta frequência. Esta lâmpada foi controlada por um circuito eletrônico para fornecer um flash com duração da ordem de 4 μs (quatro microsegundos). A iluminação de curta duração permite congelar os fenômenos de altas frequências como as instabilidades do jato, ondas, perfurações no filme líquido e formação de gotas. Instabilidades sobre o jato e sobre o filme líquido livre assim como perfurações localizadas e acúmulo de massa nas bordas do filme líquido foram também claramente evidenciadas.

Vários tipos de técnicas de iluminação são possíveis, mas após vários testes, a técnica de iluminação "*back-lighting*" foi adotada, como ilustrado na figura 1. Foi usado um filme ISO 400. Para mais detalhes veja Tarqui (1996).

Resultados

As fotografias mostram o comportamento global do processo físico envolvido na transição do escoamento sobre o sistema jato-placa. Na figura 2 pode-se visualizar a estrutura turbulenta do jato livre, tendo como parâmetro de controle o número de Reynolds, aqui definido como $\mathrm{Re}_d = Ud/\nu$, onde U é a velocidade média, d é o diâmetro do bico injetor e ν é a viscosidade cinemática. Na figura 2(a) mostra-se um regime laminar na saída do jato e na figura 2(b), continuação da anterior, mostra-se a quebra do jato, promovida pelas instabilidades de Rayleigh. Pode-se observar dois tipos de gotas: as maiores que aparecem primeiro e que geram filamentos de líquido entre elas, sobre os quais aparecem as

instabilidades de Rayleigh favorecendo o aumento das gotas menores, comumente chamadas gotas satélites. Sob esse baixo número de Reynolds, a superfície líquida tem uma aparência muito suave, sem instabilidades.

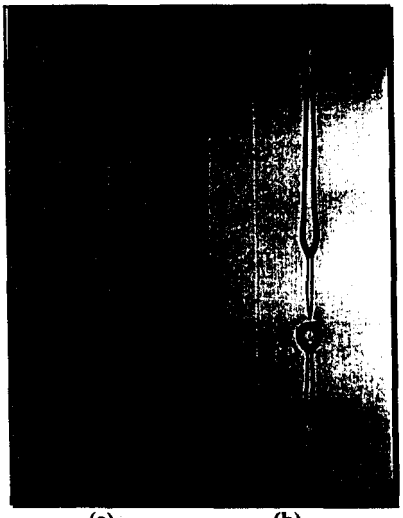

(a) (b)

Figura 2. Visualização das instabilidades de Rayleigh no jato livre de água; Re_d=5.000; (a) saída do bico injetor; (b) sequência espacial da imagem precedente.

(a) (b)

Figura 3. Visualização de instabilidades tridimensionais no jato livre de água; Re_d=120.000; (a) saída do bico injetor; (b) a 40 cm do bico injetor (*break-up* do jato).

O escoamento relacionado com alto número de Reynolds, Re_d=120.000, pode ser visualizado na figura 3. As imagens 3(a) e 3(b), mostram o escoamento numa sequência espacial. Visualiza-se nesta figura os distúrbios complexos tridimensionais sobre a superfície do jato (imagem (a)). Estes distúrbios tornam-se mais pronunciados com o desenvolvimento do escoamento e o jato perde sua regularidade (imagem (b)), mostrando instabilidades periódicas muito fortes. Eles iniciam o desprendimento de ligamentos e de pequenas gotas que caracterizam o início da quebra. As gotas são criadas pelo arraste aerodinâmico sobre as instabilidades. Estes resultados qualitativos comparam-se muito bem com aqueles fornecidos por outros autores: Taylor e Hoyt (1981), Eroglu *et al.* (1991), Chigier (1991), e Mccreery e Stoots (1996)

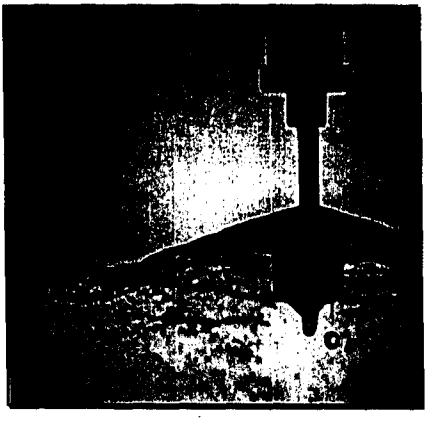

Figura 4. Visão geral do escoamento; visualização das instabilidades senoidais e quebra do filme líquido em gotas; Re_d=32.000; diâmetro da placa é 44 mm; diâmetro do bico injetor é 2,8 mm.

Figura 5. Visão superior do filme líquido; quebra em perfurações e em gotas; Re_d=32.000; diâmetro da placa é 44 mm; diâmetro do bico injetor é 2,8 mm.

A figura 4 mostra uma vista geral do escoamento, onde são observadas ondas senoidais sobre a napa de fluído as quais são amplificadas para finalmente degenerarem em gotas.

Na figura 5 mostra-se uma vista superior da napa líquida referente a Re_d=32.000. O cisalhamento do ar sobre a napa cria oscilações e variações na espessura da mesma. A ação do cizalhamento e dė ondas resulta em forças localizadas de tensões altas. Quando a espessura local do filamento cai abaixo de uma valor crítico, perfurações ocorrem, causando rupturas antes da região principal de quebra em gotas. A napa torna-se pontuada (perfurada) em buracos isolados. Este fenômeno foi também observado por Chigier (1991), Mccreery e Stoots (1996) e Reis e Silveira Neto (1991).

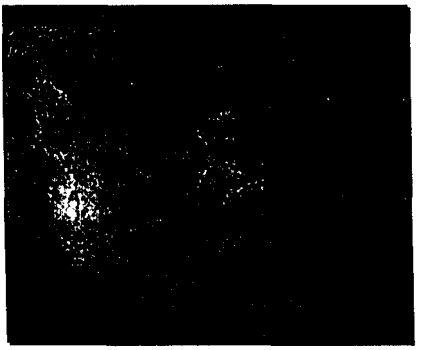

Figura 6. Visão superior do filme líquido; quebra em perfurações e em gotas; Re_d=36.000; diâmetro da placa é 44 mm; diâmetro do bico injetor é 2,8 mm.

Figura 7. Visão superior do filme líquido; quebra em perfurações e em gotas; Re_d=50.000; diâmetro da placa é 44 mm; diâmetro do bico injetor é 2,8 mm.

Nas figuras 6 e 7 mostra-se o escoamento referente a Re_d=36.000 e 50.000 respectivamente. Com o aumento do número de Reynolds, a frequência dos buracos também aumenta. Pode-se observar que o processo de formação das gotas torna-se altamente

complexo. Entretanto a natureza não homogênea da região frontal da formação de gotas permanece.

Na figura 8 mostra-se uma vista lateral do escoamento referente a Re_d=50.000, ilustrando as oscilações de altas amplitudes. Comparando as figuras 4 e 8 verifica-se que essas oscilações aumentam com o número de Reynolds.

Isto é muito importante para aplicações práticas do tipo sistemas de irrigação na agricultura, pois estas oscilações favorecem o aumento na largura da faixa de solo irrigada. Logo, um aumento no número de Reynolds permite maximizar a área irrigada. Alternativamente estas oscilações podem ser amplificadas por excitação mecânica ou por modificações geométricas.

Figura 8. Visão lateral do filme líquido, mostrando as oscilações de grande amplitude; Re_d=50.000; diâmetro da placa é 44 mm; diâmetro do bico injetor é 2,8 mm.

Conclusões

A técnica de fotografia de alta velocidade foi usada para capturar e congelar os fenômenos de altas frequências que ocorrem na transição do escoamento sobre um sistema pulverizador jato-placa. Com as fotografias mostra-se a estrutura do escoamento: as instabilidades características do jato; as oscilações sobre o filme líquido após sair da placa e as perfurações sobre o filme líquido; o processo de acúmulo de massa na borda do filme líquido e nas bordas dos buracos. Também visíveis são a emissão de gotas e ligamentos de fluido no jato livre.

Parece que o mecanismo físico mais importante para a formação de gotas são as perfurações que aparecem sobre o filme líquido. Elas são transportadas convectivamente na direção radial e determinam a natureza não homogênea das frentes de gotas.

Outro importante fenômeno observado foram as oscilações no filme líquido. Quando amplificadas, estas oscilações causam aumento na frente de gotas. Esta característica é muito importante com relação ao desempenho dos sistemas de irrigação porque elas determinam a área molhada do solo.

Agradecimentos – Os autores agradecem ao CNPQ e a Fapemig pelo suporte financeiro e ao curso de Pós-Graduação da Engenharia Mecânica da Universidade Federal de Uberlândia.

Referências

Buyevich, Y. A. and Ustinov, V. A. 1994. Hydrodynamic condition of transfer process through a radial jet spreading over a flat surface. *Int. Journal Heat and Mass Transfer*, **37**, 165-173.

Chigier, N. 1991. Optical imaging of sprays. *Prog. Energy Combust. Sci.*, **17**, 211-262.

Chin, L. P., Larose, P. G., Tankin, R. S., Jackson, T., Sturnd, J. and Switzer, G. 1991. Droplet distributions from the breakup of a cylindrical liquid jet. *Physical of Fluids A*, **3**, 1897-1906.

Dombrovski, N. and Jones, W. R. 1993. The aerodynamic instability and disintegration of viscous liquid sheets. *Chem. Eng. Science*, **18**, 203-214.

Elison, B. and Webb, B. W. 1994. Local heat transfer to impinging liquid jets in the initially laminar, transitional and turbulent regimes. *Int.* Journal *Heat and Mass Transfer*, **37**, 1207-1216.

Eroglu, H., Chigier, N. and Frago, G. 1991. Coaxial atomizer liquid intact lengths. *Phisics of Fluids A*, **3**, 303-308.

Kolev, N. I. 1993. Fragmentation and coalescence dynamics in multiphase flows. *Experimental Thermal and Fluid Science*, **6**, 211-251.

Mansour, A. and Chigier, N. 1994. Turbulence characteristics of cylindrical liquid jets. *Phys. Fluids*, **6**, 3380-3391.

Mccreery, G. E. and Stoots, C. M. 1996. Drop formation mechanisms and size distributions for spray plate nozzles. *Int. J. Multiphase Flow*, **22**, 431-452.

Reis, W. and Silveira Neto, A. 1993. Comportamento dinâmico de um jato incidente sobre placas aspersoras-cenario da transiçao à turublencia, *Proceedings of the XII Brazilian Mech. Eng. Congress*, **2**, 1033-1036.

Spielbauer, T. M. and Aidun, C. K. 1994. The wave thining and breakup of liquid sheets. *ASME Journal of Fluids Engineering*, **116**, 728-734.

Stevens, J. and Webb, B. W. 1992. Measurements of the free surface flow structure under an impinging, free liquid jet. *Journal of Heat Transfer*, **114**, 79-84.

Taylor, J. J. and Hoyt, J. W. 1981, Water jet photography - techniques and methods. *Exp. Fluids*, **1**, 113-120.

Tarqui, J. L. Z. 1996. Desenvolvimento de um método de fotografia para o estudo de fenômenos de altas frequências em aspersores jato-placa, Master of Science Dissertation, Federal University of Uberlândia.

On Kaplun Limits and the Multi-Layered Asymptotic Structure of the Turbulent Boundary Layer

by Atila P. Silva Freire
Mechanical Engineering Program (PEM/COPPE/UFRJ),
C.P. 68503, 21945-970 - Rio de Janeiro - Brazil.

Abstract

In the present work, some formal properties of singular perturbation equations are studied through the concept of "equivalent in the limit" of Kaplun, so that a proposition for the principal equations is derived. The proposition shows that if there is a principal equation at a point $(\eta, 1)$ of the $(\Xi \times \Sigma)$ product space, Ξ space of all positive continuous functions in $(0,1], \Sigma = (0,1]$, then there is also a principal equation at a point (η, ϵ) of $(\Xi, \times\Sigma)$, $\epsilon =$ first critical order. The converse is also true. The proposition is of great implication for it ensures that the asymptotic structure of a singular perturbation problem can be determined by a first order analysis of the formal domains of validity. The turbulent boundary layer asymptotic structure is then studied by application of Kaplun limits to three test cases: the zero-pressure boundary layer, the separating boundary layer and the shock-wave interacting boundary layer. As it turns out, different asymptotic structures are found depending on the test cases considered.

1 Introduction

In physics and mathematics many phenomena are modelled through intricate equations that present no analytical solution. As such, engineers, physicists and applied mathematicians are forced do develop techniques that yield approximated solutions to the problems they are faced with. These techniques often resort to sophisticated procedures which only in a very few cases are restrained to fully analytical frameworks. In most cases, analytical procedures have to be combined with numerical procedures to produce an approximated solution.

Perturbation methods have evolved along the past forty years into a powerful tool for solving a large class of complex problems. They have, therefore, become a basic working tool of many engineers and applied mathematicians. In fact, a large number of papers can be found in literature which use perturbation methods as their primary solution procedure.

The purpose of this work is twofold: i) to consider more thoroughly some fundamental concepts and ideas used in solving perturbation problems, and ii) to study the turbulent boundary layer asymptotic structure by applying Kaplun limits to the Navier-Stokes equations.

While some precise definitions can be enunciated, and exact results obtained to find uniform approximations and to perform the matching of functions, the determination of the domain of validity of an approximation is always difficult. Two important results in perturbation theory are the intermediate matching lemma and the extension theorem of Kaplun. These results are of fundamental importance for the construction of matched asymptotic expansions, but say nothing about the domain of validity of the approximations. To circumvent this difficulty, Kaplun(1967) applied the concept of limit-processes directly to the equations rather than to the solutions and enunciated an Ansatz, the Ansatz about domains of validity, which relates the domain of validity of solutions with the formal domain of validity of equations (a concept which is easily defined). Examples are known where Kaplun's ideas fail; however,

for some difficult problems, e.g., the Stokes paradox of fluid mechanics, only consideration of these ideas can clarify the conceptual structure of the problem. Here, we study some formal properties of equations yielded by the definition of "equivalent in the limit" of Kaplun, and relate them to the actual problems of determining the overlap domain and of matching asymptotic expansions. The concept of "richer than" of Kaplun and Lagerstrom(1957) is given a more elaborated interpretation which leads to the derivation of a theorem for the principal equations. The theorem shows that if there is a principal equation at a point $(\eta, 1)$ of the $(\Xi \times \Sigma)$ product space, Ξ = space of all positive continuous functions on $(0, 1]$, $\Sigma = (0, 1]$, then there is also a principal equation at a point (η, ϵ) of $(\Xi \times \Sigma)$, ϵ = first critical order. The converse is also true. The consequence of this theorem is that, no matter to what order of magnitude we want an approximation to be accurate, it is always possible to find high-order solutions at points $(\eta, 1)$ of the $(\Xi \times \Sigma)$ space (η = point of the Ξ space obtained through passage of Kaplun's limit process, where a principal equation is located) which satisfy the required degree of accuracy, overlap and cover the entire domain.

Since the basis of perturbation methods comes from heuristic ideas and intuitive concepts rather than some general theory, basic questions are normally answered by physical arguments and an acquired experience. Texts with an applied-oriented nature, such as the books of Cole(1968), Nayfeh(1973), Van Dyke(1975) and Kevorkian and Cole(1981), show through examples how these heuristic ideas can be put into practice, and how some simple rules can be devised for the analysis of perturbation problems. These rules have become very popular over the past years, but are known to fail in many situations. To formalise such rules and show the conditions under which they work, Eckhaus(1969, 1972, 1973) and Fraenkel(1969) carried out more mathematically-oriented analysis which had to be, necessarily, of a more limited scope. Further important works on perturbation methods with mathematically-oriented approaches are the books of O'Malley(1974) and of Wasow(1976) where some exact results are derived for some types of ordinary differential equations.

In an attempt to make clearer Kaplun's ideas, Lagerstrom and Casten(1972) published a work where a survey of some ideas on perturbation methods was presented. Again, a heuristic approach was used. The work, however, presented some new definitions and results which were known to work for leading-order approximate solutions. Some of these results have recently been revisited in publications by Lagerstrom(1988) and by Silva Freire and Hirata(1990).

Most of Kaplun's ideas have been developed in literature in connection with boundary value problems. Nipp(1988), however, used the concepts presented in Kaplun(1967) and Lagerstrom and Casten(1972) to work out a systematic approach to solve a large class of singularly perturbed initial value problems. His analysis considers both the formal and the rigorous aspects of the problem, yielding a procedure to find formal approximations of order unity. Although many of Nipp's ideas carry over to boundary value problems, much work still needs to be done concerning the determination of higher order approximate solutions for these problem.

The formal properties of equations here studied are aimed at boundary layer problems. The theorem of the principal equations formalises the notion of distinguished limit so often used in literature, allowing Kaplun's ideas to be used in a systematic manner. The matched asymptotic expansions method, for example, depends on two crucial guesses for the determination of approximate solutions: the choice of the stretching function and the choice of the asymptotic expansions. These choices are normally guided by physical arguments, but are in the end always made by trial-and-error. In fact, the determination of the stretching function and of the asymptotic expansions has always been seen as an art. With the theorem of the

principal equations, the stretching function is immediately found, whereas the appropriate gauge functions for the asymptotic expansions are obtained from Kaplun's concept of critical orders.

The asymptotic structure of the turbulent boundary layer has been extensively investigated by a number of authors in the past twenty years. Unlikely the laminar flow case, whose solution has been known since the sixties, the turbulent problem poses some questions which still have to be understood and answered. Of course, all difficulties stem from the introduction of the time-averaged equations. To make these equations a determined system, closure conditions must be introduced to relate the Reynolds stresses to the mean flow velocities. The Reynolds stresses, the time averages of the fluctuating velocities, describe the effect of turbulent fluctuations on the mean flow; if they could be determined, the mean flow equations could solved and the asymptotic structure unveiled. Many closure conditions have been proposed in literature but, unfortunately, none of them are generally valid.

Using only the hypothesis that the order of magnitude of the Reynolds stresses do not change throughout the boundary layer, some authors (Yajnik(1970), Mellor(1972)) have found the turbulent boundary layer to have a two-deck structure consisting of a wall region and a defect region. Other authors using closure conditions in terms of eddy-viscosity (Bush and Fendell(1972)) or $\kappa - \epsilon$ (Deriat and Guiraut(1986)) models have reached the same conclusion, making the two-deck asymptotic structure of the turbulent boundary layer the basis of most subsequent work.

Recently, however, there has been a claim that the turbulent boundary has instead a three-layered structure (Long and Chen(1981), Sychev and Sychev(1987), Melnik(1989)) and that this is the only structure that can possibly handle flows subject to pressure gradients.

In this work, the asymptotic structure of the turbulent boundary layer is investigated by applying Kaplun limits to the Navier-Stokes equation. Three cases will be investigated here: i) turbulent flow over a flat surface with zero-pressure gradient, ii) separating turbulent boundary layer flow, and iii) the interaction of a normal shock wave with a turbulent boundary layer.

2 The Fundamentals of the Theory

We shall consider perturbation methods to find approximate solutions to differential equations of the form

$$\epsilon\, E_1(x, y, ..., y^{(n)}) + E_2(x, y, ..., y^{(n-1)}, \epsilon) + ... = 0, \tag{1}$$

that is, equations where the small parameter ϵ multiplies the highest derivative term. E_i is a given function of the variables $x, y, ..., y^{(n)}, \epsilon$. Here $y^{(n)}$ is used to denote $d^n y/dx^n$.

The method to be studied here aims at developing a procedure to find approximate solutions to equations with form of Eq.(1) which are valid in different parts of the domain. This can be achieved by the introduction of a limit process that determines the terms of Eq.(1) which have a dominant effect in the various regions of the domain.

To define this limit process some basic concepts need to be introduced. The following topology is introduced on the collection of order classes (Meyer, 1967).

For positive, continuous functions of a single variable ϵ defined on $(0, 1]$, let $ord\ \eta$ denote the class of equivalence.

$$ord\,\eta = \{\theta(\epsilon) \;/\; lim\;\theta(\epsilon)/\eta(\epsilon), \quad \epsilon \to 0, \quad \text{exists and is } \neq 0\}. \tag{2}$$

A partial ordering is constructed on these functions by defining

$$ord\;\eta_1 < ord\;\eta_2 \quad \Leftrightarrow \quad lim\,\frac{\eta_1}{\eta_2} = 0, \quad \epsilon \to 0. \tag{3}$$

A set D of order classes is said to be convex if $ord\;\delta_1, ord\;\delta_2 \in D$ and $ord\;\delta_1 < ord\;\theta < ord\;\delta_2$ together imply $ord\;\theta \in D$. A set D is said to be open if it is converse and if $ord\,\theta \in D$ implies the existence of functions γ, δ such that $ord\,\theta > ord\,\gamma \in D$ and $ord\;\theta < ord\;\delta \in D$. A set D, on the other hand, is said to be closed if it is convex and has particular elements $ord\;\delta_1, ord\;\delta_2$ such that $ord\;\delta_1 \leq ord\;\theta \leq ord\;\delta_2$ for every $ord\;\theta \in D$. Two order sets, D and D' are said adjacent if: i) $D' > D$ and ii) $\eta < D'$ and $\eta' > D \to \eta' > \eta$. We may refer to D' as being the upper adjacent region of D. Analogously, D is said to be the lower adjacent region of D'.

Definition (Lagerstrom, 1988). We say that $f(x,\epsilon)$ is an approximation to $g(x,\epsilon)$ uniformly valid to order $\delta(\epsilon)$ in a convex set D (f is a δ-approximation to g), if

$$lim\,\frac{f(x,y) - g(x,y)}{\delta(\epsilon)} = 0, \quad \epsilon \to 0, \text{ uniformly for } x \text{ in } D. \tag{4}$$

The function $\delta(\epsilon)$ is called a gauge function.

The essential idea of η-limit process is to study the limit as $\epsilon \to 0$ not for fixed x near the singularity point x_d, but for x tending to x_d in a definite relationship to ϵ specified by a stretching function $\eta(\epsilon)$. Taking without any loss of generality $x_d = 0$, we define

$$x_\eta = \frac{x}{\eta(\epsilon)}, \quad G(x_\eta;\epsilon) = F(x;\epsilon), \tag{5}$$

with $\eta(\epsilon)$ a function defined in Ξ.

Definition (Meyer, 1967). If the function $G(x_\eta;+0) = lim\,G(x_\eta;\epsilon)$, $\epsilon \to 0$, exists uniformly on $\{x_\eta/|x_\eta| > 0\}$; then we define $lim_\eta\; F(x;\epsilon) = G(x_\eta;+0)$.

Thus, if $\eta \to 0$ as $\epsilon \to 0$, then, in the limit process, $x \to 0$ also with the same speed of η, so that x/η tends to a non-zero limit value.

One of the central results of Kaplun's work is the extension theorem, which is here presented in the following version (Meyer, 1967).

Kaplun's extension theorem. If $f(x;\epsilon)$ is a $\xi(\epsilon)$-approximation to $g(x;\epsilon)$ uniformly in a closed interval D_0, then it is so also in an open set $D \supset D_0$.

The above theorem was firstly published in Kaplun and Lagerstrom(1957) in connection with the Stokes paradox for flow at low Reynolds number. It needs to be complemented by an Axiom and by an Ansatz to relate the formal domain of validity of an equation with the

actual domain of validity of its solution. The idea of Kaplun was to shift the emphasis to applying limit-processes directly to the equations rather than to the solutions, establishing some rules to determine the domain of validity of solutions from the formal domain of validity of an equation.

The set of equations that will result from passage of the limit is referred to by Kaplun as the "splitting" of the differential equations. The splitting must be seen as a formal property of the equation obtained through a "formal passage of the η-limit process". To every order of η a correspondence is induced, $lim_\eta \rightarrow$ associated equation, on that subset of Ξ for which the associated equation exists.

Definition. The formal limit domain of an associated equation E is the set of orders η such that the η-limit process applied to the original equation yields E.

Passage of the η-limit will give equations that are distinguished in two ways: i) they are determined by specific choices of η, and ii) they are more complete, or in Kaplun's words, "richer" than the others, in the sense that, application of the η-limit process to them will result in other associated equations, but neither of them can be obtained from any of the other equations.

Limit-processes which yield "rich" equations are called principal limit-processes. The significance of principal limit-processes is that the resulting equations are expected to be satisfied by the corresponding limits of the exact solution. The notion of principal equation will be formalised below.

The above concepts and ideas can be given a more rigorous interpretation if we introduce Kaplun's concept of equivalent in the limit for a given set of equations for a given point (η, δ) of the (Ξ, Σ) product space.

Given any two associated equations E_1 and E_2, we define the remainder of E_1 with relation to E_2 as

$$\mathbb{R}(x_\eta; \epsilon) = E_1(x_\eta; \epsilon) - E_2(x_\eta; \epsilon), \tag{6}$$

where ϵ denotes a small parameter.

According to Kaplun(1967), $\mathbb{R}$ should be interpreted as an operator giving the "apparent force" that must be added to E_2 to yield E_1.

Definition (of equivalence in the limit) (Kaplun, 1967). Two equations E_1 and E_2 are said to be *equivalent in the limit* for a given limit-process, lim_η, and to a given order, δ, if

$$\frac{\mathbb{R}(x_\eta; \epsilon)}{\delta} \rightarrow 0, \ as \ \epsilon \rightarrow 0, \ x_\eta \text{ fixed}. \tag{7}$$

The following propositions are important; they can be found in Kaplun(1967). The symbol $\sim$ is used to indicate equivalent in the limit whereas $\not\sim$ indicates not equivalent in the limit.

Proposition 1: If $E \sim E'$ for the point (η', δ') of the product space $\Xi \times \Sigma$, then $E \sim E'$ for all points (η, δ) such that $\eta = \eta'$ and $\delta \gg \delta'$. Conversely, if $E \not\sim E'$ for the point (η', δ'), then $E \not\sim E'$ for all points (η, δ) such that $\eta = \eta'$ and $ord\, \delta \ll ord\, \delta'$.

Proposition 2: If $E \sim E'$ for the point (η, δ) of the product space $\Xi \times \Sigma$, and if associated equations for that point exist for E, then they exist also for E' and are identical for both.

Proposition 3: If associated equations exist for E and E' respectively, corresponding to $\eta = \eta'$ and the sequence $\delta = \delta'_0, \delta'_1, \ldots, \delta'_n, \delta'$ where $\delta'_n > \delta' > \delta'_{n+1}$, and are identical for both, then $E \sim E'$ for the point (η', δ').

We can make the following definition.

Definition (of formal domain of validity). The formal domain of validity to order δ of an equation E of formal limit domain D is the set $D_e = D \cup D'_i s$, where $D'_i s$ are the formal limit domains of all equations E'_i such that E and E'_i are equivalent in D'_i to order δ.

Definition (of principal equation). An equation E of formal limit domain D, is said to be principal to order δ if:
i) one can find another equation E', of formal limit domain D', such that E and E' are equivalent in D' to order δ;
ii) E is not equivalent to order δ to any other equation in D.

An equation which is not principal is said to be intermediate.

To relate the formal properties of equations to the actual problem of determining the uniform domain of validity of solutions, Kaplun(1967) advanced two assertions, the Axiom of Existence and the Ansatz about domains of validity. These assertions constitute primitive and unverifiable assumptions of perturbation theory.

Axiom (of existence) (Kaplun, 1967). If equations E and E' are equivalent in the limit to the order δ for a certain region, then given a solution S of E which lies in the region of equivalence of E and E', there exists a solution S' of E' such that as $\epsilon \to 0, |S - S'|/\delta \to 0$, in the region of equivalence of E and E'.

In other words, the axiom states that there exists a solution S' of E' such that the "distance" between S and S' is of the same order of magnitude of that between E and E'.

In using perturbation methods, the common approach is to consider the existence of certain limits of the exact solution or expansions of a certain form. This is normally a sufficient condition to find the associated equations and to assure that the axiom is satisfied (Kaplun(1967). Equivalence in the limit, however, is a necessary condition as shown by propositions (1) to (3).

To the axiom of existence there corresponds an Ansatz; namely that there exists a solution S of E which lies in the region of equivalence of E and E'. More explicitly, we write.

Ansatz (about domains of validity) (Kaplun, 1967). An equation with a given formal domain of validity D has a solution whose actual domain of validity corresponds to D.

The word "corresponds to" in the Ansatz was assumed by Kaplun to actually mean "is equal to"; this establishes the link we needed between the "formal" properties of the equation and the actual properties of the solution.

The Ansatz can always be subjected to a *canonical test* which consists in exhibiting a solution S' of E' which lies in the region of equivalence of E and E' and is determined by the boundary conditions that correspond to S.

Because the heuristic nature of the Axiom and of the Ansatz, comparison to experiments will always be important for validation purposes. The theory, however, as implemented through the above procedure, is always helpful in understanding the matching process and in constructing the appropriate asymptotic expansions.

3 The Proposition of the Principal Equations

The "splitting" of the equations obtained through the definition of equivalent in the limit may be extended to higher orders by introducing a fictitious perturbation of an arbitrary order δ. Thus, according to Kaplun(1967), for higher orders the splitting of the equations corresponding to arbitrary limit processes becomes more complicated and less significant; the operation of splitting is then merely reduced to exhibit some of the typical associated equations and some of the sufficient conditions under which they are associated. In fact, Kaplun lists three reasons why the splitting for higher orders should not be considered in detail: i) the equations associated with a given point (η, δ) depend on the choice of the δ'_n for the corresponding limit process and may depend on the amount of information used in connection with the preceding terms, ii) the δ'_n depend to greater extent on boundary conditions and hence are difficult to determine a priori, and iii) many trivial splitting of the associated equations arise, corresponding to expansions of the preceding terms by different limit processes.

Here, we want to further extend the above notions. In what follows we will show that, for certain points of the (Ξ, Σ) product space, the determination of the associated equations will depend on the choice of some discrete values of δ'_n. It results that the order of validity of an approximation is defined by open intervals determined by the discrete δ'_n's. Furthermore, no trivial splitting will result in these certain points.

To extend the previous results to higher orders, we consider solutions of the form

$$f = f_0 + \Delta(\epsilon) f_1, \tag{8}$$

where $\Delta(\epsilon) \in \Xi$.

Some questions are now in order. Which function is $\Delta(\epsilon)$ for a given differential equation? Is $\Delta(\epsilon)$ the same for all regions of the domain?

The first question is complex and involves speculating on the existence and uniqueness of solutions. Of course, uniqueness of $\Delta(\epsilon)$ can never be assured since given any $\Delta(\epsilon)$, one can always present another $\Delta'(\epsilon)$ such that $\Delta'(\epsilon)$ is exponentially close to $\Delta(\epsilon)$. Thus, according to Kaplun, there will always be a "question of choice" for the determination of the appropriate asymptotic expansions which must be solved relying on intuition and physical insight. An adequate $\Delta(\epsilon)$ can however be determined in a very natural way. We require $\Delta(\epsilon)$ to be such that the resulting equation for f_1 does not provide a trivial solution. A $\Delta(\epsilon)$ satisfying this condition is said to be a critical $\Delta(\epsilon)$. Analogously, its order, $ord\,\Delta(\epsilon)$, is called critical order. More precisely:

Definition (of critical order) (Kaplun(1967)). An order $ord\,\Delta(\epsilon)$ is said to be critical if: i) the corrections to f_0 to any order ζ in $D, D = \{\zeta / ord\,\Delta(\epsilon) < ord\,\zeta < 1\}$, are trivial;

ii) the corrections to f_0 to any order ζ in the complement of D are not trivial.

The above definition suggests that approximate solutions for different regions of the domain should not in general have the same $\Delta(\epsilon)$. Of course, equal $\Delta's$ might happen as a mere coincidence; however, it is important to give emphasis to that, normally this is not the case.

To find the several order approximate equations we substitute Eq.(8) into the original equations and perform elementary operations such as addition, multiplication, subtraction, differentiation and so on. If these operations are justified, that is, if they do not lead to any non-uniformity, we then collect the terms of same order of magnitude and construct a set of approximate equations. Thus, it is clear that in the process of collecting terms, to each term E_1 of order, say ν there will always correspond another term E_2 of order $\nu\Delta(\epsilon)$.

Consider now an equation E where E_1 and E_2 denote the first two critical order terms. We call the operator $\Pi_1(E) = E_1$ the first order projection of E onto E_1. Analogously, the operator $\Pi_2(E) = E_2$ is called the second order projection of E onto E_2.

We can then enunciate the following proposition.

Proposition (of the principal equations). If there is a principal equation, E_1, at a point $(\eta, 1)$ of the (Ξ, Σ) product space, then there is also a principal equation, E, at a point (η, ϵ) of (Ξ, Σ) with $E_1 = \Pi_1(E)$.

Proof: Suppose E_1 is a principal equation at a point $(\eta, 1)$ of the (Ξ, Σ) product space. Then one can find a term R_{1l} such that R_{1l} is order unity in D (the domain of E_1) but $ord\,1 < ord R_{1l} < ord\,\epsilon$ in D_u, the upper adjacent domain of D. Here ϵ denotes the first critical order. Define $E_1' = E_1$ - R_{1l}.

Let now E_2 and E_2' denote the first order associated equations in D and D_u respectively. Then, there is a term R_{2l} such that R_{2l} is order ϵ in D but $ord\,R_{2l} < ord\,\epsilon$ in D_u. Define E_2' = E_2 - R_{2l}.

It results that the structure of the lower adjacent region is

$$ord\ R_{1l} < ord\ E_1' < ord\ R_{2l} < ord\ E_2' \tag{9}$$

This yields that no other equation is equivalent to order ϵ to equation $E = E_1' + R_{1l} + E_2' + R_{2l}$ in D. However, E and $E'(= E_1' + R_{1l} + E_2')$ are equivalent in D_u to $ord\,\epsilon$. We conclude E is a principal equation at a point (η, ϵ) of the (Ξ, Σ) product space.

The converse of the above proposition is obviously true, that is: if E is a principal equation at a point (η, ϵ) of the (Ξ, Σ) space, where η denotes the formal limit domain of E and ϵ the first critical order, then $\Pi_1(E)$ is a principal equation at a point $(\eta, 1)$ of the (Ξ, Σ) space.

What the above proposition clearly states is that the position in the (Ξ,Σ) product space where the principal equations are located can se searched by looking only at the lowest order associated equations. Furthermore, it says that these lowest order approximations are good up to the first critical order and that no trivial splitting will arise. This fact is only valid for the particular point in (Ξ,Σ) space where the principal equation holds. In the upper and lower adjacent domains trivial splitting will occur.

It results that higher order splitting should not, in fact, be considered. The principal equations of the problem, those that retain most of the information about the problem solution,

can have their position determined only through an analysis of the lowest order terms. Then the concept of critical order can be applied to the solution to find the appropriate asymptotic expansions for the problem.

4 The Asymptotic Structure of the Turbulent Boundary Layer.

Boundary layer problems are historically important in the development of singular perturbation methods. In fact, the basic ideas of singular perturbation methods can be traced back to Prandtl's boundary layer theory of a laminar flow. Prandtl's matching principle for laminar boundary layers was systematically discussed and generalised in the fifties yielding well established procedures and solutions which have rendered the laminar flow problem solved.

In the seventies, the interest shifted to turbulent flow. Two approaches were used: in the first, asymptotic techniques were applied to the averaged equations without appealing to any closure model (Yajnik(1970), Mellor(1972)); in the second, eddy-viscosity (Bush and Fendell(1972)) or $\kappa - \epsilon$ (Deriat and Guiraud(1986)) models were used to find high order approximations. The theories divided the turbulent boundary layer into two regions, becoming the basis of most subsequent work. Other authors, Long and Chen(1981), Sychev and Sychev(1987), Melnik(1989), however, have recently claimed that the turbulent boundary layer has instead a three-layered structure. This structure considers a new region in which a balance of inertia forces, and pressure and turbulent friction forces occurs. The formulation of Melnik is based on a two-parameter expansion of the boundary layer equations, the new additional small parameter resulting from the particular turbulence closure model he uses.

The discussions that have led to the development of the three-layered asymptotic model for the turbulent boundary layer result from the recognition that two-layered models cannot deal with large flow disturbances in the stream-wise direction. When a turbulent boundary layer is subjected to a large longitudinal adverse pressure gradient, the velocity deficit is large and the mean momentum equation is non-linear; this makes the classical matching arguments which result in a log-law and in a two deck structure, not valid anymore. The classical wall characteristic velocity, the friction velocity, may become an inappropriate scaling parameter so that new formulations will have to be developed for the problem at hand.

Here, we will investigate the turbulent boundary layer from the point of view of Kaplun's single limits. The purpose is to formally arrive at a three-layered structure which is compatible with the class of problems to be studied: the zero-pressure gradient turbulent boundary layer, the separating turbulent boundary layer and the shock-wave interacting turbulent boundary layer.

4.1 The zero-pressure gradient turbulent boundary layer

For an incompressible two-dimensional turbulent flow over a smooth surface in a prescribed pressure distribution, the time-averaged motion equations; i.e., the continuity equation and the Navier-Stokes equation can be written as

$$\frac{\partial u_j}{\partial x_j} = 0, \tag{10}$$

$$u_j \frac{\partial u_i}{\partial x_j} = -\frac{\partial p}{\partial x_j} - \epsilon^2 \frac{\partial}{\partial x_j}\left(\overline{u_j' u_i'}\right) + \frac{1}{R}\frac{\partial^2 u_i}{\partial x_j^2}, \tag{11}$$

where the notation is classical. Thus $(x_1, x_2) = (x, y)$ stand for the co-ordinates, $(u_1, u_2) = (u, v)$ for the velocities, p for pressure and R for the Reynolds number. The dashes are used to indicate a fluctuating quantity. In the fluctuation terms, an overbar is used to indicate a time-average.

All mean variables are referred to some characteristic quantity of the external flow. The velocity fluctuations, on the other hand, are referred to a characteristic velocity u_R, firstly introduced in Cruz and Silva Freire(1998).

The correct assessment of the characteristic velocity is fundamental for the determination of the boundary layer asymptotic structure. For unseparated flows the characteristic velocity is known to be the friction velocity; for separating flows it reduces to $(\nu(dp/dx)/\rho)^{1/3}$. For the moment, we will consider attached flow so that we can write

$$ord\,(u_i') = ord\,(u_\tau). \tag{12}$$

This result is valid for incompressible flows as well as for compressible flows (see, e.g., Kistler(1956) and Kistler and Chen(1956)).

The small parameter ϵ is, therefore, defined by

$$\epsilon = \frac{u_R}{U_\infty} = \frac{u_\tau}{U_\infty}. \tag{13}$$

The asymptotic expansions for the flow parameters are written as

$$u(x, y) = u_1(x, y) + \epsilon u_2(x, y), \tag{14}$$

$$v(x, y) = \eta[v_1(x, y) + \epsilon v_2(x, y)], \tag{15}$$

$$p(x, y) = p_1(x, y) + \epsilon p_2(x, y), \tag{16}$$

$$u_i'(x, y) = \epsilon u_{i1}'(x, y) + \epsilon^2 u_{i2}'(x, y). \tag{17}$$

$$\overline{u'v'}(x, y) = \epsilon^2 \overline{u'v_1'}(x, y) + \epsilon^3 \overline{u'v_2'}(x, y). \tag{18}$$

To find the asymptotic structure of the boundary layer we consider the following stretching transformation

$$\hat{y} = y_\eta = \frac{y}{\eta(\epsilon)}, \quad \hat{u}_i(x, y_\eta) = u_i(x, y). \tag{19}$$

with $\eta(\epsilon)$ defined on Ξ.

Upon substitution of Eq.(19) into Eqs.(14) to 17) and upon passage of the η-limit process onto the resulting equation we get:

x-momentum equation:

	$ord(\delta) = 1$		$ord(\delta) = ord(\epsilon)$	
$\eta = 1:$	$D_{11} = P_1,$		$D_{12} + D_{21} = P_2,$	(20)
$\epsilon < \eta < 1:$	$D_{11} = P_1,$		$D_{12} + D_{21} = P_2,$	(21)
$\eta = \epsilon:$	$D_{11} = P_1,$		$D_{12} + D_{21} = P_2 - (\overline{u'v'_1})_{\hat{y}},$	(22)
$\epsilon^2 < \eta < \epsilon:$	$D_{11} = P_1,$	$(\overline{u'v'_1})_{\hat{y}} = 0,$	$D_{12} + D_{21} = P_2,$	(23)
$\eta = \epsilon^2:$	$D_{11} = P_1 - (\overline{u'v'_1})_{\hat{y}},$		$D_{12} + D_{21} = P_2 - (\overline{u'v'_2})_{\hat{y}},$	(24)
$\epsilon^3 < \eta < \epsilon^2:$	$(\overline{u'v'_1})_{\hat{y}} = 0,$	$D_{11} = P_1,$	$(\overline{u'v'_2})_{\hat{y}} = 0,$	(25)
$\eta = \epsilon^3:$	$(\overline{u'v'_1})_{\hat{y}} = 0,$		$D_{11} = P_1 - (\overline{u'v'_2})_{\hat{y}},$	(26)
$1/\epsilon^2 R < \eta < \epsilon^3:$	$(\overline{u'v'_1})_{\hat{y}} = 0,$		$(\overline{u'v'_2})_{\hat{y}} = 0,$	(27)
$\eta = 1/\epsilon^2 R:$	$(\overline{u'v'_1})_{\hat{y}} = 0,$		$(\overline{u'v'_2})_{\hat{y}} = (u_2)_{\hat{y}\hat{y}},$	(28)
$1/\epsilon R < \eta < 1/\epsilon^2 R:$	$(\overline{u'v'_1})_{\hat{y}} = 0,$	$(u_2)_{\hat{y}\hat{y}} = 0,$	$(\overline{u'v'_2})_{\hat{y}} = 0,$	(29)
$\eta = 1/\epsilon R:$	$(\overline{u'v'_1})_{\hat{y}} = (\hat{u}_2)_{\hat{y}\hat{y}},$		$(\overline{u'v'_2})_{\hat{y}} = (\hat{u}_3)_{\hat{y}\hat{y}}.$	(30)

where the following operators were used

$$D_{ij} = \hat{u}_i \frac{\partial \hat{u}_j}{\partial x} + \hat{v}_i \frac{\partial \hat{u}_j}{\partial y_\eta}, \qquad P_i = -\frac{1}{\rho} \frac{\partial \hat{p}_i}{\partial x}. \tag{31}$$

The above equations were arranged in three columns according to their respective order of approximation. The first column corresponds to the first order of approximation; the third one to the second order of approximation. The middle column corresponds to orders between the first and the second critical order. The extreme left of the lines indicates the point in the domain where the η-limit process was applied.

Passage of the η-limit process onto the y-momentum equation does not give any relevant information. In fact, we will find that for $ord\,\eta < ord\,\epsilon$ the first and second order pressure terms will dominate all the other terms. All information regarding the asymptotic structure of the boundary layer is, therefore, contained in the x-momentum equation.

The term $\hat{u}_1(x, y_\eta)$ is missing from equations (29) and (30) since from the no-slip condition $\hat{u}_1 = 0$ near the wall.

Equations (24) and (30) are distinguished in two ways: i) they are determined by specific choices of η, and ii) they are "richer" than the others in the sense that, application of the limit process to them yields some of the other equations, but neither of them can be obtained from passage of the limit process to any of the other equations. Thus, according to the definitions introduced in the previous sections, these equations are the principal equations. We have seen that principal equations are important since they are expected to be satisfied by the corresponding limits of the exact solution.

A complete solution to the problem should then according to the Axiom of Existence and Kaplun's Ansatz, be obtained from the principal equations located at points $ord\ \eta = ord\ \epsilon^2$ and $ord\ \eta = ord\ (1/\epsilon R)$. The formal domains of validity of these equations cover the entire domain and overlap in a region determined according to the definition of equivalent in limit.

To find the overlap region of equations (24) and (30), we must show these equations to have a common domain where they are equivalent. A direct application of the definition of equivalence in the limit to equations (24) and (30) yields

$$\mathbb{R} = \frac{D(\hat{u}_1) - P(\hat{p}_1) + D(\hat{u}_2) - P(\hat{p}_2) - (\hat{u}_2)_{\hat{y}\hat{y}} - (\hat{u}_3)_{\hat{y}\hat{y}}}{\epsilon^\alpha}. \tag{32}$$

Noting that the leading order term in region $ord\ (1/\epsilon R) < ord\ \eta < ord\ \epsilon^2$ is the turbulent term, of $ord\ (\epsilon^2/\eta)$, we normalise the above equation to order unity to find

$$\bar{\mathbb{R}} = \frac{\eta}{\epsilon^2}\mathbb{R}. \tag{33}$$

The overlap domain is the set of orders such that the η-limit process applied to $\bar{\mathbb{R}}$ tends to zero for a given α. Then since $ord\ (\partial/\partial y) = \epsilon$ and $ord\ (\partial/\partial x) = 1$, the formal overlap domain is given by

$$D_{overlap} = \{\eta/ \quad ord\ (\epsilon^{1+\alpha}R)^{-1} < ord\ \eta < ord\ (\epsilon^{2+\alpha})\}. \tag{34}$$

According to Kaplun's Ansatz about domains of validity, the approximate equations, Eqs. (24) and (25), only overlap if set (34) is a non-empty set, that is, if

$$0 \leq \alpha \leq -\frac{1}{2}\left(\frac{ln\, R}{ln\, \epsilon} + 3\right). \tag{35}$$

The implication is that the two-deck turbulent boundary layer structure given by the two principal equations, equations (24) and (30), provides approximate solutions which are accurate to the order of $\epsilon^{\alpha_{max}}$, where α_{max} is the least upper bound of the interval (35). This fundamental result can only be reached through the application of Kaplun's concepts and ideas to the problem.

In particular, the overlap domain of the first and second order of approximation are given respectively by

$$D_1^o \cap D_1^i = \{ord\eta / \quad ord(1/\epsilon R) < ord(\eta) < ord(\epsilon^2)\} \tag{36}$$

and,

$$D_2^o \cap D_2^i = \{ord\eta / \quad ord(1/\epsilon^2 R) < ord(\eta) < ord(\epsilon^3)\}. \tag{37}$$

We conclude that the turbulent boundary layer has a two-deck structure very much like the one derived by Sychev and Sychev. This structure, however, must change as a separation point is approached. We shall see this next.

Before we move forward, however, some comments about the intermediate equations will de made.

For the formal limit domains which are not adjacent to the principal equations two approximated equations are always defined, separated by the first two critical orders. In this case the interpretation is simple and the local approximated equations and solutions well defined. For the regions adjacent to the principal equations, however, a correction with order between the first two critical orders is found. The interpretation of these equations is more complex and must be made in an individual basis. For example, in the turbulent boundary layer problem under consideration, the solution in the upper adjacent region must take into consideration, as the first two order of approximation equations, the leading order equation and the intermediate order equation; these equations will provide non-trivial solutions with physical information. For the lower adjacent region, however, the intermediate order equation provides a trivial solution; thus, no extra information is obtained from this equation except that the overlap domain for the first two order of approximation is not given by equation (37) but by

$$D_2^o \cap D_2^i = \{ord\eta / \quad ord(1/\epsilon^2 R) < ord(\eta) < ord(\epsilon^2)\}. \tag{38}$$

4.2 The separating turbulent boundary layer

The above asymptotic structure must undergo some modifications if flows subjected to adverse pressure gradients are to be considered (Cruz and Silva Freire, 1998).

A major difficulty found for a direct translation of the classical models into models that apply for separating flows is the characteristic velocity used in the former approach. When the friction velocity, u_τ, is used to develop the asymptotic structure of the boundary layer, a non-uniformity will occur near a separation point where $u_\tau = 0$. These difficulties force into the adverse pressure gradient problem a new small parameter of the order of $R^{-1/3}$, which is used to scale a power-y layer that replaces the logarithmic layer. This new intermediate layer defines a third characteristic scale which must be considered together with the wall and defect layer characteristic scales. Thus, three sets of characteristic scales are needed for the asymptotic description of adverse pressure gradient turbulent boundary layers (see Durbin and Belcher(1992)).

The result is that any theory advanced for the problem should explain in asymptotic terms how the far upstream two-deck structure reduces to a three-deck structure near a separation point. Equivalently, any theory should show how the logarithmic layer vanishes as separation is approached, and how the $y^{1/2}$-layer is formed.

In Cruz and Silva Freire(1998) a new scaling procedure was introduced through asymptotic arguments that resulted in an algebraic equation for u_R that yielded a changeable asymptotic structure for the boundary layer consistent with the experimental data. The theory followed the approaches of Yajnik(1970) and of Mellor(1972), not imposing any functional relationship between quantities determined by the Reynolds stress field and by the velocity field.

Here we will repeat part of the theory to illustrate how the results of the previous section can be extended to separated flows.

In the region defined by the principal equation, Eq.(30), a balance between the turbulent and viscous stresses exists so that we may write

$$\frac{\partial}{\partial y}(\overline{-\rho u'v'}) + \mu\frac{\partial^2 u}{\partial y^2} = \frac{\partial p}{\partial x}. \tag{39}$$

In this region, the characteristic length is given by ν/u_R. Then, considering that the turbulent fluctuations are of the order of the reference velocity, u_R, and that the viscous term can be approximated by

$$ord(\mu\frac{\partial u_2}{\partial y}) = ord(\tau_w), \tag{40}$$

it results from simple order of magnitude arguments that the characteristic velocity can be estimated from the algebraic equation

$$u_R^3 - \frac{\tau_w}{\rho}u_R - \frac{\nu}{\rho}\frac{\partial p}{\partial x} = 0. \tag{41}$$

Passing the limit as τ_w tends to zero onto the above equation,

$$u_R \longrightarrow \left(\frac{\nu}{\rho}\frac{\partial p}{\partial x}\right)^{1/3}, \tag{42}$$

so that the characteristic velocity for the near separation point region proposed by Stratford(1959) and by Townsend(1976)is recovered.

The characteristic velocity u_R is determined by the highest real root of (41).

It follows that, close to the separation point, $ord\ (\epsilon^2) = ord\ (1/\epsilon R)$, and the two principal equations merge giving origin to a one deck structure. This merging provokes the disappearance of the log-region, reducing the flow structure to a wake region and a viscous region.

To find the asymptotic structure of the separating boundary layer we apply the following stretching transformation to the equations of the previous section

$$x_\Delta = \frac{x}{\Delta(\epsilon)}, \tag{43}$$

with $\Delta(\epsilon)$ defined on Ξ.

The resulting flow structure is given by:

x-momentum equation:

$$ord\ \Delta = ord\ 1: \quad \hat{u}_2\frac{\partial \hat{u}_2}{\partial x_\Delta} + \hat{v}_2\frac{\partial \hat{u}_2}{\partial y_\eta} + \frac{\partial \hat{p}_2}{\partial x_\Delta} = 0, \tag{44}$$

$$ord\ \epsilon^2 < ord\ \Delta < ord\ 1: \quad \hat{u}_2\frac{\partial \hat{u}_2}{\partial x_\Delta} + \hat{v}_2\frac{\partial \hat{u}_2}{\partial y_\eta} + \frac{\partial \hat{p}_2}{\partial x_\Delta} = 0, \tag{45}$$

$$ord\ \epsilon^2 = ord\ \Delta: \hat{u}_2\frac{\partial \hat{u}_2}{\partial x_\Delta} + \hat{v}_2\frac{\partial \hat{u}_2}{\partial y_\eta} + \frac{\partial \hat{p}_2}{\partial x_\Delta} = -\frac{\partial \overline{\hat{u'}_1^2}}{\partial x_\Delta} - \frac{\partial \overline{\hat{u'}_1\hat{v'}_1}}{\partial y_\eta} + \frac{\partial^2 \hat{u}_2}{\partial x_\Delta^2} + \frac{\partial^2 \hat{u}_2}{\partial y_\eta^2}, \tag{46}$$

$$ord\ \Delta < ord\ \epsilon^2: \quad \frac{\partial^2 \hat{u}_2}{\partial x_\Delta^2} + \frac{\partial^2 \hat{u}_2}{\partial y_\eta^2} = 0; \tag{47}$$

y-momentum equation:

$$ord\ \Delta = ord\ 1: \quad \hat{u}_2\frac{\partial \hat{v}_2}{\partial x_\Delta} + \hat{v}_2\frac{\partial \hat{v}_2}{\partial y_\eta} + \frac{\partial \hat{p}_2}{\partial y_\eta} = 0, \tag{48}$$

$$ord\ \epsilon^2 < ord\ 1 < ord\ \Delta: \quad \hat{u}_2\frac{\partial \hat{v}_2}{\partial x_\Delta} + \hat{v}_2\frac{\partial \hat{v}_2}{\partial y_\eta} + \frac{\partial \hat{p}_2}{\partial y_\eta} = 0, \tag{49}$$

$$ord\ \epsilon^2 = ord\ \Delta: \hat{u}_2\frac{\partial \hat{v}_2}{\partial x_\Delta} + \hat{v}_2\frac{\partial \hat{v}_2}{\partial y_\eta} + \frac{\partial \hat{p}_2}{\partial x_\Delta} = -\frac{\partial \overline{\hat{v'}_1^2}}{\partial x_\Delta} - \frac{\partial \overline{\hat{u'}_1\hat{v'}_1}}{\partial y_\eta} + \frac{\partial^2 \hat{v}_2}{\partial x_\Delta^2} + \frac{\partial^2 \hat{v}_2}{\partial y_\eta^2}, \tag{50}$$

$$ord\ \Delta < ord\ \epsilon^2: \quad \frac{\partial^2 \hat{v}_2}{\partial x_\Delta^2} + \frac{\partial^2 \hat{v}_2}{\partial y_\eta^2} = 0. \tag{51}$$

Note that in region $(\Delta, \eta) = (\epsilon^2, \epsilon^2)$ the full Navier-Stokes averaged equation is recovered. The leading order equations for $\hat{u}_1$ together with the no-slip condition at the wall gives $\hat{u}_1 = 0$.

In Cruz and Silva Freire(1998) the asymptotic structure of the thermal turbulent boundary layer is also studied through Kaplun limits. The procedure is basically the same and the

results similar to those derived for the velocity field. For more details concerning this problem the reader is referred to the original work. There, new formulations are advanced for the law of the wall for the velocity and the temperature fields for separating flows. To these formulations, experimental and numerical validation are given based on the works of Vogel and Eaton(1985) and Driver and Seegmiller(1995).

The resulting asymptotic structure for both the velocity and the temperature boundary layers is shown in Figure 1, which was taken from Cruz and Silva Freire(1998). This figure incorporates the dependence of the structure on the Prandtl number.

4.3 The shock interacting boundary layer

For a compressible flow, the two-dimensional Navier-Stokes equations of mean motion can be cast in terms of a mass-weighted-averaging procedure. The continuity and the momentum equations can then be written in the following non-dimensional form:

$$\frac{\partial}{\partial x_j}(\overline{\rho}\tilde{u}_j) = 0, \tag{52}$$

$$\frac{\partial}{\partial x_j}(\overline{\rho}\tilde{u}_i\tilde{u}_j) = -\frac{\partial \overline{p}}{\partial x_i} + \frac{\partial}{\partial x_j}\Big(-\widetilde{\rho u_i' u_j'} + \frac{1}{R}\tau_{ij}\Big), \tag{53}$$

where the stress tensor τ_{ij} is given by

$$\tau_{ij} = \lambda\delta_{ij}\frac{\partial \tilde{u}_l}{\partial x_l} + \mu\Big(\frac{\partial \tilde{u}_i}{\partial x_j} + \frac{\partial \tilde{u}_j}{\partial x_i}\Big). \tag{54}$$

These equations are complemented by the energy and the state equations. It follows that

$$a^2 = \frac{1}{2}(\gamma+1) - \frac{1}{2}(\gamma-1)\tilde{u}_i\tilde{u}_j, \qquad a = \sqrt{\frac{\overline{p}}{\overline{\rho}}}, \tag{55}$$

$$\overline{p} = \overline{\rho}\tilde{t}. \tag{56}$$

In the above equations, x, u, p, t and ρ have their classical meaning. λ is the bulk viscosity ($= -2/3\mu$), μ is the viscosity and δ_{ij} the Kronecker delta. The non-dimensional velocities, pressure, temperature and density are all referred to their critical values just outside the boundary layer and ahead of the shock. R denotes the Reynolds number. The dashes denote turbulent fluctuations; the bars and the tildes denote respectively conventional time averaging

and mass-weighted averaging. In what follows, for the sake of simplicity, the bars and the tildes will be omitted.

The order of magnitude of the turbulent terms in the equations of motion can be estimated through the experimental results of Kistler(1959), of Kistler and Chen(1963) and of Morkovin(1962). These author have shown that: (a) u', ρ', and t' have the same order of magnitude and (b) the root square-mean value of p' is proportional to u'. Thus, in view of the above remarks, the scales of fluctuation can be written as

$$ord(u') = ord(v') = ord(\rho') = ord(t') = ord(u_\tau), \tag{57}$$

$$ord(p') = ord(u_\tau^2). \tag{58}$$

To find the asymptotic structure of the flow in the interaction region, we consider the same stretching transformation used in the two previous sections of the paper, that is,

$$x_\Delta = \frac{x}{\Delta(\epsilon)}, \qquad y_\eta = \frac{y}{\eta(\epsilon)}, \qquad \hat{u}_i(x_\Delta, y_\eta) = u_i(x, y), \tag{59}$$

with $\Delta(\epsilon)$ and $\eta(\epsilon)$ defined on Ξ.

Following previous studies of the problem by Messiter(1980) and by Silva Freire(1988), in the interaction region we separate the asymptotic expansions for the solution into a rotational and an irrotational part.

Thus, we introduce here the two small-parameters

$$\epsilon = \frac{U_\infty}{a^*} - 1, \tag{60}$$

and

$$u_\tau = \frac{1}{a^*}\sqrt{\frac{\tau_w}{\rho_w}}, \tag{61}$$

where a^* is the critical sound speed in the external flow just ahead of the shock, τ_w is the laminar stress at the wall, and ρ_w is the density at the wall. From now on, the reader is asked not to confuse the new definition of ϵ with its previous definition in the previous sections.

As a result, the velocity profiles can be written as

$$u = 1 + \epsilon u_\alpha(x, y) + u_\tau u_\beta(y), \tag{62}$$

$$v = \epsilon^{3/2} v_\alpha(x, y), \tag{63}$$

where u_α and u_β represent respectively the irrotational and the rotational parts of the flow.

Upon substitution of Eqs.(62) and (63) into the equations of motion, and passage of the η-limit process onto the resulting equations, we get for the x-momentum equation:

$$ord\ \eta = 1 : \frac{\partial}{\partial x_\Delta}\left(\rho\hat{u}_\alpha\hat{u}_\alpha\right) + \frac{\partial}{\partial y_\eta}\left(\rho\hat{u}_\alpha\hat{v}_\alpha\right) = -\frac{\partial\hat{p}_\alpha}{\partial x_\Delta}, \tag{64}$$

$$ord\ u_\tau^2 < ord\ \eta < 1 : \frac{\partial}{\partial x_\Delta}\left(\rho\hat{u}_\alpha\hat{u}_\alpha\right) + \frac{\partial}{\partial y_\eta}\left(\rho\hat{u}_\alpha\hat{v}_\alpha\right) = -\frac{\partial\hat{p}_\alpha}{\partial x_\Delta}, \tag{65}$$

$$ord\ \eta = ord\ u_\tau^2 : \frac{\partial}{\partial x_\Delta}\left(\rho\hat{u}_\alpha\hat{u}_\alpha\right) + \frac{\partial}{\partial y_\eta}\left(\rho\hat{u}_\alpha\hat{v}_\alpha\right) = -\frac{\partial\hat{p}_\alpha}{\partial x_\Delta} + \frac{\partial}{\partial y_\eta}\left(-\overline{\rho\hat{u}'_\alpha\hat{v}'_\alpha}\right), \tag{66}$$

$$ord\ 1/Ru_\tau < ord\ \eta < ord\ u_\tau^2 : \frac{\partial}{\partial y_\eta}\left(-\overline{\rho\hat{u}'_\alpha\hat{v}'_\alpha}\right) = 0, \tag{67}$$

$$ord\ \eta = ord\ 1/Ru_\tau : \frac{\partial}{\partial y_\eta}\left(-\overline{\rho\hat{u}'_\alpha\hat{v}'_\alpha}\right) + \mu\frac{\partial^2\hat{u}_\beta}{\partial y_\eta^2} = 0, \tag{68}$$

$$ord\ \eta < ord\ 1/Ru_\tau : \mu\frac{\partial^2\hat{u}_\beta}{\partial y_\eta^2} = 0. \tag{69}$$

Since we are considering the flow in the interaction region, in passing the η-limit we have taken ord(Δ) = ord(ϵ). The other equations, continuity, energy and state, do not give any contribution to the asymptotic structure. In fact, Silva Freire(1989) has shown that if the full energy equation is considered, and the concepts of section two are applied to the full set of equations, then the overlap domains of the velocity field and of the temperature field will coincide.

The continuity equation simply implies that

$$ord(v) = \frac{\eta}{\Delta}ord(u). \tag{70}$$

The classical two-deck structure of the turbulent boundary layer is then clearly seen from equations (64) to (69). Note that Eqs.(66) and (68) are the principal equations; their overlap domain is identical to the overlap domain determined for the incompressible flow case.

In the vicinity of the shock wave, however, the asymptotic structure above deduced must change. The strong pressure gradient imparted to the boundary layer by the shock wave alters the balance of terms in the equations of motion, giving rise to a new structure where for most of the boundary layer the problem becomes an inviscid one. The need for the establishment of an inviscid rotational flow model for the description of the interaction has been recognised since Lighthill(1953) proposed his linearized solution for the laminar problem. The result is that all recent theories advanced for the turbulent problem must somehow accommodate the inviscid rotational interaction model without contradicting the features of the turbulent flow.

To surmount this difficulty, the theories of Melnik and Grossmann(1974), of Adamson and Feo(1975), of Messiter(1980) and of Liou and Adamson(1980) consider the introduction of a blending region in the interaction region. The blending layer is, in fact, nothing more than the turbulent region defined by the overlap domain and derived by our asymptotic analysis of the problem. The absence of an equation similar to equation (67) in the matched asymptotic expansions method is the main reason for the difficulties this method presents. Likewise, this is the reason why the structure depicted by Eqs.(66) to (69) can deal with the interaction problem.

To take into account for the presence of the shock wave, we pass the Δ-limit process onto Eqs.(64) to (69). The result is:

$$ord\ \Delta = ord\ \epsilon : \frac{\partial}{\partial x_\Delta}\left(\rho\hat{u}_\alpha\hat{u}_\alpha\right) + \frac{\partial}{\partial y_\eta}\left(\rho\hat{u}_\alpha\hat{v}_\alpha\right) = -\frac{\partial\hat{p}_\alpha}{\partial x_\Delta}, \tag{71}$$

$$ord\ \epsilon/Ru_\tau^3 < ord\ \Delta < ord\ \epsilon\eta/u_\tau^2 : \frac{\partial}{\partial x_\Delta}\left(\rho\hat{u}_\alpha\hat{u}_\alpha\right) + \frac{\partial}{\partial y_\eta}\left(\rho\hat{u}_\alpha\hat{v}_\alpha\right) = -\frac{\partial\hat{p}_\alpha}{\partial x_\Delta}, \tag{72}$$

$$\begin{aligned} ord\ \Delta = ord\ \epsilon/Ru_\tau^3 : \frac{\partial}{\partial x_\Delta}\left(\rho\hat{u}_\alpha\hat{u}_\alpha\right) + \frac{\partial}{\partial y_\eta}\left(\rho\hat{u}_\alpha\hat{v}_\alpha\right) &= -\frac{\partial\hat{p}_\alpha}{\partial x_\Delta} \\ &+ \frac{\partial}{\partial y_\eta}\left(-\overline{\rho\hat{u}'_\alpha\hat{v}'_\alpha}\right) + \mu\frac{\partial^2\hat{u}_\beta}{\partial y_\eta^2}, \end{aligned} \tag{73}$$

$$ord\ \Delta) < ord\ \epsilon/Ru_\tau^3 : \mu\frac{\partial^2\hat{u}_\beta}{\partial y_\eta^2} = 0. \tag{74}$$

The change in the asymptotic structure of the flow in the interaction region is noticeable from the above equations. In particular, we note that as the shock is approached, that is, as the order of magnitude of Δ increases, the validity domain of the outer principal equation changes position until the two principal equations merge at $(\Delta,\eta) = (\epsilon/(u_\tau^3R), 1/(u_\tau R))$. Indeed, as shown by the calculations, at the beginning of the interaction the outer principal equation is positioned at $(\Delta,\eta) = (\epsilon, u_\tau^2)$. However, as the order of magnitude of η varies from u_τ^2 to $1/u_\tau R$, this equation moves along the path $(\epsilon\eta/u_\tau^2, \eta)$ until reaching the point $(\epsilon/u_\tau^3R, 1/u_\tau R)$. The flow structure is then shown to reduce from a classical two deck structure to a one deck structure near to the foot of the shock wave. According to these results, there is a region at the foot of the shock where the full boundary layer equations are recovered.

The results of this section are shown in Figure 2; they will be compared with the experimental data of Sawyer and Long(1982).

Figures 3 and 4 reproduce, from the experimental data, a map which indicates the dominant region of every term in the equations of motion. Both cases, Mach numbers of 1.27 and of 1.37 are shown. The meaning of the shades in gray is clear. Thus, the farthest from the wall tone corresponds to the inertia and pressure gradient terms, the intermediate tone to the turbulent terms and the remaining tone to the viscous terms. The shock wave is located at $x = 0$.

Observe, as predicted by the asymptotic theory, the complete dominance of the inertia and pressure terms in the vicinity of the shock. This feature is particularly striking for the 1.37 Mach number case where the influence of the shock extends down to the viscous layer. The consequence is that the phenomenon is, for most of the interaction region, and, to a leading order, governed by inviscid equations.

5 Final Remarks

In the first part of the paper, some ideas of Kaplun concerning limit processes have been extended to higher orders through the proposition of the principal equations. This result is central to our work, for it ensures that the asymptotic structure of a singular perturbation problem can be uniquely determined by a first order analysis of the formal domains of validity. The resulting principal equations are expected to be satisfied by the corresponding limits of the exact solution, so providing approximate solutions that overlap and cover the entire domain of validity.

In the second part of the paper, application of Kaplun limits to the equations of motion has shown the zero-pressure turbulent boundary layer to have a two deck structure, the principal equations being located at points $(\epsilon^2, 1)$ and $(1/\epsilon R, 1)$ of the product space $(\Xi \times \Sigma)$. The present results are very much in accordance with the earlier works of Yajnik, of Mellor and of Bush and Fendell. They seem to corroborate the idea that a one-parameter theory can correctly describe the flow structure and, furthermore, do not give any evidence to suggest the contrary.

The present analysis has also shown how the two-deck turbulent boundary layer structure develops into a one-deck structure near a separation point. This results seems, at first, contradictory to the three-layer structure found by other authors (Melnik(1989), Durbin and Belcher(1992)). However, we point out that all local equations derived by these authors are intermediate equations, in the sense of Kaplun, being therefore, contained in the domain of validity of the principal equations here derived. In other words we may say that those theories are "contained" in the present theory. Of course, the principal equations are of difficult solution, do not providing closed analytical solutions; however, only these equations give fundamental insight to understand how the viscous and defect layers merge as a separation point is approached.

In what concerns the problem of interaction between a shock-wave and a turbulent boundary layer, the application of Kaplun limits to the equations of motion has shown the flow to attain an one deck structure, which is distinct from those of other authors but consistent with the experimental data of Sawyer and Long(1982) and with the general knowledge of the problem we have. The theory, as presented here, can formally explain how an inviscid flow region is formed at the foot of the shock wave, resulting from the disappearance of the fully turbulent region.

Acknowledgements. Many people have decisively contributed to the completion of this work. Drs. S.L.V. Coelho e N. Chokani read and commented an early draft of the first part of the paper. The author also benefited from useful discussions with Prof. R. Narasimha and Dr. J. Su. Many of the analytical difficulties were discussed with Dr. D.O.A. Cruz. This work was financially supported by the CNPq (Ministry of Sciences and Technology) through grant No 350183/93-7.

6 References

Adamson, T. C.Jr. and Feo, A.; Interaction Between a Shock Wave and a Turbulent Boundary Layer at Transonic Speeds, SIAM J Appl. Math., vol. 29, pp. 121–145, 1975.

Bush, W. B. and Fendell, F. E.; Asymptotic Analysis of Turbulent Channel and Boundary Layer Flows, J. Fluid Mechanics, vol. 56, pp. 657–681, 1972.

Cole, J. D.; Perturbation Methods in Applied Mathematics, Blaisdell, Massachussets, 1968.

Cruz, D. O. A. and Silva Freire, A. P.; On Single Limits and the Asymptotic Behaviour of Separating Turbulent Boundary Layers, Int. J. Heat Mass Transfer, vol. 41, pp. 2097–2111, 1998.

Deriat, E. and Guiraud, J. P.; On the Asymptotic Description of Turbulent Boundary Layers, J. Theor. Appl. Mech., Special issue, pp. 109–140, 1986.

Driver, D. M. and Seegmiller, H. L.; Features of a Reattaching Turbulent Shear Layer in Divergent Channel Flow, AIAA J., vol. 23, pp. 163–171, 1995.

Durbin, P. A. and Belcher, S. E.; Scaling of Adverse-Pressure-Gradient Turbulent Boundary Layers, J. Fluid Mechanics; vol. 238, pp. 699–722, 1992.

Eckhaus, W.; On the Foundations of the Method of Matched Asymptotic Expansions, J. de Mecanique, vol. 8, pp. 265–300, 1969.

Eckhaus, W.; Boundary Layer in Linear Elliptic Singular Perturbation Problems, SIAM Review, vol. 14, pp. 225–270, 1972.

Eckhaus, W.; Matched Asymptotic Expansions and Singular Perturbation; North-Holland, Amsterdam, 1973.

Fraenkel, L. E.; On the Method of Matched Asymptotic Expansions, Proc. Camb. Phil. Soc., vol. 65, pp. 209–284, 1969.

Kaplun, S.; Fluid Mechanics and Singular Perturbations, Academic Press, 1967.

Kaplun, S. and Lagerstrom, P. A.; Asymptotic Expansions of Navier-Stokes Solutions for Small Reynolds Numbers, J. Math. Mech., vol. 6, pp. 585–593, 1957.

Kevorkian, J. and Cole, J. D.; Perturbation Methods in Applied Mathematics, Springer Verlag, Heidelberg, 1981.

Kistler, A. L., Fluctuation Measurements in a Supersonic Turbulent Boundary Layer. Phys. Fluids, vol. 2, pp. 290–296, 1959.

Kistler, A. L. and Chen, W. S., A Fluctuating Pressure Field in a Supersonic Turbulent Boundary Layer, J. Fluid Mechanics, vol. 16, pp. 41–64, 1963.

Lagerstrom, P. A. and Casten, R. G.; Basic Concepts Underlying Singular Perturbation Techniques, SIAM Review, vol. 14, pp. 63–120, 1972.

Lagerstrom, P. A.; Matched Asymptotic Expansions; Springer Verlag, Heidelberg, 1988.

Lighthill, M. J.; On Boundary Layer Upstream Influence. Part II: Supersonic Flow without Separation. Proc R Soc London A, vol. 217, pp. 478–507, 1953.

Liou, M. S. and Adamson, T. C., Interaction Between a Normal Shock Wave and a Turbulent Boundary Layer at High Transonic Speeds. Part II: Wall Shear Stress. ZaMP, vol. 31, pp. 227–246, 1980.

Long, R. R. and Chen, J.-C.; Experimental Evidence for the Existence of the "Mesolayer" in Turbulent Systems, J. Fluid Mechanics, vol. 105, pp. 19–59, 1981.

Mellor, G. L.; The Large Reynolds Number Asymptotic Theory of Turbulent Boundary Layers, Int. J. Engng. Sci., vol. 10, pp. 851–873, 1972.

Melnik, R. E.; An Asymptotic Theory of Turbulent Separation, Compt. & Fluids, vol. 17, pp. 165–184, 1989.

Melnik, R. E. and Grossmann, B.; Analysis of the Interaction of a Weak Normal Shock Wave with a Turbulent Boundary Layer. AIAA paper No. 74-598, 1974.

Messiter, A. F.; Interaction Between a Normal Shock Wave and a Turbulent Boundary Layer at High Transonic Speeds. Part I: Pressure Distribution. ZaMP vol 31, pp. 204–227, 1980

Meyer, R. E.; On the Approximation of Double Limits by Single Limits and the Kaplun Extension Theorem, J. Inst. Maths. Applics., vol. 3, pp. 245–249, 1967.

Morkovin, M. V.; Effects of Compressibility on Turbulent Flows, Int Sym on "Mecanique de la turbulence", pp. 367–380, 1962.

Nayfeh, A. H.; Perturbation Methods, John Wiley, N.Y., 1973.

Nipp, K.; An Algorithmic Approach for Solving Singularly Perturbed Initial Value Problems, Dynamic Reported 1, John Wiley, N.Y., 1988.

O'Malley, R. E. Jr.; Introduction to Singular Perturbations, Academic Press, New York, 1974.

Sawyer, W. G. and Long, C. J.; A Study of Normal Shock-Wave Turbulent Boundary-Layer Interactions at Mach Numbers of 1.3, 1.4 and 1.5. Royal Aircraft Establishment, Technical Report No 82099, 1982.

Silva Freire, A. P.; An Asymptotic Approach for Shock-Wave/Transpired Turbulent Boundary Layer Interaction. ZaMP, vol. 39, pp. 478-503, 1988.

Silva Freire, A. P.; On the Matching Conditions for a Two-Deck Compressible Turbulent Boundary Layer Model. ZaMM, vol. 69, pp. 100-104, 1989.

Silva Freire, A. P. and Hirata, M. H.; Approximate Solutions to Singular Perturbation Problems: the Intermediate Variable Technique, J. Math. Analysis and Appl., vol. 145, pp. 241–253, 1990.

Stratford, B. S.; An Experimental Flow with Zero Skin-Friction throughout its Region of Pressure Rise, J. Fluid Mechanics, vol. 5, pp. 17–35, 1959.

Sychev, V. V. and Sychev, V. V.; On Turbulent Boundary Layer Structure, P.M.M. U.S.S.R., vol. 51, pp. 462–467, 1987.

Townsend, A. A.; The Structure of Turbulent Shear Flow, Cambridge University Press, 1976.

Van Dyke, M.; Perturbation Methods in Fluid Mechanics, Parabolic Press, 1975.

Vogel, J. C. and Eaton, J. K.; Combined Heat Transfer and Fluid Dynamic Measurements Downstream of a Backward Facing Step, Journal of Heat Transfer, vol. 107, pp. 922-929, 1985.

Wasow, W.; Asymptotic Expansions for Ordinary Differential Equations, Interscience, 1965.

Yajnik, K. S.; Asymptotic Theory of Turbulent Shear Flow, J. Fluid Mechanics, vol. 42, pp. 411-427, 1970.

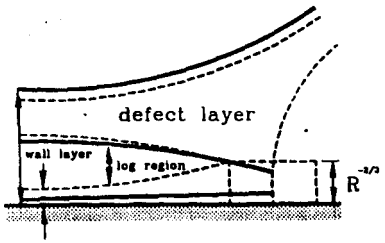

a) $P_r > 1$

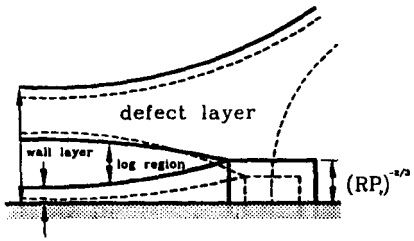

b) $P_r < 1$

Figure 1

Figure 1. Flow asymptotic structure for the separation problem.

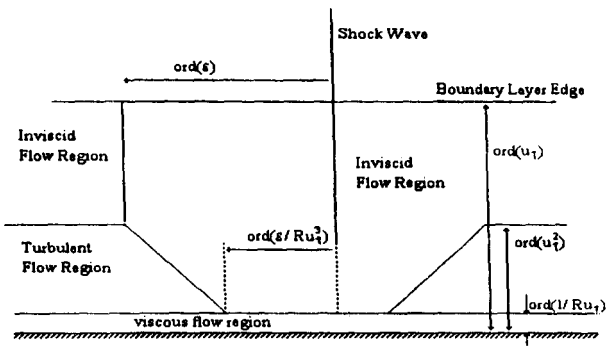

Figure 2. Flow asymptotic structure for the shock interaction problem, theory.

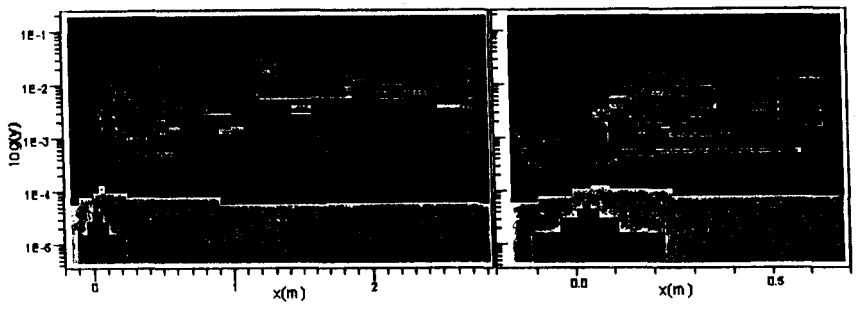

Figure 3. Flow asymptotic structure for the shock interaction problem. Data of Sawyer and Long(1982), Mach number = 1.27.

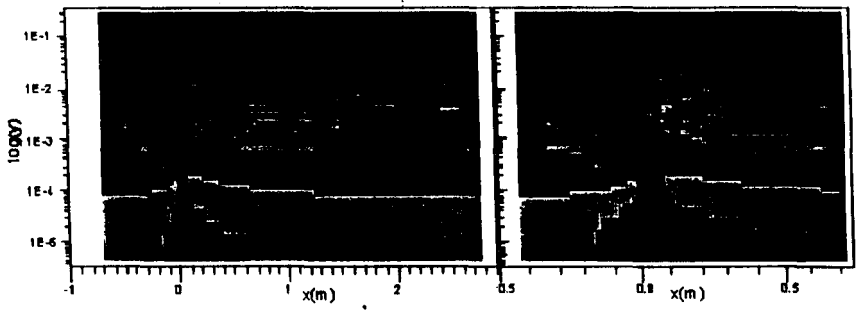

Figure 4. Flow asymptotic structure for the shock interaction problem. Data of Sawyer and Long(1982), Mach number = 1.37.

NONLINEAR EVOLUTION OF A THREE-DIMENSIONAL WAVETRAIN IN A FLAT PLATE BOUNDARY LAYER

Marcello A. Faraco de Medeiros
Departamento de Engenharia Mecânica
Pontifícia Universidade Católica de Minas Gerais
Av. Dom José Gaspar, 500, Belo Horizonte, 30535-610 - MG - Brazil
E-mail:marcello@mea.pucminas.br

Abstract

This paper presents results of an experimental study of the transition in boundary layers. The experiments were conducted in a low-turbulence wind tunnel. The process was triggered by a three-dimensional Tollmien-Schlichting wavetrain excited by a harmonic point source in the plate. Hot-wire anemometry was used to measure the signal and investigate the nonlinear regime of these waves. It was observed that the three-dimensional wavetrain behaved very differently from two-dimensional ones. In particular, it did not involve the growth of subharmonics or higher harmonics. The first nonlinear signal to appear was a mean flow distortion. This had a spanwise structure consisting of regions of positive and negative mean distortion distributed like longitudinal streaks, which became more complex as the nonlinearity developed. The structure in the direction perpendicular to the wall has also been studied. Initially the distortion profiles resembled Klebanoff modes, but further downstream it also became more complex. Elsewhere studies have revealed the existence of streak-structures in turbulent flows. It is conjectured that the current experiments may provide a link between early wave-like instabilities and some coherent structures of turbulent boundary layers.

1 Introduction

The laminar-turbulent transition point is often a crucial element in the design of wings. In spite of it, the prediction of the transition point is still a challenge in fluid mechanics. Transition is affected by a large number of parameter, such as free-stream turbulence, pressure gradient, conditions of the leading edge and degree of isotropy and homogeneity of the free-stream turbulence.

It has now been established that there are a number of different routes to transition. Among them the most studied is the Tollmien-Schlichting route. This route involves the exponential amplification of two dimensional waves, which, if the amplitude is large enough, give rise to three dimensional waves via a secondary instability mechanism (Herbert 1988). The three dimensional waves can be of two types depending on the kind of resonant interaction that occurs. With primary resonance the three dimensional waves have frequency equal to the fundamental two dimensional waves, whereas with parametric resonance the three dimensional waves are subharmonics of the fundamental. In both cases the wave system that arises, saturates in the form lambda vortices (Corke & Mangano 1989, Kachanov & Levchenko 1984, Kachanov 1987, Kachanov 1994). With subahrmonic resonance the vor-

tices exhibit a staggered pattern whereas for fundamental resonance they are aligned in the streamwise direction. High amplitude fundamental waves tend to favour primary resonance. In any case, the lambda vortices give rise to high frequency oscillations by a mechanism as yet not established. Some researchers attribute the breakdown to the instability of an inflexional profile that would be created by the vortical structure. Others argue that the tip of the lambda vortices stretch under the action of the shear layer giving rise to high frequency oscillations, but there may be other plausible explanations.

Another route to transition is the so called by-pass transition. The scenario consists of the formation and transient growth of longitudinal streaks, that is, regions of higher and lower streamwise velocity (Henningson, Lundbladh & Johansson 1993). If the amplitude of the streaks is sufficiently large the appearence of high frequency disturbances is observed. It has been suggested that the high frequency disturbances are caused by spanwise inflexional instability of the streaks (Elofsson & Alfredsson 1997). The transient growth is caused by a mechanism different from that causing the growth of the Tollmien-Schlichting waves. In fact transient growth can occur under subcritical conditions, that is, conditions for which all Tollmien-Schlichting modes are stable. These route is generally connected with disturbances of amplitudes considerably larger than those of the classical Tollmien-Schlichting route.

Both routes have been shown theoretically and confirmed by experiments. The current work is primarily concerned with the Tollmien-Schlichting route to transition, but, as will be seen, the experimental observations do not display the appearence of subharmonic modes as would be expected from secondary instability theory. The results display the formation of longitudinal streaks. Possible connection of this streak structure with those observed in by pass transition have not been fully investigated, but, despite a few similarities, the process appears to be different.

Both theoretical and experimental studies of the Tollmien-Schlichting route to transition have concentrated on a rather restrictive case, namely, the situation when the primary wave driving the process is a plane monochromatic wave. While this is a very important study, and almost certainly a necessary step towards more generic situations, the case of more practical interest is the so called natural transition. In natural transition the waves arise from free-stream turbulence, wall vibration, acoustic waves, and others sources which are not controlled. In this context the waves that arise are not plane-monochromatic but are highly modulated involving a large number of two and three-dimensional modes.

Gaster suggested that a possible way to model the natural transition is to disturb the flow with a pulse emanating from a point source. The idealized pulse contains all frequencies of the spectrum including three-dimensional modes. Gaster tested the idea in his classical experiment (Gaster & Grant 1975) and observed that, owing to the selective amplification of modes in the boundary layer, the pulse generated a wavepacket in agreement with the linear instability theory (Gaster 1975). The nonlinear evolution was also investigated and the observations indicated that nonlinearity appeared at surprisingly low wave amplitudes, in fact, amplitudes for which monochromatic wavetrains would display linear behaviour. This was later confirmed by experiments in which the nonlinear evolution of wavepackets were compared with that of wavetrains (Gaster 1978, Gaster 1993). Later other experiments with wavepackets in boundary layers were carried out by Breuer & Haritonidis (1990), Cohen, Breuer & Haritonidis (1991), Cohen (1993) and Breuer, Cohen & Haritonidis (1997). In all the experiments the nonlinear evolution of the packets were connected to the appearence of waves with frequency close to the subharmonic of the fundamental.

Following Gaster, Shaikh (1993, 1994, 1997) studied a more generic type of distur-

bance, namely, that generated by a white noise excitations. Shaikh compared the evolution of disturbances generated from different white noise sequences. The sequences had the same spectral content, only the phase of the components relative to each other were different. He observed that the transition point was very sensitive to the phase composition of the disturbance, and concluded that the amplitude was not the only parameter affecting the process.

The works of Gaster and Shaikh pointed to the fact that the nonlinear mechanisms in the evolution of modulated waves were different from those observed in plane wavetrains. However the wavepackets of Gaster were too restrictive while the white noise sequences of Shaikh were too generic, making it difficult to interpret the results. By allowing the amplitude of the wavepackets to be complex, Medeiros (1996, 1996) generated experimentally a set of wavepackets with identical envelopes but with different phase relative to the envelope. With this he was able to show the influence on the phase of the evolution of modulated waves (Medeiros 1997*b*). Later he also showed experimentally that although the subharmonic resonance appeared to be present in the process, it alone could not explain the observations (Medeiros 1997*c*). The nonlinear mechanism observed involved the production of subharmonic waves. The fact that not only amplitude but also phase affects the transition process is of large practical importance because the transition prediction methods so far used have only accounted for the amplitude of the waves.

The wavepackets are modulated both in streamwise and spanwise directions. At first it appeared that the important ingredient was the streamwise modulation, rather than the spanwise modulation (Gaster 1984, Medeiros & Gaster 1994, Medeiros & Gaster 1995), however numerical simulations of two-dimensional wavepackets by Medeiros (1996) have shown that spanwise modulation is essential to the process. This has led to the investigation of the nonlinear evolution of waves that are only spanwise modulated, namely, a wavetrain emanating from a point source. This paper presents some results of these investigations. Preliminary results have been presented by Medeiros (1997*d*) and Medeiros (1997*a*)

Investigation of three-dimensional wavetrains has also been carried out by other researchers (Kachanov 1985, Mack 1985, Seifert 1990, Seifert & Wygnanski 1991, Wiegand, Bestek, Wagner & Fasel 1995), but these were restricted to the linear stage.

2 Experimental Results

The experiments were conducted in the low turbulence wind tunnel of the University of Cambridge, Cambridge, UK [1]. The boundary layer developed over a flat plate. The pressure gradient was controlled with the help of a flap at the trailing edge of the plate. With this set up a fairly small pressure gradient was obtained, figure 1. Also, the profiles measured were close to the theoretical Blasius profile, figure 2. The measurements covered the region ± 200mm in the spanwise direction from the centreline with profiles 2cm apart.

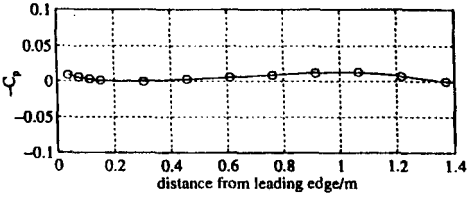

Figure 1: The static pressure distribution over the plate

The disturbances were introduced in the flow via a loudspeaker embedded in the plate and communicated to the flow through a .3mm hole, located on the centreline of the plate 203mm from the leading edge. The velocity records were measured with a 2.5μm gold plate tungsten hot-wire connected to a constant

[1] This tunnel is now located at Queen Mary and Westfield College, London University, London, UK

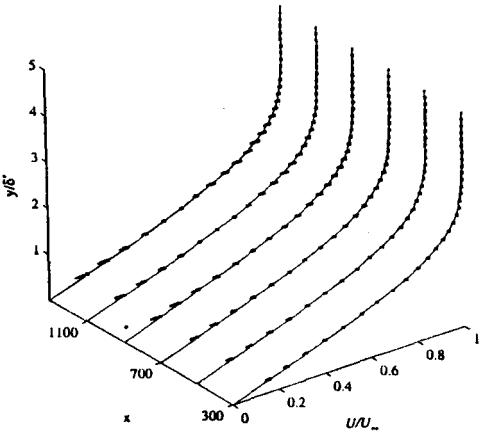

Figure 2: The mean flow. Lines represent the theoretical Blasius profile. Asterisks represent the measured values

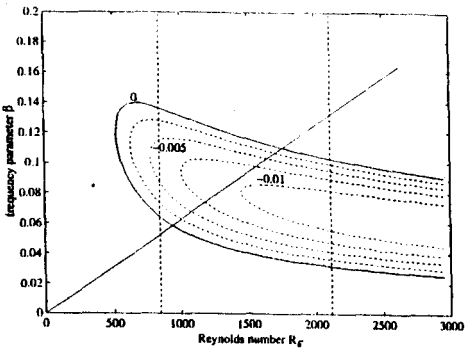

Figure 3: The instability diagram showing the path of the 200Hz Tollmien Schlichting wave.

temperature anemometer. The hot-wire was mounted on a three-dimensional traverse gear. The streamwise and spanwise positions of the wire could be directly measured from the traverse mechanism. The distance from the wall had to be obtained indirectly by measuring the velocity profile and comparing to the theoretically obtained. The procedure has been used in similar experiments in this tunnel (Shaikh 1993) and has proved to be fairly accurate. More details of the experimental set up are given by Medeiros (1996).

In experiments with wavetrains the flow is usually disturbed by a continuous harmonic source. In the current series of experiments a long but finite 200Hz wavetrain is excited from a point source. The linear evolution a two dimensional mode with frequency 200Hz is shown by the straight line on the instability diagram, figure 3. The excitation was introduced at R_δ about 800 and measurements were taken up to R_δ^* 2100, as indicated by the dashed lines in the figure. One can see that the excitation was introduced upstream of branch I of the neutral curve and that measurements were taken beyond branch II, after which the Tollmien-Schlichting waves decay. The waves cross branch II at R_δ^* around 1700.

The evolution of the disturbances observed experimentally along the centreline is shown in figure 4. The measurements were taken at a nondimensional distance of $0.52\delta^*$. Using finite wavetrains, the disturbance is an event that can be repeated. Therefore ensemble averages can be taken in order the get a clearer signal. The records displayed here, as well as those shown in other figures, were obtained from 64 ensembles. The first important observation is that wave amplitudes grow up to R_δ^* about 1700 and thereafter decay, consistent with the linear theory, figure 3. A mean flow distortion is also observed that is not predicted by the linear theory. Initially the distortion is negative, but further downstream switches to positive. It is remarkable that the change in the trend of the mean flow distortion occurs close to where the disturbance crosses branch II. The mean flow distortion is made very clear by the use of finite length wavetrains. It could have remained undetected if a continuous wavetrains were used. It is possible that the use of continuous wavetrains have prevented these mean flow distortions from being observed in previous experiments with three-dimensional wavetrains.

Figure 5 shows the evolution of a wavetrain of considerably smaller amplitude. Here

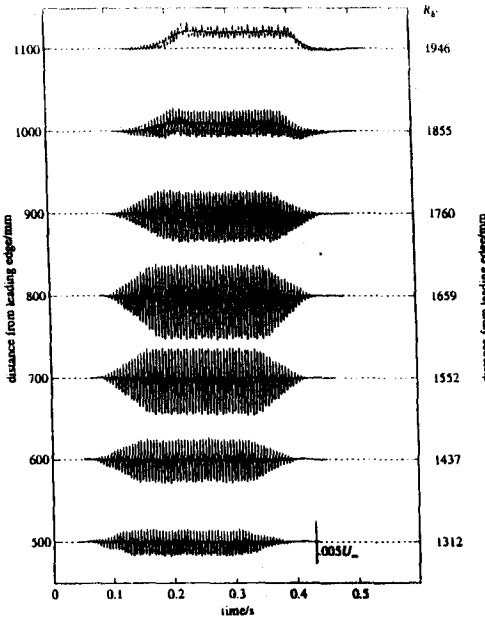

Figure 4: The evolution of the 200Hz three-dimensional wavetrain along the centerline of the plate at a distance of $0.52\delta^*$ from the wall.

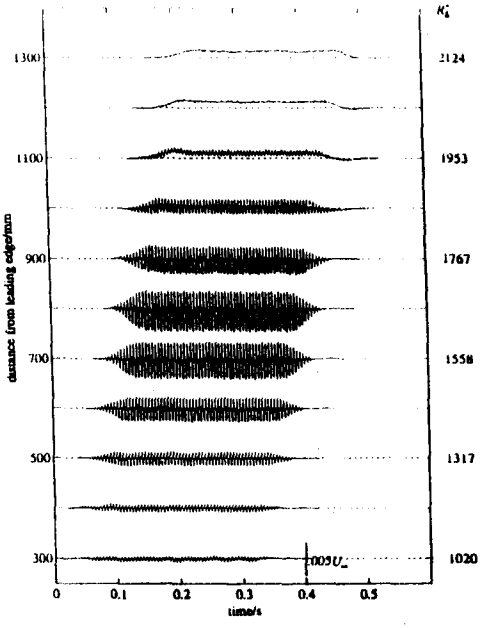

Figure 5: The evolution of a very small amplitude 200Hz three-dimensional wavetrain along the centerline of the plate at a distance of $0.52\delta^*$ from the wall.

again the nonlinear mean flow distortion is observed, despite the low amplitude of the oscillations. The oscillations are so small that slightly downstream of branch II they are very difficult to measure. The mean flow distortion, on the other hand, can be observed up until the end of the flat plate. This phenomenon may come as a surprise, but it is possible that the decay of the mean flow distortion is governed by the recovery response of the boundary layer which for a laminar boundary layer is very slow. Also interesting is that the change in the sign of the mean flow distortion for the very small disturbance occurs at the same location as for the relatively large disturbance.

Measurements were also taken off the centerline of the flow in order to study the spanwise structure of the wave system. Measurements were taken at different spanwise locations 10mm apart from each other covering the entire width of the disturbance field. This provided a view of the disturbance as it crosses a streamwise location, figures 6, 7 and 8. Initially the disturbances display swept back wavecrests with a smooth modulation across the span. Further downstream , the signal develops strong distortions and the appearence of streaks is observed.

The structure of the streaks is made clearer if the oscillating part of the signal is digitally filtered, figure 9. A picture of the evolution of the streak structure as it evolves downstream is shown in figure 10. Initially there is a central region of negative mean flow distortion together with two lateral regions of positive mean

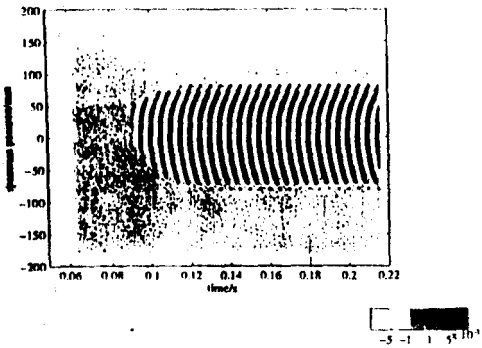

Figure 6: Spanwise structure of the disturbance field 700mm from the leading edge and $0.52\delta^*$ from the wall.

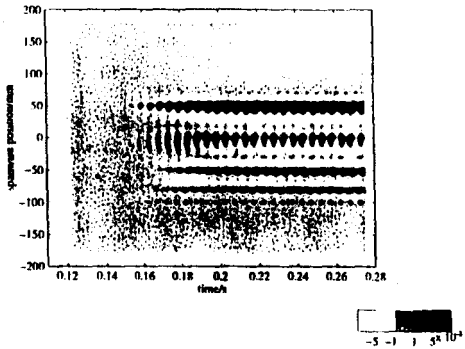

Figure 8: Spanwise structure of the disturbance field 1100mm from the leading edge and $0.52\delta^*$ from the wall.

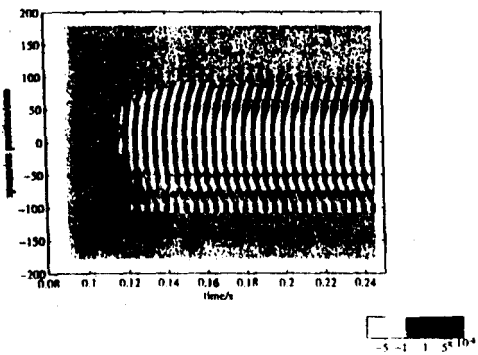

Figure 7: Spanwise structure of the disturbance field 900mm from the leading edge and $0.52\delta^*$ from the wall.

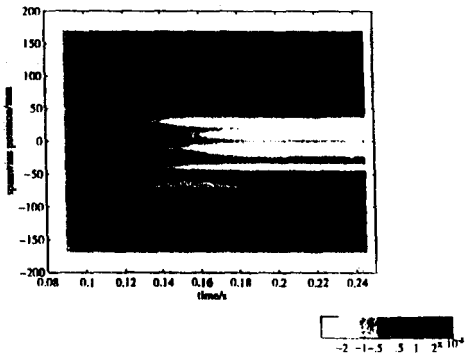

Figure 9: Spanwise structure of the mean flow distortion (streaks) 900mm from the leading edge and $0.52\delta^*$ from the wall.

flow distortion. This structure suggests the existence of a pair of counter-rotating concentrations of vorticity which would push down high momentum fluid in the lateral regions and lift up low momentum fluid in the central region. However, it is as yet unclear whether these mechanisms are actually taking place. The concentrations of vorticity are probably too weak to be considered vortices and perhaps the lift up/push down effect is too small to affect the flow. As the waves evolve, the structure becomes more complex. At x=1000mm the appearence of a region of positive mean flow distortion right at the center of the wavetrain is observed. This corresponds to the change in the sign of the mean flow distortion observed in figure 4. From station x=1000mm onwards the structure doesn't experience remarkable changes, apart from the broadening of the central positive mean flow distortion.

It is interesting to look at the evolution in the frequency domain which was carried out by Medeiros (1997*a*). However, the spanwise resolution of the experiment is relatively low. The

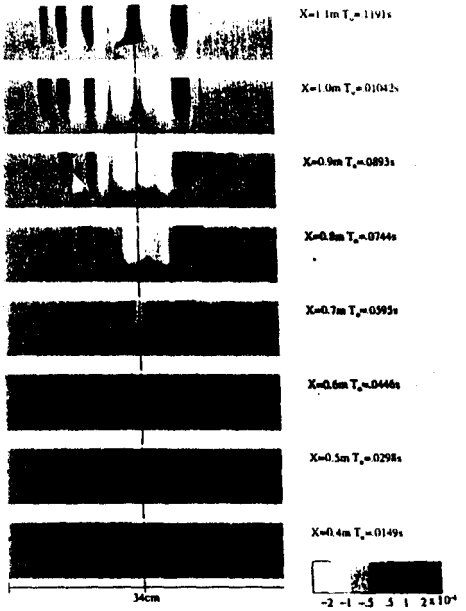

Figure 10: Downstream evolution of the streaks

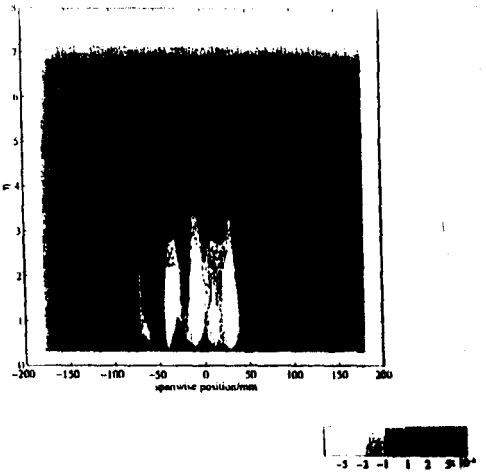

Figure 11: The mean flow distortion distribution on a plane perpendicular to the flow direction 900mm from the leading edge.

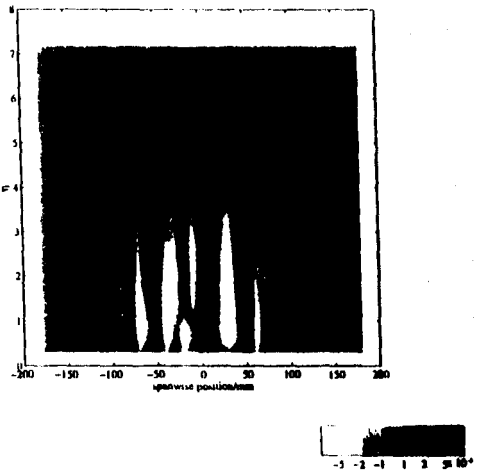

Figure 12: The mean flow distortion distribution on a plane perpendicular to the flow direction 1100mm from the leading edge.

results became difficult to interpret because alias effects could not be ruled out. Therefore, care should be taken in analyzing those results. What is clear is that initially the nonlinear mechanism generates only two region of positive mean flow distortion and one central region where the distortion is negative, while further downstream the spanwise wavenumbers become significantly larger.

Also important is to investigate the structure of the mean flow distortion in the direction normal to the wall. Figures 11 and 12 show contour plots of the mean flow distortion on planes perpendicular to the flow direction 900mm and 1100mm. The mean flow distortion is concentrated inside the boundary layer. In the external part of the flow no sign of the mean flow distortion is observed. At x=900mm the structure is basically composed of two regions of positive mean flow distortion and a central region of negative mean flow distortion. Whereas the positive lumps are fairly concentrated the negative region spreads over a larger portion. Moreover, the negative region appears to be composed of several lumps. The profile

resembles that of a Klebanoff mode with a single maximum inside the boundary layer, particularly for the positive streaks. The maximum is located between $\eta(= y\sqrt{\frac{U_\infty}{\nu x}})$ 1 and 2, which is also similar to that of Klebanoff modes. At x=1100mm the negative central region splits into a number of regions and lumps of positive mean flow distortion arise. At this stage the central part of the disturbance the signal is too complex for any definite conclusion concerning the location of the maximum.

The evolution of the profile along the streamwise direction may be more meaningful than the analysis of the signal at a particular streamwise station, figure 13. The figure shows

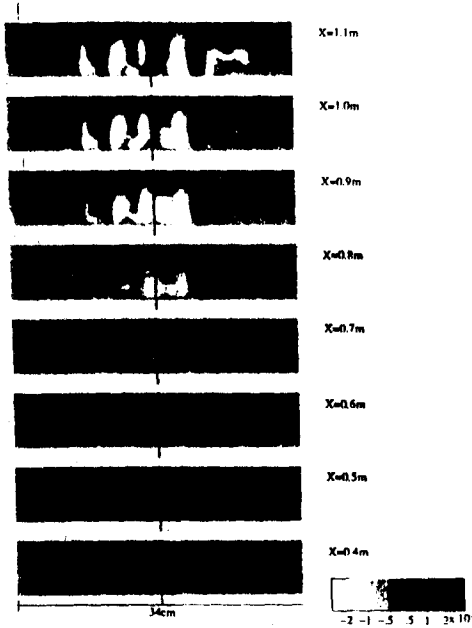

Figure 13: Evolution of the mean flow distortion.

how the disturbance field slowly evolves from a relatively simple structure into a much more complex one at x=1100mm.

An overall view of the transfer of momentum from the low velocity streaks to the high velocity streaks is given by the distribution of the displacement thickness variation over the entire disturbance field, figure 14. In this pic-

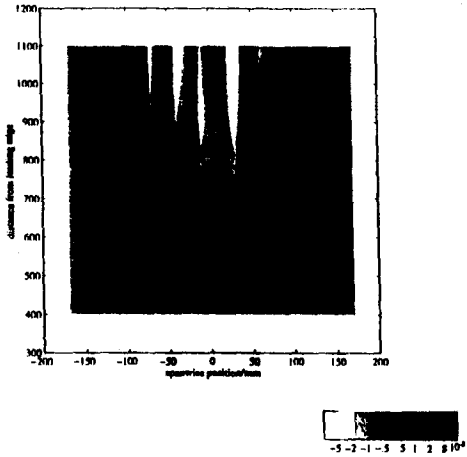

Figure 14: Distribution of the displacement thickness variation over the plate relative to displacement thickness of the Blasius profile.

ture the details of the complex distribution in the direction perpendicular to the wall are lost, and an averaged view of the distortions results. The figure shows a somewhat more symmetric pictures of the flow than that of figure 10. For the positive lateral regions the displacement thickness distribution indicates a structure similar to that suggested by figure 10. The central region, on the other hand, indicated that the central negative region splits into three regions separeted by two newly generated positive regions.

3 Conclusion and Discussion

The work studies the nonlinear evolution of wavetrains emanating from a point source in a flat plate boundary layer. The first interesting result was that the first indication of nonlinear behaviour was not a subharmonic signal, but a mean flow distortion that formed longi-

tudinal streaks. This mean flow distortion may have arisen from self interaction of the modes via the Reynolds stresses term, but this conjecture is yet unproven. Initially the mean flow distortion displayed a relativelly simple spanwise structure with a central region of negative mean flow distortion and two lateral regions of positive mean flow distortion. It appeared that the strength of the nonlinear interaction at this stage was stronger off the centerline of the flow. This might be linked to the fact that for some frequencies the three-dimensional wavetrains also display amplitude maxima off the centerline in the linear regime (Wiegand et al. 1995). This would be consistent with these being generated from the Reynolds stresses.

The structure of these distortions in the direction perpendicular to the wall was also investigated. Initially they resemble klebanoff modes with one amplitude peak at a position η between 1 and 2.

The relativelly simple structure gives rise to a fairly complicated flow field further downstream. The more complicated field appears to originate at a position close to the second branch. The more complicated structure arises in the central portion of the wavetrain, where the initial negative mean flow distortion was formed. There, regions of positive mean flow distortion arises and the profiles of the distortions do not display the Klebanoff mode shape. Despite the complexity, an overall view shown by the displacement thickeness variation over the plate, suggests that the central negative region splits into three. The positive mean flow distortion regions do not change considerably along the process, except in amplitude.

Streaks have also been observed in by pass transition. However, there the streaks tend to keep their spanwise spacing, as oppose to what is observed in the current experiment. Longitudinal streaks have been observed in turbulent flow. In same cases they appear to be a key ingredient of the mechanism of production of turbulence. It has also been shown that modulated waves give rise to transition at smaller amplitudes in comprison with plane wavetrains. It is possible that the modulation of the waves provide a short cut between the early wavelike behaviour and the vortical structures observed in turbulent flows. These conjecture is currently being investigated. The possibility that the initial mean flow distortion be generated from the self interaction of waves is also being investigated.

References

Breuer, K. S. & Haritonidis, J. H. (1990), 'The evolution of a localised disturbance in a laminar boundary layer - part 1 - weak disturbances', *J. Fluid Mech.* **220**, 569–594.

Breuer, K. S., Cohen, J. & Haritonidis, J. H. (1997), 'The late stages of transition induced by a low-amplitude wavepacket in a laminar boundary layer', *J. Fluid Mech.* **340**, 395–411.

Cohen, J. (1993), 'The initial evolution of a wave packet in a boundary layer', *Phys. Fluids* **6**(3), 1133–1143.

Cohen, J., Breuer, K. S. & Haritonidis, J. H. (1991), 'On the evolution of a wave packet in a laminar boundary layer', *J. Fluid Mech.* **225**, 575–606.

Corke, T. C. & Mangano, R. A. (1989), 'Resonant growth of three-dimensional modes in transitioning Blasius boundary layers', *J. Fluid Mech.* **209**, 93–150.

Elofsson, P. A. & Alfredsson, P. H. (1997), 'An experimental study of oblique transition in plane poiseuille flow'. (submitted to the J. Fluid Mech.).

Gaster, M. (1975), 'A theoretical model of a wave packet in the boundary layer on a flat plate', *Proc. R. Soc. London A* **347**, 271–289.

Gaster, M. (1978), The physical process causing breakdown to turbulence, *in*

'12th Naval Hydrodynamics Symposium', Washington.

Gaster, M. (1984), A non-linear transfer function description of wave growth in a boundary layer, *in* V. V. Kozlov, ed., 'Laminar-turbulent transition', IUTAM Symposium, IUTAM, Springer-Verlag, pp. 107–114.

Gaster, M. (1993), The origins of turbulence, *in* 'Proc. Conf. on New Approaches and Concepts in Turbulence', Birkhauser Basel, Switzerland.

Gaster, M. & Grant, I. (1975), 'An experimental investigation of the formation and development of a wavepacket in a laminar boundary layer', *Proc. Royal Soc. of London A* **347**, 253–269.

Henningson, D. S., Lundbladh, A. & Johansson, A. V. (1993), 'A mechanism for bypass transition from localized disturbances in wall-bounded shear flows', *J. Fluid Mech.* **250**, 169–207.

Herbert, T. (1988), 'Secondary instability of boundary layers', *Ann. Rev. Fluid Mech.* **20**, 487–526.

Kachanov, Y. S. (1985), Development of spatial wave packets in boundary layer, *in* V. V. Kozlov, ed., 'Laminar-turbulent transition', springer-Verlag, pp. 115–123.

Kachanov, Y. S. (1987), 'On the resonant nature of the breakdown of a laminar boundary layer', *J. Fluid Mech.* **184**, 43–74.

Kachanov, Y. S. (1994), 'Physical mechanisms of laminar boundary layer transition', *Ann. Rev. Fluid Mech.* **26**, 411–482.

Kachanov, Y. S. & Levchenko, V. Y. (1984), 'The resonant interaction of disturbances at laminar-turbulent transition in a boundary layer', *J. Fluid Mech.* **138**, 209–247.

Mack, L. M. (1985), Instability wave patterns from harmonic point sources and line sources in laminar boundary layers, *in* V. V. Kozlov, ed., 'Laminar-turbulent transition', springer-Verlag, pp. 125–132.

Medeiros,. M. A. F. (1996), The nonlinear behaviour of modulated Tollmien-Schlichting waves, PhD thesis, Cambridge University - UK.

Medeiros, M. A. F. (1997*a*), Laminar-turbulent transition: the nonlinear evolution of three-dimensional wavetrains in a laminar boundary layer, *in* 'Proc. of the XIV Brazilian Congress of Mechanical Engineering', Bauru. in CD-ROM.

Medeiros, M. A. F. (1997*b*), 'The nonlinear evolution of wavepackets in a laminar boundary layers: Part i'. (submitted to the J. Fluid Mech.).

Medeiros, M. A. F. (1997*c*), 'The nonlinear evolution of wavepackets in a laminar boundary layers: Part ii'. (submitted to the J. Fluid Mech.).

Medeiros, M. A. F. (1997*d*), Nonlinear mean-flow distortion caused by a wavetrain emanating from a harmonic point source in a flat-plate boundary layer, *in* 'EUROMEC colloquium on stability and transition of boundary layer flows', Stuttgart.

Medeiros, M. A. F. & Gaster, M. (1994), The nonlinear behaviour of modulated Tollmien-Schlichting waves: experiments and computations, *in* 'Second EUROMEC Conference', Warsaw – Poland.

Medeiros, M. A. F. & Gaster, M. (1995), The nonlinear behaviour of modulated Tollmien-Schlichting waves, *in* 'IUTAM Conference on nonlinear instability and transition in tri-dimensional boundary layers', Manchester, pp. 197–206.

Medeiros, M. A. F. & Gaster, M. (1996), 3d structures of nonlinear wavepackets generated from different excitations in a boundary layer, *in* 'EUROMEC colloquium on dynamics of localised disturbances in engineering flows', Kalrsruhe.

Seifert, A. (1990), On the interaction of small amplitude disturbances emanating from discrete points in a Blasius boundary layer, PhD thesis, Tel-Aviv University.

Seifert, A. & Wygnanski, I. (1991), On the interaction of wave trains emanating from point sources in a Blasius boundary layer, *in* 'Proc. Conf. on Boundary Layer Transition and Control', The Royal Aeronautical Society, Cambridge, pp. 7.1–7.13.

Shaikh, F. N. (1993), Turbulent spot in a transitional boundary layer, PhD thesis, Cambridge University.

Shaikh, F. N. (1997), 'Investigation of transition to turbulence using white noise excitation and local analysis techniques', *J. Fluid Mech.* **348**, 29–83.

Shaikh, F. N. & Gaster, M. (1994), 'The nonlinear evolution of modulated waves in a boundary layer', *Journal of Engineering Mathematics* **28**, 55–71.

Wiegand, T., Bestek, H., Wagner, S. & Fasel, H. (1995), Experiments on a wave train emanating from a point source in a laminar boundary layer, *in* '26th AIAA Fluid Dynamics Conference', San Diego, CA.

ANÁLISE DE TRANSIÇÃO DA CAMADA LIMITE SOBRE A PÁ DE UM MODELO DE TURBINA EÓLICA DE EIXO HORIZONTAL

ANALYSIS OF BOUNDARY LAYER TRANSITION ON A BLADE OF HORIZONTAL AXIS WIND TURBINE MODEL

Jaqueline B. do Nascimento

Fernando Martini Catalano

Universidade de São Paulo – USP

Escola de Engenharia de São Carlos – EESC

Departamento de Engenharia Mecânica

Laboratório de Aeronaves

Av. Dr. Carlos Botelho, 1465

CEP 13560-250 - São Carlos - SP - Brasil

e-mail:jaquelin@sc.usp.br

Abstract

This work presents an aerodynamic analysis of boundary layer transition on blades of a horizontal axis wind turbine model. The techniques used were a mixture of naphthaline and trichloride sprayed on surfaces of blade. The tests were performed with a blade in and out of the wind tunnel (stopped and rotating, respectively), in the Aircraft Laboratory of the University of São Paulo. The visualization tests present qualitative and quantitative informations about boundary layer transition phenomenon upon the blade. The results obtained show that the boundary layer transition took place before the inner of the regions blade, where the after part of the airfoils are concavet, showing the influence of airfoil type on transition position.

Key-words: boundary layer transition, airfoil, wind turbines, visualization.

Resumo

Este trabalho apresenta uma análise aerodinâmica do fenômeno de transição de camada limite, sobre as pás de um modelo de turbina eólica de eixo horizontal. A metodologia adotada utiliza uma técnica de visualização por sublimação (mistura de naftaleno com um diluente), cuja mistura é pulverizada sobre todas as superfícies das pás (intradorso e extradorso). Os ensaios foram realizados com a pá parada, dentro da câmara de ensaio do túnel de vento do Laboratório de Aeronaves da Universidade de São Paulo; bem como com o rotor girando livremente. O ensaio de visualização apresenta informações não apenas qualitativas, mas também quantitativas sobre o fenômeno de transição do escoamento sobre a pá. Os resultados obtidos mostram que a transição da camada limite ocorreu mais cedo na região da pá próxima a raiz, onde os perfis aerodinâmicos possuem concavidade na parte traseira, comprovando a influência do tipo de perfil na posição da transição.

Palavras-chave: transição da camada limite, aerofólios, turbinas eólicas, visualização.

Introdução

O estudo aerodinâmico de turbinas eólicas tem, nos últimos tempos, despertado o interesse por parte dos pesquisadores do mundo inteiro. A análise aerodinâmica dessas máquinas envolve parâmetros variados. Entre estes, a escolha do perfil adequado para o uso em turbinas eólicas é de grande importância. Com o desenvolvimento de perfis específicos para este tipo de uso, que surgiu com o conhecimento adquirido na área aeronáutica, vários métodos de análise têm sido desenvolvidos, os quais tem contribuido muito para o desenvolvimento científico e tecnológico das turbinas eólicas de eixo horizontal.

Björck (1989) apresenta um estudo sobre o desenvolvimento de novos aerofólios no Instituto de Pesquisa Aeronáutica da Suécia, e como ponto de partida do estudo, foram colocadas as características desejáveis de um aerofólio, as quais podem ser divididas em propriedades estruturais e propriedades aerodinâmicas. Estruturalmente, a espessura e a geometria dos aerofólios são os parâmetros mais importantes. Já as propriedades aeodinâmicas consideradas são: relação sustentação-arrasto, coeficiente

de sustentação de projeto, coeficiente de sustentação máximo e comportamento do estol, baixa sensibilidade à diminuição do desempenho devido a rugosidade do bordo de ataque e momento de 'pitching'.

Este trabalho, desenvolvido no Laboratório de Aeronaves da Universidade de São Paulo, apresenta um método de análise aerodinâmica sobre a pá parada (dentro da câmera de ensaio do túnel de vento) e com a pá girando (rotor girando livremente na saída do túnel), cujo objetivo foi estudar o fenômeno de transição da camada limite. Os perfis adotados na construção da pá foram FFA-W1-xxx (com espessura variada de 27.1% a 12.8%c e são perfis específicos para turbinas eólicas.

O Estudo Aerodinâmico e a Visualização da Camada Limite

O estudo aerodinâmico das pás de um rotor eólico concentra-se basicamente no comportamento da camada limite sobre estas, ou seja, no comportamento do fluxo que escoa em região limitada ao redor das pás. Isto, de um modo geral, envolve esforços para que o desempenho aerodinâmico seja o maior possível, obtendo-se um aumento no desempenho total do sistema.

Os métodos de visualização de escoamento são importantes não apenas para apresentar uma visão qualitativa clara do fenômeno do escoamento, mas também, em muitos casos, produzir informação quantitativa. Existem uma série de técnicas para indicação da posição da transição de escoamento laminar para turbulento na camada limite do corpo, e estes dependem do comportamento físico ou químico do depósito localizado na superfície do corpo (Pankhust & Holder,1968).

Existe uma série de métodos para indicação da posição de transição de fluxo laminar para turbulento na camada limite de um corpo, dentre os quais destaca-se o método de sublimação, que foi adotado por Nascimento (1998a). Esta consiste, basicamente, na pulverização de uma mistura de nafataleno (por exemplo) com um líquido volátil, sobre a superfície da pá, de modo que o depósito

resultante torna-se sensivelmente aparente e podem, desta forma, serem registrados por meio de imagens fotográficas (Figura 1).

Os perfis adotados e suas características aerodinâmicas

Os perfis adotados na pá estudada neste trabalho (W1-271, W1-242, W1-211, W1-182, W1-152 e W1-128) foram desenvolvidos pelo Instituto de Pesquisa Aeronáutica da Suécia (The Aeronautical Research Institute of Sweden, FFA)(Björck, 1989).

Segundo (Björck, 1989), o desenvolvimento de novos perfis na FFA foi uma tentativa de se obter aerofólios com boas características tanto em fluxo turbulento, como em fluxo laminar. Este,, realizando ensaio de visualização em túnel de vento, através de tufos de lã, sobre o aerofólio W1-152 e W1-128 (espessura de 15.2% e 12.8% da corda, respectivamente), verificou que, na lateral de pressão, apresentaram um comportamento completamente laminar. Já na lateral de sucção apresentaram um comportamento laminar numa faixa de 40% do fluxo sobre a superície.Uma outra observação importante quanto a estes aerofólios é o seu desempenho em alto Número de Reynolds, uma vez que, à medida que o número de Reynolds aumenta, aumenta também a margem de separação.

Método de Visualização de Escoamento por meio da Técnica de Sublimação

Foi realizado um ensaio de visualização de escoamento sobre a pá de um modelo de turbina eólica, projetado e construído no Laboratório de Aeronaves da Universidade de São Paulo. A pá ensaiada tem 0.9m de raio (considerando o diâmetro total do rotor), mas o comprimento de raio adotado no ensaio foi de 0.84m, o qual corresponde o comprimento entre a primeira estação (aerofólio W!-271) e a última (aerofólio W1-128).

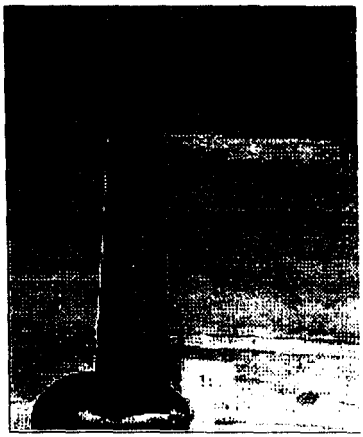

Figura 1 – Imagem da pá dentro da câmara de ensaio do túnel de vento (ângulo de ataque de 16 graus), após o registro da transição da camada limite por meio do método de sublimação com naftaleno.

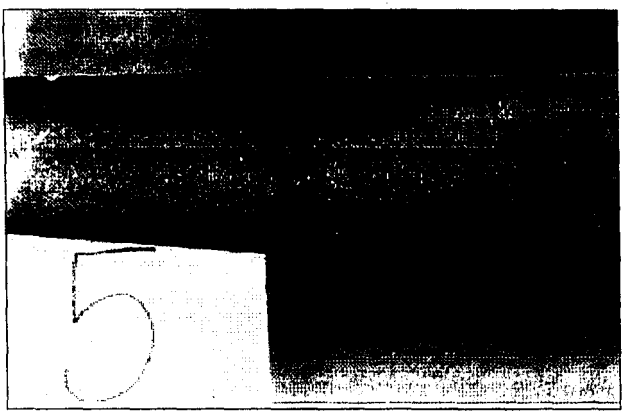

Figura 2 – Imagem (aproximada) da pá na saída do túnel de vento (ângulo de passo de 5 graus), após o registro da transição da camada limite por meio da técnica de sublimação , com o registro da transição da camada limite.

O ensaio foi dividido basicamente em duas etapas, ambas com Número de Reynolds de 200000. A primeira etapa consistiu no ensaio da pá parada dentro da câmara de ensaio do túnel de vento, com ângulo de ataque (α) variando de 0 a 16 graus. A segunda etapa consistiu no ensaio com o rotor girando, utilizando o fluxo na saída do túnel de vento, na região próximo ao ventilador. Para este ensaio, o túnel de vento recebeu alguns cuidados técnicos quanto a uniformização de seu fluxo, uma vez que este apresentava-se bastante turbulento e rotacional. Desta forma, foi colocada uma tela próxima ao ventilador e uma colméia na saída do túnel como meio de uniformizar o fluxo de saída naquela seção. Quanto a faixa de ângulo de ataque (α) do ensaio, este foi calculado considerando o ângulo de passo (β – ângulo de montagem da pá no cubo do rotor). Uma vez fixado o ângulo de passo da pá, calculou-se o ângulo de ataque equivalente. Assim, foi possível estabelecer uma comparação entre os dados levantados com a pá parada e com as pás do rotor em funcionamento. Deve-se ressaltar que este ângulo de ataque, quando o rotor está em funcionamento, varia de acordo com a posição radial.

O material utilizado para visualização do escoamento foi uma mistura de naftaleno com um solvente (tricloroetano). Esta mistura foi pulverizada sobre toda a superfície da pá, tanto no intradorso como no extradorso, e após a sublimação desta, considerando o efeito do fluxo sobre a pá, registrou-se imagens (Figuras 1 e 2) que possibilitaram a visualização da região de ocorrência da transição, da camada limite laminar para turbulenta. As imagens registradas foram transpostas em curvas a fim de fornecerem a posição (em percentual da corda, x/c), da transição da camada limite, ao longo de todo a envergadura (percentuais do raio, r/R), em cada ângulo de ataque.

Resultados e Discussão

Conforme citado anteriormente, o ensaio de visualização de escoamento com o rotor girando, na saída do túnel de vento, foi feito variando-se o ângulo de passo e calculando-se o ângulo de ataque equivalente. Deste modo, foi possível analisar o comportamento do fluxo (transição da camada limite), escoando sobre a superfície da pá, comparando-o com o caso parado.

Enquanto a faixa de ângulos de ataque no ensaio com a pá parada foi de 0 a 16 graus, no caso girando, esta faixa foi mais ampla, de –6 graus (na ponta) a 14 graus (na raiz), o que comprova que que as turbinas eólicas de eixo horizontal trabalham em ângulos de ataques altos nas regiões próximas à raiz.

Os gráficos apresentados nas Figuras a seguir apresentam as curvas representativas do caso parado, enquanto que para o caso do rotor girando são apresentados pontos indicativos do ângulo de ataque, corresponde a situação da pá parada como forma de manter uma relação para análise.

Considerando inicialmente a posição a 10% do raio da pá, conforme apresentado na FIGURA 3, onde o ângulo de ataque da pá girando variou entre 11 e 14 graus, observou-se que a transição ocorreu antes paro o caso parado do que no caso como rotor. A mesma tendência pode ser observada para o caso com o rotor girando, a 20% do raio, conforme apresentado na FIGURA 4.

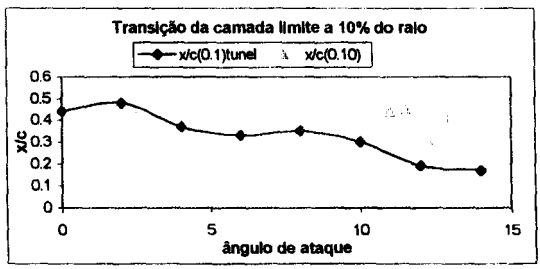

Figura 3 - – Local da transição da camada limite em relação à corda, a 10% do raio da pá.

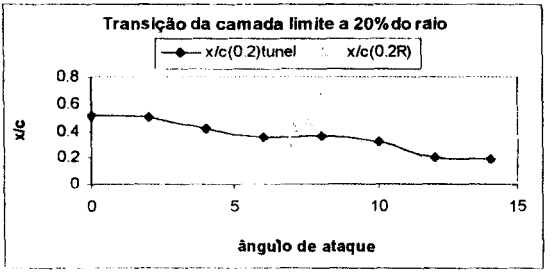

Figura 4 – Local da transição da camada limite em relação à corda, a 20% do raio da pá.

Apesar de os efeitos da rotação serem maiores na ponta da pá, observa-se de resultados anteriores (Wood, 1991) que o estol é amenizado na parte da pá próxima à raiz. O resultado das FIGURAS 3 e 4 apontam para uma extensão maior de camada limite laminar nesta região, o que pode confirmar o atraso na separação da parte turbulenta, pois a camada limite laminar só se sustentará se o gradiente de pressão for favorável. Este gradiente favorável de pressão pode ter sido resultado da rotação. Deve-se ressaltar que os testes foram restritos (pequena variação de ângulo de ataque) e que não foram utilizadas técnicas de visualização da separação da camada limite turbulenta. Além disso seria necessário o levantamento da distribuição de pressão ao longo da corda para observar o gradiente de pressão. Resultados anteriores confirmam que, com a pá girando, o gradiente de pressão é aliviado na raiz.

Até 20% do raio, conforme observado anteriormente, a pá, no caso em que o rotor estava girando, apresentou uma faixa mais ampla de camada limite laminar a que pode ser, explicado pelo fato de os efeitos tridimensionais e de rotação são menores na raiz do que na ponta.

Prosseguindo com a análise da transição ao longo de todo o raio da pá, observou-se que em torno de 30 a 40% do raio a tendência anterior começou a se inverter, conforme pode ser visto nas FIGURAS 5 e 6.

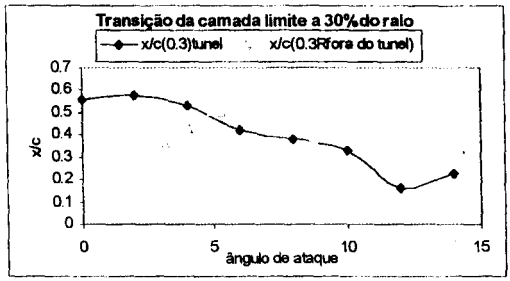

Figura 5 – Local da transição da camada limite em relação à corda, a 30% do raio da pá.

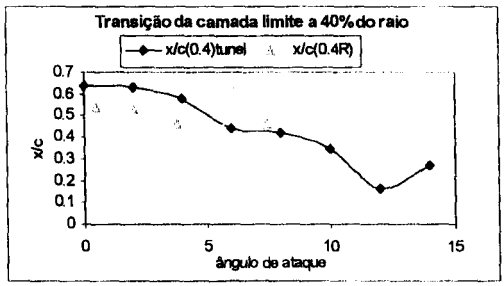

Figura 6 – Local da transição da camada limite em relação à corda, a 40% do raio da pá.

Para r/R maiores, com a pá girando, em ângulos de ataques menores, a transição ocorreu em posições da corda inferiores, comparados ao caso da pá parada dentro do túnel (FIGURA 6). Em posições médias da pá, em torno de 40 e 50% do raio (FIGURAS 6 e 7),esta inversão é mais evidente, uma vez que, a partir desta região, os efeitos são mais intensos, promovendo desta forma, transição da camada limite laminar para turbulenta, mais cedo.

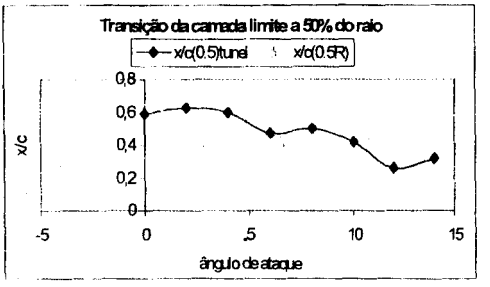

Figura 7 – Local da transição da camada limite em relação à corda, a 50% do raio da pá.

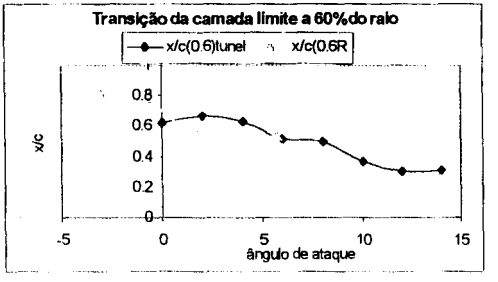

Figura 8 – Local da transição da camada limite em relação à corda, a 60% do raio da pá.

Além da região média da pá, quando os ângulos de ataque passam a ser negativos, a tendência de transição ocorrer mais cedo do que no caso parado continuou, conforme mostram as Figuras 8, 9 e 10.

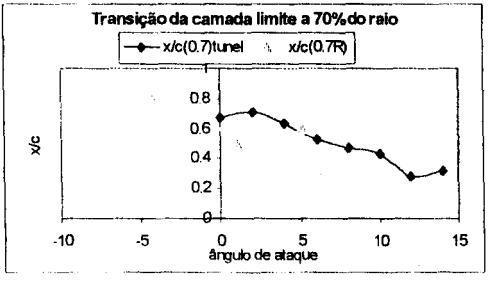

Figura 9 – Local da transição da camada limite em relação à corda, a 70% do raio da pá.

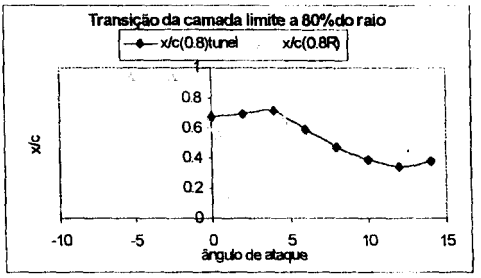

Figura 10 – Local da transição da camada limite em relação à corda, a 80% do raio da pá.

Observou-se também, ao longo do experimento, o efeito de alguns grãos maiores de nafataleno que induziram a transição da camada limite mais cedo, conforme mostra a Figura 2.

Conclusões

Observou-se que o escoamento sobre o perfil apresenta uma extensão laminar bastante considerável. Com relação ao perfil aerodinâmico, nota-se que na região onde este possui concavidade na parte traseira, devido ao gradiente de pressão adverso nesta região, a transição ocorreu mais cedo. Este efeito é ainda maior nesta região de concavidade, para pequenos ângulos de ataque, podendo, inclusive ocorrer separação. Por esta razão é que que se utilizam, geralmente, estes tipos de perfis em regiões da pá que operam a altos ângulos de ataque e baixa velocidade. Nota-se ainda que o tipo de perfil influencia sobremaneira, na posição da transição; uma asa com um mesmo perfil ao longo da envergadura tenderia a apresentar uma faixa constante de escoamento laminar.

Referências Bibliográficas

Anderson Jr., J. D. (1991). Fundamentals of Aerodynamics. 2ª edição, McGraw-Hill, New York.

Björck, A. (1989). Airfoil design for variable RPM horizontal axis wind turbines. Proceedings of AMSTERDAM EWEC'89.

Björck, A. (1990). Coordinates and Calculations for the FFA-W1-xxx, FFA-W2-xxx and FFA-W3-xxx series of airfoils for horizontal axis wind turbines. FFA TN. Stockholm.

Hill, D. C. & Garrad, A. D. (1989). Design of airfoils for wind turbine use. Wind energy: Technology and Implementation. Proceedings of Amsterdam EWEC'89. Garrad Hassan and Partners Bristol.

Nascimento, J. B. and Catalano, F. M. (1998[a]) (submetido). "Ensaio de Visualização de Fluxo sobre as Pás de um Modelo de Turbina Eólica de Eixo Horizontal". Octavo Congreso Chileno de Ingenieríí Mecánica, Santiago, Chile.

Nascimento, J. B. and Catalano, F. M. (1998). "Estudo Aerodinâmico do Efeito da Rugosidade no Desempenho de um Modelo de Turbina Eólica de Eixo Horizontal". Tese de Doutorado, EESC-USP, São Carlos.

Pankhurst, R. S. and Holder, D.W. (1968). Wind-tunnel technique (an account of experimental methods in low- and high speed wind tunnels). Sir Isaac Pitman&Sons Ltd., London.

Schlichting, H., "Boundary Layer Theory", 7th ed., McGraw-Hill Book Company, New York, 1974.

Tangler, J. L. & Somers, D. M. (1985). Advanced airfoils for HAWTs. Proceedings Wing Power'85 Conference, SERI/CP-217-2902, Washington, DC. American Wind Energy Association, pp. 45-51.

Wood, D. H. (1991). "A three-dimensional analysis of stall-delay on a horizontal axis turbine". Journal of Wind Engineering and Industrial Aerodynamics, 37, 1-14, Amsterdam.

Uma Solução para Turbulência Gerada por Grades Oscilantes

A Theoretical Solution for Turbulence Generated by Oscillating Grids

Harry Edmar Schulz e Fazal Hussain Chaudhry
Laboratório de Hidráulica Ambiental-CRHEA
Departamento de Hidráulica e Saneamento
Escola de Engenharia de São Carlos-Universidade de São Paulo
C.P. 359, 13560-270, São Carlos, S.P., Brasil.
(Trabalho desenvolvido no Institut für Hydromechanik, Universität Karlsruhe, Alemanha)

Abstract

The k-ε model is used to quantify the turbulent field generated by oscillating grids for the situation of stationary turbulence. A theoretical solution for a single oscillating grid is obtained, which superimposes well with experimental data from other sources. Further, a general solution is furnished, which is applied to the case of two oscillating grids. The relevant phenomena in this kind of flow are the diffusion and the dissipation of the turbulent kinetic energy. Exact solutions for the power consumption are furnished, as well as series solutions for the spatial behaviour of the turbulent kinetic energy and the energy dissipation rate. The series solutions show to be adequate to study the situation of two oscillating grids.
***Keywords**: grid turbulence, diffusion-dissipation in turbulence, k-ε model, isotropic turbulence.*

Resumo

O problema do equacionamento do campo turbulento gerado por grades ou grelhas oscilantes é abordado a partir do uso do modelo k-ε. As simplificações possíveis neste tipo de escoamento permitem propor uma solução teórica simples para o caso de uma única grelha oscilante imersa em um fluido. Esta solução sobrepõe-se bem a dados experimentais encontrados na literatura da área. A turbulência para regiões não-próximas das grelhas envolve os processos de difusão e dissipação da energia cinética turbulenta, sem haver advecção ou produção desta energia. Esta característica é utilizada para explorar o uso do equacionamento básico k-ε também para uma situação geral, apresentando-se equações que permitem averiguar mais imediatamente a forma esperada para os perfis da energia cinética turbulenta, além de permitir calcular a potência dissipada como função de valores limites da energia cinética turbulenta. O equacionamento é utilizado, então, para obter a solução para o caso de duas grelhas oscilantes.
***Palavras-chave**: turbulência gerada por grelhas, difusão-dissipação em turbulência, modelo k-ε, turbulência isotrópica.*

Introdução

Textos clássicos de turbulência, como Hinze (1959), apresentam formas de abordagem para resolver o problema de turbulência gerada em um escoamento a jusante de uma grelha, esta colocada

perpendicularmente à direção preferencial do escoamento. O uso da hipótese de congelamento de Taylor e da teoria da semelhança de von Karman conduzem a resultados observados em laboratório, sendo, portanto, um caso clássico de solução para escoamentos turbulentos que podem ser denominados de "simples". Este caso clássico é resolvido no contexto da turbulência isotrópica. É, contudo, interessante observar que outro escoamento de geometria razoavelmente simples envolvendo grelhas, não é tão largamente discutido na literatura da área, no sentido de divulgar amplamente uma solução teórica. É o caso do escoamento gerado por grelhas ou grades oscilantes. Evidentemente o termo"escoamento", no caso de grelhas oscilantes, está vinculado já ao campo turbulento em si, uma vez que não existe um escoamento médio que venha a se estabelecer em uma direção preferencial, mesmo considerando diferentes "compartimentos" ou regiões menores no interior do fluido em estudo. Todas as escalas de velocidade são decadentes na direção normal à grade, não havendo uma velocidade de referência conhecida *a priori*. O problema é difusivo-dissipativo e aí reside a dificuldade de sua resolução. Para os termos difusivos devem ser feitas hipóteses simplificadoras que conduzam a uma solução viável.

Algumas propostas de solução, visando descrever o comportamento de diferentes variáveis, são encontradas na literatura, sempre associadas a hipóteses que buscam vínculo com a realidade física (Bouvard e Dumas, 1967, Thompson e Turner, 1975, Hopfinger e Toly, 1976, Nokes, 1988, De Silva e Fernando, 1994, Voropayev e Fernando, 1996, Srdic et al., 1996). No presente trabalho também é apresentada uma proposta de solução, a qual foi elaborada ainda no contexto da turbulência isotrópica, utilizando aproximações vinculadas à hipótese de Boussinesq e ao modelo k-ε. Esta proposta reproduz de forma satisfatória o comportamento observado para a energia cinética turbulenta e para a taxa de dissipação de energia em uma região do escoamento gerado por uma grelha oscilante. Para o caso de duas grelhas oscilantes, o equacionamento permite obter uma expressão para o cálculo da potência dissipada na região entre as grelhas e ainda sugerir soluções por expansão em série de potências, para as variáveis k e ε.

O Caso da Advecção da Turbulência

Visando justificar algumas hipóteses adotadas no caso da difusão-dissipação, apresenta-se aqui, inicialmente, a solução usual do problema de advecção da turbulência a partir da equação da energia cinética turbulenta. A equação de conservação da energia cinética turbulenta, em sua forma completa, é geralmente apresentada como:

$$\frac{\partial k}{\partial t} + \overline{U_i}\frac{\partial k}{\partial x_i} = -\frac{\partial}{\partial x_i}\left[\overline{u_i\left(\frac{u_i u_j}{2} + \frac{p}{\rho}\right)}\right] - \overline{u_i u_j}\frac{\partial \overline{U_i}}{\partial x_j} - \nu\overline{\frac{\partial u_i}{\partial x_j}\frac{\partial u_i}{\partial x_j}} \qquad (1)$$

$$\varepsilon = \nu\overline{\frac{\partial u_i}{\partial x_j}\frac{\partial u_i}{\partial x_j}} \qquad (2)$$

k é a energia cinética turbulenta, ε é a taxa de dissipação desta energia, U_i é a velocidade média na direção i, u_i é a flutuação de velocidade na direção i, ν é a viscosidade cinemática e p é a flutuação de pressão. Sem variações temporais e havendo apenas transferência por advecção, esta equação assume a forma:

$$\overline{U_i}\frac{\partial k}{\partial x_i} = -\varepsilon \qquad (3)$$

As observações mostram que o número de Reynolds da turbulência (escala de velocidade turbulenta multiplicada pela macro-escala de turbulência, sendo este produto dividido pela viscosidade cinemática) é constante para uma região do escoamento a jusante de grelhas colocadas transversalmente ao mesmo. Desta forma, uma vez que a viscosidade cinemática turbulenta também é definida como o produto entre uma escala de velocidade da turbulência (em turbulência isotrópica, a raiz quadrada da média quadrática das flutuações de velocidade, aqui brevemente referida como intensidade turbulenta) e uma escala de turbulência (a macro-escala), vemos que esta viscosidade deve ser constante. Utilizando o modelo k-ε para descrever a viscosidade turbulenta, resulta:

$$\nu_t = C_\mu \frac{k^2}{\varepsilon} \tag{4}$$

$$\frac{\partial k}{\partial x} = -\frac{C_\mu}{\nu_t \overline{U}_i} k^2 \tag{5}$$

C_μ é uma constante de proporcionalidade. O termo multiplicativo no segundo membro é constante, se considerarmos a velocidade constante. A solução para a equação diferencial 1.5 é:

$$k = \frac{1}{\frac{C_\mu}{\nu_t \overline{U}_i} x + \frac{1}{k_0}} \qquad \text{ou} \qquad k = \frac{a}{x + x_0} \tag{6a}$$

$$\varepsilon = \frac{C_\mu / \nu_t}{\left(\frac{C_\mu}{\nu_t \overline{U}_i} x + \frac{1}{k_0}\right)^2} \qquad \text{ou} \qquad \varepsilon = \frac{b}{\left(x + x_0\right)^2} \tag{6b}$$

a, b e x_0 são constantes. As equações 6a e 6b são confirmadas experimentalmente, sendo as constantes relacionadas, ainda, com características geométricas das grelhas utilizadas. (Hinze 1959, Monin e Yaglom, 1979, 1981). A equação 6b satisfaz também a equação diferencial para ε, geralmente apresentada no modelo k-ε. Para o caso de advecção, esta equação assume a forma:

$$\frac{\partial \varepsilon}{\partial x_i} = -\frac{C_2}{\overline{U}_i} \frac{\varepsilon^2}{k} \tag{7}$$

Utilizando as equações 6b e 7 obtém-se o resultado C_2=2, que é bastante próximo do resultado 1,92 geralmente utilizado (ver Eiger e Shen., 1997, por exemplo).

O Caso de Difusão-Dissipação da Turbulência para uma Grelha Oscilante

Para o estudo da evolução da energia cinética turbulenta em processos difusivos, unidimensionais, novamente parte-se das equações 1 e 2. Para escoamento estacionário e admitindo a situação de grelha oscilante em fluido em repouso, a equação se reduz a:

$$\frac{\partial}{\partial x_i}\left[\overline{u_i\left(\frac{u_i u_j}{2} + \frac{p}{\rho}\right)}\right] = -\nu \overline{\frac{\partial u_i}{\partial x_j} \frac{\partial u_i}{\partial x_j}} \tag{8}$$

O termo entre colchetes, sem equacionamento definitivo, é usualmente substituído pelo produto do coeficiente de Boussinesq (viscosidade turbulenta) multiplicado pelo gradiente da energia cinética turbulenta e por uma constante de proporcionalidade (σ_k). Tem-se, então:

$$\frac{\partial}{\partial x}\left(\frac{\nu_t}{\sigma_k}\frac{\partial k}{\partial x}\right) = \varepsilon \tag{9}$$

O sucesso em representar o campo turbulento para o transporte advectivo com número de Reynolds constante (viscosidade turbulenta constante) induz que o mesmo procedimento seja adotado para o transporte difusivo. Assim, a equação 9 passa ser escrita como:

$$\frac{\nu_t}{\sigma_k}\frac{\partial}{\partial x}\left(\frac{\partial k}{\partial x}\right) = \varepsilon \tag{10}$$

Com a definição 4 para a viscosidade turbulenta tem-se:

$$\frac{\partial}{\partial x}\left(\frac{\partial k}{\partial x}\right) = \theta_1 \, k^2 \qquad \theta_1 = \frac{C_\mu \sigma_k}{\nu_t^2} \tag{11}$$

Uma solução explícita para a equação não-linear 11 é:

$$k = \frac{\left(\frac{6}{\theta_1}\right)}{\left(x+\theta_2\right)^2} \tag{12}$$

θ_2 é uma constante de integração. Para a taxa de dissipação de energia obtém-se, a partir das equações 4 e 12:

$$\varepsilon = \frac{\frac{C_\mu}{\nu_t}\left(\frac{36}{\theta_1^2}\right)}{\left(x+\theta_2\right)^4} \tag{13}$$

Para grandes distâncias da origem (centro de oscilação da grelha), a energia cinética turbulenta segue uma lei de decaimento com a potência -2 da distância, enquanto que a taxa de dissipação de energia segue uma lei de decaimento com a potência -4 da distância. As figuras 1 e 2, adaptadas de Matsunaga et al. (1991), mostram resultados experimentais (convenientemente normalizados e indicados, devido a esta normalização, com "*") que confirmam as tendências previstas para uma região do escoamento. A linha fina na figura 2 foi construída utilizando a equação 14, com as constantes nela indicadas.

$$\varepsilon^* = \frac{0{,}146}{\left(x^* + 0{,}550\right)^4} \tag{14}$$

Convém frisar que as constantes utilizadas não pretendem ser constantes universais. A equação 13 satisfaz também a equação diferencial para ε, geralmente apresentada no modelo k-ε. Para o caso de difusão-dissipação, esta equação assume a forma:

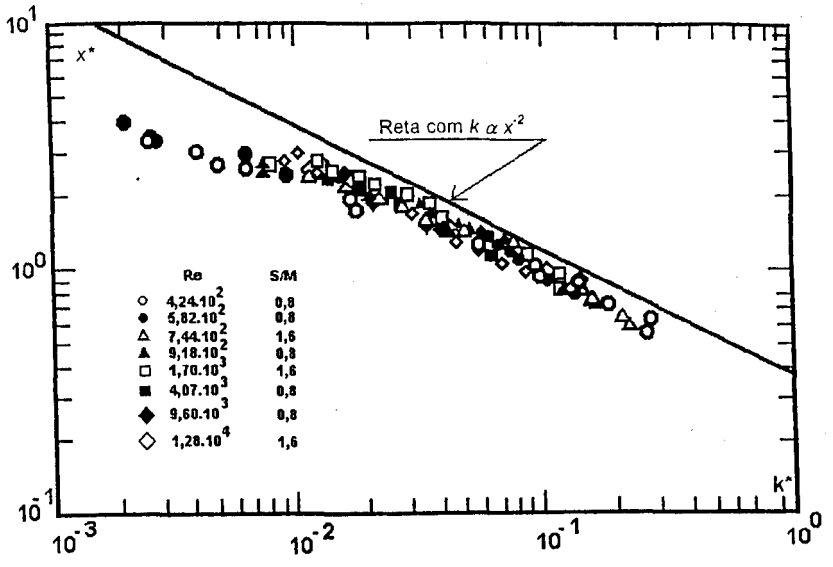

Figura 1: Dados de energia cinética turbulenta (normalizada k^*) de Matsunaga et al. (1991) em função da distância ao centro de oscilação da grelha (normalizado x^*). Observa-se a região com o expoente -2 da distância. S é a amplitude de oscilação, M é a largura da malha quadrada, Re é o número de Reynolds calculado como $Re=(S^2f)/v$, onde f é a freqüência de oscilação.

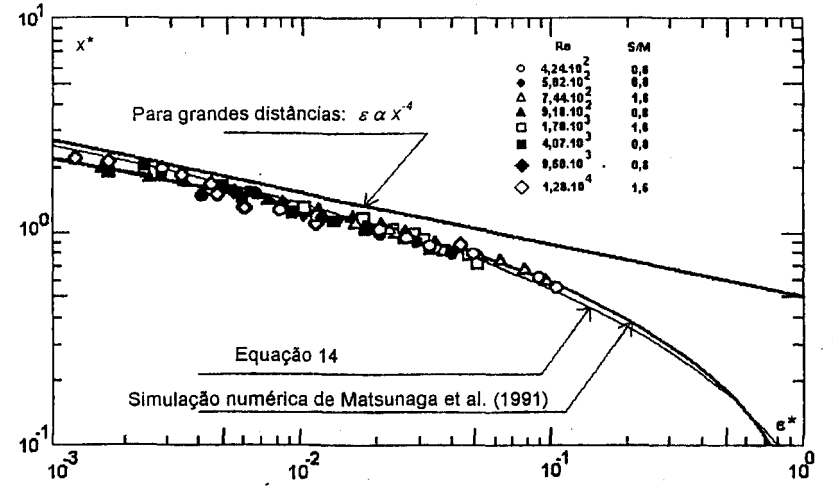

Figura 2: Dados de taxa de dissipação de energia (normalizada ε^*). de Matsunaga et al. (1991) em função da distância ao centro de oscilação da grelha. São comparados os dados experimentais, a tendência para grandes distâncias (x^{*-4}), a equação 14 e o resultado numérico de Matsunaga et al. (1991).

$$\frac{\partial}{\partial x}\left(\frac{\nu_t}{\sigma_\varepsilon}\frac{\partial \varepsilon}{\partial x}\right) = C_2\frac{\varepsilon^2}{k} \qquad (15)$$

σ_ε e C_2 são constantes. O uso desta equação, em conjunto com a solução 13, mostra a validade desta última e produz ainda uma relação interessante entre as diferentes "constantes" do modelo k-ε. Tem-se:

$$\frac{10}{3} = \frac{C_2\,\sigma_\varepsilon}{\sigma_k} \,. \qquad (16)$$

A equação 16 deve ser satisfeita para os valores "universais" das constantes envolvidas que são encontrados na literatura. Utilizando os valores de Matsunaga et al. (1991), tem-se, para o segundo membro, o valor 2,50. Já os valores apresentados por Eiger e Shen (1997), produzem o resultado 1.92. Ambos os resultados não coincidem com o valor 3,33 sugerido pelo primeiro membro, mas podem ser admitidos satisfatórios, se considerarmos a sua ordem de grandeza.

O Caso Geral de Difusão-Dissipação da Turbulência

Uma equação governante semelhante à equação 10 já foi apresentada na literatura da área, para grelhas oscilantes, por Bouvard e Dumas (1967), seguindo argumentos diferentes daqueles aqui apresentados. É interessante mencionar que esses autores não fornecem a solução explícita, mas comentam que a equação tem solução, que pode ser obtida com a aplicação dos procedimentos usuais para as equações elípticas. Posteriormente, Thompson e Turner (1975) apresentam um modelo de decaimento espacial que se fundamenta no decaimento temporal proposto por Batchelor e obtém uma equação diferencial de primeira ordem, que conduz também a uma expressão na forma de potência da distância, porém sem a presença da origem virtual representada pela constante no denominador. Os procedimentos seguidos parecem suficientemente saudáveis para interpretar as características turbulentas de escoamentos gerados por uma única grelha oscilante. Neste caso, tanto o modelo de primeira ordem de Thompson e Turner (1975) como o modelo de segunda ordem aqui apresentado ou aquele de Bouvard e Dumas (1967) poderiam ser utilizados. Isto porque o modo como os modelos foram desenvolvidos conduz sempre a uma solução na forma de uma lei de potência. No caso aqui apresentado esta lei de potência já contém o expoente -2. No caso do modelo de Thompson e Turner, o expoente permanece incógnito, o que permite ajustá-lo a diferentes dados. Embora esta característica pareça apontar para uma maior generalidade do modelo de primeira ordem, é preciso lembrar que estè modelo decorre de uma aproximação temporal (sempre de primeira ordem em qualquer formulação de turbulência), que uma equação diferencial de primeira ordem admite apenas um contorno e que o modelo de Thompson e Turner, com coeficientes constantes, portanto, fica restrito àquela situação de turbulência gerada por apenas uma grade oscilante. Em outras palavras, se duas grades oscilantes forem introduzidas em um escoamento de modo que fiquem paralelas e com um espaçamento entre as mesmas, o modelo de primeira ordem não permite prever com acerto a evolução da energia cinética turbulenta no espaço entre as grades ou mesmo no espaço externo próximo às grades. Isto é evidente porque a solução da equação diferencial com coeficientes constantes proposta será sempre uma lei de potência que admite um único expoente, não importando o seu valor. Como no caso de duas grades oscilantes tem-se duas regiões com alta agitação (próximo às grades) e uma região de mínimo para a agitação turbulenta (meia distância entre as grades), nenhuma variação exponencial com um único expoente pode preencher esses requisitos. A questão ainda mais relevante, entretanto, talvez seja a o fato de ter sido gerada uma equação governante para o fenômeno (bastante bem aceita na literatura da área) que não

parece refletir corretamente a realidade física do fenômeno. A equação diferencial de primeira ordem, como é normalmente apresentada, não representa bem o processo difusivo em um escoamento genérico, o que englobaria, por exemplo, o caso das duas grades oscilantes. É possível que considerações adicionais acerca das variáveis envolvidas permitam adequar o modelo de forma que possibilite avaliar escoamentos difusivos mais abrangentes. Este estudo, contudo, não foi encontrado na literatura consultada.

A equação proposta por Bouvard e Dumas, por outro lado, parte já da discussão de que em um experimento com grelhas oscilantes a difusão e a dissipação da energia cinética são os fenômenos mais relevantes.A forma da equação final é idêntica à equação 11, sendo talvez esta a razão porque o seu uso não se generalizou (equação diferencial de segunda ordem não-linear). Admitindo alguns parâmetros como constantes, para chegar à equação final, os autores deram margem ao surgimento de críticas ao equacionamento devido a essas hipóteses simplificadoras. Entretanto, o mérito da formulação é que a mesma se fundamenta em uma argumentação que mantém as principais características físicas do problema e parece não impor resultados fisicamente inviáveis para o problema em questão. O desenvolvimento da formulação que aqui foi seguido é semelhante àquele apresentado em Schulz (1997). Outros autores, como Matsunaga et al. (1991) utilizam este desenvolvimento para estudar o escoamento através de simulações numéricas com o modelo k-ε. Todavia, apesar das demonstrações de viabilidade desta formulação, a mesma ainda não é utilizada como uma forma de exploração de características básicas dos escoamentos difusivo-dissipativos.

A equação 9 apresenta um grau de liberdade que merece ainda ser explorado, que é a presença da viscosidade turbulenta. Utilizando a definição 4 resulta:

$$\frac{\partial}{\partial x}\left(\frac{C_\mu}{\sigma_k}\frac{k^2}{\varepsilon}\frac{\partial k}{\partial x}\right)=\varepsilon \tag{17}$$

A integração desta equação produz:

$$k^3=\frac{3}{2}\frac{\sigma_k}{C_\mu}\left\{\int \varepsilon\, dx + B_1\right\}^2 + B_2 \tag{18}$$

B_1 e B_2 são constantes de integração. Note-se que é possível representar diretamente uma variável (na caso a energia cinética turbulenta) como função de operações efetuadas apenas sobre a segunda variável (no caso a taxa de dissipação de energia). Esta forma de representação é uma simplificação aguda do problema não-linear existente e permite explorar, por exemplo, como soluções empíricas para uma variável interferem no desenvolvimento da segunda variável. Evidentemente, uma vez havendo uma relação direta, é possível obter a relação inversa, de forma a explicitar a taxa de dissipação de energia. Neste caso, tem-se:

$$\varepsilon=\pm\frac{d}{dx}\sqrt{\frac{2}{3}\frac{C_\mu}{\sigma_k}\left(k^3-B_2\right)} \tag{19}$$

A equação 19 envolve apenas uma derivação para a energia cinética turbulenta, o que representa uma vantagem substancial em relação à equação correspondente 17. As equações 18 e 19 são características para escoamentos difusivo-dissipativos. A partir da equação 19 pode-se calcular a potência consumida em um espaço no qual apenas existem processos difusivos e dissipativos. Assim, admitindo que em uma posição x=0 a energia cinética turbulenta assume o valor k_0 e que em uma posição genérica x a mesma assume um valor máximo para o espaço considerado(k=k_{max}), obtém-se:

$$\dot{W} = 2\rho A\left(\sqrt{\frac{2}{3}\frac{C_\mu}{\sigma_k}\left(k_{\max}^3 - B_2\right)} - \sqrt{\frac{2}{3}\frac{C_\mu}{\sigma_k}\left(k_0^3 - B_2\right)}\right) \tag{20}$$

ρ é a massa específica do fluido e A é a área transversal à direção x, que define o volume do espaço de trabalho. A constante de integração remanescente deve ser resolvida para cada caso particular de estudo. Como exemplo, a integração da equação 19 para um escoamento entre duas grelhas oscilantes é apresentada no ítem seguinte. A equação 18 permite, por outro lado, verificar tendências para a variação de k a partir de variações conhecidas de ε. O caso mais simples é a situação de ε constante, que conduz à seguinte relação para a energia cinética turbulenta:

$$k = \left[\frac{3\sigma_k}{2C_\mu}\left(\varepsilon^2 x^2 + 2B_1\varepsilon x + B_1^2\right) + B_2\right]^{1/3} \tag{21}$$

Para pequenos valores de x, tem-se que a energia cinética assume um valor constante. Para grandes valores de x, por outro lado, verifica-se que há a tendência à seguinte proporcionalidade:

$$k \sim \left(\frac{3\sigma_k}{2C_\mu}\right)^{1/3}(\varepsilon x)^{2/3} \tag{22}$$

Esta forma de dependência pode ser extraída da literatura, por exemplo no estudo das condições de contorno em superfícies livres e superfícies sólidas para a resolução numérica de problemas de escoamentos em mecânica dos fluidos (ver Eiger e Shen, 1997, e Demuren e Rodi, 1984, por exemplo). Esses estudos estão fundamentados basicamente em proposições empíricas e argumentos dimensionais para a definição das variáveis relevantes. Os autores citados apresentam uma equação que, se utilizada para explicitar k com a representação de variáveis aqui definida, resulta em:

$$k = \left(\frac{\kappa}{C_\mu^{3/4}}\right)^{2/3}(\varepsilon x)^{2/3} \tag{23}$$

κ é a constante de von Kárman, com valor da ordem de 0,41. Valores encontrados na literatura (Matsunaga et al. 1991) para as constantes envolvidas nos coeficientes de $(\varepsilon x)^{2/3}$ conduzem ao coeficiente 2,55 para a equação 22 e ao coeficiente 1,85 para a equação 23. Embora não haja igualdade nos resultados obtidos, mais uma vez a comparação da ordem de grandeza de ambos é satisfatória. Resultados como a equação 22 são animadores e mostram que a formulação apresentada pode ser aplicada em situações nas quais se espera que processos difusivo-dissipativos sejam os mais relevantes na descrição de um fenômeno. Assim, junto a superfícies livres, por exemplo, espera-se que a produção de energia cinética turbulenta seja reduzida, uma vez que os gradientes de velocidade são suprimidos. Restam, então, a difusão e a dissipação como mecanismos que determinam as características turbulentas do escoamento nessas regiões.

Para a obtenção de uma avaliação dos perfis de k e ε optou-se, neste trabalho, utilizar expansões em séries de potências para as duas variáveis e calcular os valores dos coeficientes através de operações sucessivas. A equação 18 serve de base para o primeiro conjunto de resultados.

As variáveis k e ε são expressas da seguinte maneira:

$$\varepsilon = \sum_{i=0}^{\infty} \varepsilon_i x^i \qquad k = \sum_{j=0}^{\infty} k_j x^j \tag{24}$$

A utilização dessas relações na equação 18 conduz a uma igualdade entre séries de potências, cujos coeficientes de igual ordem devem ser iguais. Isto produz o seguinte conjunto de igualdades (aqui apresentado apenas até o termo de quarta ordem, mas que pode ser expandido até qualquer ordem):

Ordem zero: $k_0 = \sqrt[3]{S_k B_1^2 + B_2}$ $\qquad S_k = \dfrac{3}{2}\dfrac{\sigma_k}{C_\mu}$ (25a)

Ordem 1: $k_1 = \dfrac{2 S_k B_1 \varepsilon_0}{3 k_0^2}$ (25b)

Ordem 2: $k_2 = \dfrac{S_k}{3 k_0^2}\left(B_1 \varepsilon_1 + \varepsilon_0^2\right) - \dfrac{k_1^2}{k_0}$ (25c)

Ordem 3: $k_3 = \dfrac{S_k}{3 k_0^2}\left(\dfrac{2 B_1 \varepsilon_2}{3} + \varepsilon_0 \varepsilon_1\right) - \dfrac{k_1^3}{3 k_0^2} - \dfrac{2 k_1 k_2}{k_0}$ (25d)

Ordem 4: $k_4 = \dfrac{S_k}{3 k_0^2}\left(\dfrac{B_1 \varepsilon_3}{2} + \dfrac{\varepsilon_1^2}{4} + \dfrac{2 \varepsilon_0 \varepsilon_2}{3}\right) - \dfrac{k_1^2 k_2}{k_0^2} - \dfrac{k_2^2}{k_0} - \dfrac{2 k_1 k_3}{k_0}$ (25e)

.
.
.

As constantes B_1 e B_2 devem ser obtidas a partir dos contornos. Vê-se que cada novo coeficiente k_i é dependente dos coeficientes anteriores da energia cinética turbulenta, que as operações envolvidas no cálculo dos novos coeficientes conduzem sempre a números reais (não existem operações que geram números complexos) e que há, também, uma dependência para com os coeficientes da taxa de dissipação de energia. As duas primeiras características são positivas, no que tange à obtenção de um perfil. Porém a terceira característica exige que se utilize uma equação adicional para a taxa de dissipação de energia. Aqui convém utilizar a equação 15, que é equação diferencial de ε para o caso de difusão-dissipação. Efetuando as derivações indicadas e rearranjando os termos, obtém-se:

$$2k^2\varepsilon \frac{dk}{dz}\frac{d\varepsilon}{dz} - k^3 \frac{d\varepsilon}{dz}\frac{d\varepsilon}{dz} + k^3 \varepsilon \frac{d^2\varepsilon}{dz^2} = S_\varepsilon \varepsilon^4 \tag{26}$$

$$S_\varepsilon = \frac{C_2 \sigma_\varepsilon}{C_\mu}$$

Verifica-se que a equação 26 é linear para k^3, o que implica que uma equação equivalente à equação 18 pode ser também obtida, se isto for desejado. Entretanto, no presente texto, interessa utilizar as definições 24 para obter novas relações para os coeficientes de k e ε. Mais uma vez, a utilização dessas relações na equação 26 conduz a uma igualdade entre séries de potências, cujos coeficientes de igual ordem devem ser iguais. Isto produz, agora, o seguinte conjunto de igualdades

(apresentado apenas até o termo de terceira ordem devido ao espaço requerido, mas que pode ser expandido até qualquer ordem):

Ordem zero:

$$2k_0^2\varepsilon_0\varepsilon_1k_1 - k_0^3\varepsilon_1^2 + 2\varepsilon_0\varepsilon_2k_0^3 = S_\varepsilon\varepsilon_0^4 \tag{27a}$$

Ordem 1:

$$\begin{aligned}&2\left[\left(2k_0k_1\varepsilon_0 + k_0^2\varepsilon_1\right)\varepsilon_1k_1 + 2k_0^2\varepsilon_0\left(\varepsilon_1k_2 + \varepsilon_2k_1\right)\right] - \left[\left(3k_0^2k_1\right)\varepsilon_1^2 + 4k_0^3\varepsilon_1\varepsilon_2\right] + \\ &+\left[2\varepsilon_2\varepsilon_1 + 6\varepsilon_0\varepsilon_3\right]k_0^3 + \left(3k_0^2k_1\right)2\varepsilon_0\varepsilon_2 = 4S_\varepsilon\varepsilon_0^3\varepsilon_1\end{aligned} \tag{27b}$$

Ordem 2:

$$\begin{aligned}&2\left\{\left[\left(k_1^2 + 2k_0k_2\right)\varepsilon_0 + 2k_0k_1\varepsilon_1 + k_0^2\varepsilon_2\right]\varepsilon_1k_1 + \left(2k_0k_1\varepsilon_0 + k_0^2\varepsilon_1\right)\left(2\varepsilon_1k_2 + 2\varepsilon_2k_1\right)\right\} + \\ &+2\left(k_0^2\varepsilon_0\right)\left(3\varepsilon_1k_3 + 4\varepsilon_2k_2 + 3\varepsilon_3k_1\right) - \left[\left(k_1^2 + 2k_0k_2\right)k_0 + 2k_0k_1^2 + k_0^2k_2\right]\varepsilon_1^2 - \\ &-12k_0^2k_1\varepsilon_1\varepsilon_2 - k_0^3\left(6\varepsilon_1\varepsilon_3 + 4\varepsilon_2^2\right) + \left[2\varepsilon_2^2 + 6\varepsilon_1\varepsilon_3 + 12\varepsilon_0\varepsilon_4\right]k_0^3 + \\ &+\left[2\varepsilon_1\varepsilon_2 + 6\varepsilon_0\varepsilon_3\right]\left(3k_0^2k_1\right) + 2\varepsilon_0\varepsilon_2\left[\left(k_1^2 + 2k_0k_2\right)k_0 + 2k_0k_1^2 + k_0^2k_2\right] = \\ &= S_\varepsilon\left(6\varepsilon_0^2\varepsilon_1^2 + 4\varepsilon_0^3\varepsilon_2\right)\end{aligned} \tag{27c}$$

Ordem 3:

$$\begin{aligned}&2\left[2\left(k_0k_3 + k_1k_2\right)\varepsilon_0 + \left(k_1^2 + 2k_0k_2\right)\varepsilon_1 + 2k_0k_1\varepsilon_2 + k_0^2\varepsilon_3\right]\varepsilon_1k_1 + \\ &+2\left[\left(k_1^2 + 2k_0k_2\right)\varepsilon_0 + 2k_0k_1\varepsilon_1 + k_0^2\varepsilon_2\right]\left(2\varepsilon_1k_2 + 2\varepsilon_2k_1\right) + \\ &+2\left(2k_0k_1\varepsilon_0 + k_0^2\varepsilon_1\right)\left(3\varepsilon_1k_3 + 4\varepsilon_2k_2 + 3\varepsilon_3k_1\right) + \\ &+4k_0^2\varepsilon_0\left(2\varepsilon_1k_4 + 3\varepsilon_2k_3 + 3\varepsilon_3k_2 + 2\varepsilon_4k_1\right) - \\ &-\left[2\left(k_0k_3 + k_1k_2\right)k_0 + \left(k_1^2 + 2k_0k_2\right)k_1 + 2k_0k_1k_2 + k_0^2k_3\right]\varepsilon_1^2 - \\ &-12\left(k_0^2k_2 + k_0k_1^2\right)\varepsilon_1\varepsilon_2 - 3k_0^2k_1\left(6\varepsilon_1\varepsilon_3 + 4\varepsilon_2^2\right) - k_0^3\left(8\varepsilon_1\varepsilon_4 + 12\varepsilon_2\varepsilon_3\right) + \\ &+\left[8\varepsilon_2\varepsilon_3 + 12\varepsilon_1\varepsilon_4 + 20\varepsilon_5\varepsilon_0\right]k_0^3 + \left[2\varepsilon_2^2 + 6\varepsilon_1\varepsilon_3 + 12\varepsilon_0\varepsilon_4\right]\left(3k_0^2k_1\right) + \\ &+\left[2\varepsilon_1\varepsilon_2 + 6\varepsilon_0\varepsilon_3\right]\left[\left(k_1^2 + 2k_0k_2\right)k_0 + 2k_0k_1^2 + k_0^2k_2\right] + \\ &+2\varepsilon_0\varepsilon_2\left[2\left(k_0k_3 + k_1k_2\right)k_0 + \left(k_1^2 + 2k_0k_2\right)k_1 + 2k_0k_1k_2 + k_0^2k_3\right] = \\ &= 2S_\varepsilon\left[2\varepsilon_0^2\left(\varepsilon_0\varepsilon_3 + \varepsilon_1\varepsilon_2\right) + 2\varepsilon_0\varepsilon_1\left(\varepsilon_1^2 + 2\varepsilon_0\varepsilon_2\right)\right]\end{aligned} \tag{27d}$$

A apresentação algo rica em caracteres não deve impressionar, porque também aqui os coeficientes são sucessivamente calculados a partir dos valores já conhecidos, de menor ordem. Assim, vê-se que na equação 27a pode-se isolar o coeficiente ε_2, na equação 27b pode-se isolar o coeficiente ε_3, na equação 27c pode-se isolar o coeficiente ε_4, na equação 27d pode-se isolar o coeficiente ε_5, e assim sucessivamente. As operações envolvidas para a obtenção de cada coeficiente

produzem apenas valores reais, o que viabiliza este cálculo.Por outro lado, a obtenção das expressões 25 e 27 segue padrões bem definidos, ditados pelas equações diferencias e integrais iniciais, que podem ser facilmente reproduzidos em uma rotina de cálculo. Como ocorreu com as equações 25, também aqui os coefientes dependem de forma interligada com aqueles para a energia cinética turbulenta. É preciso notar ainda que se tem coeficientes que dependem de quatro constantes que devem ser difinidas a partir dos contornos. Essas constantes são aqui apresentadas como k_0, ε_0, ε_1 e B_1 ***ou*** B_2. Note-se que, devido à equação 25a, que relaciona três das constantes mencionadas, uma delas é supérflua (quando duas forem conhecidas, a terceira é imediatamente conhecida). Essas quatro constantes são evidentemente esperadas, uma vez que se tem um problema composto de duas equações diferenciais de segunda ordem, cada qual envolvendo, portanto, duas constantes de integração.

A obtenção sucessiva dos coeficientes pode ser assim conduzida:

- k_0, ε_0 e ε_1 são considerados conhecidos, assim como B_1, que aparece nas equações 25.
- k_1 e k_2 são obtidos das equações 25b e c.
- ε_2 e ε_3 são obtidos das equações 27a e b.
- k_3 e k_4 são obtidos das equações 25d e e.
- ε_4 e ε_5 são obtidos das equaçoes 27c e d.

...

Dois a dois, os coeficientes podem ser calculados alternando-se o conjunto de equações para a energia cinética turbulenta e para a taxa de dissipação de energia. Apesar da simplicidade aparente, é preciso mencionar que a determinação das constantes de integração pode ser complexa (primeiro passo acima arrolado) e que o uso prático das expressões aqui obtidas provavelmente exige o truncamento em ordens inferiores das séries infinitas apresentadas. Não obstante, trata-se de uma solução teórica e geral, a qual pode ser utilizada para estudar o comportamento de casos particulares de escoamentos turbulentos difusivo-dissipativos. No presente trabalho, o caso de duas grelhas oscilantes é abordado a seguir.

O Caso da Difusão-Dissipação da Turbulência para Duas Grelhas Oscilantes

No problema de duas grelhas oscilantes, as propriedades turbulentas (como a energia cinética turbulenta) devem passar por pontos críticos (mínimos ou máximos) no centro do espaçamento entre as grelhas, se a geração de turbulência for igualmente intensa em ambas. Assim, o plano central age como um espelho e qualquer função que descreva uma propriedade deste escoamento deve ser forçosamente uma função par em torno da origem do sistema de coordenadas, localizado convenientemente neste plano central. As grelhas ficam então posicionadas em $x=+/-L$, sendo L o valor da meia-distância. Como tanto a energia cinética turbulenta como a taxa de dissipação de energia são funções pares de x tem-se que a constante B_1 da equação 1.18 deve ser zero, o que acarreta o valor k_0^3 para a constante B_2, sendo k_0 o valor de k na origem. A equação 1.19 passa a ser representada, então, por:

$$\varepsilon = \pm \frac{d}{dx}\sqrt{\frac{2}{3}\frac{C_\mu}{\sigma_k}\left(k^3 - k_0^3\right)} \tag{28}$$

A partir da equação 28 pode-se calcular a potência consumida no espaço entre as grelhas ($\dot{W}$), considerando que em $x=+/-L$ tem-se $k=k_{max}$, que representa o maior valor da energia cinética turbulenta. Tem-se, então:

$$\dot{W} = 2\rho\, A \sqrt{\frac{2}{3}\frac{C_\mu}{\sigma_k}\left(k_{max}^3 - k_0^3\right)} \tag{29}$$

ρ é a massa específica do fluido e A é a área das grelhas oscilantes. Pode-se avaliar aproximadamente o coeficiente da equação 29 a partir de valores de literatura para as constantes envolvidas. Tem-se, então:

$$\dot{W} \approx 0{,}44\rho\, A\left(\sqrt{k_{max}^3 - k_0^3}\right) \tag{30}$$

Como avaliação adicional, o valor médio da taxa de dissipação de energia por unidade de massa na região entre as grades oscilantes pode ser obtido diretamente das equações 29 ou 30, fornecendo, para esta última, a previsão:

$$\bar{\varepsilon} \approx \frac{0{,}22}{L}\left(\sqrt{k_{max}^3 - k_0^3}\right) \tag{31}$$

Finalmente, os perfis de energia cinética turbulenta e de taxa de dissipação de energia podem ser obtidos das equações 25 e 27, para as quais os termos de ordem ímpar devem ser anulados. Desta forma, tem-se, a partir das equações 25:

Ordem zero: $k_0 = B_2^{1/3}$ *ou* $B_2 = k_0^3$ (32a)

Ordem 1: $k_1 = 0$ (32b)

Ordem 2: $k_2 = \frac{S_k}{3k_0^2}\left(\varepsilon_0^2\right)$ $\qquad S_k = \frac{3}{2}\frac{\sigma_k}{C_\mu}$ (32c)

Ordem 3: $k_3 = 0$ (32d)

Ordem 4: $k_4 = \frac{S_k}{3k_0^2}\left(\frac{2\varepsilon_0\,\varepsilon_2}{3}\right) - \frac{k_2^2}{k_0}$ (32e)

Ordem 5: $k_5 = 0$ (32f)

.
.
.

Das equações 27 obtém-se:

Ordem zero:

$$\varepsilon_2 = \frac{S_\varepsilon \varepsilon_0^3}{2k_0^3} \qquad S_\varepsilon = \frac{C_2\,\sigma_\varepsilon}{C_\mu} \tag{33a}$$

Ordem 1:

$$\varepsilon_3 = 0 \tag{33b}$$

Ordem 2:

$$\varepsilon_4 = \frac{2S_\varepsilon \varepsilon_0^3 \varepsilon_2 - 7k_0^2 k_2 \varepsilon_0 \varepsilon_2 + k_0^3 \varepsilon_2^2}{6k_0^3 \varepsilon_0} \tag{33c}$$

Ordem 3:

$$\varepsilon_5 = 0 \tag{33d}$$

Ordem 4:

$$\varepsilon_6 = \frac{S_\varepsilon \left(3\varepsilon_0^2 \varepsilon_2^2 + 2\varepsilon_0^2 \varepsilon_4\right) - 11k_0 k_2^2 \varepsilon_0 \varepsilon_2 - 11k_0^2 k_4 \varepsilon_0 \varepsilon_2 - 20k_0^2 k_2 \varepsilon_0 \varepsilon_4 + k_0^3 \varepsilon_2 \varepsilon_4}{15k_0^3 \varepsilon_0} \tag{33e}$$

Ordem 5:

$$\varepsilon_7 = 0 \tag{33f}$$

Observa-se, portanto, no caso de duas grades oscilantes, uma sensível simplificação do problema dos contornos. Apenas k_0 e ε_0 necessitam ser determinados, ambos com sentido físico claro, ou seja, o primeiro é o valor da energia cinética turbulenta na origem e o segundo é o valor da taxa de dissipação de energia na origem. As outras duas constantes já foram definidas a partir da condição de simetria. Tanto a energia cinética turbulenta como a taxa de dissipação desta energia na origem podem ser obtidas experimentalmente, o que simplifica a construção dos perfis. Trabalhos experimentais efetuados no sentido de estudar o comportamento de características turbulentas para a situação de duas grelhas oscilantes ainda são escassos, porém estudos como os de Srdic et al. (1996) mostram a potencialidade deste tipo de escoamento, no que tange ao estudo de características básicas da turbulência.

Conclusões

Os escoamentos turbulentos gerados por grelhas ou grades oscilantes foram analisados a partir das equações do modelo k-ε, gerando-se soluções teóricas para o caso geral, o caso de uma grelha oscilante imersa em um fluido e o caso de duas grelhas oscilantes imersas em um fluido. As soluções propostas permitem o cálculo da potência consumida no escoamento, bem como a construção de perfis de evolução espacial da energia cinética turbulenta e da taxa de dissipação de energia.

Para o caso de uma grelha oscilante, resultados experimentais de outras fontes puderam ser utilizados e confirmam as tendências teóricas previstas. Para o caso de duas grelhas oscilantes, o espaço entre as grelhas foi analisado, obtendo-se as equações para potência dissipada nesta região e para os perfis acima mencionados. A solução para a potência dissipada é exata, incorporando apenas as hipóteses que conduzem ao próprio modelo k-ε . As soluções para os perfis de energia cinética turbulenta e taxa de dissipação desta energia são apresentadas na forma de séries de potências, que fornecem aproximações truncando-se as séries nos termos de ordens inferiores.

Agradecimentos

O autor agradece à FAPESP, pelo apoio obtido através do processo 1997/11743-0 para execução de pesquisa no exterior, na qual o presente trabalho se insere, e ao Prof. Gerhard Jirka, anfitrião no Institut für Hydromechanik, Universität Karlsruhe, Alemanha.

Referências Bibliográficas

Bouvard , M. e Dumas, H., 1967, "Application de la Méthode du Fil Chaud a la Mesure de la Turbulence dans l'Eau", La Houille Blanche, nº 7, pp. 723-734.

Demuren , A.O. e Rodi, W., 1984, "Calculation of Turbulence-driven Secondary Motion in Non-circular Ducts", Journal of Fluid Mechanics, Vol.140, pp.189-222.

De Silva, I.P.D. e Fernando, H.J.S., 1994, "Oscillating Grids as a Source of Nearly Isotropic Turbulence", Physics of Fluids, Vol.6, nº 7, pp. 2455-2464.

Eiger, S. e Shen, H.W., 1997, "An Analysis of the Free Surface Boundary Condition of the Dissipation Rate of Turbulent Kinetic Energy", trabalho submetido para publicação, cedido como informação pessoal..

Hinze, J.O., 1959, "Turbulence", McGraw-Hill, New York.

Hopfinger, E.J. e Toly, J.A., 1976, "Spatially Decaying Turbulence and ist Relation to Mixing Across Density Interfaces", Journal of Fluid Mechanics, Vol.78, pp. 155-175.

Matsunaga, N.; Sugihara, Y. e Komatsu, T., 1991, "A Numerical Simulation of Oscilating-Grid Turbulence by using the k-ε Model", in Lee, J.H.W. e Cheung, Y.K., (editors) "Environmental Hydraulics", Vol.1, A.A. Balkema, Rotterdam, the Netherlands, pp.427-432.

Monin, A.S. e Yaglom, A.M., 1979, "Statistical Fluid Mechanics-Mechanics of Turbulence", Vol 1, the MIT Press, Massachusets.

Monin, A.S. e Yaglom, A.M., 1981, "Statistical Fluid Mechanics-Mechanics of Turbulence", Vol 2, the MIT Press, Massachusets.

Nokes, R.I., 1988, "On the Entrainment Rate Across a Density Interface", Journal of Fluid Mechanics, Vol 188, pp.185-204.

Schulz, H.E., 1997, "Teste de uma Formulação Alternativa em Turbulência", Tese apresentada à Escola de Engenharia de São Carlos, Universidade de São Paulo, 86 p.

Srdic, A.; Fernando, H.J.S. e Montenegro, L., 1996, "Generation of Nearly Isotropic Turbulence using Two Oscilating Grids", Experiments in Fluids, 20, pp.395-397.

Thompson, S.M. e Turner, J.S., 1975, "Mixing Across an Interface due to Turbulence Generated by an Oscilating Grid", Journal of Fluid Mechanics, Vol.67, pp. 349-368.

Voropayev, S.I. e Fernando, H.J.S., 1996, "Propagation of Grid Turbulence in Homogeneous Fluids", Physics of Fluids, Vol.8, nº 9, pp. 2435-2440.

COMPARASIONS OF SOME MODELS OF TURBULENT PRANDTL NUMBER FOR LOW AND VERY LOW-PRANDTL-NUMBER FLUIDS

Marcelo C. Silva*
Ricardo F. Miranda
Lutero C. De Lima

(*) Department of Energy
UNICAMP - Campinas SP - Brazil

Department of Mechanical Engineering
Universidade Federal de Uberlândia
38400 089 Uberlândia MG Brazil

ABSTRACT

The present article studies some models of turbulent Prandtl number for low and very low-Prandtl-number fluids. It was investigated model of Cebeci, two models of Kays, and model of Wassel and Catton. Three different low and very low-Prandtl-number fluids and aire were studiedand compared with experimental data found in the literature. It was verified the behaviour of the turbulent Prandtl number close to the wall as function of dimensionless wall distance and eddy diffusivity of heat. It was observed that near the wall Pr_t shows asymptotic behaviour for all models and fluids, except for model of Cebeci and air. For the wall distance, y+, greater than 700 all models and fluids show values of Pr_t around 0.9-1.0.

Keywords: Turbulence; Turbulent Prandtl Number; Boundary Layer.

NOMENCLATURE

A+	Van Driest Constant
B+	function of Eq. (15)
C	specific heat at constant pressure, J/kg° C
C_1, C_2, C_3, C_4	constants (equation 18)
k	molecular thermal conductivity, W/m°C
l	Prandtl mixing length, m
Pr	Prandtl number = ν/α
Pr_t	turbulent Prandtl number = $\varepsilon_M/\ \varepsilon_H$
T	time-averaged temperature, °C
T_∞	temperature of free stream, °C
T_w	temperature at wall surface, °C
u	time-averaged velocity in x direction, m/s
$\overline{u'v'}$	turbulent shear stress, m^2/s^2
u^+	mean velocity in wall coordinates = u/u^*
U_∞	velocity at outer edge of boundary layer, m/s
u^*	shear velocity = $\sqrt{\tau_o / \rho}$, m/s
v	time-averaged velocity in y direction, m/s
$\overline{v'T'}$	turbulent heat flux, m°C/s
x	distance measured in direction of mean flow, m
y	distance measured in direction normal to mean flow, m
y^+	distance from wall in wall coordinates = yu^*/ν
α	thermal diffusivity, m^2/s
δ	boundary layer thickness, m
ε_H	eddy diffusivity of heat, m^2/s
ε_M	eddy diffusivity of momentum, m^2/s
η	transformed y-coordinate
μ	dynamic viscosity coefficient, kg/ms
γ	intermittency factor
ν	kinematic viscosity coefficient, m^2/s
ξ	transformed x-coordinate
ρ	density, kg/m^3
τ_w	shear stress at wall surface, N/m^2
θ	dimensionless temperature = $(T - T_\infty)/(T_w - T_\infty)$

INTRODUCTION

Prediction of heat transfer in turbulent flows demands the solution of the energy equation, which in its turn depend on solution of the momentum equations. The fact is that such equations have fluctuation terms and those terms usually are expressed as function of the mean velocity and temperature gradients. For the case of the momentum equation, the concept of eddy diffusivity of momentum ε_m has been introduced and, together with the theory of the Prandtl's mixing-length, it was reached satisfactory numerical prediction in comparison to experimental data. Similarly for the case of the energy equation, the concept of eddy diffusivity of heat ε_h is used although it is not yet completely consensus. As stressed by Cebeci (1973), various assumptions have been made about eddy diffusivity of heat, and several expressions have been proposed in attempts to predict the mean temperature distribution within the boundary layer. The solution of the governing equations of a turbulent flow needs the application of turbulence models which are based on the ratio of the eddy diffusivity of momentum ε_m to the eddy diffusivity of heat ε_h that is the turbulent Prandtl number (Bremhorst and Krebs, 1993). One assumption that has been used extensively is the one due to Reynolds. According to his assumption, heat and momentum are transferred by the same process, which means that both eddy diffusivities are the same. This assumption leads to a turbulent Prandtl number of unity (Cebeci, 1973).

More than four decades, the literature discusses the behaviour of the turbulent Prandtl number mostly for air boundary layer and until now no definite conclusions has been reached. Reynolds (1975), in a review, has examined more than 30 different ways of predicting the turbulent Prandtl number and affirmed that the existing procedures range from purely empirical to formal analyses based on the Reynolds stress equation. Kays (1994) examined available experimental data on Pr_t for two-dimensional turbulent boundary layer and for fully developed flow in a circular duct or a flat duct. More recently, De Lima, Silva and Miranda (1998) made a comparative analysis of different models for the turbulent Prandtl number for air boundary layer. The influence on the calculation of various thermal parameters such as dimensionless temperature profile, turbulent heat flux, eddy conductivity of heat and Stanton number were also investigated. They observed that the behaviour of the turbulent Prandtl number is relatively constant along the boundary layer. Discrepancies in Pr_t shown by almost all models and experimental data at mainly to the near wall region and in the "wake" region of the boundary layer had little effect both on the calculation of Stanton number and on the calculation of such other thermal parameters.

If on one hand there are extensive data on turbulent Prandtl number for fluids such as air and water, on the other hand there are few publications on turbulent Prandtl number for low and very low Prandtl number fluids. The scarcity of publications on Pr_t for low and very low Prandtl number fluids make difficult the evaluation of models and experimental data. Notwithstanding these aspects are very important then considerable interest does exist in applications of such fluids as, for example, cooling of nuclear reactors and valves of internal combustion engines.

While for air and fluids with molecular Prandtl number greater than 0.7 the turbulent Prandt number can be assumed constant (for example 0.9) along the boundary layer, for the case of fluids with low and very low Prandtl that

assumption can not be considered. As it will be shown in this article close to the wall the majority of models of Pr_t for such class of fluid points to values much higher than 0.9. However higher values of y+ (say y+ > 700) all models of Pr_t, independently of fluid, its values goes to 0.9.

GOVERNING EQUATIONS

For a steady, two-dimensional, constant property turbulent air boundary layer over a flat plate with negligible body force, negligible viscous dissipation and no pressure gradient, the governing equations can be expressed as follows.

Continuity equation

$$\frac{\partial u}{\partial x} + \frac{\partial v}{\partial y} = 0 \tag{1}$$

Momentum equation

$$u\frac{\partial u}{\partial x} + v\frac{\partial u}{\partial y} = \frac{\partial}{\partial y}\left[(\nu + \varepsilon_M)\frac{\partial u}{\partial y}\right] \tag{2}$$

Energy equation

$$u\frac{\partial T}{\partial x} + v\frac{\partial T}{\partial y} = \frac{\partial}{\partial y}\left[(\alpha + \varepsilon_H)\frac{\partial T}{\partial y}\right] \tag{3}$$

and the definition of the turbulent Prandtl number is:

$$Pr_t = \frac{\varepsilon_M}{\varepsilon_H} = \frac{\overline{u'v'}(\partial T / \partial y)}{\overline{v'T'}(\partial U / \partial y)} \tag{4}$$

Substituting for ε_H in Eq. (3) and after rearranging, thus it has, for energy equation:

$$u\frac{\partial T}{\partial x} + v\frac{\partial T}{\partial y} = \frac{\partial}{\partial y}\left\{\nu\left[\frac{1}{Pr} + \frac{\varepsilon_M / \nu}{Pr_t}\right]\frac{\partial T}{\partial y}\right\} \tag{5}$$

The conservation of mass and momentum equations (1) and (2) require specification of the velocity components at the wall and at the free stream. That is,

$$y = 0; \quad u = 0; \quad y \to \infty; \quad u = U_\infty \tag{6}$$

Doing the same for the thermal energy equation requires specification of the temperature at the wall and in the free stream:

$$y = 0; \quad T = T_w; \; y \to \infty; \; T = T_\infty \tag{7}$$

In order to solve equations (1), (2), (3) and (5) with their corresponding boundary conditions, a turbulence model has to be introduced to evaluate the eddy quantities ε_M and ε_H and consequently the turbulent Prandtl number Pr_t.

After Chyou (1991), the theory of turbulent wall shear layers is still in a state of intense study, and new breakthroughs are continually in sight. But the simplest of all the schemes proposed remains the very old Prandtl mixing-length model, and with new information available on the very important behaviour of the viscous sublayer, the mixing-layer model provides a remarkably adequate basis for many engineering applications especially for some simple flow patterns. The following calculations were based on this turbulence model:

$$\varepsilon_m = \ell^2 |\partial u / \partial y| \tag{8}$$

To evaluate the mixing length ℓ, the outer region of the boundary layer and the near wall region must be considered separately. Still after Chyou (1991), for flows remote from walls, ℓ is usually taken as uniform across the layer and proportional to the thickness of the layer. For a boundary layer on a wall, the variation of ℓ in the outer part is similar to that in free turbulent flows, but ℓ is proportional to the distance from the wall for the near wall region. The coefficient of proportionality between the Prandtl mixing-length ℓ and the thickness of the layer is normally the Von Karman constant K = 0.4, that is $\ell = 0.4y$.

However, for the region close to the wall, the viscous sublayer, equation (8) needs to be modified. The Van Direst's hypothesis was applied to the wall region as

$$\ell = 0.4y\left[1 - \exp\left(-y^+ / A^+\right)\right] \tag{9}$$

where $A^+ = 26$ (the Van Driest's constant) and y^+ a dimensionless distance defined as $y^+ = y(\rho \tau_w)^{1/2}/\mu$, in which τ_w is the shear stress on the wall.

By that way the eddy-viscosity expression based on Prandtl's mixing length modified by Van Driest for the inner viscous sublayer will be

$$\varepsilon_{mi} = 0.16 y^2 \left[1 - \exp\left(-y^+ / A^+\right)\right]^2 |\partial u / \partial y| \tag{10}$$

For the outer region the eddy-viscosity expression is given by

$$\varepsilon_{mo} = 0.0168 U_\infty \delta^* \gamma \tag{11}$$

being γ the Klebanoff's intermittence factor under the formula

$$\gamma = \left[1 + 5.5(y / \delta)^6\right]^{-1} \tag{12}$$

and δ^* the boundary layer displacement thickness defined as

$$\delta^* = \int_0^\infty \left(1 - \frac{u}{U_\infty}\right) dy \qquad (13)$$

For the turbulent Prandtl number Cebeci (1973) proposed a model which is dependent upon the distance of the wall, given as follows:

$$\mathrm{Pr}_t = \frac{K[1 - \exp(-y^+/A^+)]}{K_H[1 - \exp(-y^+/B^+)]} \qquad (14)$$

where K = 0.4, K_H = 0.44, A^+ = 26 and B^+ is given by the following equation.

$$B^+ = \frac{1}{\sqrt{\mathrm{Pr}}} \sum_{i=1}^{5} C_i \left(\log_{10} \mathrm{Pr}\right)^{i-1} \qquad (15)$$

being C_1 = 34.96, C_2 = 28.79, C_3 = 33.95, C_4 = 6.3 and C_5 = -1.186.

A very simple model was proposed by Kays (1994) who considered Pr_t as a function of Pr and ε_M / ν which is the turbulent Peclét number (Pe_t). As highlighted by him his model is similar to one suggested by Reynolds (1975). The Kays' model is in the form:

$$\mathrm{Pr}_t = \left[0.7 / \mathrm{Pr} \cdot (\varepsilon_M / \nu)\right] + 0.85 \qquad (16)$$

Kays (1994) has proposed another equation for Pr_t, modifying equation (16) to the form:

$$\mathrm{Pr}_t = \left[2.0 / \mathrm{Pr} \cdot (\varepsilon_M / \nu)\right] + 0.85 \qquad (17)$$

Equation (17) was proposed by Kays with the intention of including experimental data on liquid metals.

The step of introducing an analogous variation for ε_M / ν as cited by Reynolds (1975) was early taken by Wassel and Catton (1973) in the form:

$$\mathrm{Pr}_t = \frac{C_3}{C_1 \cdot \mathrm{Pr}} \cdot \frac{\left[1 - \exp\left(\frac{-C_4}{\varepsilon_M / \nu}\right)\right]}{\left[1 - \exp\left(\frac{-C_2}{\mathrm{Pr} \cdot (\varepsilon_M / \nu)}\right)\right]} \qquad (18)$$

where C_1 = 0.21, C_2 = 5.25, C_3 = 0.20 and C_4 = 5.0

The limit between both regions is determined by the condition where $\varepsilon_{mi} = \varepsilon_{mo}$.

The following dimensionless parameters and variables were adopted in Eqs. (1) - (13):

$$u = \frac{u}{U_\infty}, \qquad v = \frac{v}{U_\infty} \quad \text{and} \quad \theta = \frac{T - T_\infty}{T_w - T_\infty} \tag{19}$$

and independent variables as

$$\xi(x) = \int_o^x \frac{U_\infty}{\nu} dx \quad \text{and} \quad \eta(x, y) = y \frac{U_\infty}{\nu(2\xi)^n} \tag{20}$$

being η function ξ and δ. After Schlichting (1979) η varies between 0.5 and 0.8. In a study of validation of this turbulence model made by the present author (De Lima and Pereira, 1983) n = 0.5 was used because good results were reached in comparison with experimental data.

Therefore equations (1), (2) and (5) with boundary conditions will be:

$$(2\xi)^{2n} \frac{\partial u}{\partial \xi} + \frac{\partial V}{\partial \eta} = 0 \tag{21}$$

$$(2\xi)^{2n} \frac{\partial u}{\partial \xi} + V \frac{\partial V}{\partial \eta} = \frac{\partial}{\partial \eta}\left[(\nu + \varepsilon_m)\frac{\partial u}{\partial \eta}\right] \tag{22}$$

$$(2\xi)^{2n} u \frac{\partial \theta}{\partial \xi} + V \frac{\partial \theta}{\partial \eta} = \frac{\partial}{\partial \eta}\left[\nu\left(\frac{1}{\mathrm{Pr}} + \frac{\varepsilon_m / \nu}{\mathrm{Pr}_t}\right)\frac{\partial \theta}{\partial \eta}\right] \tag{23}$$

being

$$V = \frac{\nu(2\xi)^{2n}}{U\infty(x)} u \frac{\partial \eta}{\partial x} + (2\xi)^n v \tag{24}$$

The boundary conditions for equations (16-19) are

$$\begin{aligned} &\xi = 0: u = 0, v = 0, \theta = 0 \\ &\eta = 0: u = 0, v = 0, \theta = 1 \\ &\eta \to \infty: u = 1, v = 0, \theta = 0 \end{aligned} \tag{25}$$

Equations (21-24) were numerically discretized and solved by an tri-diagonal implicit finite-difference method as outlined by De Lima and Pereira (1983). The finite-difference equations use a variable grid in the η direction which permits shorter steps close to the wall and longer steps away from the wall (Cebeci, 1970). The grid has the property that the ratio of lengths of any two adjacent

intervals is a constant, that is, $\Delta\eta_j = B\Delta\eta_{j-1}$. The grid has five points in the ξ-direction and three points in the η-direction.

The computer program used in this study was used a grid wich 300 points in the η-direction. The choice of B = 1.03 and $\Delta\eta_1$ = 0.035 shown a satisfactory combination which permitted a computation time per station of 3 seconds under the convergence criterion of 10^{-4}. Concerning ξ-direction there is no restriction on the number of stations, and the starting position was at x = 0.0914 m.

The calculations were started with an initial velocity profile based on the concept of friction velocity and the logarithmic laws of the wall. Since the velocity and temperature profiles are decoupled for non-buoyant flows, velocity fields are solved first. Thereafter temperature field was solved with an initial one-seventh law profile.

RESULTS AND DISCUSSION

For the present comparative study of different models of Pr_t for low and very low Prandtl number fluids, were selected liquid sodium (Pr = 0.0058), mercury (Pr = 0.025), a fluid with P_r = 0.1 which corresponds to a gas mixtures as for example hydrogen-xenon and air (Pr = 0.71). Due to the few data in the literature, with the purpose of validation and comparison, this selection of fluids was intentionally made as similar to the selection of Bremhorst and Krebs (1993).

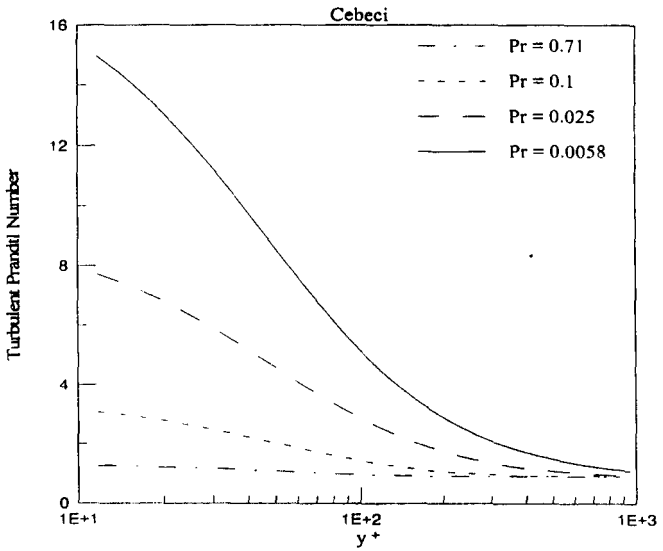

Figure 1. Turbulent Prandtl Number Calculated from Model of Cebeci.

Figure 1 shows the variation of the turbulent Prandtl number as a function of the wall distance y+. In this case the model used was the one of Cebeci (eq. 14). The effect for liquid sodium and mercury is very remarkable and it is apparent that Pr_t is a strong function of the molecular Prandtl number close to the wall and constant away from the wall. It can also be noted that increasing the molecular Prandtl number will result in the decreasing of the turbulent Prandtl number near the wall. As expected air did not show such behaviour.

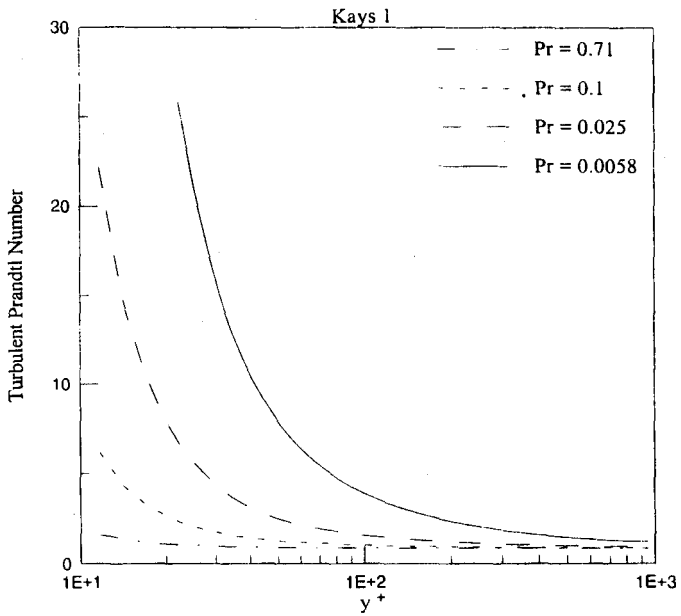

Figure 2. Turbulent Prandtl Number Calculated from Model of Kays (I).

Figures 2 and 3 show the variation of Pr_t as a function of y+ and fluids representing the models of Kays (Kays 1 - eq. 16 and Kays 2 - eq. 17). Firstly Kays (1994) used equation 16 for Pr_t observing that its calculation were very close to experimental data and DNS results published in the literature. Subsequently Kays proposed equation 17 for the turbulent Prandtl number for low and very low Prandtl fluids. He explained that although equation 16 is well adjusted to experimental and DNS results, when temperature profiles and Nusselt numbers were measured directly equation 17 is more consistent than equation 16.

With exception of air, the turbulent Prandtl number calculated by models of Kays (eq. 16 and eq. 17) present a very dramatic behaviour close to the wall. Some investigators argue that the region close to the wall is unimportant (Mc Eligot and Taylor, 1995) since at such location and for low and very low Prandtl number fluids the molecular transport of energy or momentum is expected to be high than the turbulent transport. Notwithstanding the molecular Prandtl number has a strong

effect on Pr_t close to the wall as shown by the present investigation. As highlighted by Mc Eligot and Taylor (1995) it is difficult to measure Pr_t accurately near the wall. As the wall is approached, the experimental uncertainties grow to the point where the measurements can not be used with confidence to discriminate between hypothesized models. In particular, both the turbulent shear stress and the turbulent heat flux go to zero as the wall is approached, so Pr_t becomes ~0/~0 and its limiting value is bound to be uncertain. On the other hand the same Mc Eligot and Taylor affirm that for gas mixtures with Pr ranging from about 0.18 to 0.7, and where in our opinion could be included liquid metals, predicted heat transfer parameters are expected to be strongly dependent on the representation of thermal energy transport in the viscous layer, $y+ < 30$. This expectation evolves since, in a typical high Reynolds number flow, about 40% of the thermal resistance can be concentrated in the region $5 < y+ < 30$, which covers only about 0.2% of the radius or boundary layer thickeness.

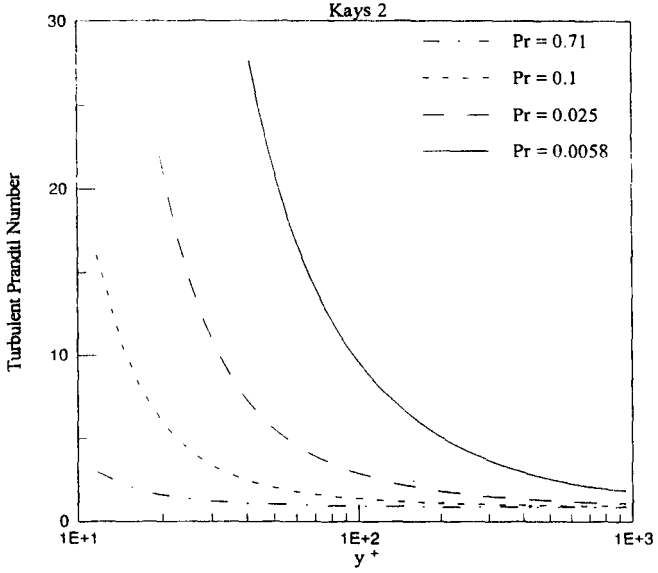

Figure 3. Turbulent Prandtl Number Calculated from Model of Kays (II).

The model of Wassel and Catton (eq. 18) was applied to the same fluids treated in this study and curves of Pr_t are shown in the Figure 4. Again as occurred with the model of Cebeci and models of Kays, the model of Wassel and Catton show dramatic behaviour of the turbulent Prandtl number of liquid metals (sodium and mercury). In fact, with the exception of air, the model of Wassel and Catton present valued of Pr_t greater than value present by the other models studied here. If one takes a closer look on the behaviour of liquid metals as shown in Figures 5 and 6 for mercury and sodium , respectively, it is observed that most of the models point to a value of infinity to the turbulent Prandtl number when the wall is approached.

The model of Cebeci is the only one which points a finite value to Pr_t close to the wall.

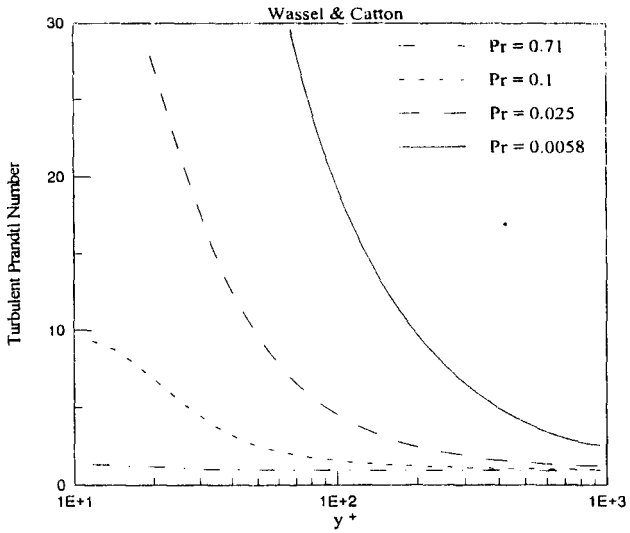

Figure 4. Turbulent Prandtl Number Calculated from Model of Wassel and Catton.

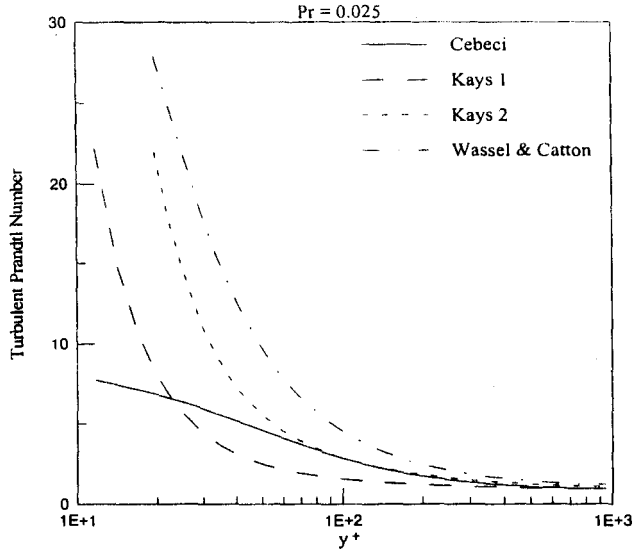

Figure 5. Turbulent Prandtl Number Calculated from various models and liquid mercury.

For the case of liquid mercury flow (Fig. 5) model of Wassel and Catton and models of Kays converge to infinite value of Pr_t when the wall is approached. The model of Cebeci points to a value 8 for Pr_t at the wall. All models converge to a constant value of Pr_t (around 0.9) for y+ > 400. The same behaviour will be seen for the case of liquid sodium flow (Fig. 6). However estimation of all four models is higher than for mercury and the convergence to about 0.9 will be displaced to y+ > 1000.

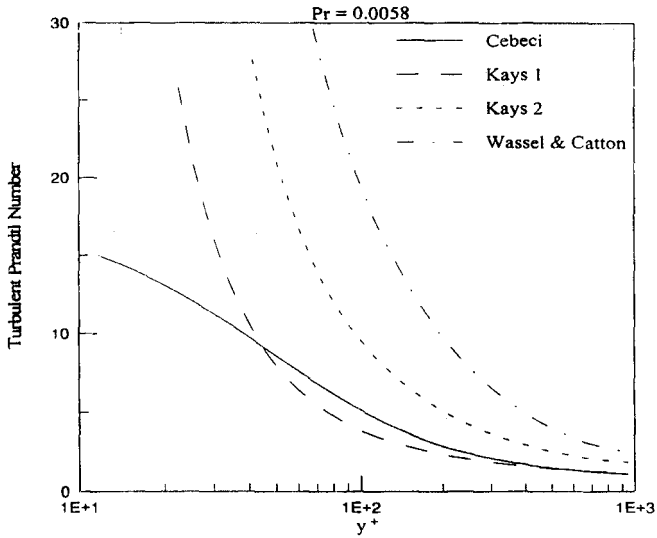

Figure 6. Turbulent Prandtl Number Calculated from various models and liquid sodium.

In general, it is noticeable that the lower the molecular Prandtl number the higher will be the turbulent Prandtl number mainly for situation of flows close to the wall. Although many researchers agree that the turbulent Prandtl number goes to values very high for a low and very low molecular Prandtl number fluid it is very difficult through the knowledge of the relationship Pr_t x y+ discriminate what would be the value of Pr_t close to the wall of a certain fluid flow. Attempts of scaling Pr_t as a function of Reynolds number proved fruitless. However Bremhorst and Krebs (1992) found that for liquid sodium their data collapsed with experimental data of many researchers and with a curve given by $Pr_t = 1.8 \exp(-1.5\ \varepsilon_H/\alpha) + 0.9$ for the range of $0.053 < \varepsilon_H/\alpha < 3.0$. Figures 7 to 11 will show calculated Pr_t using all models studied here as function of ε_H/α for this referenced range.

Additionally will be used liquid sodium experimental data of Bremhorst and Krebs, Fuchs and of Sheriff and O'Kane, as a representative data and as a tool for the comparative analysis of the models here studied. Fuchs (referenced by Bremhorst and Krebs, 1993) measured temperature profiles in fully developed pipe flow with constant wall heat flux at a nominal temperature of 220°C. These gave ε_H

in the core region and ε_M was obtained by use of published velocity field data. Sheriff and O'Kane (1981) reported ε_H and Pr_t data for point source injection placed on the centerline of fully developed pipe flow at Pr = 0.0071 - 0.0072. Bremhorst et al. (1989) performed measurements in water and liquid sodium with a point source using a multibore jet block. As no cross-stream velocity gradients existed, direct calculation of a turbulent Prandtl number was not readily possible, although eddy diffusivities of heat were determinable. Subsequently Bremhorst and Krebs (1992) extended the latter experiment by significantly reducing the ambient flow surrounding the point source flow. The resultant flow was similar to a free jet for which Pr_r could be calculated from measured velocity and temperature profiles however comparison with boundary layer measurements were difficult.

It was firstly observed by Bremhorst and Krebs (1992) that experimental results on Pr_t from different researchers show good consistency when Pr_t is considered as a function of ε_H/α than other parameters such as U_∞ or Reynolds number directly even that this procedures excludes the case of $\varepsilon_H/\alpha = 0$, as seen in Figures 7 - 11. However, as pointed by Sheriff and O'Kane (1973) omission this limit is not of practical significance, since turbulent heat transfer becomes negligible close to the wall. The procedure of studying Pr_t against ε_H/α as put henceforth will be a useful tool for the comparative analysis of different models of Pr_t for flows of low and very low molecular Prandtl fluids.

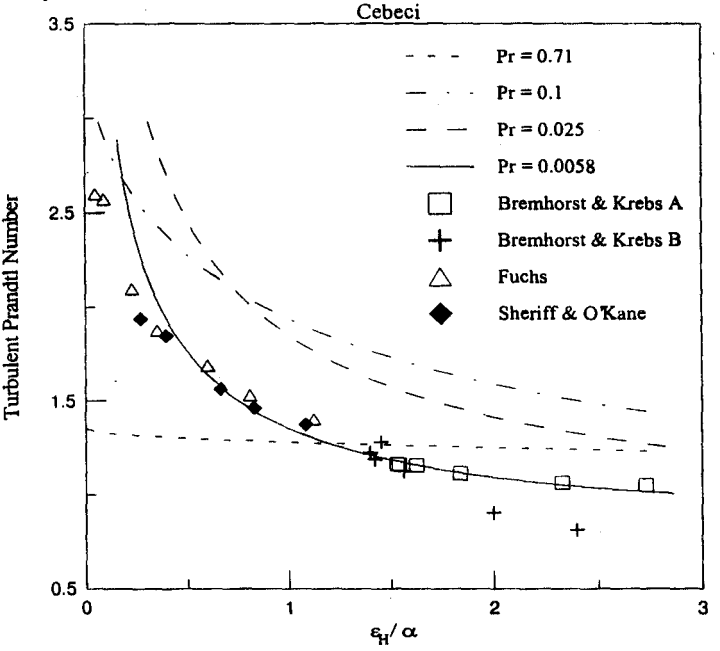

Figure 7. Turbulent Prandtl Number Calculated from Model of Cebeci as function of ε_H/α.

The model of Cebeci (eq. 14) as represented in Figure 1 for various fluids, when put in terms of eddy diffusivities of heat ε_H/α will present behaviour as shown in Figure 7. For fluids such as air (Pr = 0.71) and gas-mixture (Pr = 0.1) the model of Cebeci show finite values of Pr_t at the wall. The same does not happen to very low Prandtl number fluids such as liquid mercury (Pr = 0.025) and liquid sodium (Pr = 0.0058). The fact is that for the region $\varepsilon_H/\alpha < 0.5$, for liquid metals, the turbulent Prandtl, calculated by model of Cebeci, increases significantly, being apparent that this model is not able to predict Pr_t of flow of very low Prandtl number fluids in the range $\varepsilon_H/\alpha < 2$.

For the case of liquid sodium the model of Cebeci follow very closely experimental data at the region $\varepsilon_H/\alpha > 0.5$.

The model Kays, represented by equation 16, was calculated for all fluids studied here and is present in Figure 8. Excluding air the calculated curves of all other fluids collapsed in one curve which follow closely experimental data for liquid sodium (Pr = 0.0058). It is also interesting to observe that other expression proposed by Kays (Eq. 17) presented the same behaviour as the one presented by equation 16, but with higher calculated values of the turbulent Prandtl number, when compared with experimental results. The calculated curves of Pr_t, for all fluids, using equation 17, are shown in Figure 9. It seems that both expressions proposed by Kays for the turbulent Prandtl number for low and very low Prandtl number fluids do not discriminate between one and another fluid collapsing all to one single curve for each expression.

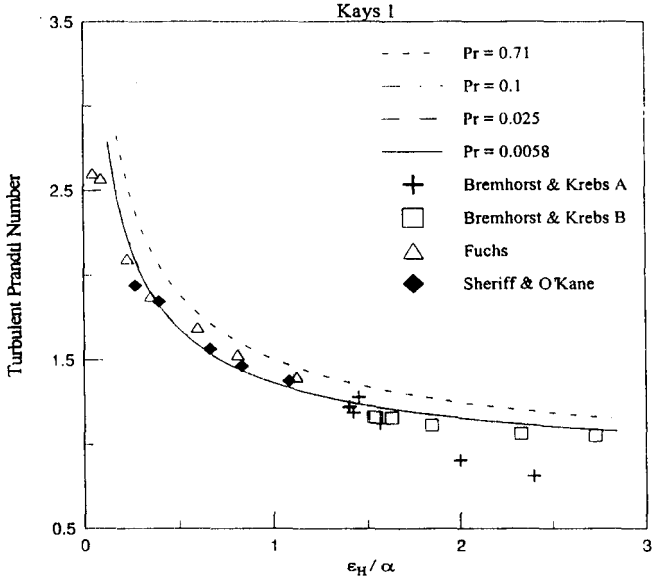

Figure 8. Turbulent Prandtl Number calculated from various and Kays (1) as function of ε_H/α.

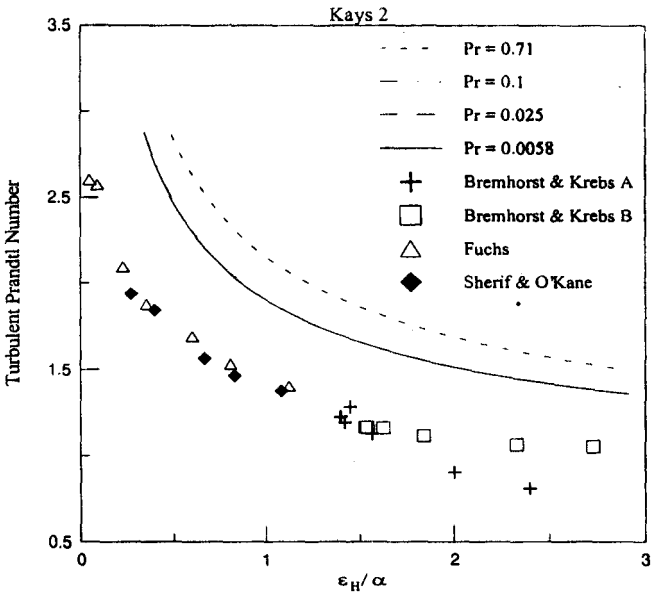

Figure 9. Turbulent Prandtl Number calculated from various and Kays (II) as function of ε_H/α.

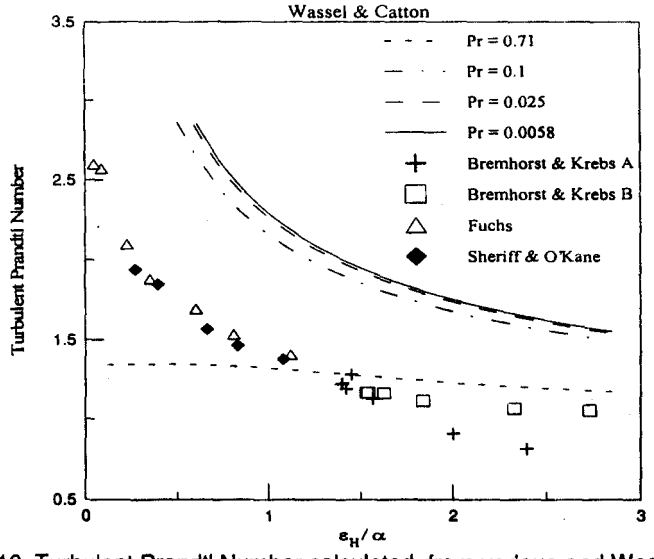

Figure 10. Turbulent Prandtl Number calculated from various and Wassel and Catton (II) as function of ε_H/α.

The model of Wassel and Catton for Pr_t represented by equation 18 is shown in Figure 10. The model of Wassel and Catton did show the usual behaviour of Pr_t for the fluid air. However for the case of low and very low Prandtl number fluids, as can be seen in that figure, calculated value of Prandt are higher than experimental data of liquid sodium, and practically all curves collapse in one curve showing the same aspect of the expressions of Kays.

Considering that the most available experimental data of low and very low Prandtl number fluids is for liquid sodium, it is interesting to make comparative analysis of all proposed models relative to such fluid.

In Figure 11 there are experimental data on liquid sodium taken from Bremhorst and Krebs, from Fuchs and from Sheriff and O'Kane and calculated Pr_t using call models studied here.

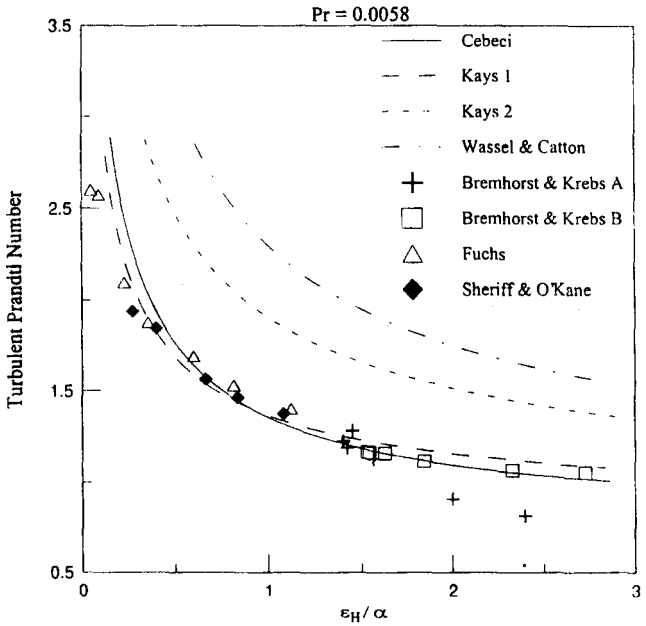

Figure 11. Turbulent Prandtl Number calculated from various models with experimental data of liquid sodium.

Experimental results of Fuchs and of Sheriff and O'Kane cover the range $\varepsilon_H/\alpha < 1$. For the range $0.2 < \varepsilon_H/\alpha < 1$ results of Fuchs and Sheriff and O'Kane are practically the same. Fuchs present some experimental results for the region $\varepsilon_H/\alpha < 0.2$ indicating that Pr_t approach a limit of 2.6, as seen in Figure 11. For the region $\varepsilon_H/\alpha > 1$ available experimental results for liquid sodium are due to Bremhorst and Krebs. Exclusively for the case of liquid sodium experimental results of many researchers evidently indicate that when $\varepsilon_H/\alpha < 0.2$ the turbulent Prandtl number

increases significantly but to a limited valued of 2.6 Pr_t will decrease to 1.3 in the range $0.2 \leq \varepsilon_H/\alpha \leq 1$ and Pr_t will be approximately 0.9 - 1.0 when $\varepsilon_H/\alpha > 3$.

As seen in Figure 11 one model of Kays (equation 17) and model of Wassel and Catton overpredict the turbulent Prandtl number relative to experimental data of liquid sodium. For the region $\varepsilon_H/\alpha > 0.2$ the model of Cebeci and the other model of Kays (equation 16) follow experimental results very closely though the model of Kays could not discriminate among fluids, practically collapsing to one single curve. For the situation where $\varepsilon_H/\alpha < 0.2$ all models point to values going to infinity although experimental results point to limited value for Pr_t.

CONCLUSIONS

Various models of turbulent Prandtl number for low and very low Prandtl number were studied in this article. There were investigated model of Cebeci, models of Kays, and model of Wassel and Catton. It was verified that different from studying the relationship Pr_t against dimensionless wall distance y+ the relationship Pr_t against eddy diffusivities of heat ε_H/α provides a better tool which make it easier to compare models. Experimental data for liquid sodium pointed that Pr_t is 2.6 when $\varepsilon_H/\alpha \rightarrow 0$, Pr_t goes to 1.3, when $\varepsilon_H/\alpha \rightarrow 1$ and Pr_t goes to 0.9 - 1.0 when $\varepsilon_H/\alpha > 3$; The wall distance based model of Cebeci was the only one which followed closely experimental data and which discriminated better among various low and very low Prandtl number fluid. One model of Kays followed very closely experimental however could not discriminate among fluid, collapsing all to one single curve. None of the models could follow experimental data on the region $\varepsilon_H/\alpha < 0.2$ but in that region the molecular conduction dominates and Pr_t is of little importance.

REFERENCES

Bremhorst, K. and Krebs, L. "Experimental Determined Turbulent Prandtl Numbers in Liquid Sodium at Low Reynolds Numbers", International Journal of Heat and Mass Transfer, vol. 35, n. 2, pp. 351-359, 1992.

Bremhorst, K. and Krebs, L. "Eddy Diffusivity Based Comparisons of Turbulent Prandtl Number for Boundary Layer and Free Jet Flows With References to Fluids of Very Low Prandtl Number", Journal of Heat Transfer, vol. 115, pp. 549-552, 1993.

Cebeci, T. "Laminar and Turbulent Incompressible Boundary Layer on Slender Bodies of Revolution in Axial Flow", ASME Journal of Basic Eng., vol. 92, pp. 545-554, 1970.

Cebeci, T. "A Model for Eddy Conductivity and Turbulent Prandtl Number", ASME Journal of Heat Transfer, vol. 95C, pp. 227-234, 1973.

De Lima, L.C.; Silva, M.C. and Miranda, R.F. "Comparative Analysis of Different Models for the Turbulent Prandtl Number", accepted to the Journal of the Brazilian Society of Mechanical Sciences, 1988.

De Lima, L.C. and Pereira Filho, H.V. "Turbulent Boundary Layer with Heat Transfer on Curved Surfaces" (in Portuguese), VII Brazilian Congress of Mechanical Engineering, pp. 107-114, Uberlândia MG, Brazil, 1983.

Jischa, M. and Rieke, H.B. "About the Prediction of Turbulent Prandtl and Schmidt Numbers from Modeled Transport Equations", International Journal of Heat and Mass Transfer, vol. 22, pp. 1547-1555, 1979.

Kays, W. M., "Turbulent Prandtl Number - Where Are We?", ASME Journal of Heat Transfer, Vol. 116, pp. 284-295, 1994.

Na, T.Y. and Habib, I.S. "Heat Transfer in Turbulent Pipe Flow Based on a New Mixing Lenght Model", Appl. Sci. Res., vol. 28, pp. 415, 1973.

Reynolds, A. J., "The Prediction of Turbulent Prandtl Schmidt Numbers", International Journal of Heat and Mass Transfer, Vol. 18, pp. 1055-1069, 1975.

Sheriff, N. and O'Kane, D.T. "Sodium Eddy Diffusivity of Heat Measurements in a Circular Duct", International Journal of Heat and Mass Transfer, vol. 24, pp. 205-211, 1981.

Wassel, A. T., and Catton, I., "Calculation of Turbulent Boundary Layer Over Flat Plates with Different Phenomenological Theories of Turbulence and Variable Turbulent Prandtl Number", International Journal of Heat and Mass Transfer, Vol. 16, pp. 1547-1563, 1973.

DYNAMICS OF COHERENT VORTICES IN MIXING LAYERS USING DIRECT NUMERICAL AND LARGE-EDDY SIMULATIONS

Jorge H. SILVESTRINI

Departamento de Matemática Pura e Aplicada
Universidade federal do Rio Grande do Sul
Av. Bento Gonçalves 9500
91501-970 Porto Alegre – RS, Brasil
e-mail: silvestr@mat.ufrgs.br

DYNAMICS OF COHERENT VORTICES IN MIXING LAYERS USING DIRECT NUMERICAL AND LARGE-EDDY SIMULATIONS

Abstract.

Coherent vortices in turbulent mixing layers are investigated by means of Direct Numerical Simulation (DNS) and Large-Eddy Simulation (LES). Subgrid-scale models defined in spectral and physical spaces are reviewed. The new "spectral-dynamic viscosity model", that allows to account for non-developed turbulence in the subgrid-scales, is discussed. Pseudo-spectral methods, combined with sixth-order compact finite differences schemes (when periodic boundary conditions cannot be established), are used to solve the Navier-Stokes equations. Simulations in temporal and spatial mixing layers show two types of pairing of primary Kelvin-Helmholtz (KH) vortices depending on initial conditions (or upstream conditions): quasi-2D and helical pairings. In both cases, secondary streamwise vortices are stretched in between the KH vortices at an angle of 45° *with the horizontal plane. These streamwise vortices are not only identified in the early transitional stage of the mixing layer but also in self-similar turbulence conditions. The Re dependence of the "diameter" of these vortices is analyzed. Results obtained in spatial growing mixing layers show some evidences of pairing of secondary vortices; after a pairing of the primary Kelvin-Helmholtz (KH) vortices, the streamwise vortices are less numerous and their diameter has increased than before the pairing of KH vortices.*

Key words: *Coherent Vortices, Mixing Layer, Direct Numerical Simulation, Large-Eddy Simulation, Subgrid Scales Models.*

Introduction

Since coherent vortices play a crucial role in mass, heat and momentum transport in geophysical and industrial turbulent flows, their identification has been one of the main objectives of research in turbulence theory in the last years. To be characterized as coherent three conditions are required (Lesieur, 1997):

i) a concentration of vorticity ω enough so that fluid trajectories can wind around,

ii) with a life time longer than their local turnover time scale ω^{-1} and,

iii) that has the property of unpredictability, in the sense of the sensibility to initial or boundary conditions.

These coherent vortices are normally called by the name of the hydrodynamic instability which originated them (Kelvin-Helmholtz vortices, Görtler vortices), or by their orientation (streamwise vortices), or by their form (hairpins, lambda vortices). Here is presented some numerical evidences of streamwise vortices, their origin and evolution, in transitional and turbulent mixing layers.

Two numerical techniques for the simulation of turbulent flows were used: Direct Numerical Simulation (DNS) and Large-Eddy Simulation (LES). In DNS, all turbulent scales should be simulated explicitly, in three dimensions of space, from the integral scale l down to the Kolmogorov scale $(\nu^3/\epsilon)^{1/4}$ for free shear flows (in wall shear flows the dissipative scale is the viscous thickness ν/u_*). This implies high-order schemes, small time steps, very fine 3D grids and, in practice, low Reynolds numbers, since it can be proved that the total number of degrees of freedom to represent a turbulent flow is of the

order of R_l^3. This is the main restriction of DNS to simulate turbulent flows of practical interest.

Since, in general, one is interested in the large scales of the flow, which contains most of the information about momentum and heat transfer, LES strategy consists in simulating, explicitly and in three dimensions, all motion larger than a certain cut-off scale. The smaller scales are modeled through a *sub-grid* model.

Full pseudo-spectral methods (for temporal mixing layers) and pseudo-spectral methods combined with high order compact finite differences methods (for spatial developing mixing layers) are used to solve the incompressible Navier-Stokes equations. Within this context, it is firstly presented, the general formalism of LES carried out in spectral space for the case where periodicity may be assumed in the three directions *i.e. the temporal case*. Extension to flows where only two directions may be assumed as periodic *i.e. the spatial mixing layer*, is then briefly described. The subgrid-scale modelisation strategy is explained and some subgrid-scale models defined in spectral and physical space are described. In particular, the new *spectral-dynamic viscosity model*, is presented. Finally some DNS and LES results of temporal and spatial mixing layers, denoting the origin and evolution of streamwise vortices, are discussed.

Large-Eddy Simulation

In this section, the LES formalism for incompressible flows in spectral space is considered. The detailed description of this formalism may be found elsewhere (Lesieur and Métais, 1996; Lesieur, 1997). For compressible flows, the LES formalism may be found in Comte *et.al.* (1994), Ducros *et.al.* (1996) and Silvestrini (1996), among others.

Full Periodic Problem

Let $\hat{u}(k,t)$ and $\hat{\theta}(k,t)$ be the spatial Fourier transform of the velocity $u(x,t)$ and the scalar $\theta(x,t)$ fields of an incompressible flow. Assuming periodicity in the three spatial directions, and using pseudo-spectral methods (Canuto *et.al.*, 1988), the conservation equations of mass, momentum and scalar read in spectral space as :

$$\hat{u}(k,t) \cdot k = 0, \tag{1}$$

$$(\frac{\partial}{\partial t} + \nu k^2)\ \hat{u}(k,t) = F[F^{-1}(\hat{u}(k,t)) \times F^{-1}(\hat{\omega}(k,t))] - ik\hat{P}, \tag{2}$$

$$(\frac{\partial}{\partial t} + \kappa k^2)\ \hat{\theta}(k,t) = -ik.F[F^{-1}(\hat{\theta}(k,t))F^{-1}(\hat{u}(k,t))], \tag{3}$$

where $k = (k_x, k_y, k_z)$ stands for the wave number vector, F denotes the Fourier transform operator, ω is the vorticity vector and $P = p/\rho + u \cdot u/2$, is the generalized pressure. The pressure P is eliminated in eq. (2) by projection on the plane orthogonal to k, in order to respect the incompressibility condition.

The LES formalism introduces the filtering operation :

$$\bar{\hat{f}}(k) = \hat{G}(k)\hat{f}(k), \tag{4}$$

where $\hat{G}(k)$ is the Fourier transform of the filter function $G(x)$. Here is used the cut-off filter in Fourier space, defined as :

$$\hat{G}(k) = \begin{cases} 1, & \text{if } |k| \leq k_c, \\ 0, & \text{otherwise} \end{cases}, \tag{5}$$

where $k_c = \pi/\Delta$ is the cutoff wave number associated to the grid mesh Δ. Introducing the operation (5) in Eq. (1), (2) and (3), the LES equations read :

$$(\frac{\partial}{\partial t} + \nu k^2)\ \bar{\hat{u}}(k,t) = t_{|k|<k_c}(k,t) + t_{|k|>k_c}(k,t), \tag{6}$$

$$(\frac{\partial}{\partial t} + \kappa k^2)\ \bar{\hat{\theta}}(\boldsymbol{k},t) = t^{\theta}_{|\boldsymbol{k}|<k_c}(\boldsymbol{k},t) + t^{\theta}_{|\boldsymbol{k}|>k_c}(\boldsymbol{k},t). \tag{7}$$

The terms on the r.h.s of Eqs. (6) and (7) denote the supergrid-scale and sub-grid scale transfers due to nonlinear terms involved in Navier-Stokes equations in Fourier space. The supergrid-scale transfers need no modelling since they can be explicitly calculated in the large-eddy simulation as :

$$t_{|\boldsymbol{k}|<k_c}(\boldsymbol{k},t) = \left\{\Pi\{F[F^{-1}(\bar{\tilde{\boldsymbol{u}}}(\boldsymbol{k},t)) \times F^{-1}(\bar{\tilde{\boldsymbol{\omega}}}(\boldsymbol{k},t))]\}\right\}_{|\boldsymbol{k}|<k_c} \tag{8}$$

$$t^{\theta}_{|\boldsymbol{k}|<k_c}(\boldsymbol{k},t) = \left\{-i\boldsymbol{k}.F[F^{-1}(\bar{\tilde{\theta}}(\boldsymbol{k},t))F^{-1}(\bar{\tilde{\boldsymbol{u}}}(\boldsymbol{k},t))]\right\}_{|\boldsymbol{k}|<k_c} \tag{9}$$

where Π is the projector on the plane normal to the wave number vector $\boldsymbol{k}$. The unknown subgrid-scale transfers $t_{|\boldsymbol{k}|>k_c}(\boldsymbol{k},t)$ and $t^{\theta}_{|\boldsymbol{k}|>k_c}(\boldsymbol{k},t)$, should be modelled. Following Kraichnan ideas (Kraichnan, 1976), it was proposed to model these transfers with the aid of the spectral eddy viscosity and diffusivity (Chollet and Lesieur, 1981), as :

$$t_{|\boldsymbol{k}|>k_c}(\boldsymbol{k},t) = -\nu_t(k,k_c,t)\ k^2\bar{\hat{\boldsymbol{u}}}(\boldsymbol{k},t), \tag{10}$$

$$t^{\theta}_{|\boldsymbol{k}|>k_c}(\boldsymbol{k},t) = -\kappa_t(k,k_c,t)\ k^2\bar{\hat{\theta}}(\boldsymbol{k},t), \tag{11}$$

where models to calculate $\nu_t(k,k_c,t)$ and $\kappa_t(k,k_c,t)$ should be introduced.

Partial Periodic Problem

Now we want to take into account the streamwise developing character of the mixing layer and therefore we need to change the temporal problem to a spatial developing problem, where no periodic conditions may be assumed in the streamwise direction.

Let now $\hat{\boldsymbol{u}}(x,\boldsymbol{k}_{2D},t)$ and $\hat{\theta}(x,\boldsymbol{k}_{2D},t)$ be the spatial bidimensional Fourier transform of the velocity and passive scalar fields, where we assume that x is the streamwise no

periodic direction and $\boldsymbol{k}_{2D} = (k_y, k_z)$ is the wave vector defined in yz plane. With this decomposition the mass conservation equation read now as :

$$\frac{\partial \hat{u}}{\partial x} + i(k_y \hat{v} + k_z \hat{w}) = 0, \tag{12}$$

and the momentum and passive scalar conservation equations as :

$$\left\{ \frac{\partial}{\partial t} - \nu \left(\frac{\partial^2}{\partial x^2} - k^2 \right) \right\} \hat{\boldsymbol{u}} = \widehat{\boldsymbol{u} \times \boldsymbol{\omega}} - \nabla \hat{P}, \tag{13}$$

$$\left\{ \frac{\partial}{\partial t} - \kappa \left(\frac{\partial^2}{\partial x^2} - k^2 \right) \right\} \hat{\theta} = -\nabla \cdot \widehat{\boldsymbol{u}\theta}, \tag{14}$$

where $\nabla = (\partial/\partial x, ik_y, ik_z)$ and $\widehat{\ }$ denotes the Fourier transform.

The main difference between the system of Eqs. (12,13,14) with reference to the system Eqs. (1,2,3), is that now the pressure can no longer be eliminated by projection and then we should solve the Poisson equation that arrives when we take $\nabla\cdot$ of Eq. 13, that is :

$$\nabla \cdot \nabla \hat{P} = \nabla \cdot \widehat{\boldsymbol{u} \times \boldsymbol{\omega}}. \tag{15}$$

Since we have now two directions where the variables are described in spectral space and one in physical space, two filters should be introduced: the cutoff in spectral space (the 2D counterpart of Eq. (5)) and a top-hat filter for the physical direction, which may be defined as :

$$G(x) = \begin{cases} 1, & \text{if } |x| \leq \frac{\Delta x}{2}, \\ 0, & \text{otherwise} \end{cases}, \tag{16}$$

The filtering operation applied to Eqs. (13,14, 15) give us the LES equations to be used in the spatial developing mixing layer case.

Subgrid-Scale Models

Here will be discussed some subgrid-scale models developed at the Grenoble turbulence school (for a complete description of these models see Lesieur & Métàis, 1996). Others models developed elsewhere may be found in Smagorinsky (1963), Germano *et al.* (1991) and Ghosal *et al.* (1995). Comparison of some of these subgrid-scale models in academic tests cases were reported in Comte *et al.* (1994) and Comte *et al.* (1995).

In Spectral Space

Assuming a $k^{-5/3}$ inertial range at wave numbers greater than k_c, it was proposed (Chollet & Lesieur, 1981) to renormalize the eddy viscosity with the aid of $[E(k_c,t)/k_c]^{\frac{1}{2}}$, where $E(k,t)$ is the three-dimensional kinetic-energy spectrum. More precisely, the eddy viscosity in spectral space writes

$$\nu_t(k,k_c,t) = K(k/k_c)\ \nu_t^{\infty}(k_c,t) \tag{17}$$

$$\kappa_t(k,k_c,t) = C(k/k_c)\ \kappa_t^{\infty}(k_c,t) \tag{18}$$

with

$$\nu_t^{\infty}(k_c,t) = 0.267\ \left[\frac{E(k_c,t)}{k_c}\right]^{\frac{1}{2}} \tag{19}$$

$$K(k/k_c) = 1 + 34.5\ e^{-3.03(k_c/k)}\ . \tag{20}$$

The constant 0.267 was obtained with the aid of the EDQNM (Eddy-Damped Quasi-Normal Markovian) non-local interactions theory (Lesieur, 1997), using leading-order expansions in powers of the small parameter k/k_c, and assuming that $E(k)$ follows a

Kolmogorov law extending above the cutoff. In eq. (20), $K(k/k_c)$ displays a strong overshoot (cusp-behaviour) in the vicinity of $k/k_c = 1$ (Kraichnan, 1976). This is due to local or semi-local interactions in the neighborhood of k_c. If one goes back to physical space, the plateau part of the spectral eddy viscosity corresponds to a classical eddy-viscosity formulation, which assumes, in fact, a separation of scales between supergrid and subgrid scales. This is of course wrong, and fixes the limits of the eddy-viscosity formulation. Therefore, the cusp part of the spectral eddy viscosity is important since it contains effects beyond the classical eddy-viscosity concept. The eddy-diffusivity was found to have, qualitatively, the same behaviour, with a corresponding turbulent Prandtl number $P_r^t = \nu_t^\infty / \kappa_t^\infty$ approximately constant and taken equal to 0.6 (Lesieur, 1997).

The major drawback of the eddy viscosity described by Eq. (17) is that it assumes a Kolmogorov spectrum at the cutoff. This condition is obviously not satisfied in transitional regions, or close to a wall, even at high Reynolds numbers. To avoid this problem, eddy coefficients may now be evaluated in a less restrictive context than previously. Assuming that the kinetic energy spectrum follows a power law $E(k) \propto k^{-m}$ instead of a Kolmogorov law, it is found (Métais & Lesieur, 1992) :

$$\nu_t^\infty(k_c,t) = 0.31\ C_k^{-\frac{3}{2}}\ \frac{5-m}{m+1}\ (3-m)^{\frac{1}{2}}\ \left[\frac{E(k_c,t)}{k_c}\right]^{\frac{1}{2}} \tag{21}$$

where the Kolmogorov constant $C_k = 1.4$ and the associated turbulent Prandtl number

$$P_r^t = 0.18\ (5-m)\ . \tag{22}$$

The model defined by equations (17), (21) and (22) was called the ***spectral-dynamic model*** (SDM). The model was used by Lamballais (1996) for LES of turbulent channel flow with excellent results. A full presentation of the model may be found in Silvestrini *et al.*, 1998.

Note finally that eq. (21) is valid only for $m \leq 3$. For $m > 3$, the choice was to set the eddy-viscosity equal to zero. From a practical viewpoint, this may be justified by considering that if the kinetic energy spectrum is steep enough, there is no energy pile-up at high wave numbers, so that no subgrid-scale modelling is actually necessary.

In Physical Space

To determine eddy viscosities in physical space, the kinetic energy at the smallest resolved scale $\Delta = \pi/k_c$ should be measured. One of these local spectra is $F_{2\Delta}(\boldsymbol{x}, t)$, the second-order structure function of the resolved velocity field, defined as :

$$F_{2\Delta}(\boldsymbol{x}, t) = \left\langle \|\tilde{\boldsymbol{u}}(\boldsymbol{x} + \boldsymbol{r}, t)) - \tilde{\boldsymbol{u}}(\boldsymbol{x}, t)\|^2 \right\rangle_{\|\boldsymbol{r}\|=\Delta}, \tag{23}$$

and related to the three dimensional kinetic energy spectrum in isotropic turbulence through Batchelor's formula (Batchelor, 1953) :

$$F_{2\Delta}(\boldsymbol{x}, t) = 4 \int_0^{k_c} E(k, t) \left(1 - \frac{\sin k\Delta}{k\Delta}\right) dk. \tag{24}$$

In the case of infinite Kolmogorov spectra, energy-conservation arguments yield the *structure-function model* (SF model) (Métais & Lesieur, 1992), defined by

$$\nu_t^{SF}(\boldsymbol{x}, t) = 0.105\ C_K^{-3/2}\ \Delta\ \sqrt{F_{2\Delta}(\boldsymbol{x}, t)}, \tag{25}$$

As it involves velocity increments instead of derivatives, the SF model has the advantage of being defined independently of the numerical scheme used. It is nevertheless not much better for transitional flows than the Smagorinsky model: low wave number velocity fluctuations corresponding to unstable modes yield ν_t's so large that affects the growth rate of weak instabilities, like Tollmien-Schlichting waves (Ducros, 1995).

One way of remedying this is to apply a high-pass filter onto the resolved velocity field before computing its structure function (Ducros *et al.* 1996). With a triply-iterated second-order finite-difference Laplacian filter denoted $\tilde{}$, one finds $\tilde{E}(k)/E(k) \approx 40^3\ (k/k_c)^9$ for all k, almost independently of the grid mesh and the velocity field. With the same formalism used for the structure-function model, this yields the *filtered structure-function model* (FSF model), defined by :

$$\nu_t^{FSF}(\boldsymbol{x},t) = 0.0014\ C_K^{-3/2}\ \Delta\ \sqrt{\tilde{F}_{2\Delta}(\boldsymbol{x},t)}. \tag{26}$$

With this model it was possible to perform a LES of a spatially-growing boundary layer (at Mach 0.5) between $Re_x = 3.3\ 10^5$ and $1.14\ 10^6$, which widely encompasses the transition region (Ducros *et al.*1996).

Mixing Layers Simulations

In this section simulations of temporal and spatial growing mixing layers are presented. The temporal approximation is obtained by taking a reference frame moving with the average velocity $(U_1+U_2)/2$ (where U_1 and U_2 are the velocity of the two parallel streams).

Temporally Growing Mixing Layer

A DNS and a LES of temporal mixing layers differing in the Reynolds number will be presented at first. In both cases, the temporal mixing layers are initiated by a hyperbolic-tangent velocity profile, $U \tanh 2y/\delta_i$ to which is superposed a small quasi-2D random perturbation. δ_i denotes the initial vorticity thickness. Then we will analyze the influence of the initial conditions by showing coherent vortices formed in two LES which differ only

in the initial perturbation added to the base profile.

For all the simulations the computational domain is cubic of side $L_x = L_y = L_z = 4\ \lambda_a$, where $\lambda_a = 7\ \delta_i = 2\pi/k_a$ is the wavelength of the most amplified streamwise mode predicted by the inviscid linear-stability theory (Michalke, 1964). Such a domain allows two successive pairings of Kelvin-Helmholtz (KH) vortices during a simulation. Periodic boundary conditions are imposed in the streamwise (x) and spanwise (z) directions, while free-slip boundary conditions are employed for $y = \pm L_y/2$, by means of pure sine or cosine expansions. The time derivative is approximated by a third-order low-storage Runge-Kutta scheme (Williamson, 1980). Aliasing errors (Canuto *et al.* 1988) are minimized by taking more collocation points in physical space (120^3) than Fourier modes (96^3).

The DNS with an initial Reynolds number of $Re_{\delta_i} = U\delta_i/\nu = 100$, is presented first. This simulation is called DNSQ2DT. Fig. 1 denotes the vorticity structures of the mixing layer by visualization of vorticity lines. The threshold value of the vorticity norm is $\omega_i/3$ (ω_i being the initial maximal vorticity modulus equal to $2U/\delta_i$). At $t = 35\delta_i/U$, the first pairing of Kelvin-Helmholtz (KH) vortices is complete. At this time, two KH vortices can be seen, with stretching of vorticity lines in between. These streamwise vortices are called hairpins and are characterized (as we will see) by pairs of vortices of different signs. At $t = 70\delta_i/U$, the end of the simulation, only one KH vortex remains. The side views show the stretching of vorticity lines at an angle near of 45° with respect to a horizontal plane. The origin of these streamwise vortices, which has been observed in laboratory experiments for a long time (Konrad 1976, Bernal & Roshko 1986), may be explained by the intense deformation rate imposed by the KH vortices in the stagnation zones. The KH vortices strain the vorticity lines, which are originally oriented in the spanwise direction,

and align them in the streamwise direction.

The stretching of vorticity lines may be analyzed considering the vorticity equation for a perfect fluid :

$$\frac{D\omega_i}{Dt} = \omega_j S_{ij}, \tag{27}$$

and assuming that the vorticity in the stagnation region is weak ($\|\omega_j\| << \|S_{ij}\|$). Eq. (27) gives the main direction of straining of streamwise vorticity of 45° with respect to a horizontal plane.

Now, results from a LES using the spectral-dynamic model (DM) with an initial Reynolds number of $Re_{\delta_i} = 2000$, are presented. This simulation is called LESQ2DT. In this LES, the spectral-dynamic model is used in its "standard" version, defined by equations (17),(20) and (21). The spectrum slope m is calculated at each time step (and at each sub-step of the Runge-Kutta method), from the three-dimensional kinetic energy spectrum, using a least-square method applied to wave numbers ranging between $k_c/2 < k < k_c$.

The time evolution of the slope of the three-dimensional kinetic energy spectrum close to the cutoff (m), and of $E(k_c)$ is presented on Fig. 2. Until $t = 10\ \delta_i/U$ no eddy-viscosity model is applied since $m \leq 3$. Between $t = 10\ \delta_i/U$ (time of KH vortices roll-up) and $20\ \delta_i/U$ (beginning of the first pairing), the slope of the 3D kinetic energy spectrum takes a rather constant value of $m = 2.5$. After that, and until the end of the simulation, m tends asymptotically to 2. At this time, the Reynolds number based on the local vorticity thickness δ (defined as $2U/|\langle\omega_z\rangle(y=0)|$) is $Re_\delta = 24000$.

In Fig. 3 can be seen the time evolution of the non-normalized three-dimensional kinetic energy spectrum, for the simulation LESQ2DT. Mixing-layer experiments at this Reynolds number do possess a very good $k^{-5/3}$ Kolmogorov law over a quite long range at large wave

numbers. The figure shows a Kolmogorov law only over a short range, whereas the slope is steeper near k_c, (close to -2, in agreement with Fig. 2). This is the main disagreement between the spectral dynamic model and experiments in mixing layers.

Fig. 4 shows the vorticity-modulus isosurfaces of the quasi 2D mixing layer at $t = 35$ and $75\delta_i/U$ with a threshold value of ω_i. The figure shows the moment of the two pairing of KH vortices and the intense stretching of streamwise vortices. Note that the isovalue has increased three times with reference to the previous DNS. At the end of the simulation, there is only one KH vortex. Note finally the presence of intense small-scale vortices.

For the two simulations presented, DNSQ2DT and LESQ2DT, we analyze now the evolution of the "diameter" of the streamwise vortices with viscosity. Fig. 5 shows isolines of vorticity modulus in the same transversal plane and at the same time, for the DNS at Re=100 and for LES at Re=2000. In the DNS we can measure $d \approx 2\delta_i$ while in the LES $d \approx \delta_i$. These values may be compared with an experimental one, $d \approx 1.3\delta_i$, obtained at $Re \approx 1400$ (Huang & Ho, 1990). The agreement is fairly good and the tendency is correct. This shows the strength of LES to reproduce features of turbulent flows.

Now, we present results of a LES (also with the SDM model) where the initial conditions are defined by the same base profile but the perturbation is a three-dimensional isotropic one. The initial Reynolds number is also $Re_{\delta_i} = 2000$. The simulation was stopped at $t = 60\ \delta_i/U$ and is called LES3DT.

Figure 6 shows the temporal evolution of m and $E(k_c)$ for the whole simulation. The spectrum slope decreases initially from the high initial value ($m \approx 9$). At $t = 10\ \delta_i/U$, which correspond to the time of the vortex roll-up, we have $m \approx 3$. It means that the eddy-viscosity was inactive (see equation 21) up to this instant, and that all the dissipation was

due to molecular viscosity. Hence instabilities are allowed to grow without any influence of the eddy viscosity, which is certainly desirable. Between $t = 10$ and 30 δ_i/U (moment of the first pairing), the slope m decreases from 3 to 2. After that, m remains very close to 2 up to the end of the simulation. The temporal evolution of $E(k_c)$, which reaches its maximum at $t = 25\ \delta_i/U$ and then decreases slowly, might indicates that a "quasi-equilibrium state" characteristic of the self-similar regime was attained.

Statistics of the recorded velocity profiles were used to determine the temporal evolution of the local vorticity thickness, and compared with experimental data of spatially-growing mixing layers carried out by Bell and Mehta (1990). The l.h.s. of figure 7 shows $\delta(t)$. A fairly good linear growth is established very early at a rate of $U^{-1}d\delta/dt = 0.19$. During the first pairing ($t \approx 30$), the spreading slows down, and then it starts rising again at the same linear rate. In spite of the differences in the spatial growth of mixing layers reported in several works (Silvestrini, 1996), and also between the spatial and the temporal problem, the growth rate found here is very close the traditionally accepted mixing layer spatial growth of 0.18 reported in Brown and Roshko's experiments (Brown and Roshko, 1974).

The r.h.s. of figure 7 and figure 8 show, respectively, the mean streamwise velocity and velocity components variances at the end of the simulation ($t = 60\ \delta_i/U$). The agreement between numerical and experimental data is good and seems to indicate that a self-similar state has been established at the end of the simulation, as far as mean and variances of velocity are concerned. To confirm this point, normalized three-dimensional kinetic energy spectra are presented on figure 9 (the normalization is made by U and the local vorticity thickness δ). The good collapse of the different spectra for $t = 50$, 55 and 60 δ_i/U is another good indicator that a self-similar regime is attained. Note also that Bell & Metha

have considered that a self-similar regime was established at a streamwise distance of about 250 δ_i from the splitter plate, with the velocity ratio $\lambda = \dfrac{U_1 - U_2}{U_1 + U_2} = 0.25$. If this distance is transformed in a corresponding elapsed time for a temporal mixing layer, using the convection velocity $U_c = (U_1 + U_2)/2$ and writing

$$t_{self} = \frac{x_{self}}{U_c} = \lambda \, \frac{x_{self}}{U} \, , \tag{28}$$

the value found $t_{self} = 62.5 \; \delta_i/U$ is very close to the time considered for present statistics.

Let us look now at the three-dimensional vortical structure. Figure 10 presents a perspective view of vorticity-modulus isosurfaces (threshold ω_i), at $t = 14$, 26, 40 and 60 δ_i/U. At $t = 14 \; \delta_i/U$, one can see a dislocated array of four rolling-up Kelvin-Helmholtz vortices, similar to the configuration found in previous DNS of Comte *et al.* (1992) and laboratory experiments of Chandrsuda *et al.* (1978), and called "helical pairing". Secondaries streamwise vortices are also stretched by the deformation field induced between the big vortices. At $t = 26 \; \delta_i/U$ large structures pair. The subsequent pairing is more difficult to identify from the vorticity isosurfaces, mainly because of a rapid growth of small-scale structures. At the end of the simulation ($t = 60 \; \delta_i/U$), the vorticity field displays only the presence of intense small-scale vortices, with no obvious preponderant orientation. By contrast, the low-pressure field (see figure 11) indicates the presence of one big quasi two-dimensional vortex, stretching thinner longitudinal vortices. Note however that the computational domain is too small at this instant, with regard to the vortex size.

Spatially Developing Mixing Layer

Here, results from a LES using the filtered structure-function (26) of a spatial growing mixing layer are presented. The simulation is called FSFQ2DS. The numerical code used,

that solves Eqs. (13,15), combines pseudo-spectral methods in the spanwise and transverse directions with compact finite-difference of sixth order (Lele, 1992) in the streamwise direction. Free-slip conditions are still imposed upon the boundaries. Non-reflective outflow boundary conditions are approximated by a multi-dimensional extension of Orlansky's discretization scheme. The temporal integration is performed by means of a low-storage 3rd order Runge-Kutta scheme, with a fractional step procedure for the pressure-gradient correction.

The profile prescribed at the inlet is :

$$\bar{u}(y) = \frac{U_1 + U_2}{2} + \frac{U_1 - U_2}{2} \tanh \frac{2y}{\delta_i}. \tag{29}$$

plus small-amplitude random perturbations. The velocity ratio is chosen as: $R = (U_1 - U_2)/(U_1 + U_2) = 0.5$. The domain's dimension are $L_x = 112\delta_i$, $L_y = 28\delta_i$ and $L_z = 14\delta_i$, and the grid mesh is cubic with $384 \times 96 \times 48$ collocation points. The last record from a previous DNS run a $Re = 100$ was used to initialize the FSFQ2DS run (Silvestrini, 1996).

Fig. 12 shows an isosurface of vorticity modulus at the end of the simulation, with a threshold value of $2/3\omega_i$ In the figure may be identified, from left to right, two KH vortices undergoing a first pairing, after that a cluster of three KH vortices undergoing also a first pairing, and, at the end, a billow made of 4 fundamental KH vortices, whose second pairing is in progress. Between the KH vortices, streamwise vortices are stretched by the same mechanism observed in temporal mixing layers.

Fig. 13 shows an isosurface of streamwise vorticity. The black and grey colors, denoting pairs of vortex of different sign, identify the "legs" of the hairpins. The figure enables us to analyze the evolution of the diameter of the streamwise vortices with the pairing of the KH vortices. After the pairing of the three KH vortices, streamwise vortices are less numerous

but bigger than before the pairing. More quantitatively, if two transversal planes are fixed, before ($x = 58\delta_i$), and after this pairing ($x = 88\delta_i$), the diameter of the streamwise vortices can be measured. A loose estimation gives $d_{bef} \approx 0.5\delta_i$ and $d_{aft} \approx \delta_i$, which may be transformed to the local vorticity thickness $d_{bef} \approx 0.13\delta$ and $d_{aft} \approx 0.14\delta$ with the aid of the streamwise evolution of the vorticity thickness (Silvestrini, 1996). These values seem to reinforce the idea that a pairing of KH vortices induces a merging of streamwise vortices, with their diameter being scaled with the local vorticity thickness δ.

But this calculation has not reached self-similarity: kinetic-energy spectra in the downstream region are in $k^{-5/2}$ and r.m.s. velocity fluctuations have a departure of about 20% from experiments. Therefore simulations in longer domain are necessary to understand the downstream evolution of coherent vortices to self-similar conditions.

Results from a LES using the filtered structure function model but where the upstream conditions are now perturbed by an isotropic noise is full reported in Comte *et al.* (1998).

Conclusions

The LES formalism in spectral space for incompressible turbulence was reviewed. Some subgrid-scale models defined in spectral or physical space were discussed and their limitations discussed. LES in temporal and spatial mixing layers show the main characteristic of these flows: the formation and pairing of KH vortices with intense stretching of streamwise vortices in between. These streamwise vortices may also merge when the KH vortices pair. The diameter of these vortices seems to be scaled with the local vorticity thickness suggesting that both kind of merging are related. The strength of LES to reproduce the coherence of the vortex organization in a turbulent flows is to be remarked.

Acknowledgments

This work was developed at the MOST/LEGI team in Grenoble, France. The author is grateful to Prof M. Lesieur, E. Lamballais and P. Comte for useful discussions, and to P. Begou for computational assistance. Calculations were carried out at the IDRIS (Institut du Développement et des Ressources en Informatique Scientifique, Paris). The author is supported by a Research Fellowship from FAPERGS/RS.

References

G. K. BATCHELOR, *The Theory of Homogeneous Turbulence*, Cambridge Univ. Press., 1953.

J. BELL and R. MEHTA, Development of a two-stream mixing layer from tripped and untripped boundary layers, *AIAA Journal*, **28**, 2034–2042, 1990.

L. BERNAL and A. ROSKHO, Streamwise vortex structure in plane mixing layer, *J. Fluid Mech.*, **170**, 499–525, 1986.

G. BROWN and A. ROSKHO, On density effects and large structure in turbulent mixing layers, *J. Fluid Mech.*, **64**, 775–816, 1986.

C. CANUTO, M. Y. HUSSAINI, A. QUARTERONI, and T. A. ZANG, *Spectral Methods in Fluid Dynamics*, Springer-Verlag, New York, 1988.

J. P. CHOLLET and M. LESIEUR, Parameterization of small scales of the three-dimensional isotropic turbulence utilizing spectral closures, *J. Atmos. Sci.*, **38**, 2747–2757, 1981.

J.P. CHOLLET and M. LESIEUR, Modélisation sous maille des flux de quantité de

mouvement et de chaleur en turbulence tridimensionnelle isotrope, *La Météorologie*, **29-30**, 183–191, 1982.

P. COMTE, F. DUCROS, J. SILVESTRINI, E. LAMBALLAIS, O. MÉTAIS, and M. LESIEUR, Simulation des grandes échelles d'écoulements transitionnels, In *Proc. 74th Fluid Dynamics AGARD Symposium on "application of direct and large eddy simulation to transition and turbulence"*, Chania, Crete, 1994.

P. COMTE, J.H. SILVESTRINI, and E. LAMBALLAIS, A straightforward 3d multi-block unsteady Navier-Stokes solver for direct and large-eddy simulations of transitional and turbulent compressible flows, In *Proc. 77th Fluid Dynamics AGARD Symposium on "progress and challenges in CFD methods and algorithm"*, Seville, Spain, 1995.

P. COMTE, J.H. SILVESTRINI, and P. BEGOU, Streamwise vortices in large-eddy simulations of mixing layers, *European Journal of Mech. B/ Fluids*, **17**(3), 1998.

F. DUCROS, *Simulations numériques directes et des grandes échelles de couches limites compressibles*, Thèse, Institut National Polytechnique de Grenoble, 1995.

F. DUCROS, P. COMTE, and M. LESIEUR, Large-eddy simulation of transition to turbulence in a weakly compressible boundary layer over a flat plate, *J. Fluid Mech.*, **326**, 1–36, 1996.

M. GERMANO, U. PIOMELLI, P. MOIN, and W. H. CABOT, A dynamic subgrid-scale eddy viscosity model, *Phys. Fluids A*, **3**(7), 1760–1765, 1991.

S. GHOSAL, T. LUND, P. MOIN, and K. AKSELVOLL, A dynamic localization model for large-eddy simulation of turbulent flows, *J. Fluid Mech.*, **286**, 229–255, 1995.

L. HUANG and C. HO, Small-scale transition in a plane mixing layer, *J. Fluid Mech.*, **210**, 475–500, 1990.

J. KONRAD, *An experimental investigation of mixing in two-dimensional turbulent shear flows with applications to diffusion-limited chemical reactions*, PhD thesis, California Institute of Technology, 1976.

R. H. KRAICHNAN, Eddy viscosity in two and three dimensions, *J. Atmos. Sci.*, **33**, 1521–1536, 1976.

E. LAMBALLAIS, *Simulations numériques de la turbulence dans un canal plan tournant*, Thèse, Institut National Polytechnique de Grenoble, 1996.

S. K. LELE, Compact finite difference schemes with spectral-like resolution. *J. Comp. Phys.*, **103**, 16–42, 1992.

M. LESIEUR, *Turbulence in fluids, (Third Edition)*, Kluwer Academic Publishers, 1997.

M. LESIEUR and O. MÉTAIS, New trends in large-eddy simulations of turbulence, *Annu. Rev. Fluid Mech.*, **28**, 1996.

O. MÉTAIS and M. LESIEUR. Spectral large-eddy simulation of isotropic and stably stratified turbulence. *J. Fluid Mech.*, **239**, 157–194, 1992.

A. MICHALKE. On the inviscid instability of the hyperbolic tangent velocity profile. *J. Fluid Mech.*, **19**, 543–556, 1964.

J.H. SILVESTRINI. *Simulations des grandes échelles des zones de mélange; application à la propulsion solide des lanceurs spatiaux.* Thèse, Institut National Polytechnique de Grenoble, 1996.

J.H. SILVESTRINI, E. LAMBALLAIS, and M. LESIEUR. Spectral dynamic model for LES of free and wall shear flows. in press *Int. Journal of Heat and Fluid Flow*, 1998.

J. SMAGORINSKY. General circulation experiments with the primitive equations. *Mon. Weath. Rev.*, **91**(3), 99–164, 1963.

J. H. WILLIAMSON. Low-storage runge-kutta schemes. *J. Comp. Phys.*, **35**, 48, 1980.

FIGURES

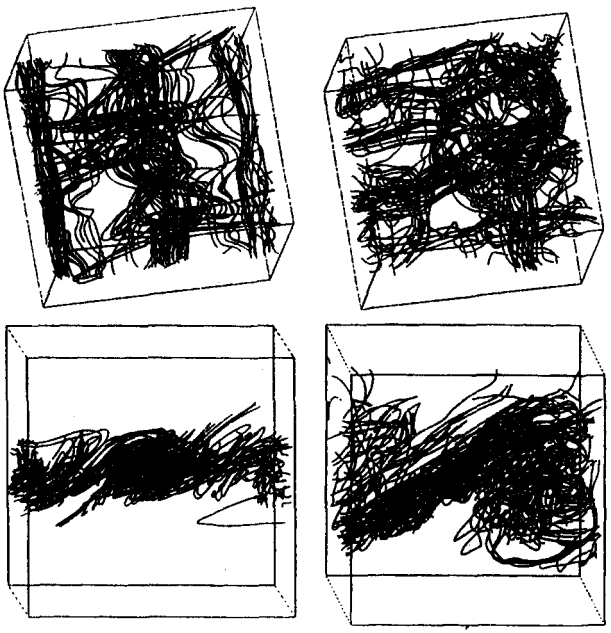

Figure 1: Vorticity lines at $t = 35$ and $70\ \delta_i/U$ (top views above and side views below) - Simulation DNSQ2DT.

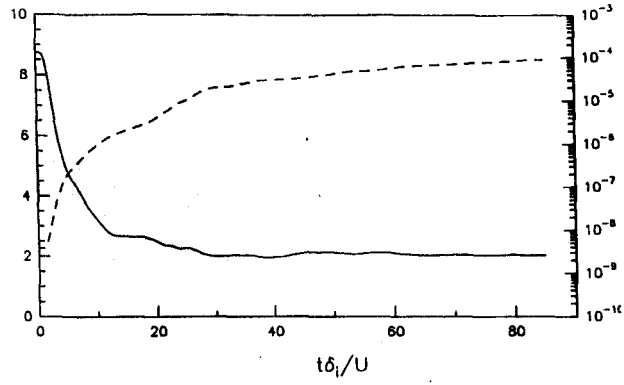

Figure 2: Time evolution of m (—) and of $E(k_c)$ (- - -) - Simulation LESQ2DT.

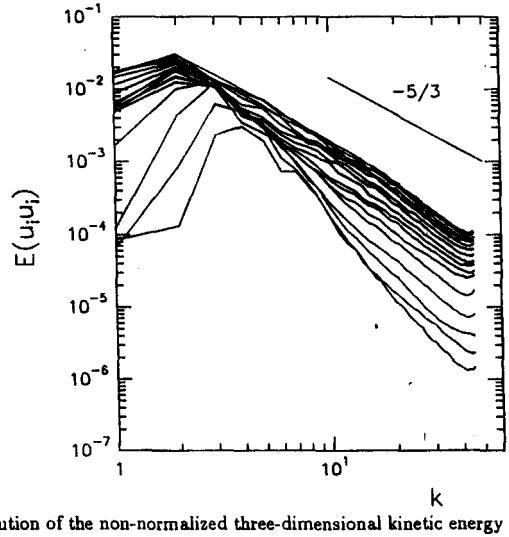

Figure 3: Time evolution of the non-normalized three-dimensional kinetic energy spectrum from $t = 10$ to 85 δ_i/U - Simulation LESQ2DT.

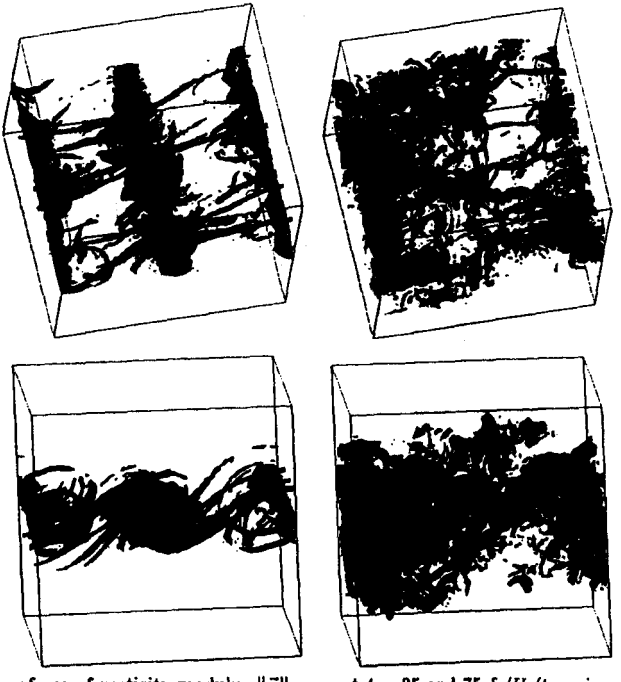

Figure 4: Isosurfaces of vorticity modulus $\|\vec{\omega}\| = \omega_i$ at $t = 35$ and 75 δ_i/U (top views above and side views below) - Simulation LESQ2DT.

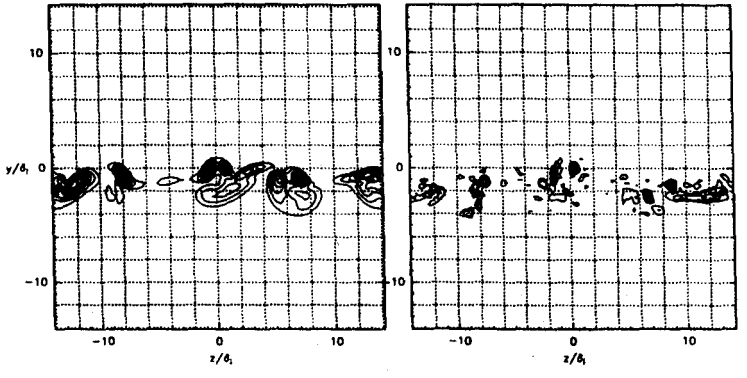

Figure 5: Isolines of vorticity modulus at the same transversal plane in the stagnation region between KH vortices, for the DSNQ2DT (left) and LESQ2DT (right), at $t = 35\ \delta_i/U$.

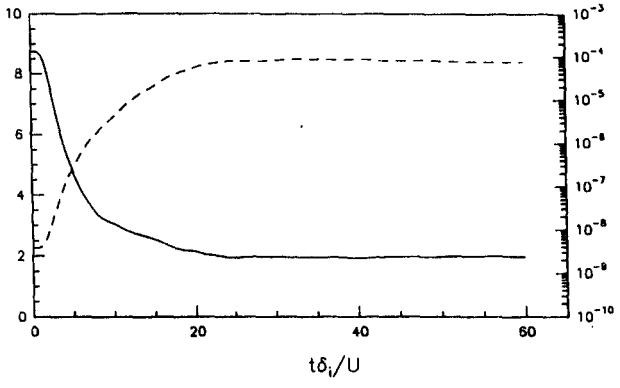

Figure 6: Time evolution of m (—) and of $E(k_c)$ (- - -) - Simulation LES3DT.

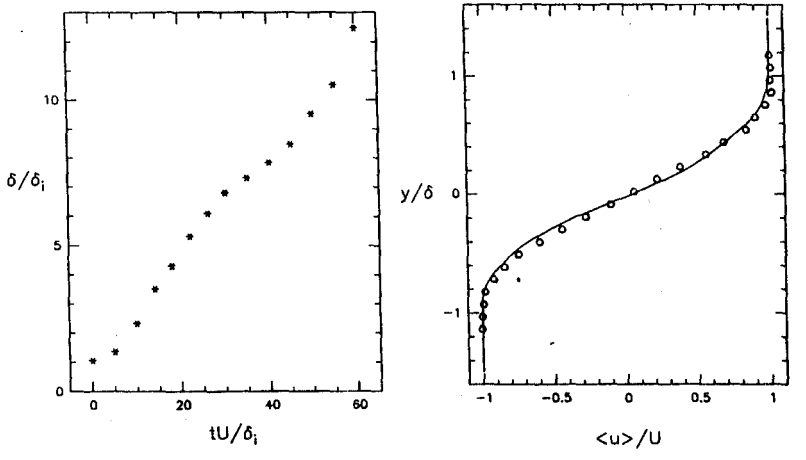

Figure 7: Left, time evolution of the local vorticity thickness ; right, comparison of mean streamwise velocity (straight line) with experimental data of Bell and Mehta (1990) (circles) - Simulation LES3DT.

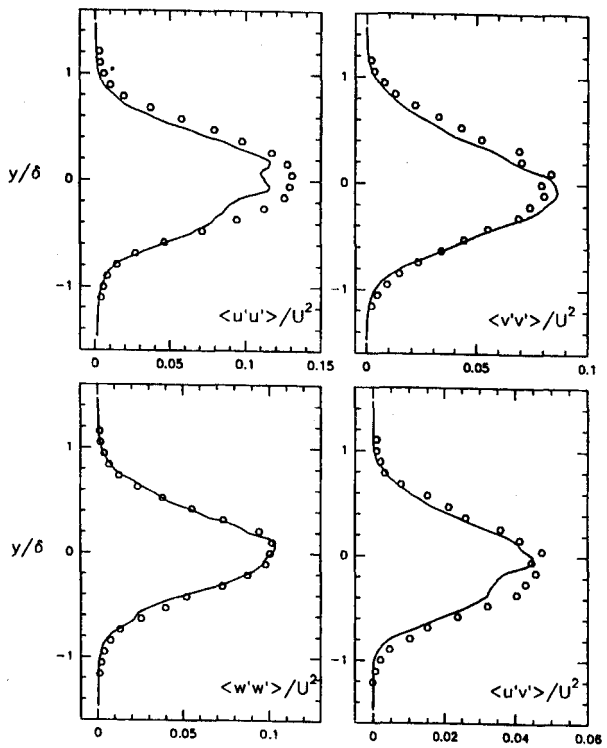

Figure 8: Comparison of present velocity fluctuations variances (lines) with experimental data (symbols) of Bell and Mehta (1990) - Simulation LES3DT.

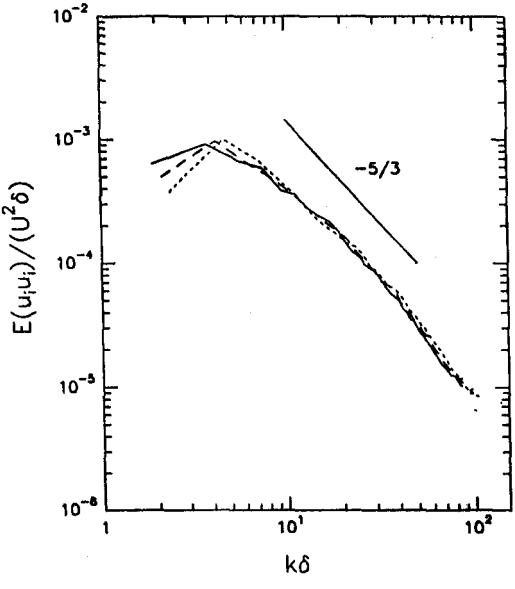

Figure 9: Normalized three-dimensional kinetic energy spectra at $t = 50$ (—), 55 (- - -) and 60 δ_i/U (- - -) - Simulation LES3DT.

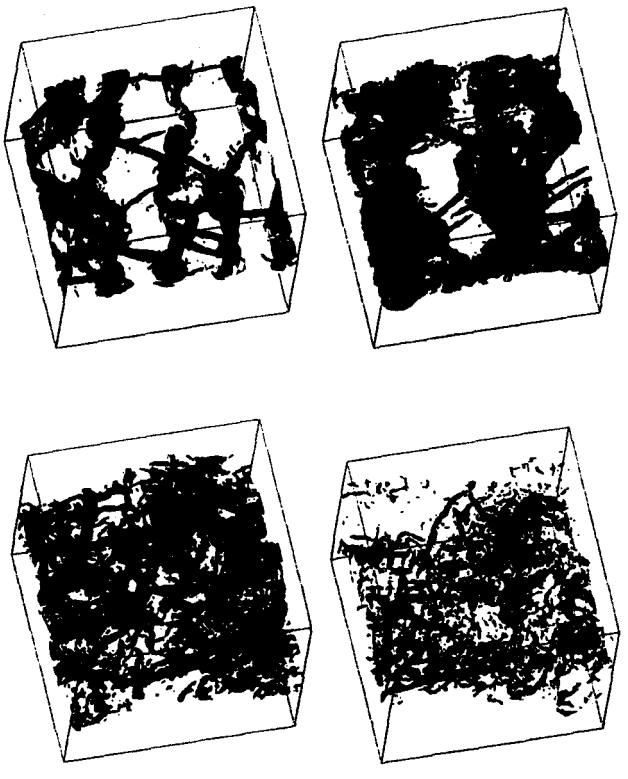

Figure 10: From left to right and top to bottom, perspective views of the mixing layer at $t = 14, 26, 40$ and 60 δ_i/U showing isosurfaces of the vorticity modulus at a threshold of ω_i - Simulation LES3DT.

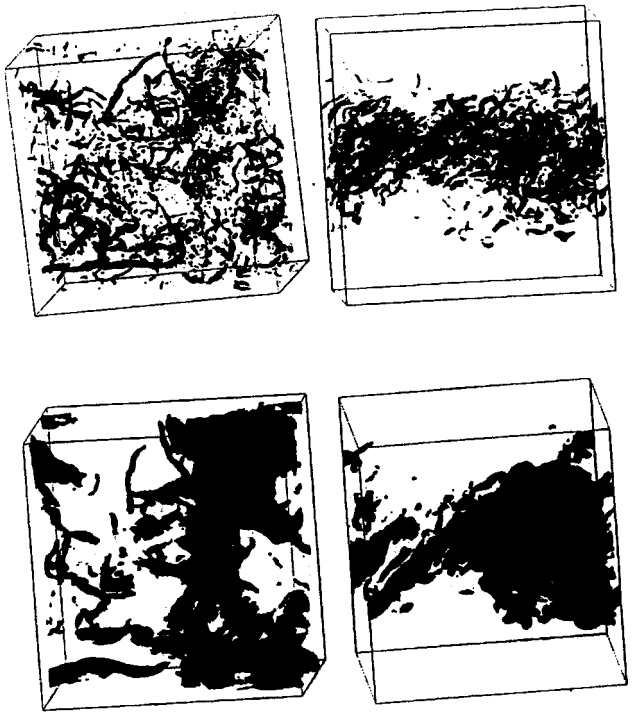

Figure 11: Top (left) and side (right) views of vorticity modulus (threshold 1.4 ω_i) and low-pressure isosurfaces (bottom) at $t = 60\ \delta_i/U$ - Simulation LES3DT.

Figure 12: Isosurfaces of vorticity modulus $\|\vec{\omega}\| = 2/3\,\omega_i$ of a spatially growing mixing layer - Simulation LESQ2DS.

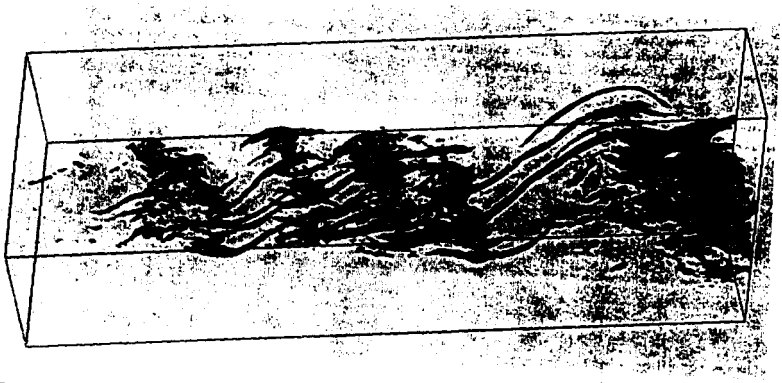

Figure 13: Isosurfaces $\omega_x = 0.5\omega_i$ (black) and $\omega_x = -0.5\omega_i$ (grey) - Simulation LESQ2DS.

TURBULENT SHALLOW-WATER MODEL FOR OROGRAPHIC SUBGRID-SCALE PERTURBATIONS

Norberto Mangiavacchi, Alvaro L. G. A. Coutinho, Nelson F. F. Ebecken

Center for Parallel Computations
COPPE/Federal University of Rio de Janeiro
PO Box 68506, RJ 21945-970, Rio de Janeiro, Brazil
E-mail: norberto,alvaro@coc.ufrj.br, nelson@ntt.ufrj.br
Web page: http://www.nacad.ufrj.br

Key Words: Turbulent flows, shallow-water equations, subgrid-scale models, orographic perturbations, parallel processing, spectral methods

Abstract.

A parallel pseudo-spectral method for the simulation in distributed memory computers of the shallow-water equations in primitive form was developed and used on the study of turbulent shallow-waters LES models for orographic subgrid-scale perturbations. The main characteristics of the code are: momentum equations integrated in time using an accurate pseudo-spectral technique; Eulerian treatment of advective terms; and parallelization of the code based on a domain decomposition technique. The parallel pseudo-spectral code is efficient on various architectures. It gives high performance on vector computers and good speedup on distributed memory systems.

The code is being used for the study of the interaction mechanisms in shallow-water flows with regular as well as random orography with a prescribed spectrum of elevations. Simulations show the evolution of small scale vortical motions from the interaction of the large scale flow and the small-scale orographic perturbatiqns. These interactions transfer energy from the large-scale motions to the small (usually unresolved) scales. The possibility of including the parametrization of this effects in turbulent LES subgrid-stress models for the shallow-water equations is addressed.

1 INTRODUCTION

The shallow-water model is used as a testbench for understanding many fundamental dynamical problems, such as atmospheric flows, tides, storm surges, river and coastal flows. In many such applications, the flow is mostly a two-dimensional turbulent flow.

Numerical simulations usually are performed using Large-Eddies Simulation (LES) techniques, which require the parametrization of scales smaller than the computational grid, which is done by subgrid-scale models. The best known subgrid-scale model for LES of turbulent flows is the Smagorinsky model [1]. Later models, such as Germano [2], and Lilly [3] overcome some of Smagorinsky model limitations, in particular the need to specify a parameter, and the tendency of beeing over-dissipative.

None of these models, however, address the effects of the perturbations introduced by an irregular orography with scales smaller than the computational grid. Small scale orographic perturbations play an important role in the dynamic cascade in turbulent shallow-water flows. Neglecting these effect can result in degraded forecast capabilities in atmospheric simulations. Therefore, better subgrid-scale models, including subgrid-scale orographic effects, may result in significantly improved weather forecasts.

Numerical simulations of the detailed behaviour of turbulent shallow-water flows in the presence of small scale orographic perturbations can provide a fundamental understanding of the mechanisms involved in such flows, and provide valuable data for the development and validation of new sub-grid models. Such simulations require the space and time accurate integration of the turbulent flow field and additionally model accurately the effects due to the orography.

Since such simulations are very computationally intensive, higher resolution shallow-water flow simulations could profit from the scalable performance available on parallel arquitectures. Pseudo-spectral methods, due to their high accuracy and performance when used in simple domains, and their intrinsic parallelism, can be applied successfully for the simulation of shallow-water flows in distributed memory computers. In this work we describe a new parallel pseudo-spectral code designed to perform high resolution, space and time accurate simulation of shallow-water flows on various current distributed memory architectures. The parallel algorithm explores the intrinsic parallelism of the pseudo-spectral method and it is based on a domain decomposition approach. The remainder of this paper is organized as follows. In the next section we briefly review the governing equations of shallow-water flows. The section that follows details our pseudo-spectral method, based on Fourier expansions. The next section presents the parallel implementation, designed to achieve high performance, while retaining portability across different platforms. The following section shows the numerical results for a test case and discusses the parallel performance of the code on several computers, and results of several simulations of the shallow-water equations with various orographic perturbations are discussed. Finally, the paper ends with a summary of the main conclusions of this work.

2 GOVERNING EQUATIONS

The governing equations are the shallow-water equations, also known as Barré de Saint-Venant equations. The derivation is given, for example, by Lesieur [4]. Here we will restate the main assumptions.

We start from the Navier-Stokes equations locally on a sphere, with a fluid of constant uniform density ρ. The fluid is assumed to have a free surface with elevation $H(x,y,t)$ above a reference plane, and to lie above a topography of height $h_s(x,y)$. The depth of the fluid layer is $h(x,y,t)$, and the surface elevation is $H = h + h_s$ (see figure 1).

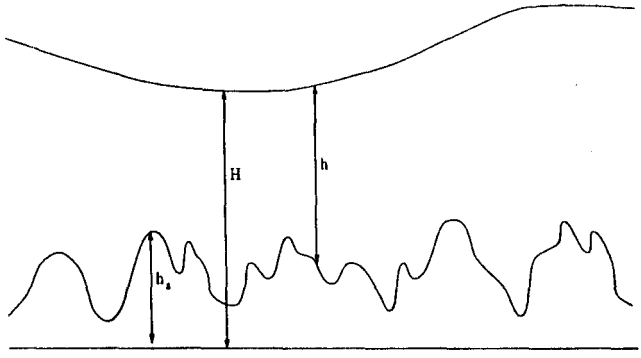

Figure 1: Schematic vertical cross-section of the shallow layer.

The pressure at the free surface is uniform and equal to p_0. The pressure is hydrostatically distributed along the vertical, and the horizontal velocity field $\mathbf{v}$, depends only on the horizontal space variables x and y, and on the time. Integrating the equations along the vertical, one obtains

$$\frac{\partial \mathbf{v}}{\partial t} = -(\omega + f)\hat{k} \times \mathbf{v} - \nabla(\frac{1}{2}\mathbf{v} \cdot \mathbf{v} + gH) + \nu_t \nabla^2 \mathbf{v} \tag{1}$$

$$\frac{\partial h}{\partial t} = -\nabla \cdot (h\mathbf{v}) \tag{2}$$

where $\omega = \hat{k} \cdot \nabla \times \mathbf{v}$, is the vorticity, $f = 2\Omega \sin(\theta)$ is the projection of the planetary vorticity 2Ω, $\omega = |\Omega|$, and θ is the local latitude.

3 THE NUMERICAL METHOD

We use a Fourier Pseudo-Spectral Method in order to discretize the system of partial differential equations into ordinary differential equations. The pseudo-spectral approach avoids the high cost of computing quadratic and higher terms in Fourier representation, which require convolutions, but still preserving the *Spectral Convergence* properties of standard spectral methods. The Pseudo-spectral approach gives the best computational cost/benefit for simple geometries, in particular for periodic domains.

We proceed using the expansion of the flow variables in Fourier series in the (x) and (y) horizontal directions,

$$\mathrm{u(x)} = \sum_{\mathbf{k}} \mathrm{U(k)} \exp(ik_x x) \exp(ik_y y) \tag{3}$$

The thickness h is updated using

$$h^{n+1} = h^n + \Delta t \left(-\frac{3}{2} \nabla \cdot (h\mathbf{v})^n + \frac{1}{2} \nabla \cdot (h\mathbf{v})^{n-1} \right) \tag{4}$$

The time integration for the transport equation is performed using operator splitting. The velocity field is solved using Adams-Bashfort for the advection terms

$$\mathbf{v}^{n+\frac{1}{2}} = \mathbf{v}^n + \frac{3}{2}\Delta t\,(NL)^n - \frac{1}{2}\Delta t\,(NL)^{n-1} \tag{5}$$

where

$$NL = -(\omega + f)\hat{k} \times \mathbf{v} - \nabla \left(\frac{1}{2}\mathbf{v} \cdot \mathbf{v} + gH \right)$$

and Cranck-Nickolson for the viscous terms.

$$\left(\frac{1}{\Delta t} - \frac{\nu_t}{2} \nabla^2 \right) \mathbf{v}^{n+1} = \left(\frac{1}{\Delta t} + \frac{\nu_t}{2} \nabla^2 \right) \mathbf{v}^{n+\frac{1}{2}} \tag{6}$$

To be able to perform high resolution simulations, which are required to perform direct numerical simulations, the code was parallelized using a domain decomposition approach, which is described next.

4 PARALLEL ALGORITHM

The parallel algorithm explores intrinsic parallelism of the pseudo-spectral technique. It is based on a domain decomposition approach in *latu sensu*. Three kinds of operations are involved in the parallel pseudo-spectral method: (1) computation of products in physical space, (2) inversion of the Poisson operators, computation of derivatives, and filtering operations in Fourier space, and (3) computation of the discrete two-dimensional Fourier transforms. The first two kinds of operations can be performed without any communication, when the domain is partitioned among the processors, in physical space and in

Fourier space respectively. The only part that requires communication is the computation of the the discrete two-dimensional Fourier transforms. Here also, for portability, we have chosen to use the transposition approach, that allows to use highly optimized single processor one-dimensional FFT routines, that are normally found in most architectures, and a transposition algorithm that can be easily ported to different distributed memory architectures.

The transposition algorithm used in the FFT is the so called *direct* transposition algorithm where at each stage of the communication algorithm each node sends to his pair all the data that has that node as final destination. At each stage the processor pairs are defined using a mapping of the processors onto a hypercube, and a relative addressing strategy. The number of stages is $p-1$ where p is the number of processors. The transposition algorithm can be summarized as follows:

- For i=1, 2, ...,$p-1$ do:
  - Each node m collects and sends to $n = XOR(m,i)$ all blocks that have node n as final destination, and replaces them with the blocks that receives from n.
- Unshuffle the resulting data in each node.

Here XOR stands fo the *exclusive or* boolean operation. The Poisson operator is diagonal in Fourier space. After decomposition of the domain among the nodes, the Poisson operator will require $O(\frac{N^2}{p})$ computations per node, at each time step, and no communications. Here N is the resolution in each dimension. The two-dimensional FFT's will require $O(\frac{2N^2\log_2(N)}{p})$ computations and $(p-1)$ bidirectional communications of length $\frac{N^2}{p^2}$ when using the described transposition algorithm. Since the latency time is much shorter than the communication time for large problem sizes, the total communication time is essentially $O(\frac{N^2}{p})$. Therefore the ratio of communications to computations is $O(\frac{1}{\log_2(N)})$.
Except for a few global operations, all the communication are lumped in the transposition algorithm making it easily portable to other distributed memory computers. The implementation using PVM, as the one given in [5], can run on a CRAY T3D and an IBM SP2 without changes in the transposition algorithms, only requiring to load the appropriate machine dependent single-processor one-dimensional FFT routines. To achieve better performance on the SP2, versions employing the MPI and MPL libraries were also implemented with minor additional effort, and considerable improvement in the performance.

5 SINGLE NODE AND PARALLEL PERFORMANCE

To evaluate the performance of the code in parallel machines, two-dimensional computations were performed with resolutions ranging from 256 × 256 to 1024 × 1024.

Table 1: Single-processor performance (256 × 256 resolution)

CPU	FFT	TIME(s/100 iters)	*Mflop/s*
IBM SP2 wide	Fortran	246	10
IBM SP2 thin	ESSL	90	28
IBM SP2 wide	ESSL	49	50
CRAY T3D	scalar library	156	16
CRAY J90	vector library	24.7	100
CRAY T90	vector library	3.38	731

High single-processor performance is obtained across various platforms using the provided optimized high performance libraries for the FFTs. The first and third cases in table 1 (SP2 wide using FORTRAN and ESSL library respectively) show that single-processor performance in the IBM SP2 can be improved by a factor of 5 by using the ESSL library. On CRAY T3D implementation, the scalar FFT library subroutines CCFFT, SCFFT, and CSFFT were used. On the CRAY J90 and T90 version, the vector library FFT subroutines CFFTMLT, SCFFTM, and CSFFTM where used.
Parallel performance was measured on a 4-processor IBM SP2. and on a 32-processor CRAY T3D. When using the PVM libraries on the SP2, the speed-up curves show that the parallel efficiency drops to about 75% for two processors. This is caused by the transposition algorithm, which is not present in the single processor case, and that introduces a significant overhead even when using only 2 processors. However efficiency continues above 50% even for quite larger numbers of nodes, as long as the problem size is adequate. When using the dedicated MPL library on the SP2 we obtain some improvement in the efficiency (on two processors about 80% for 256 × 256), showing that the communication cost is reduced by using the MPL library.

In fact, the efficiency is about 50% even when using 32 T3D nodes for the case 1024 × 1024. Hence, a CRAY T3D with 32 nodes outperforms a single CPU of a CRAY J90 running in vector mode. The scalability of the parallel code clearly indicates its potential to beat more powerful vector processors, as the T90, if more processors were added to the parallel machine.

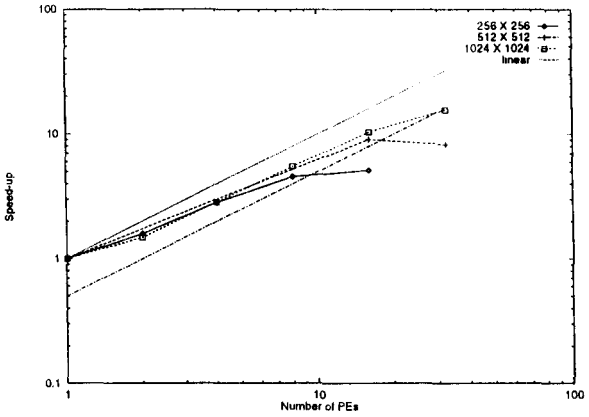

Figure 2: Speedup on CRAY T3D.

6 RESULTS

For the scope of this work we will analize the case of negligible rotation ($f = 0$). The following simulation were performed using a physical space resolution of 64 by 64 points, unless otherwise specified.

6.1 Test problem

A number of runs were performed to assess the correctness of the code. One usual test for shallow-water solvers is the dam-break problem. In this problem, there is sharp variation in the surface elevation H, in otherwise quiescent initial conditions. The elevation is $H = H_0$ at the left, and $H = H_1$ at the right of the dam. From this initial sharp front, two waves propagate in opposite directions, at two different speeds. The wave travelling in the shallower side is a shock wave, while the wave propagating on the deep side is a rarefaction wave. In this test it is assessed the ability to accurately simulate the propagation of sharp waves on the surface elevation. A typical result from this test is shown in figure 3.

A two-dimensional extension to the dam-break problem was also simulated, in order to verify if the code accurately accounts for more complex two-dimensional wave interactions. Results are shown in figure 4.

6.2 Regular Orography

Some simulations were performed using regular orographic perturbations. In such simulations the orography is given by sinusoidal perturbations of the form

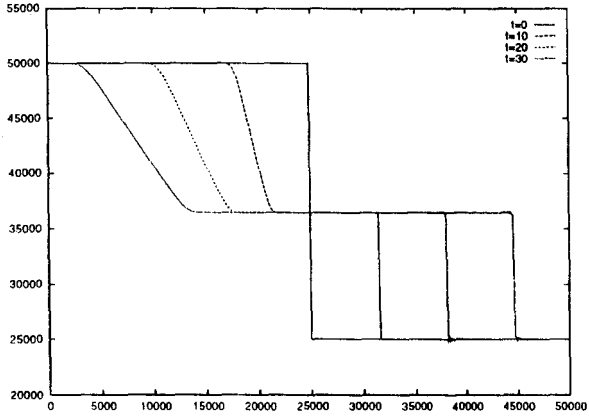

Figure 3: Simulation of the dam-break problem. One-dimensional wave. Times $t = 0$, $t = 10$, $t = 20$, and $t = 30$. Resolution is 512 points in the half box.

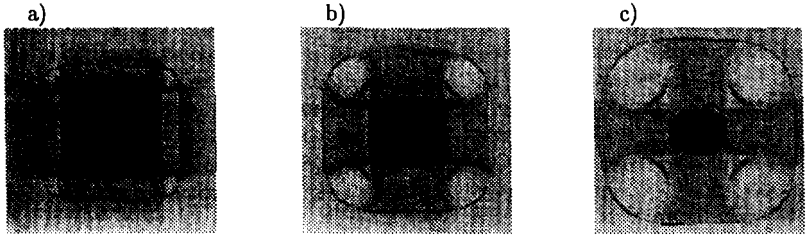

Figure 4: Simulation of shallow-water flow over regular orography. Two-dimensional extension of the dam-break problem. Surface elevation field for (a) $t = 10$, (b) $t = 20$, (c) $t = 30$. The simulation shows the displacement of sharp waves propagating from the initial sharp surface discontinuity.

$$h_s = \sin(\alpha x)\sin(\beta y) \tag{7}$$

Two different kinds of initial conditions were analised. On the first case, shown in figure 5, a single vortex with a scale larger than the orographic perturbation is left to evolve.

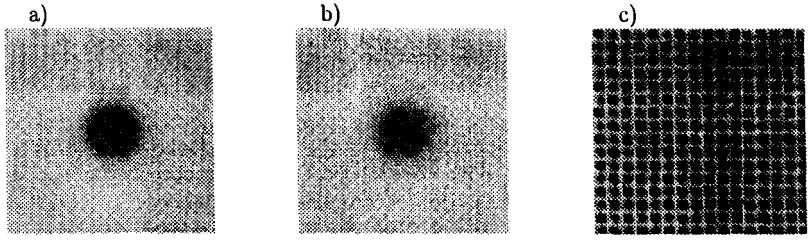

Figure 5: Simulation of shallow-water flow over regular orography. Single vortex. Vorticity field for (a) flat orography, and (b) sinusoidal orography (single 2-d mode). Interactions with the orography cause the development of six small-scale peaks close to the center of the vortex. (c) Elevation of the orographic perturbation.

In the abscence of the orographic perturbations, the vortex undergoes a slow decay, since the backgroung viscosity is very small. In the presence of the orographic perturbation the vortex develops small-scale peaks, which are originated from interactions between the vorticity field and the orography. The occurrence of the peaks can be explained simply by conservation of potential vorticity $(\omega + f)/h$. When passing over deeps, h increases causing the increase of vorticity by vortex stretching, and the opposite occours over the hights.

On a second case, the initial conditions are given by a turbulent flow, as shown in figure 6.

In this case, the interaction cause a faster rate of decay of the turbulent motions with scales close to the scale of the orographic perturbation than the case without perturbation.

The effect of the orographic perturbation can be better visualized looking at the energy spectra $E(k)$ of the two flows, shown in figure 7. Two kinds of effects can be seen. The first most ostensive effect is the forcing of modes close to the perturbation scale $(8\sqrt{2})$ and its harmonics. The forcing causes the peaks observed in the spectrum at discrete points. The other effect is the reduction of energy at scales away from the forcing frequencies, in particular for the large scales (small k). This is the most important effect as far as parametrization of subrid-scale perturbations is concerned.

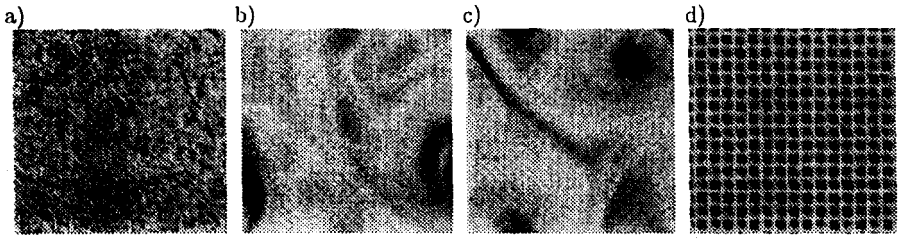

Figure 6: Simulation of shallow-water turbulent flow decay over a flat orography and over regular orographic perturbations. (a) Vorticity field of the initial condition. (b) Vorticity field for $t = 1 \times 10^5$ with flat orography, and (c) with sinusoidal orographic perturbation, showing vortical structures with scales larger than in (b). (d) Elevation of the sinusoidal orography (single 2-d mode). Interactions with the perturbed orography in (c) cause a much faster rate of decay of the turbulent motions with scales close to the scale of the orographic perturbation than the previous case (b). The decay of the large scales is also affected.

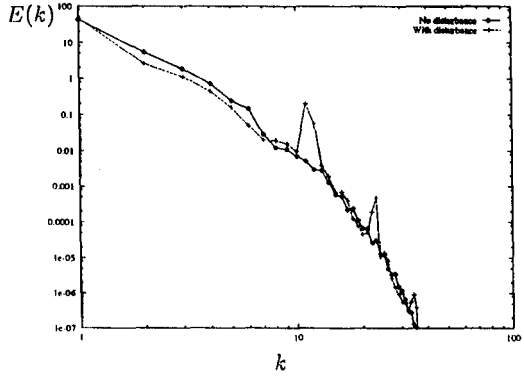

Figure 7: Simulation of shallow-water turbulent flow decay over a flat orography and over regular orographic perturbations. Interactions with the perturbed orography in (c) cause a much faster rate of decay of the turbulent motions with scales close to the scale of the orographic perturbation than the previous case (b). The decay of the large scales is also affected.

6.3 Irregular Orography

A more complex behaviour can be expected in the case that the orography has a continuous spectrum of perturbations. Two particular cases are of interest. In the first case the spectrum of perturbation is similar to the spectrum of the velocity, while in the second case the spectrum of the orographic perturbation is peaked at higher modes. The elevation spectra for this two cases are shown in figure 8, and the resulting spatial distributions are shown in figure 9.

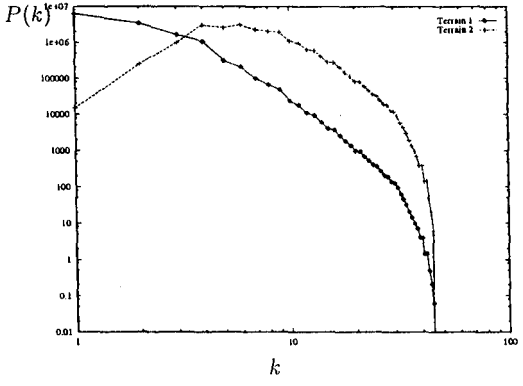

Figure 8: Perturbation spectra of terrains with irregular orography used in the simulations.

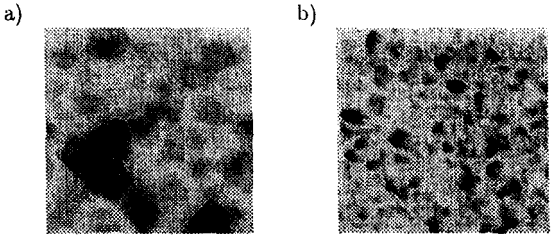

Figure 9: Terrain for irregular orography. Elevation of the orographic perturbation used in the simulations. a) with spectrum similar to the velocity spectra. b) with spectrum with more energy at higher modes.

The resulting kinetic energy spectra for the turbulent flow without disturbace, and for the two types of terrains are shown in figure 10. While for the terrain 1 the effects of the orographic perturbations are already quite considerable, the effects due to terrain 2 are certainly dramatic, leading to a much higher kinetic energy level at the small scales, and a lower energy level at the large scales.

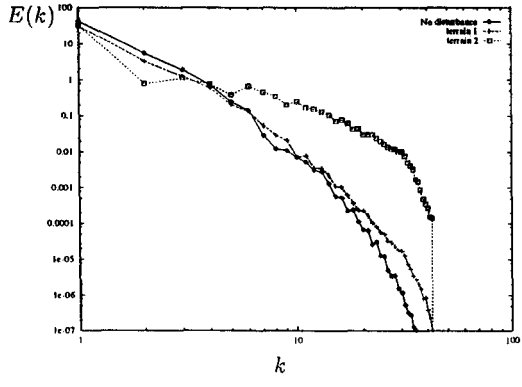

Figure 10: Energy spectra of the flow over terrains with irregular orography.

6.4 Considerations on Parametrization of Orographic Subgrid-scale Perturbations

From the results of the previous simulations it has been shown that the effect of the subgrid orographic perturbations is not a simple dissipative mechanism, acting instead in the full range of dynamic scales. The transfer of energy among scales is enhanced, and, in the case of of orography with a elevation spectrum containing perturbations with high energy at small scales, there is strong transfer of kinetic energy from large to small scales.

No simple dissipative model can reproduce this kind of mechanism with accuracy. In order to take into account these effects in large eddies simulations, one crude approach is to add a perturbation at the smallest resolved scales with the same energy than the subgrid scale perturbations. A very promising approach, however is to use upscaling techniques to accurately compute the energy transfer due to the smallest scales, and to use this information in the large scale model.

7 CONCLUSIONS

A method to solve two-dimensional shallow-water flows using pseudo-spectral methods was developed. Resuls of simulations using the method show physically consistent results. Based on this method, a high performance parallel pseudo-spectral method for the simulation of two-dimensional shallow-water flows was developed. The code is designed to perform high resolution, space and time accurate simulations of shallow-water flows on various distributed memory architectures. The parallel Pseudo-Spectral code is efficient on various architectures. It gives good speedup on distributed memory systems (IBM SP2 and T3D).

Simulations performed with the code show that the interaction mechanisms between orography and the vorticity field lead to the development of small scale vortical motions that have a faster decay rate, at the expense of the energy of the large scales.

This kind of interaction cannot be accurately represented by a simple dissipative model, requiring more refined techniques such as upscaling.

8 ACKNOWLEDGEMENTS

We gratefully acknowledge the Center of Parallel Computations of the Federal University of Rio de Janeiro (NACAD-COPPE) for providing us time on the IBM SP2. and CRAY J90 machines. We are also indebted to Silicon Graphics/Cray Research Division by the computer time in their CRAY T3D and T90 machines at Eagan, MN, USA. The first author is currently supported by a Research Grant from FAPERJ (E-26/151.018/97).

REFERENCES

[1] J. Smagorinsky. General circulation experiments with the primitive equations. *Mon. Weath. Rev.*, **91**, 99–164 (1963).

[2] M. Germano, U. Piomelli, P. Moin, and W. H. Cabot. A dynamical subgrid-scale eddy viscosity model. *Phys. Fluids A*, **3**, 1760–1765 (1991).

[3] D. K. Lilly. A proposed modification to the germano subgrid scale closure method. *Phys. Fluids A*, **4**, 663 (1993).

[4] M. Lesieur. *Turbulence in Fluids.* Kluwer Academic Publishers, 2nd edition, (1990).

[5] N. Mangiavacchi, A.L.G.A. Coutinho, and N.F.F. Ebecken. Parallel pseudo-spectral computations at NACAD. *Proc. of SBAC-PAD*, **1** (1997).

Instabilidade e Turbulência: Uma Forma de Não-Linearidade Encontrada no Caos

Instability and Turbulence: A Kind of Nonlinearity found in Chaos

Harry Edmar Schulz
Laboratório de Hidráulica Ambiental - CRHEA
Departamento de Hidráulica e Saneamento
Escola de Engenharia de São Carlos-Universidade de São Paulo
C.P.359, 13560-270, São Carlos, S.P., Brasil
(Trabalho desenvolvido no Institut für Hydromechanik, Universität Karlsruhe, Alemanha)

Abstract

The Navier-Stokes equations and the Reynolds equations are used to generate a simplified one-dimensional model, which maintains the nonlinear characteristic of the original equations. The discretization of this simplified model leads to an equation similar to the population growth equation used in the earlier studies of chaos. As a consequence, the behaviour of data obtained using the growth equation must also be observed in mathematical systems which use the Navier-Stokes or the Reynolds equations. As these models are believed to be representative of a physical reality, also physical systems found in the nature may follow the same behaviour. The example of flow in shallow water layers is used in this study.
***Keywords**: chaos, nonlinear systems, transition flows, period doubling.*

Resumo

As equações de Navier-Stokes e de Reynolds são utilizadas para gerar um modelo simplificado, unidimensional, que mantém a característica não-linear das equações originais. Através da discretização deste modelo simplificado mostra-se que a equação final obtida reproduz a equação logística de crescimento populacional, que foi utilizada nos estudos pioneiros acerca do caos. Desta forma, o comportamento descrito pela equação logística de crescimento populacional também pode ser esperado em sistemas matemáticos descritos pelas equações de Navier-Stokes e de Reynolds discretizadas. Sendo esses modelos matemáticos representativos da realidade que pretendem descrever, é possível esperar o mesmo comportamento nos sistemas físicos encontrados na natureza. No presente estudo utiliza-se como exemplo o escoamento em águas rasas.
***Palavras-chave**: caos, sistemas não-lineares, escoamentos de transição, duplicação de períodos.*

Introdução

O estudo de turbulência recebeu um impulso algo inovador a partir das décadas 70-80 com os trabalhos referentes ao caos, que mostraram que esquemas numéricos simples podem conduzir a evoluções complexas das grandezas envolvidas. Uma quantidade razoável de trabalhos foi conduzida desde então, mostrando as coincidências comportamentais entre os sistemas físicos naturais e os resultados qualitativos desses esquemas numéricos simples. Mesmo resultados numéricos, relacionados com a obtenção de constantes vinculadas ao modelo de duplicação de período de May e Feigenbaum (ver Feigenbaum, 1978) foram também observados experimentalmente com aproximação razoável.

Neste sentido, o modelo de duplicação de período permitiu efetuar uma conexão, ainda que mnemônica, entre a evolução prevista para as variáveis matemáticas e a evolução estabilidade-instabilidade-turbulência observada em muitas situações em mecânica dos fluidos. A grande vantagem didática em visualizar o processo de instabilidade e evolução para a turbulência, baseada

no modelo de duplicação de período, como resultante das interações não-lineares existentes na natureza e reproduzidas nos modelos matemáticos, sugere que se utilize este modelo de forma mais intensa como ferramenta de suporte ao estudo da mecânica dos fluidos. Entretanto, também é preciso que uma conexão mais formal seja elaborada, vinculando a expressão de recorrência básica dos estudos de caos via duplicação de período, com expressões numéricas decorrentes do uso das equações de Navier-Stokes ou das equações de Reynolds (no caso de escoamentos turbulentos). Evidentemente as equações de Navier-Stokes podem ser discretizadas de diferentes maneiras, mas mostra-se, neste trabalho, que é possível seguir uma forma de discretização em uma situação de escoamento simplificada, a qual conduz a uma expressão similar à equação básica adotada para o estudo da duplicação de períodos. Desta forma, a não-linearidade presente nas equações de Navier-Stokes ou nas equações de Reynolds mostra ser do mesmo tipo daquela existente na equação de recorrência dos estudos de caos, sendo que evoluções comportamentais obtidas para esta equação podem ser esperadas também para as equações de Navier-Stokes ou de Reynolds, bem como para os sistemas reais que elas pretendem representar.

No presente trabalho considera-se uma situação uni-dimensional e pretende-se que o mesmo seja fundamentalmente um texto didático. O objetivo básico é mostrar que a não-linearidade presente nas equações estudadas pode conduzir à instabilidade e, posteriormente, à turbulência. Esta forma de abordagem é mais adequada a uma introdução acerca de instabilidade em mecânica dos fluidos do que o usual tratamento formal, que sobrecarrega matematicamente o primeiro contato com o tema.

Situação de Águas Rasas e Simplificação Conveniente das Equações Governantes

O escoamento em águas rasas, tanto no estudo de casos laminares como no estudo de casos turbulentos, gera esteiras de vórtices que, a despeito da grande diferença entre os números de Reynolds correspondentes a cada caso, mantém uma semelhança plástica notável entre si. Este fato desperta novamente a curiosidade acerca das causas deste tipo de movimento e de como podemos descrevê-lo da melhor forma. A questão torna-se ainda mais interessante porque acreditamos que já dispomos da equação governante para este fenômeno, isto é, as equações de Navier-Stokes devem ser válidas para escoamentos laminares ou turbulentos. Possuímos também equações (construídas a partir das equações de Navier-Stokes) que, acredita-se, descrevam corretamente os escoamentos turbulentos (equações para grandezas médias, como as equações de Reynolds). Assim, temos as equações, ou mesmo um conjunto delas, que são de difícil tratamento, não permitindo uma visualização imediata das características dos escoamentos que pretendemos entender.

No caso dos escoamentos de águas rasas, as características dos mesmos permitem que uma série de simplificações seja feita nas equações de Navier-Stokes ou nas equações de Reynolds, que conduz a uma forma final que mantém a característica não-linear do equacionamento original. Esta não-linearidade é aqui explorada através de uma aproximação numérica, nos moldes dos trabalhos de May e Feigenbaum (ver Feigenbaum, 1978), procurarando reproduzir as propriedades que os autores mencionados enfatizaram.

A situação física que aqui se explora é o escoamento superficial (ou o escoamento da superfície) em um corpo de água raso, com direção do escoamento paralela ao eixo x. O equacionamento básico para a direção x, para as equações de Navier-Stokes e para as equações de Reynolds, é dado por:

Equações de Navier-Stokes:

$$\frac{\partial U}{\partial t}+U\frac{\partial U}{\partial x}+V\frac{\partial U}{\partial y}+W\frac{\partial U}{\partial z}=-\frac{1}{\rho}\frac{\partial p}{\partial x}+\nu\left(\frac{\partial^2 U}{\partial x^2}+\frac{\partial^2 U}{\partial y^2}+\frac{\partial^2 U}{\partial z^2}\right)+B_x \qquad (1)$$

U, V e W são as componentes da velocidade do escoamento nas direções x, y e z, respectivamente. p é a pressão, ρ é a massa específica do fluido, ν é a viscosidade cinemática do fluido e B_x é a força de campo na direção x.

Equações de Reynolds (com as tensões de Reynolds decorrentes dos produtos entre flutuações de velocidades):

$$\frac{\partial \overline{U}}{\partial t}+\overline{U}\frac{\partial \overline{U}}{\partial x}+\overline{V}\frac{\partial \overline{U}}{\partial y}+\overline{W}\frac{\partial \overline{U}}{\partial z}= -\frac{1}{\rho}\frac{\partial \overline{p}}{\partial x}+\left(\frac{\partial}{\partial x}\left(\nu\frac{\partial \overline{U}}{\partial x}-\overline{uu}\right)+\frac{\partial}{\partial y}\left(\nu\frac{\partial \overline{U}}{\partial y}-\overline{uv}\right)+\frac{\partial}{\partial z}\left(\nu\frac{\partial \overline{U}}{\partial z}-\overline{uw}\right)\right)+\overline{B}_x \quad (2)$$

A barra superior indica a operação de média temporal efetuada sobre as grandezas já definidas nas equações de Navier-Stokes. u, v e w são as flutuações de velocidade nas direções x, y e z. As simplificações que podemos fazer, para o estudo do escoamento da superfície em um experimento em tanque para águas rasas, são as seguintes:

1 - O escoamento é horizontal. Assim, não há componente na direção x para as forças de campo (B_x=0).

2 - O escoamento preferencial é na direção paralela a x. Assim, no momento, desprezam-se as velocidades nas direções y e z.

3 - Por se tratar de um escoamento de superfície, não existe variação de pressão ao longo de x.

4 - Efeitos viscosos são desprezados junto à superfície livre.

5 - As flutuações de velocidade mantém características constantes ao longo de toda a superfície.

Convém frisar que a simplificação 2 dá ao sistema a característica unidimensional procurada. Mas esta simplificação também faz com que, em um escoamento de características bi-dimensionais, não se possa evocar o princípio da conservação de massa, o que implica que os procedimentos aqui seguidos devam ser encarados válidos quanto ao aspecto qualitativo do comportamento da velocidade, e não quanto ao valor numérico desta última. Esta ressalva é pertinente porque o problema físico real precisa da segunda dimensão (sem a qual não se pode descrever a formação de vórtices).

As simplificações apresentadas conduzem às seguintes equações:

Equações de Navier-Stokes:

$$\frac{\partial U}{\partial t}+U\frac{\partial U}{\partial x}=0 \quad (3)$$

Equações de Reynolds:

$$\frac{\partial \overline{U}}{\partial t}+\overline{U}\frac{\partial \overline{U}}{\partial x}=0 \quad (4)$$

O que se observa é que a característica não-linear das equações originais foi mantida. No caso das equações de Reynolds, a hipótese de homogeneidade da turbulência na superfície elimina o problema de ser necessário considerar os produtos de flutuações de velocidade. Evidentemente as equações 3 e 4 possuem soluções explícitas, que podem ser obtidas, por exemplo, por separação de variáveis. Esta solução é mostrada aqui na equação 5, mas a mesma não é utilizada neste texto no estudo dos aspectos referentes à não-linearidade das equações 3 e 4. Além disso, a solução carrega consigo a questão referente ao princípio da conservação de massa anteriormente mencionado.

$$U \text{ ou } \overline{U} = \frac{C_1 - \sigma x}{C_2 - \sigma t} \tag{5}$$

C_1, C_2 e σ são constantes. Como o escoamento em águas rasas com a formação de esteira de vórtices ocorre tanto em pequenos números de Reynolds (o caso clássico da instabilidade em torno de um cilindro, por exemplo) como em grandes números de Reynolds (isto é, em escoamentos seguramente turbulentos, como aqueles descritos por Dracos et al., 1992), optou-se por utilizar aqui a situação de grandes números de Reynolds para o desenvolvimento do trabalho. Assim, a notação da velocidade envolve a média temporal associada com a equação 4. Esta escolha visa conduzir a discussão no sentido de discutir as instabilidades que surgem tanto em escoametnos laminares como em escoamentos turbulentos com características médias bem definidas. Na figura 1 é mostrada a situação de trabalho. Apresenta-se, nesta figura, um escoamento preferencial na direção x no qual uma fonte de perturbação (cilindro) foi colocado. Os pontos que correspondem à malha de discretização espacial (direção x) são também indicados.

Discretização das Equações Simplificadas

Para efetuar a análise numérica nos moldes dos modelos simples de caos, utilizou-se aqui uma discretização por diferenças finitas progressiva no tempo e regressiva no espaço, ou seja:

$$\frac{\partial \overline{U}}{\partial t} = \frac{\overline{U}\,(i, j+1) - \overline{U}\,(i, j)}{\Delta t} \tag{6}$$

$$\frac{\partial \overline{U}}{\partial x} = \frac{\overline{U}\,(i, j) - \overline{U}\,(i-1, j)}{\Delta x} \tag{7}$$

Neste caso, i representa a posição espacial na malha de discretização e j representa a posição temporal nesta malha. A união das equações 4, 6 e 7 produz:

$$\overline{U}(i, j+1) = \overline{U}(i, j)\left[1 + \frac{\Delta t}{\Delta x}\overline{U}(i-1, j) - \frac{\Delta t}{\Delta x}\overline{U}(i, j)\right] \tag{8}$$

Pela figura 1 vê-se que a velocidade na posição i-1 sempre será a velocidade do escoamento imperturbado, isto é, U_0. Assim, a equação 8 passa a ser representada por:

$$\overline{U}(i, j+1) = \overline{U}(i, j)\left[1 + \alpha\, U_0 - \alpha \overline{U}(i, j)\right] \tag{9}$$

$$\alpha = \frac{\Delta t}{\Delta x}$$

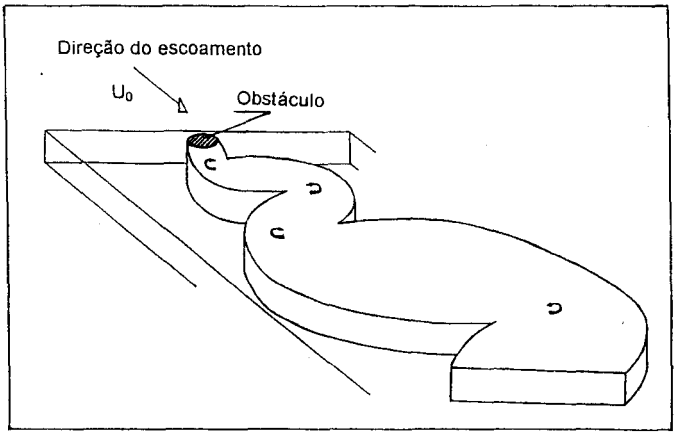

Figura 1a: Situação considerada para ilustrar o presente trabalho. O escoamento de águas rasas em regime turbulento, gerando a esteira de vórtices para as grandezas médias.

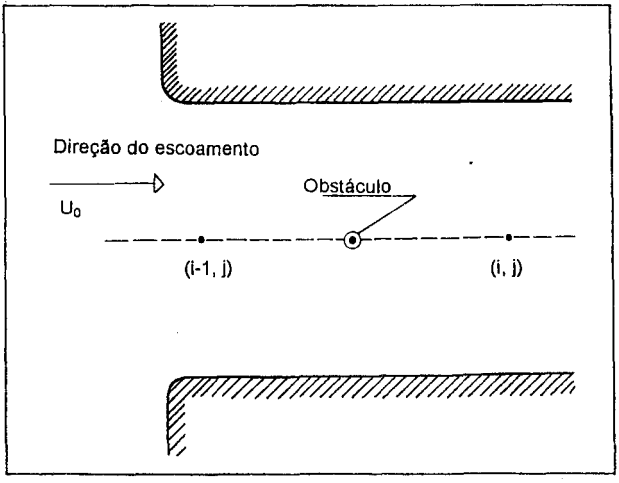

Figura 1 b: Nós da malha de discretização na direção x. O índice i representa a posição no espaço e o índice j representa a dimensão temporal

Uma simplificação substancial da equação 9 é obtida aplicando a transformação:

$$\begin{cases} y_t = \dfrac{\alpha}{1+\alpha U_0}\overline{U}(i,j) \\ \\ \lambda = \dfrac{1+\alpha\, U_0}{4} \end{cases} \tag{10}$$

Resulta, então:

$$y_{t+1} = 4\lambda\, y_t\left(1 - y_t\right) \tag{11}$$

t representa a discretização do tempo para a nova variável y. Assim como a equação 5, esta equação conduz a valores absolutos que não devem ser aplicados diretamente como solução do escoamento. Convém lembrar, mais uma vez, que interessa verificar o comportamento esperado (qualitativo) decorrente da não-linearidade das equações governantes.

O fato notável é que a equação 11 é exatamente a equação discretizada de crescimento populacional que foi utilizada nos trabalhos de May e Feigenbaum (ver Feigenbaum, 1978) para o estudo das propriedades inerentes a sistemas não-lineares simples que apresentam características comportamentais complexas. Entretanto, esta equação deriva aqui de simplificações e discretizações feitas sobre as equações de Navier-Stokes e de Reynolds.

A equação 11 possui um parâmetro de "controle", representado pelo coeficiente λ ao qual podemos arbitrar valores e estudar o comportamento temporal do sistema. Os trabalhos clássicos de Feigenbaum (1978) foram reproduzidos em uma grande quantidade de artigos e livros (ver Briggs & Peat, 1989, por exemplo), adicionando informações relevantes e dando base para a teoria do caos. Esses resultados podem ser aqui utilizados, no âmbito do problema físico em estudo. As transformações que foram efetuadas permitiram ainda apresentar a equação 11 em uma forma normalizada, de modo que y varia entre 0,0 e 1,0 se o coeficiente λ também variar entre 0,0 e 1,0. Na presente análise os valores dos intervalos de tempo e espaço são mantidos constantes, de forma que o valor de λ passa a ser dependente apenas do valor da velocidade do escoamento. Vê-se, pela equação 10, que quanto maior a velocidade, maior λ.

Características das Respostas de acordo com o valor de λ

O experimento numérico efetuado para entender o "caminho para o caos" é notavelmente simples. Os cálculos são efetuados de forma a se obter a evolução temporal e o assim denominado "comportamento eventual" da velocidade no nó a jusante do cilindro (fonte de perturbação) indicado na figura 1. Cada cálculo deste comportamento eventual é efetuado para um valor fixo de λ. Em outras palavras, impomos valores para a velocidade de montante e verificamos, experimentalmente, o comportamento da velocidade de jusante. O valor de montante é refletido no valor constante de λ para cada experimento. As seguintes características podem ser observadas:

1 - Valores da velocidade de montante que mantém $0 \le \lambda < 1/4$ conduzem a um valor final de y=0 (comportamento eventual). Evidentemente não se espera um valor final da velocidade igual a zero, mas sabemos que, para velocidades baixas, a velocidade média de entrada e a velocidade média no ponto (i,j) da figura 1 são iguais, isto é, sua diferença é nula. A figura 2a mostra um esquema desta situação.

2 - Valores de velocidade de montante que mantém $1/4 < \lambda < 3/4$ conduzem a comportamentos eventuais diferentes de zero, porém constantes. Isto implica que, para velocidades maiores que aquelas do ítem 1, podemos ter situações nas quais a diferença entre as velocidades de entrada e no ponto de interesse (para manter a mesma analogia feita no ítem 1) não é zero, isto é, podemos ter velocidades diferentes nos dois pontos. Nós sabemos que isto é possível quando temos a formação de vórtices a jusante de um cilindro, que permanecem fixos ao cilindro. Estando o ponto de interesse na região afetada pelo vórtice, a velocidade de jusante não é, com certeza, a velocidade de montante. A figura 2b mostra um esquema desta situação.

3 - Valores de velocidade de montante que mantém $3/4 < \lambda <\sim 0{,}892498$ conduzem a comportamentos eventuais diferentes de zero, mas que podem ser variáveis no tempo. A figura 2c mostra um esquema desta situação. A evolução desses comportamentos periódicos desenvolve-se de uma maneira perfeitamente definida, na qual diferentes estágios são reconhecidos:

- Estágio de duplicação de períodos

Neste estágio, o comportamento eventual que era, para baixas velocidades, constante, passa a apresentar oscilações periódicas, similares àquelas observadas para a componente longitudinal da velocidade na formação da esteira de vórtices a jusante de um cilindro (figura 2c). As oscilações apresentam-se, inicialmente, com estrutura interna simples, lembrando uma repetição senoidal (valores altos e baixos repetidos alternadamente). Neste caso, tem-se um fenômeno que se repete após 2 intervalos de tempo (período 2). Posteriormente, aumentando cada vez mais a velocidade, a estrutura interna das oscilações torna-se cada vez mais complexa. Assim, passa-se por um período 4 (isto é, os valores se repetem após quatro intervalos de tempo), por um período 16, seguido de um período 32, e assim por diante. Tem-se, então, o que se denominou de estágio de duplicação de período, que segue a relação 2^n, onde n indica em qual duplicação nos encontramos. Esta forma de evolução, na qual a estrutura interna do escoamento mostra-se cada vez mais complexa em aumentando a velocidade (ou o número de Reynolds, se quizermos utilizar a terminologia usual para este tipo de observação experimental) é amplamente conhecida em mecânica dos fluidos.

- Estágio de caos

Neste estágio, o comportamento eventual da velocidade de jusante, que era periódico, passa a apresentar um "período infinito", ou, o que é o mesmo, os seus valores passam a não se repetir mais. Tem-se um comportamento dito caótico. Em mecânica dos fluidos, após as passagens de escoamentos laminares estáveis para escoamentos periódicos, tem-se, com o aumento do número de Reynolds, (da velocidade, no presente exemplo) a transição para a turbulência (figura 2d). No presente equacionamento esta transição é-nos apresentada como caos (muito embora não se pretenda aqui discorrer sobre as semelhanças ou discrepâncias entre caos e turbulência). O valor limite de λ para o estágio de duplicação de períodos é, conforme indicado no ítem anterior, algo em torno de 0,892498. Para o caso dos escoamentos em águas rasas que aqui utilizamos como exemplo, sabemos que os mesmos já se encontram na situação de escoamento turbulento. O que é interessante observar é que, em termos de propriedades médias desses escoamentos turbulentos, novamente há a passagem por um processo de instabilização e geração de movimentos periódicos, semelhante à instabilidade que ocorre nos movimentos laminares. Este fato está bem exemplificado nos trabalhos experimentais de Jirka (1992), Dracos et al. (1992) e Chen e Jirka (1995), por exemplo.

A questão natural que então surge é: por que o processo de instabilização das propriedades médias em escoamentos turbulentos segue os padrões existentes no processo de instabilização de escoamentos laminares? A resposta está contida nas equações governantes para ambos os fenômenos. No caso dos escoamentos laminares, utilizamos as equações de Navier-Stokes, sem

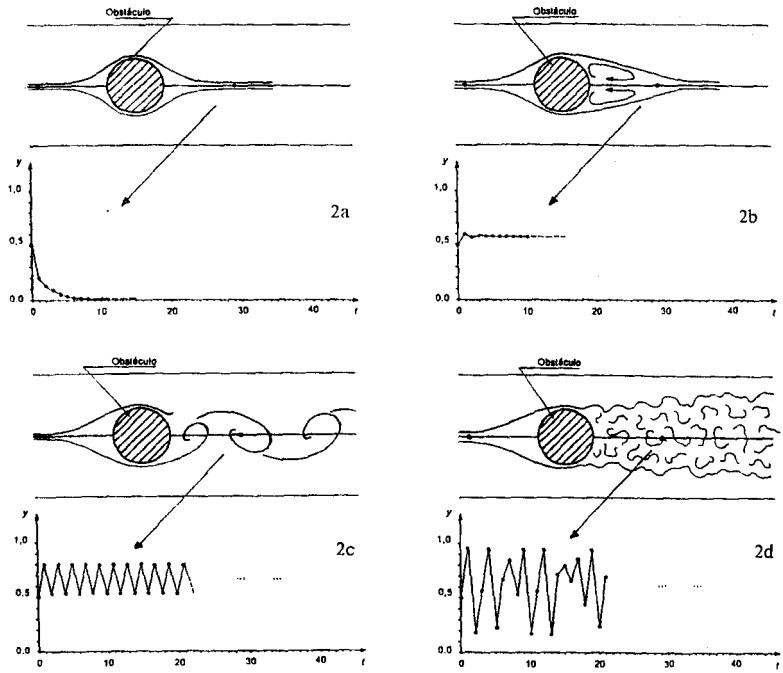

Figura 2: Evoluções temporais de y para diferentes valores de λ.
Todas as evoluções foram obtidas com um valor inicial de 0,5 para y.
(a) Evolução de y para λ=0,2. (b) Evolução de y para λ=0,6.
(c) Evolução de y para λ=0,8. (d) Evolução de y para λ>0,892498.

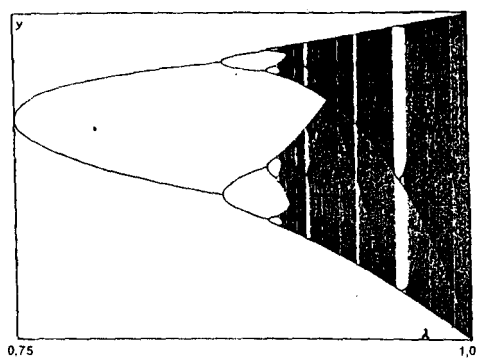

Figura 3: Bifurcações observadas para os valores de y em função do parâmetro de controle λ.

restrições. No caso dos escoamentos turbulentos utilizamos as equações de Reynolds para as grandezas médias, as quais mantém as mesmas características não-lineares do equacionamento original (Navier-Stokes). As equações 3 e 4 mostram isto e permitem concluir que os comportamentos observados em baixos números de Reynolds, dependentes da não-linearidade das equações (instabilidades), também podem ocorrer em altos números de Reynolds para as grandezas médias.

Resultado Quantitativo Universal

A determinação do encadeamento de duplicação de período no caminho ao caos (ou ao estado de turbulência, no presente trabalho) é uma característica do tipo de não-linearidade encontrado nas equações governantes da mecânica dos fluidos. Quando o escoamento observado passa de um estágio com um período T para um estágio com período $2T$, ocorre o que é denominado de bifurcação, que pode ser visto talvez com mais propriedade no gráfico do comportamento eventual em função de λ. A figura 3 apresenta um esquema das principais características deste gráfico, onde os valores de possíveis de y para cada λ duplicam a partir de valores bem definidos de λ. Uma forma de visualização experimental da duplicação de períodos é efetuar uma análise espectral sobre os dados coletados, localizando as freqüências dominantes. Assim, para valores de λ no intervalo $3/4 < \lambda <\sim 0{,}892498$ tem-se, inicialmente, uma única freqüência, porque o fenômeno se repete a cada dois valores da velocidade (lembra os máximos e mínimos de uma onda senoidal). A figura 4a representa este estágio do experimento. Quando o evento passa a se repetir a cada 4 valores, tem-se uma situação equivalente à soma de duas funções senoidais, com frqüências diferentes por um fator dois. Isto implica que o espectro apresenta, agora, a característica esquematizada na figura 4b. Este processo se repete, sempre havendo a inclusão de uma nova freqüencia, a qual é resultante da multiplicação da freqüência anterior por um fator ½. Os sucessivos espectros apresentam o desenvolvimento indicado nas figuras 4c e 4d, sendo que esta última corresponde já à situação de caos. Este tipo de comportamento espectral é observado em vários experimentos em mecânica dos fluidos, sendo um exemplo típico o experimento das células de circulação por convecção no interior de um ambiente com forma de paralelepípedo, efetuado por Libchaber e Maurer e analisado por Feigenbaum (ver Feigenbaum, 1978).

A possibilidade de se estabelecer valores de λ para cada bifurcação permite que a análise qualitativa até o momento apresentada possa, adicionalmente, ser seguida de uma análise quantitativa. Neste caso, como a equação estudada não permite o cálculo absoluto das velocidades, pode-se procurar prever qual o intervalo em λ que produz a próxima bifurcação. Como o valor de λ não decorre do modelo de cálculo da velocidade de jusante, mas é função apenas da velocidade de montante (constante para cada experimento e arbitrada pelo pesquisador), o cálculo do intervalo desejado deve ter características universais para o tipo de não-linearidade em questão. O que se observa neste experimento matemático é que a duplicação de período segue uma evolução exponencial para o parâmetro de controle, que tende rapidamente ao limite do caos. A lei de obtenção dos sucessivos valores de λ conduz ao número de Feigenbaum, definido conforme visto na equação 12.

$$\lim_{n\to\infty} \frac{\lambda_{n+1} - \lambda_n}{\lambda_{n+2} - \lambda_{n+1}} \cong 4{,}6692 \qquad (12)$$

O número de Feigenbaum é irracional. Assim, a validade do valor apresentado restringe-se às casa decimais utilizadas. A pergunta natural que segue a esta proposta numérica é: esta constante pode ser observada em problemas de mecânica dos fluidos? Como já foi dito, esta é uma expressão que tem características universais. Assim, resultados experimentais obtidos em mecânica dos fluidos

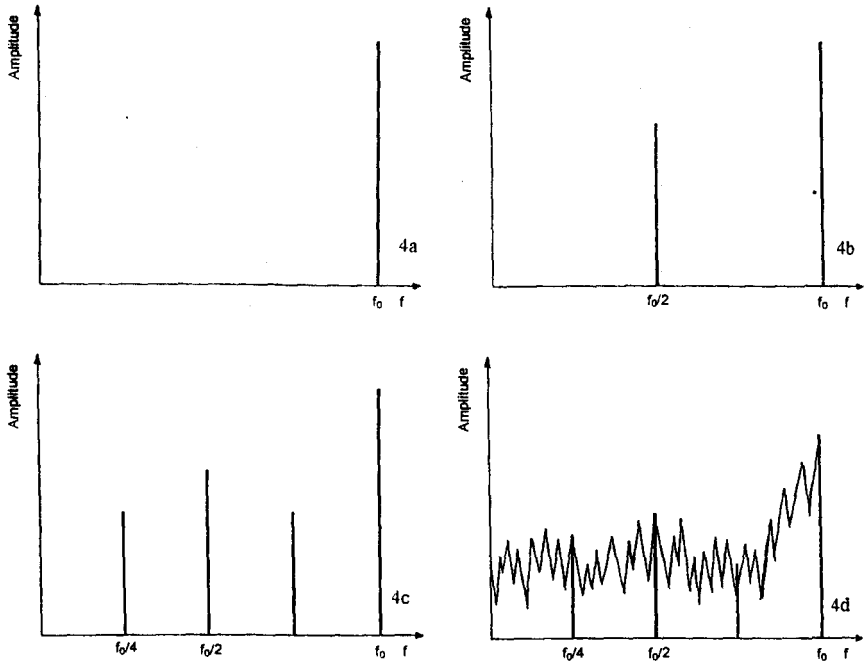

Figura 4: A duplicação de período vista a partir de uma análise espectral. Cada duplicação de período implica em uma freqüência adicional com metade do valor da freqüência anterior. A última figura mostra a situação de turbulência, onde o espectro apresenta-se sem picos preponderantes.

conduzem ao número de Feigenbaum quando analisados com respeito à duplicação de períodos. A análise seguida pode ser considerada elegante, porque permitiu, através de um exemplo numérico simples, no qual simplificações fortes como unidimensionalidade e desconsideração dos processos difusivos foram feitas, obter um resultado de características universais.

Conclusões

Mostrou-se, neste trabalho, uma forma de obter a equação de recorrência normalmente utilizada no estudo do caos, a partir de simplificações e de discretizações convenientemente conduzidas nas equações usuais da mecânica dos fluidos.

Mostrou-se que a característica relevante a ser analisada, neste tipo de estudo, é o tipo de não-linearidade que a equação original contém. No presente caso, as equações analisadas conduzem a um processo de duplicação de períodos e ao caos, que foi associado à instabilização com geração de vórtices e ao estado de movimento turbulento do escoamento utilizado como exemplo. No presente texto foi mantido o aspecto didático. Questões referentes à associação entre caos e turbulência não foram levantadas.

Mostrou-se a simplicidade existente no entendimento da instabilidade de escoamentos utilizando este ponto de vista, o qual minimiza a carga matemática necessária ao iniciante. Evidentemente frisa-se que os métodos tradicionais devem ser também analisados, porém em um estágio posterior de formação do pesquisador.

Mostrou-se resultados clássicos da teoria do caos, como o número de Feigenbaum, que demonstram a universalidade das conclusões obtidas.

Mostrou-se que as equações de Navier-Stokes e as equações de Reynolds, para as grandezas médias em escoamentos turbulentos, apresentam o mesmo tipo de não-linearidade, o que faz com que se esperem comportamentos semelhantes para as variáveis nos escoamentos laminares e as variáveis médias nos escoamentos turbulentos.

Utilizou-se como exemplo o escoamento turbulento em águas rasas.

Agradecimentos

O autor agradece à FAPESP, pelo apoio obtido através do processo 1997/11743-0 para execução de pesquisa no exterior, na qual o presente trabalho se insere, e ao Prof. Gerhard Jirka, anfitrião no Institut für Hydromechanik, Universität Karlsruhe, Alemanha.

Referências Bibliográficas

Briggs, J. e Peat, D., 1990, "Die Entdeckung des Chaos", Carl Hanser Verlag, München, Wien.

Chen, D. e Jirka, G.H., 1995, "Experimental Study of Plane Turbulent Wakes in a Shallow Water Layer", Fluid Dynamics Research. Vol.16, pp. 11-41.

Dracos, T., Giger, M. e Jirka, G.H., 1992, "Plane Turbulent Jets in a Bounded Fluid Layer", Journal of Fluid Mechanics, Vol.241, pp.587-614.

Feigenbaum, M.J. 1978, "Quantitative Universality for a Class of Nonlinear Transformations", Journal of Statistical Physics, Vol.19, nº1, pp.25-52.

Jirka, G.H., 1992, "In Support of Experimental Hydraulics: Three Examples from Environmental Fluid Mechanics", Journal of Hydraulic Research, Vol.30, nº3, pp.293-301.

Effect of Wave Frequency on the Nonlinear Interaction Between Görtler Vortices and Three-Dimensional Tollmien-Schlichting Waves

Márcio T. MENDONÇA, Laura L. PAULEY[†] & Philip J. Morris[†]
Centro Técnico Aeroespacial
Pc. Mal. Eduardo Gomes, 50 – CTA/IAE/ASA-P
12228-904 São José dos Campos - SP, Brazil
e-mail: mendonca@valley-bbs.com.br

[†] The Pennsylvania State University
Dept of Aerospace Engineering
University Park, PA 16802, USA

Abstract

The nonlinear interaction between Görtler vortices (GV) and three-dimensional Tollmien-Schlichting (TS) waves is studied with a spatial, nonparallel model based on the Parabolized Stability Equations (PSE). In this investigation the effect of TS wave frequency on the nonlinear interaction is studied. As verified in previous investigations using the same numerical model, the relative amplitudes and growth rates of GV and TS waves is one of the dominant parameters in GV/TS wave interaction. In this sense, the wave frequency influence is important in defining the streamwise distance traveled by the disturbances in the unstable region of the stability diagram. For three-dimensional TS waves, in the range of frequencies that result in significant disturbance growth, there is little change in the total growth of the disturbances for different wave frequencies, and so the influence of frequency on the nonlinear interaction is small.

Keywords: Görtler vortices, Tollmien-Schlichting waves, boundary layer stability, instability, transition.

Introduction

Due to centrifugal effects, laminar boundary layer flows over concave surfaces may develop counter rotating longitudinal vortices called Görtler vortices (GV). These vortices develop inflectional velocity profiles that are sensitive to other types of instabilities leading to transition to turbulence. The transition may be undesirable since it increases skin friction and heat transfer rates and, if inevitable, it must be predicted with accuracy to allow, for example, the correct design of cooling systems. Among the Aerospace Engineering applications where laminar flow over concave surfaces is important, one can highlight the flow over the pressure side of turbine blades and the flow inside supersonic converging diverging nozzles. Besides the presence of the vortices, other types of instabilities may also be present and the nonlinear interaction between the GV (Görtler vortices) and these other instabilities may anticipate the transition to turbulence. More specifically, when the curvature of the wall is small the flow may become unstable also to Tollmien-Schlichting (TS) waves which interact nonlinearly with the vortices.

Tani and Aihara (1969) presented experimental results for the interaction between GV developing on a concave wall and TS (Tollmien-Schlichting) waves generated by a vibrating ribbon. They concluded that the main effect of the vortices on the TS waves is through the spanwise change in boundary layer thickness.

Nayfeh (1981) used the method of multiple scales to study the effect of GV on the development of TS waves. He found that the vortices strongly destabilize TS waves having spanwise wavelength twice the wavelength of the vortices. His results were not confirmed by Malik (1986) who used a temporal, parallel model and found an inconsistent length scale in Nayfeh's formulation. Malik (1986) found that TS waves with spanwise wavelength half

the wavelength of the vortices are destabilized by the nonlinear interaction.

Srivastava and Dallmann (1987) used the method of multiple scales to study the same problem, but also allowed for TS wave amplitudes of the same order of magnitude as the vortices. Their results showed good agreement with Nayfeh's results despite the fact that Nayfeh's formulation was incorrect. This result raises doubts about their other findings.

To correct the problem in his previous paper, Nayfeh reworked his formulation and presented new results in Nayfeh and Al-Maaitah (1988). They solved the stability equations using both Floquet theory and the method of multiple scales. This time, their results agreed with Malik (1986) in the sense that resonance occurs when the spanwise wavelength of the oblique wave is half that of the wavelength of the vortices. They also presented some parametric studies on the effect of Reynolds number and frequency.

Malik and Hussaini (1990) extended Malik's (1986) temporal, parallel formulation to allow TS wave amplitudes of the same order of magnitude as the vortices. They studied the interaction between GV and two-dimensional TS waves and concluded that the growth rate is larger than the growth of the unperturbed wave. Their results agree with Nayfeh and Al-Maaitah's (1988) results in the sense that interactions take place at a relatively large amplitude of the vortices. Although the model could be used for amplitudes of the waves of the same order of magnitude as the amplitude of the vortices, they only presented results for small amplitude waves.

Malik and Godil (1990) presented another paper using the same formulation used by Malik (1986). They showed that the nonlinear interaction between GV and two-dimensional TS waves leads to the development of oblique waves with a spanwise wavelength equal to that of the vortices. Again, they limited their study to small amplitude TS waves. Their results indicate that the upper branch TS waves are excited while the lower branch waves

are relatively insensitive to the vortices.

All these investigations have used local models or temporal, parallel models. Local models are not suitable to study the development of GV which are governed by parabolic equations that, rigorously, can not be simplified to ordinary differential equations, except at large wavenumbers. In this way, local models have been used to study the development of TS waves in boundary layer flows with embedded streamwise vortices. Temporal models are not the most appropriate to describe the physics of spatially developing vortices, and nonparallel effects are important both for low spanwise wavenumber vortices and for three-dimensional TS waves. Only results for TS waves with small amplitudes have been presented in previous works.

Mendonça, Morris and Pauley (1997) used a spatial, nonparallel model to verify the conclusions obtained in previous investigations that used local or temporal, parallel models. Their model was based on the Parabolized Stability Equations (PSE) (Bertolotti, 1991). They showed that the conclusions obtained in previous investigations are valid, but the assumption of parallel mean flow does influence the results. They also presented results for TS wave amplitudes of the same order of magnitude of the vortices which result in significant nonlinear interaction. In this case the breakdown to turbulence may be anticipated. Their results show the importance of growth rates and initial amplitudes as controlling parameters in GV/TS wave interaction.

In a second paper Mendonça, Morris and Pauley (1998a) used the same spatial model based on the PSE equations to investigate the effect of Görtler number and spanwise wavenumber on the nonlinear interaction between GV and two-dimensional TS waves. They showed that it is not possible to isolate the effects of initial amplitude, growth rate, Görtler number and wavenumber. This controlling parameters are interrelated and the nonlinear

interaction is strongly dependent on the relative amplitudes of the vortices and TS waves. In this sense two types of interactions have been identified. If the TS wave amplitude is of the same order of magnitude of the vortices, the development of the mean flow distortion and of the vortices higher harmonics are strongly destabilized. If the vortices are stronger than the TS wave, the vortices damp the development of the TS wave. These two different types of nonlinear interaction has been called "Type I" and "Type II" interactions.

The effect of wave frequency on the interaction between GV and two-dimensional waves has been studied by Mendonça, Morris and Pauley (1999). They concluded that the longer the path of the TS wave under the unstable region of the TS wave stability diagram, the stronger the disturbance and the higher the nonlinear interaction with the vortices. As observed in previous studies, when the TS wave amplitudes are of the same order of magnitude as the vortices, very strong nonlinear interaction takes place resulting in earlier breakdown to turbulence or strong destabilization of the vortices.

The present investigation expands the results presented by Mendonça, Morris and Pauley (1999). It uses the same spatial, nonparallel model to study the influence of frequency on the nonlinear interaction between GV and three-dimensional TS waves. Again, the model allows TS wave amplitudes of the same order of magnitude as the vortices so that the influence of the TS waves on the development of the vortices can be accounted for.

Formulation

The coordinate system used in the present work is the same coordinate system presented by Floryan (1980). It is based on the streamlines (ψ^*) and potential lines (ϕ^*) of the inviscid flow over a constant radius of curvature wall. This coordinate system has the

advantage of producing a decay of the curvature away from the wall; at the wall it is surface oriented, but away from the wall it approaches a Cartesian system. In the normal direction a transformation is applied in order to cluster grid points close to the wall.

The Navier-Stokes equations for an incompressible flow of a Newtonian fluid are simplified by assuming that the dependent variables are decomposed into a mean component and a fluctuating component as follows:

$$\vec{u^*} = \vec{U^*} + \vec{u^*}', \qquad \text{and} \qquad p^* = P^* + p^{*\prime}. \tag{1}$$

where $\vec{u^*} = [u^*, v^*, w^*]^T$ is the velocity vector and p^* is the pressure. The superscript * indicates dimensional variables.

The equations are nondimensionalized using δ_0^* and U_∞^* as the length and velocity scaling parameters, where $\delta_0^* = (\nu^* \phi_0^* / U_\infty^*)^{1/2}$ is the boundary layer thickness parameter, U_∞^* is the free stream velocity, ϕ_0^* is a reference length taken as the streamwise location where initial conditions are applied, and ν^* is the kinematic viscosity.

Floryan (1980) derived the equations for the zeroth order and first order approximations for the mean flow and for the perturbation quantities. He concluded that for the zeroth order approximation the mean flow equations reduce to the Prandtl boundary layer equations for the flow over a flat plate. The only remaining curvature term for the perturbation equations zeroth order approximation is the term in the momentum equation in the normal direction given by:

$$\frac{Go^2}{Re^2}(2Uu' + u'^2), \qquad \text{where} \qquad Go = Re(k^* \delta_0^*)^{(1/2)}, \qquad Re = \frac{U_\infty^* \delta_0^*}{\nu^*}. \tag{2}$$

Go is the Görtler number, k^* is the curvature of the wall, and Re is the Reynolds number.

The resulting momentum and continuity equations are written in vector form:

$$A\frac{\partial \Phi'}{\partial t} + B_1\frac{\partial \Phi'}{\partial \phi} + C_1\frac{\partial \Phi'}{\partial \psi} + D_1\frac{\partial \Phi'}{\partial z} + E\left(\frac{\partial^2 \Phi'}{\partial \phi^2} + \frac{1}{g^2}\frac{\partial^2 \Phi'}{\partial \psi^2} + \frac{\partial^2 \Phi'}{\partial z^2}\right) + F_1\Phi' = G, \qquad (3)$$

where $\Phi' = [u', v', w', p']^T$, and the expressions for the coefficient matrices can be found in Mendonça (1997).

The boundary conditions are given by:

$$u' = v' = w' = 0 \qquad \text{at} \qquad \psi = 0, \qquad (4)$$

$$\frac{\partial u'}{\partial \psi}, \frac{\partial v'}{\partial \psi}, \frac{\partial w'}{\partial \psi}, p' \to 0 \qquad \text{as} \qquad \psi \to \infty. \qquad (5)$$

The boundary condition for pressure at the wall is given by the momentum equation in the normal direction applied at $\psi = 0$.

Parabolized Stability Equations

The governing equations for the perturbation variables are simplified, leading to the Parabolized Stability Equations (PSE) developed by Herbert and Bertolotti (Bertolotti, 1991). The resulting set of equations describes the spatial evolution of disturbances, and allows nonparallel, nonlinear effects to be accounted for without the heavy demands of a direct numerical simulation. The simplifications leading to the PSE are presented below.

The set of equations represented by Eq. (3) are elliptic and the perturbations propagate in the flow field as wave structures. The governing equations can be simplified if the wavelike nature of the perturbations are represented by their frequency ω, wavenumbers α

and β, and growth rate γ. The perturbation Φ' is assumed to be composed of a slowly varying shape function $\Phi_{n,m}$ and an exponential oscillatory wave term $\chi_{n,m}$. It is represented mathematically as a Fourier expansion truncated to a finite number of modes:

$$\Phi' = \sum_{n=-N}^{N} \sum_{m=-M}^{M} \Phi_{n,m}(\phi, \psi)\, \chi_{n,m}(\phi, z, t), \tag{6}$$

where $\Phi_{n,m}(\phi, \psi) = [u_{n,m}, v_{n,m}, w_{n,m}, p_{n,m}]^T$ is the complex shape function vector, and

$$\chi_{n,m}(\phi, z, t) = \exp\left[\int_{\phi_0}^{\phi} a_{n,m}(\xi) d\xi + im\beta z - in\omega t\right], \tag{7}$$

$$a_{n,m}(\phi) = \gamma_{n,m}(\phi) + in\alpha(\phi). \tag{8}$$

This procedure is similar to a normal mode analysis but, in this case, the shape function $\Phi_{n,m}$ is a function of both ϕ and ψ.

The streamwise growth rate $\gamma_{n,m}$, the streamwise wavenumber α, and the spanwise wavenumber β were nondimensionalized using the boundary layer thickness parameter δ_0^*. The frequency ω was nondimensionalized using the free stream velocity U_∞^* and the boundary layer thickness parameter δ_0^* .

For linear problems only the fundamental mode is significant. With the growth of the amplitude of the fundamental, higher harmonics become significant as well as the mean flow distortion (MFD) $n = 0$, $m = 0$. As the nonlinearities become stronger, higher harmonics are considered by increasing the number of modes N, M in the truncated Fourier expansion. The form of $a_{n,m}$ (Eq. 8) reflects the fact that the phase speed of higher harmonics should be the same as the phase speed of the fundamental mode to avoid dispersion of the wave structure.

The perturbation variable Φ', as defined in Eq. (6), is substituted in Eq. (3). The equation is then simplified by assuming that the shape function, wavelength, and growth rate vary slowly in the streamwise direction. In this way, second order derivatives and products of first order derivatives can be neglected in the streamwise direction.

After substituting these terms into Eq. (3) and performing a harmonic balance of the frequency, a set of coupled nonlinear equations is obtained. For each mode (n, m) the equation is given in vector form by:

$$\overline{A}_{n,m}\Phi_{n,m} + \overline{B}_{n,m}\frac{\partial \Phi_{n,m}}{\partial \phi} + \overline{C}_{n,m}\frac{\partial \Phi_{n,m}}{\partial \psi} + \overline{D}_{n,m}\frac{\partial^2 \Phi_{n,m}}{\partial \psi^2} = \frac{\overline{E}_{n,m}}{e^{\left(\int_{\phi_0}^{\phi} a_{n,m}(\xi)d\xi\right)}}, \tag{9}$$

where the coefficient matrices can be found in Mendonça (1997)

The resulting equations are parabolic in ϕ and the solution can be marched downstream given initial conditions at a starting position ϕ_0. This is true as long as the instabilities are convected instabilities such that they propagate in the direction of the mean flow and do not affect the flow field upstream.

The pressure gradient in the streamwise momentum equation also makes the system of equations nonparabolic. For incompressible flow Malik and Li (1993) suggest that sufficiently large steps in the streamwise direction will avoid the elliptic behavior of the problem. They also show that dropping the pressure gradient term altogether does not change the results for the level of approximation given by the PSE. In the present model the pressure gradient term is not included.

The boundary conditions for Eq. (9) are derived from Eq. (5). At the wall, homogeneous Dirichlet no-slip conditions are used. In the far field, Neumann boundary conditions are used for the velocity components and a homogeneous Dirichlet condition is used for

pressure.

For the parabolic formulation, it is necessary to specify initial conditions at a starting position ϕ_0 downstream of the stagnation point at the leading edge of the curved plate. For TS waves the initial conditions are obtained from the solution of the eigenvalue problem posed by the Orr-Sommerfeld equation. For GV the initial conditions are also given by a local normal mode analysis.

Normalization Condition

The splitting of $\Phi'(\phi, \psi, z, t)$ into two functions, $\Phi_{n,m}(\phi, \psi)$ and $\chi_{n,m}(\phi, \psi, z, t)$, is ambiguous, since both are functions of the streamwise coordinate ϕ. It is necessary to define how much variation will be represented by the shape function $\Phi_{n,m}(\phi, \psi)$, and how much will be represented by the exponential function $\chi_{n,m}(\phi, \psi, z, t)$. This definition has to guarantee that rapid changes in the streamwise direction are avoided so that the hypothesis of slowly changing variables is not violated. To do this, it is necessary to transfer fast variations of $\Phi_{n,m}(\phi, \psi)$ in the streamwise direction to the streamwise complex wavenumber $a_{n,m}(\phi) = \gamma_{n,m}(\phi) + in\alpha(\phi)$. If this variation is represented by $b_{n,m}$, for each step in the streamwise direction it is necessary to iterate on $a_{n,m}(\phi)$ until $b_{n,m}$ is smaller than a given threshold. At each iteration k, $a_{n,m}(\phi)$ is updated according to:

$$(a_{n,m})_{k+1} = (a_{n,m})_k + (b_{n,m})_k \tag{10}$$

The variation $b_{n,m}$ of the shape function can be monitored in different ways. In the present implementation the following is used:

$$b_{n,m} = \frac{1}{\int_0^\infty \|\vec{u}_{n,m}\|^2 d\psi} \int_0^\infty \left(\vec{u}^{\dagger}_{n,m} \cdot \frac{\partial \vec{u}_{n,m}}{\partial \phi} \right) d\psi, \tag{11}$$

where $\vec{u}^{\dagger}_{n,m}$ is the complex conjugate of $\vec{u}_{n,m}$. The integral of $\|\vec{u}_{n,m}\|^2$ was used to assure that the variation is independent of the magnitude of $\vec{u}_{n,m}$.

Numerical Method

The system of parabolic nonlinear coupled equations given by Eq. (9) is solved numerically using finite differences. The partial differential equation is discretized implicitly using a second order backward differencing in the streamwise direction, and fourth order central differencing in the normal direction. The resulting coupled algebraic equations form a block pentadiagonal system which is solved by LU decomposition.

To start the computation a first order backward differencing is used. The first order approximation is also used in a few subsequent steps downstream in order to damp transients more efficiently. For the points neighboring the boundaries, second order central differencing in the normal direction is applied.

The nonlinear terms are evaluated iteratively at each step in the streamwise direction. The iterative process is used both to enforce the normalization condition and to enforce the convergence of the nonlinear terms. A Gauss-Siedel iteration with successive overrelaxation is implemented. The nonlinear products are evaluated in the time domain. To do this, the dependent variables in the frequency domain are converted to the time domain by an inverse Fast Fourier Transform subroutine. The nonlinear products are evaluated and the results are transformed back to the frequency domain.

The complex wavenumber is updated at each iteration according to Eq. (10), and the

variation in the shape function is monitored through Eq. (11). The iteration is considered converged when the normalization condition is no larger than a given small threshold. In the present implementation this threshold is 10^{-8}.

Code Validation

A comparison between PSE results and the experimental results from Kachanov and Levchenko (1984) for subharmonic breakdown is presented. The subharmonic breakdown is characterized by the nonlinear interaction between a finite amplitude two-dimensional TS wave and small amplitude three-dimensional waves with half the frequency of the 2D TS wave. The starting conditions are: $Re = 400$, frequency $\omega_{2,0} = 0.0496$, spanwise wavenumber $\beta_{1,1} = 0.1333$, frequency $\omega_{1,1} = 0.0248$, initial amplitudes $\epsilon_{2,0} = 0.439\%$, and $\epsilon_{1,1} = 0.0039\%$.

Figure 1 presents a comparison between the PSE results and the experimental results from Kachanov and Levchenko (1984) for the amplitude of different harmonics. It shows that the PSE is able to reproduce the development of all harmonics with good accuracy. According to Joslin, Street and Chang (1993), the small differences between experimental and computational results observed for higher harmonics can be attributed to small differences between the experimental conditions reported by Kachanov and Levchenko and the actual experimental conditions. Those differences were due to a small streamwise pressure gradient and a larger frequency.

Good comparisons were also obtained with numerical results from Bertolotti (1991) for K-type breakdown and with numerical and experimental results from Malik and Li (1993) and Swearingen and Blackwelder (1987) respectively for nonlinear GV development.

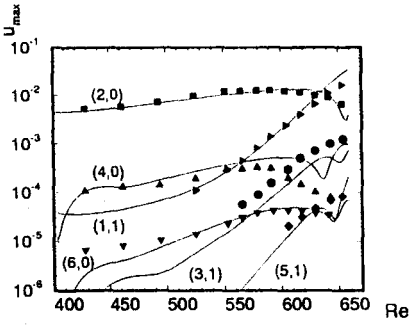

Figure 1: Subharmonic breakdown. Comparison between the PSE results and experimental results from Kachanov and Levchenko (1984).

Results

In this section the effect of TS wave frequency on the nonlinear interaction between GV and three-dimensional TS waves is studied. The following computational parameters are used in the calculations: the number of grid points used in the normal direction is 250 with 200 grid points clustered inside the boundary layer region, the step size dx is 10, the number of Fourier modes N in the streamwise direction is 6 and in the spanwise direction M is 5 (given the symmetry conditions, a total of 143 modes are considered, but only 42 modes are stored). For a typical case, 180 steps in the streamwise direction takes 133.1 minutes of CPU time, with 8.5 seconds per iteration on an IBM RS6000 workstation Model 560.

The following test cases consider vortices specified by $Go = 5, b = \beta/re\ 10^3 = 0.1$, with an initial amplitude $\epsilon_{GV} = 1\%$, interacting with TS waves of different frequencies. The TS waves initial amplitude is $\epsilon_{TS} = 0.5\%$. Four different frequencies are considered:

$F = \omega/re\ 10^6 = 30, 50, 75$ and 100. The starting streamwise positions are defined by the lower branch of the neutral curve and are given, with respect to the frequencies above, by $Re = 700, 575, 465$, and 400. The vortices and the TS waves are followed to a streamwise position past the upper branch of the neutral curve. Both fundamental resonance and subharmonic resonance are investigated.

Before investigating the effect of wave frequency on GV/TS waves interaction it is helpful to look at the general conclusions about GV/3D-TS wave interaction. A study on the nonlinear interaction between GV and three-dimensional TS waves was presented by Mendonça, Morris and Pauley (1998b). For fundamental resonance the nonlinear interaction results in the following: the nonlinear interaction has little effect on the development of the fundamental modes; a Fourier spectrum broadening is observed, resulting in the development of Fourier modes that would not grow without interaction (e.g. modes (1,0), (1,2), (2,0), (2,2), etc.); the development of mode (0,2) is governed by the development of the TS wave; the development of the MFD (mean flow distortion, mode (0,0)) is governed by the development of either the vortices or the TS waves, depending on which one results in the stronger MFD. These nonlinear effects can be observed in figures 2 through 9 for the four levels of wave frequency investigated in the present study. For subharmonic resonance, with the spanwise wavenumber of the vortices two times the spanwise wavenumber of the TS waves, the nonlinear interaction results in a strong effect on the development of the GV. This is due to the development of longitudinal vortices associated with the development of the TS waves. Again, the development of the MFD is governed by either the vortices or the TS waves, depending on which one results in the stronger MFD. These nonlinear effects can be observed in figures 10 through 17.

The results for the effect of wave frequency on GV/3D-TS waves interaction for fun-

damental resonance are presented in figures 2 through 9. Figures 2 through 5 show the development of the Fourier modes (0,0), (0,1), and (0,2) due to the nonlinear interaction (symbols) and due to the development of the vortices and TS waves without interaction (solid lines and dashed lines respectively). It can be observed that the variation of the TS wave frequency does not significantly change the results of the nonlinear interaction. The only noticeable difference is on the development of the MFD which depends on the strength of the MFD due to the vortices and TS waves: for $F = 50$ the MFD is governed mostly by the development of the MFD due to the TS waves, while for $F = 100$ the influence of the TS waves on the development of the MFD is delayed until a position farther downstream.

Figures 6 through 9 show the development of the Fourier modes (1,1), (1,0), (1,3), and (1,2). The symbols are the results due to the nonlinear interaction and the dashed lines due to the development of the TS waves without interaction. Again, for the four levels of wave frequency investigated there is no significant change in the nonlinear interaction characteristics. The growth of the TS waves is not strongly affected by the change in the wave frequency. The only exception is for $F = 100$ where the TS waves reach a lower final amplitude. These weaker TS waves are more strongly affected by the nonlinear interaction through the stronger development of additional harmonics (e.g. the Fourier modes (1,0) and (1,2)) that reach final amplitudes of the same order of magnitude of the fundamental mode (1,1).

The results for subharmonic resonance are presented in figures 10 through 17. The development of modes (0,2), (0,0) and (0,4) are presented in figures 10 through 13, and the development of modes (1,1), (1,3), (2,0), and (2,2) are presented in figures 14 through 17. The results show that the nonlinear interaction characteristics are not significantly dependent on the wave frequency. Again, the only exception is for $F = 100$, where the

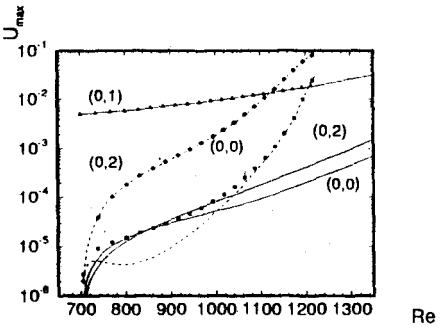

Figure 2: Fundamental resonance. $Re = 700$, $F = 30$, $\beta_{TS} = 0.07$. $\beta_{GV} = 0.07$.

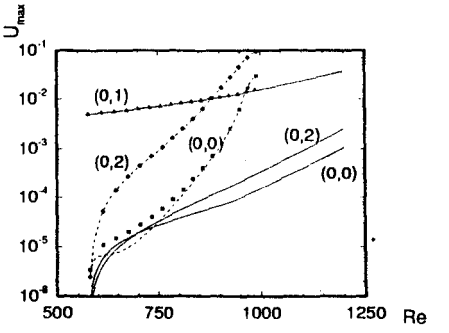

Figure 3: Fundamental resonance. $Re = 575$, $F = 50$, $\beta_{TS} = 0.0575$. $\beta_{GV} = 0.0575$.

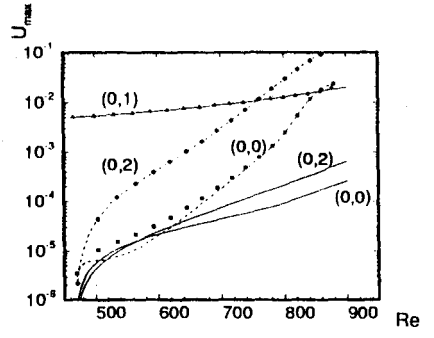

Figure 4: Fundamental resonance. $Re = 465$, $F = 75$, $\beta_{TS} = 0.0465$. $\beta_{GV} = 0.0465$.

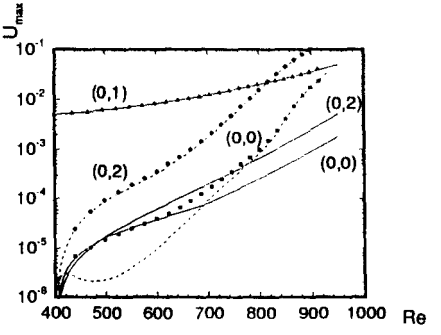

Figure 5: Fundamental resonance. $Re = 400$, $F = 100$, $\beta_{TS} = 0.04$. $\beta_{GV} = 0.04$.

Note: solid lines represent results due to the GV without interaction, dashed lines represent results due to TS waves without interaction, symbols represent results due to GV/TS waves interaction.

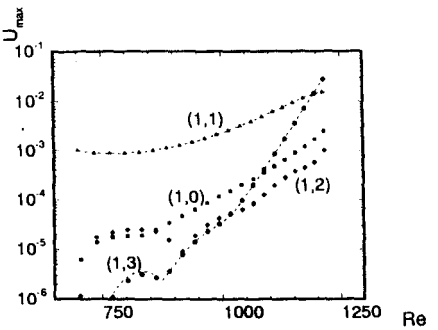

Figure 6: Fundamental resonance. $Re = 700$, $F = 30$, $\beta_{TS} = 0.07$. $\beta_{GV} = 0.07$.

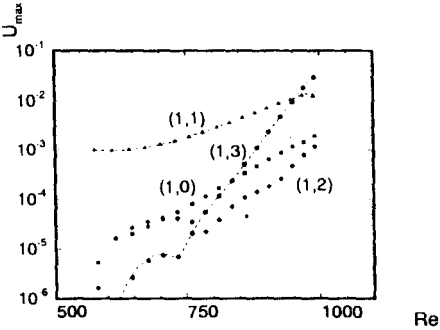

Figure 7: Fundamental resonance. $Re = 575$, $F = 50$, $\beta_{TS} = 0.0575$. $\beta_{GV} = 0.0575$.

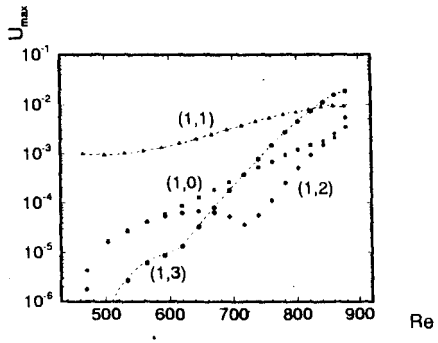

Figure 8: Fundamental resonance. $Re = 465$, $F = 75$, $\beta_{TS} = 0.0465$. $\beta_{GV} = 0.0465$.

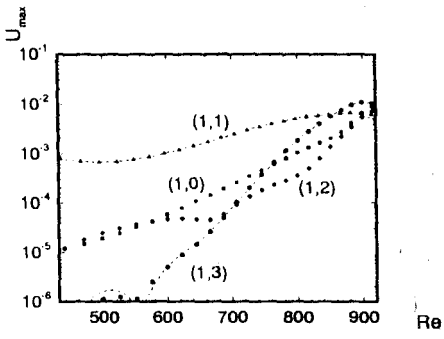

Figure 9: Fundamental resonance. $Re = 400$, $F = 100$, $\beta_{TS} = 0.04$. $\beta_{GV} = 0.04$.

Note: dashed lines represent results due to TS waves without interaction, symbols represent results due to GV/TS waves interaction.

strength of the TS waves is not enough to disturb the development of the GV as strongly as in the first three cases ($F = 30, 50, 75$).

Discussion

The results show that for three-dimensional TS waves the wave frequency does not have the same strong influence on the nonlinear interaction as it does for two-dimensional TS waves, at least for the range of frequencies investigated. For two-dimensional TS waves the results from Mendonça Morris and Pauley (1998a) indicate that the most important controlling parameters in GV/TS wave interaction is the relative amplitudes of the vortices and TS waves. In the instability diagram presented in Figure 18 a given TS wave follows a line of constant frequency F as it travels downstream. The higher the frequency F of the two-dimensional TS waves the weaker the TS wave. The TS wave travels a shorter streamwise distance in the unstable region in the stability diagram and is subject to lower growth rates. The weaker the TS waves, the stronger the dominance of the vortices in the nonlinear interaction. Lower frequencies result in stronger two-dimensional waves which may grow to amplitudes on the same order of magnitude as the vortices, resulting in a TS wave dominance over the nonlinear interaction.

For three-dimensional TS waves, the stability diagram shows that the unstable region may define a closed region as seen in Figure 18. In these cases low frequencies may result in little or no disturbance growth. In a certain range of TS wave frequencies there is little variation on the streamwise distance traveled by the disturbances under unstable condition and TS waves with different frequencies have similar growth along the streamwise direction. Since the growth rate of the TS waves does not vary much with frequency in that range of frequencies, the effect of frequency is lower in that range. When the frequency F is

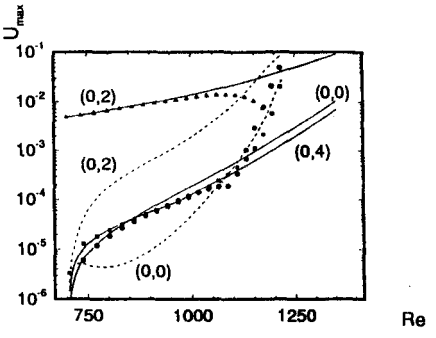

Figure 10: Subharmonic resonance. $Re = 700$, $F = 30$, $\beta_{TS} = 0.07$, $\beta_{GV} = 0.14$.

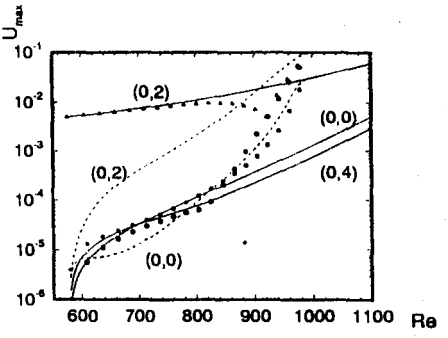

Figure 11: Subharmonic resonance. $Re = 575$, $F = 50$, $\beta_{TS} = 0.0575$, $\beta_{GV} = 0.115$.

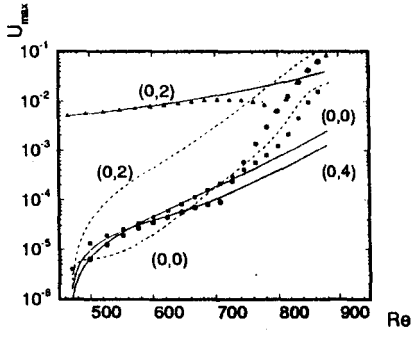

Figure 12: Subharmonic resonance. $Re = 465$, $F = 75$, $\beta_{TS} = 0.0465$, $\beta_{GV} = 0.093$.

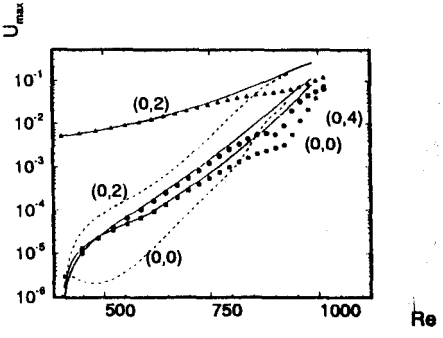

Figure 13: Subharmonic resonance. $Re = 400$, $F = 100$, $\beta_{TS} = 0.04$, $\beta_{GV} = 0.08$.

Note: solid lines represent results due to the GV without interaction, dashed lines represent results due to TS waves without interaction, symbols represent results due to GV/TS waves interaction.

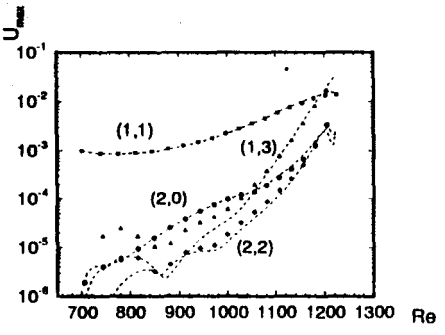

Figure 14: Subharmonic resonance. $Re = 700$, $F = 30$, $\beta_{TS} = 0.07$, $\beta_{GV} = 0.14$.

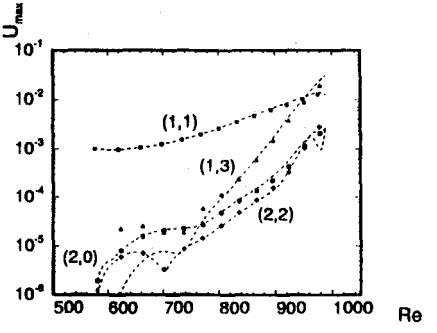

Figure 15: Subharmonic resonance. $Re = 575$, $F = 50$, $\beta_{TS} = 0.0575$, $\beta_{GV} = 0.115$.

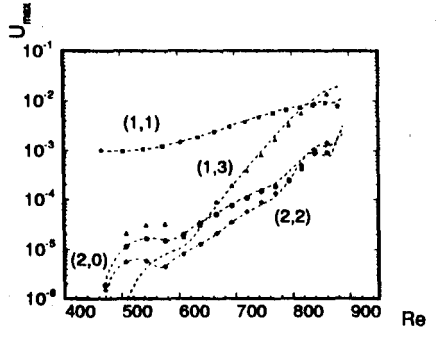

Figure 16: Subharmonic resonance. $Re = 465$, $F = 75$, $\beta_{TS} = 0.0465$, $\beta_{GV} = 0.093$.

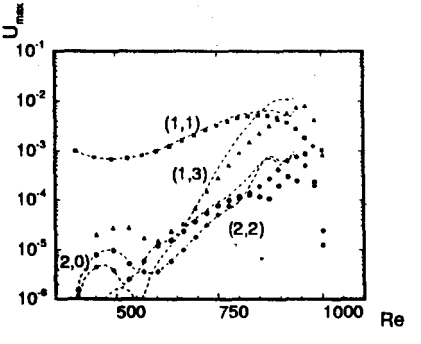

Figure 17: Subharmonic resonance. $Re = 400$, $F = 100$, $\beta_{TS} = 0.04$, $\beta_{GV} = 0.08$.

Note: dashed lines represent results due to TS waves without interaction, symbols represent results due to GV/TS waves interaction.

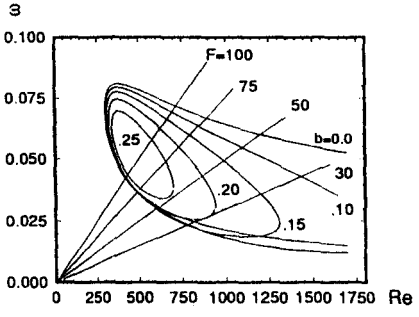

Figure 18: Neutral curves for oblique waves for different spanwise wavenumbers.

close to the boundaries of the closed region defined by the stability diagram, and at certain frequencies and spanwise wavenumbers that result in small growth of the disturbances, the effect of frequency on the nonlinear interaction is lower.

Conclusions

As observed in previous investigations the relative amplitude of the vortices and TS waves is one of the most important parameters in the GV/TS wave nonlinear interaction. Three-dimensional TS waves are characterized by little variation in the total growth of the disturbance for different frequencies in a certain range of frequencies. In this way, since the change in frequency in this range does not result in strong change in the total growth of the TS waves, no significant change in the nonlinear interaction was be observed. At frequencies that are close to the limits that define the closed unstable region, and for wave frequencies that result in little growth of the fundamental waves, a weaker influence of the TS waves on the nonlinear interaction can be observed.

References

Bertolotti, F. P. 1991. *Linear and Nonlinear Stability of Boundary Layers With Streamwise Varying Properties.* Ph.D. thesis, The Ohio State University, Columbus, Ohio.

Floryan, J. M. 1980. *Stability of boundary layer flows over curved walls.* Ph.D. thesis, Virginia Polytechnic Institute and State University.

Joslin, R. D., Street, C. L., and Chang, C.-L. 1993. Spatial Direct Numerical Simulation of Boundary-Layer Transition Mechanics: validation of PSE Theory. *Theoretical and Computational Fluid Dynamics*, 4(6), 271–288.

Kachanov, Y. K., and Levchenko, V. Y. 1984. The Resonant Interaction of Disturbances at Laminar-Turbulent Transition in a Boundary Layer. *J. Fluid Mechanics*, **138**, 209–247.

Malik, M. R. 1986. Wave Interaction in Three-Dimensional Boundary Layers. *AIAA Paper 86-1129.*

Malik, M. R., and Godil, A. A. 1990. Nonlinear Development of Görtler and Crossflow Vortices and Görtler/ Tollmien-Schlichting Wave Interaction. *NTIS,.AD A 221 107.*

Malik, M. R., and Hussaini, M. Y. 1990. Numerical Simulation of Interactions Between Görtler Vortices and Tollmien-Schlichting Waves. *J. Fluid Mechanics*, **210**, 183–199.

Malik, M. R., and Li, F. 1993. Transition Studies for Swept Wing flows Using PSE. *AIAA Paper, 93-0077.*

Mendonça, M. T. 1997. *Numerical Analysis of the Interaction between Görtler Vortices and Tollmien-Schlichting Waves using a Spatial Nonparallel Model.* Ph.D. thesis, The Pennsylvania State University.

Mendonça, M. T., Morris, P. J., and Pauley, L. L. 1997. Görtler Vortices Tollmien-Schlichting waves interaction: reassessment of previous results with a spatial/nonparallel model. *In: XIV Brazilian Congress of Mechanical Engineering.*

Mendonça, M. T., Morris, P. J., and Pauley, L. L. 1998b. Interaction Between Görtler Vortices and three-dimensional Tollmien-Schlichting waves. *Submited to The Physics of Fluids.*

Mendonça, M. T., Morris, P. J., and Pauley, L. L. 1998a. Interaction Between Görtler Vortices and two-dimensional Tollmien-Schlichting waves: Effect of Görtler number and spanwise wavenumber. *Submited to The Physics of Fluids.*

Mendonça, M. T., Pauley, L. L., and Morris, P. J. 1999. Effect of Wave Frequency on Görtler vortices Tollmien-Schlichting waves interaction. *Submited to the 37th AIAA Aerospace Science Meeting and Exhibit.*

Nayfeh, A. H. 1981. Effect of Streamwise Vortices on Tollmien-Schlichting Waves. *J. Fluid Mechanics*, **107**, 441–453.

Nayfeh, A. H., and Al-Maaitah, A. 1988. Influence of Streamwise Vortices on Tollmien-Schlichting Waves. *Physics of Fluids*, **31**(12), 3543–3549.

Srivastava, K. M., and Dallmann, U. 1987. Effect of Streamwise Vortices on Tollmien-Schlichting Waves in Growing Boundary Layers. *Physics of Fluids*, **30**(4), 1005–1016.

Swearingen, J. D., and Blackwelder, R. F. 1987. The Growth and Breakdown of Streamwise Vortices in the Presence of a Wall. *J. Fluid Mechanics*, **182**, 255–290.

Tani, I., and Aihara, Y. 1969. Görtler Vortices and Boundary Layer Transition. *ZAMP*, **20**, 609–618.

MEDIÇÕES EM PROTÓTIPO DE FLUTUAÇÕES DE PRESSÃO NA BACIA DE DISSIPAÇÃO DA USINA DE PORTO COLÔMBIA

Jayme Pinto Ortiz
Universidade de São Paulo
Escola Politécnica -Departamento de Engenharia Mecânica
São Paulo - SP
Escola de Engenharia Mauá - IMT
Email: jportiz@usp.br
Fátima Moraes de Almeida
Furnas Centrais Elétricas S.A.
Rio de Janeiro - RJ
Email: fatimama@furnas.com.br
Erton Carvalho
Furnas Centrais Elétricas S.A.
Rio de Janeiro - RJ
Ricardo Daruiz Borsari
Centro Tecnológico de Hidráulica e Recursos Hídricos - CTH
Universidade de São Paulo
Escola Politécnica - Departamento de Hidráulica e Sanitária

Abstract

The hydraulic jump stilling basin of the Porto Colômbia Hydroelectric Power Plant was severely eroded due the formation of horse-shoe vortex in the chute-blocks region. The problem ocurred for normal operation flow rate, which were only of order of 36% (5700 m^3/s) of the maximum flow rate (16000 m^3/s).

A Subcommission was stablished inside the Commission of Hydraulic and Fluid Mechanics of the "Associação Brasileira de Recursos Hídricos - ABRH" to study the problem, which involved the participation of the three major hydraulic laboratory of Brazil (LAHE/FURNAS - Rio de Janeiro, CTH/FCTH - São Paulo and CEHPAR - Curitiba). This Subcomission developed a work that was presented in the last biannual symposium of the ABRH, which took place in Vitória/ES, in november, 1997. As a recomendation of the Consulting Board, FURNAS decided to remove all the chute blocks and to design a new end-sill for the stilling basin; in the other hand, following the recommendations of the Subcommission, decided too for the instrumentation of the stilling basin, using pressure transducers.

In the article here presented, it is showed the instrumentation work developed in the prototype to install seven pressure transducer in one vain of the spillway and the stilling basin, the proceedings for the calibration process and data acquisition, and, the results of the pressure fluctuations measurements.

The simultaneous data acquisition results from the seven pressure transducers aligned on the spillway and stilling basin permit a criterious analysis of the behavior of the pressure fluctuations in the hydraulic jump. The prototype results, which are rare in the literature, together with the hydraulic models studies, which are been developed, give a unique possibility for the development not only of applied research to solve hydraulic structures problems, but also, of basic research in turbulence.

Introdução

Em novembro de 1990 foi criada uma Subcomissão de Pesquisa no âmbito da Comissão de Hidráulica e Mecânica dos Fluidos da Associação Brasileira de Recursos Hídricos - ABRH. Esta Subcomissão foi composta pelos Laboratórios de Hidráulica de Furnas (LAHE)/Rio de Janeiro,

CTH/FCTH/São Paulo e CEHPAR/Curitiba, que se comprometeram a somar esforços em torno de um tema para pesquisa conjunta.
Em novembro de 1993, no X Simpósio Brasileiro de Recursos Hídricos da ABRH, realizado na cidade de Gramado - RS, o Laboratório de FURNAS (LAHE) prôpos a escolha do tema " Estudo de Flutuação de Pressão em Bacia de Dissipação". Tal proposta foi vinculada a oportunidade surgida com o ensecamento da Bacia de Dissipação do Verdedouro da UHE de Porto Colômbia, de propriedade de FURNAS Centrais Elétricas S.A., programado para o periodo de estiagem do ano de 1995. O ensecamento da bacia permitiria o desenvolvimento dos trabalhos preliminares necessários à sua instrumentação.
No período de 17 a 23 de maio de 1996, realizou-se na UHE de Porto Colômbia, uma campanha de medição de flutuações de pressão instantâneas na bacia de dissipação do vertedouro. Para as vazões vertidas de 500, 1000, 2000, 3000 e 4000 m^3/s foram aquisitados dados instantâneos de pressão em sete pontos da bacia de dissipação, distribuídos ao longo do vão do vertedouro extremo direito e distantes 7,20 m do muro lateral da bacia (ver figura 1).
Os dados foram aquisitados em conjunto pelas equipes e sistemas de aquisição das seguintes instituições:
- Laboratório de Hidráulica de Furnas - LAHE/FURNAS;
- Centro Tecnológico de Hidráulica e Recursos Hídricos/Fundação Centro Tecnológico de Hidráulica - CTH/FCTH.

Um relato sobre os trabalhos desenvolvidos pela Subcomissão acima referida foi apresentado no XII Simpósio da Associação Brasileira de Recursos Hídricos – ABRH, em Vitória/ES, em novembro de 1997 (ABRH/FURNAS, 1997).
O trabalho aquí apresentado mostra alguns resultados de flutuações de pressão medidas no protótipo a partir dos referidos sistemas de aquisição de dados. Os resultados obtidos a partir da aquisição simultânea de sinais de sete transdutores de pressão, alinhados na bacia, permitem uma análise criteriosa do comportamento das flutuações de pressão no ressalto, no domínio do tempo e da frequência.

Histórico

Identificação do Problema

A Usina Hidrelétrica de Porto Colômbia, que iniciou sua operação no ano de 1973, situa-se no Rio Grande, na divisa dos Estados de Minas Gerais e São Paulo.
Seu vertedouro possuía uma bacia de dissipação convencional tipo II do **USBR**, cujos parâmetros de projeto haviam sido alterados em função dos estudos em modelo realizados naquela época.
Uma inspeção subaquática realizada em outubro de 1983 revelou o péssimo estado de conservação das estruturas componentes da bacia. Observou-se que, ao longo dos, até então, 10 anos de operação da Usina, um par de erosões laterais e simétricas havia surgido em cada um dos seus 36 blocos de queda (" chute blocks"). Na laje da bacia, imediatamente a jusante dos " chute blocks" , crateras de erosão que atingiam as dimensões médias de 2,00 m de comprimento por 1,65 m de largura e 0,70 m de profundidade, possuíam sinais evidentes de arrancamento das ferragens do concreto. No restante da laje apenas duas irregularidades superficiais foram encontradas. Em alguns blocos da soleira terminal ("end sill") também foi observada a existência de pequenas erosões.
Pesquisando-se o histórico das vazões vertidas na Usina, verificou-se que, ao longo de todo o seu período de operação, a descarga máxima ocorrida de 5700 m3/s, registrada em fevereiro de 1983, não havia atingido 36% de sua capacidade plena de vazão (16000 m3/s). Nesta ocasião mediu-se sobre a bacia a carga total de 20, 80 m.
Desta forma, as erosões encontradas na bacia ocorreram para condições de operação bem inferiores àquela que seria sua solicitação máxima (q = 98 m3/s.m, para I = 163,oo m).

Diagnóstico Preliminar

Todos os dados coletados sobre o vertedouro foram submetidos à apreciação de consultores que forneceram a FURNAS seus pareceres técnicos acerca do assunto. A análise destes documentos, juntamente com os registros de casos semelhantes ao de Porto Colômbia, possibilitou o diagnóstico preliminar de que os danos ocorridos na bacia tiveram origem em um processo típico de cavitação por vórtice.
Este processo estaria instalado apenas na região dos "chute blocks" e na laje da bacia logo a jusante dos mesmos, atribuindo-se as erosões ocorridas no restante da laje e no "end sill", a um processo de desgaste devido a circulação de material erodido dentro da bacia. Este diagnóstico foi reavaliado ao longo do tempo.

Pesquisa em Modelo

Estudos em modelo físico realizados no LAHE/FURNAS, que contaram com a participação do CTH/FCTH (ABRH/FURNAS, 1997) comprovaram o diagnóstico preliminar. Em que pesem as limitações de análise do fenômeno de formação de vórtices ferradura ("horse-shoe vortex") em modelos em escala Froude, os resultados destes modelos são extremamente úteis na indicações de tendências cavitantes em estruturas hidráulicas.
Os estudos em modelo conduziram a formulação da hipótese de que, as erosões encontradas na inspeção subaquática de outubro de 1983, na região do "end sill", também eram resultado de um processo de cavitação por vórtice ferradura. A realização de uma segunda inspeção sub-aquática na bacia, em outubro de 1990, confirmou as suspeitas levantadas no estudo em modelo. Os estudos em modelo permitiram ainda estudar algumas alternativas de bacia a partir da remoção completa dos "chute blocks", otimizando-se portanto a soleira terminal de modo a minimizar o risco de cavitação por vórtice, mesmo que comprometendo o melhor desempenho hidráulico do ressalto hidráulico dentro da bacia.
Com o ensecamento da bacia de dissipação do vertedouro da UHE de Porto Colômbia (ver fotos 1, 2 e 3) foi implantada a bacia otimizada em modelo, removendo-se os "chute blocks" e construindo-se uma nova soleira terminal ("end sill").

Objetivos do Estudo

O estudo sistemático das flutuações de pressão em bacias de dissipação tem sido conduzido por diversos investigadores, entretanto, a obtenção destes dados, em sua grande maioria, é efetuada em modelos hidráulicos reduzidos e dificilmente, confrontados com medições em protótipo.
Com o ensecamento da bacia de dissipação do vertedouro da UHE de Porto Colômbia, para realização das obras de recuperação a que a mesma foi submetida, surgiu, para a Subcomissão "Desenvolvimento de Pesquisa" da ABRH, a oportunidade de instrumentação dessa bacia visando, não só a uma análise comparativa entre os dados obtidos no protótipo e em modelos, como também a determinação da real eficiência hidráulica da bacia após as modificações introduzidas em sua geometria, a determinação dos esforços hidrodinâmicos que a mesma estará submetida em diversas situações de operação e o início da formação de um banco de dados que, certamente, em muito contribuirá para o projeto de novas bacias.
Tendo em vista a importância desses dados que, se não inéditos, são raros dentro da literatura nacional e internacional, no que se refere à medição em protótipo, pôde-se contar com o apoio de FURNAS que teve especial interesse na realização desse trabalho.

Portanto o principal objetivo do trabalho aqui apresentado é relatar alguns resultado de flutuações de pressão medidas na bacia de dissipação do protótipo da UHE de Porto Colômbia a partir dos sistemas de aquisição de dados mencionados anteriormente. A análise dos gráficos de espectros de potência, variação dos sinais no tempo, distribuição de probabilidade etc, dão uma idéia clara do caminhamento dos picos (maiores escalas de turbulência) , associados às estruturas de coerência do ressalto, que é um fenômeno hidráulico caracterizado por baixas frequências e grandes amplitudes de flutuações de pressão.

Instrumentação do Protótipo

A escolha dos pontos de medição de pressão no protótipo foi norteada a partir de estudos prévios em modelo hidráulico (ABRH/FURNAS, 1997).
Decidiu-se pela instalação em protótipo de sete transdutores alinhados longitudinalmente ao longo do eixo da bacia de dissipação relativa ao vão n°1 da extremidade direita do vertedouro. Os pontos de medição de pressão estão identificados na figura 1 por: DA, DB, DC, D1, D2, D3, D5 e D7. Os pontos DA,DC e DB estão localizados, respectivamente, nos pontos extremos de tangência e no centro da curva de concordância existente entre o perfil vertente e a laje horizontal da bacia de dissipação. Os demais pontos estão localizados todos na bacia de dissipação.

Projeto dos Embutidos

Para a instalação dos transdutores de pressão no protótipo adotaram-se os seguintes critérios de projeto:

- Durante a obra de modificação e reparos na bacia, seriam embutidas, na mesma, tubulações e dispositivos de espera para a futura instalação dos transdutores (ver figura 2);
- A instalação dos transdutores só ocorreria por ocasião da realização da campanha de medição;
- Após o término da campanha os transdutores seriam removidos;
- Ao lado de cada ponto de medição de pressão instantânea seria instalada uma tomada piezométrica que serviria de testemunho para as medições.

Maiores detalhes sobre o projeto e instalação dos embutidos podem ser encontrados em ABRH/FURNAS (1997) e Carvalho et alli (1997).

Transdutores

Para a realização das medições, foram especificados transdutores cuja faixa de trabalho englobasse o intervalo de valores de pressão de possível ocorrência. Como precaução quanto ao surgimento de pressões negativas, os transdutores foram ajustados pelo fabricante, para operarem na faixa de -0,5 a 5 bar (-5,1 a 51 m.c.a.). Esta faixa corresponde a uma variação de 4 a 20 mA que, convertida, fornece um sinal de tensão de 1 a 5 Volts. Este sinal de tensão foi monitorado e aquisitado pelos sistemas de aquisição de dados do LAHE e do CTH/FCTH.
Foram utilizados sete transdutores com as seguintes características:

- Fabricante: Hytronic;
- Modelo: H-25;
- Tipo de sensor: Piezoresistivo;
- Faixa de operação: -0,5 a 5 bar;
- Repetibilidade: ± 0,25% FE;
- Histerese: ± 0,25% FE;
- Linearidade: ± 0,25% FE;
- Saída: 2 fios: 4 a 20 mA;
- Tempo de resposta: 2 ms;
- Alimentação: 15 a 30 Vcc.

Externamente os transdutores foram identificados segundo o código do fabricante como segue: IK-112 (DA); IK-121 (DB); IK-116 (DC); JG-19 (D1); IK-127 (D3); IK-122 (D5); IK-133 (D7).

Adaptações Efetuadas

Os transdutores foram rosqueados em flanges metálicas, juntamente com cápsulas metálicas cilíndricas (ver foto 4). Tais flanges tem as mesmas dimensões dos flanges cegos, usados para tamponar as caixas metálicas embutidas no piso da bacia. Os fios do transdutor (sinal de corrente) foram emendados isoladamente e vedados, e o cabo de extensão foi introduzido em uma mangueira ("poli-flow") de diâmetro 3/8 pol. Nas extremidades foram usadas conexões anilhadas, para fixação das mangueiras e vedação das cápsulas e cabos elétricos. Na outra extremidade da mangueira foi providenciado um bujão com uma presilha, para enlaçar o cabo-de-aço guia, colocado no interior da mangueira nervurada usada como conduite. Com o auxílio destes cabos, as mangueiras foram puxadas até a superfície. Detalhes sobre as adaptações efetuadas e a metodologia de instalação dos transdutores podem ser vistos em Carvalho et alli (1997).
Originalmente os transdutores eram de pressão relativa, mas esta opção mostrou-se inadequada, tendo em vista a possibilidade de penetração de água no interior das cápsulas, a despeito de todas as precauções tomadas para que tal não ocorresse. Caso houvesse entrada de água nas cápsulas e, consequentemente, no interior dos invólucros dos transdutores, os componentes eletrônicos e os elementos sensores dos transdutores sofreriam danos irreparáveis, impossibilitando qualquer tipo de medida. Desta forma, em função das responsabilidades e riscos envolvidos e, conforme sugestão do fabricante, os transdutores foram ajustados e lacrados, sendo que no interior dos invólucros e atuando na membrana sensora interna, havia uma pressão de 914 mbar, referente à pressão atmosférica na data em que os transdutores foram lacrados.
Sendo assim, quando sem carga, porém submetido a uma pressão atmosférica diferente de 914 mbar, os mesmos indicavam uma saída em corrente correspondente a uma carga fictícia igual à diferença entre a pressão atmosférica e 914 mbar. Portanto, uma vez conhecida a pressão atmosférica local, ajustava-se a curva do fabricante à nova situação.
Ao longo de todos os ensaios foi efetuada a medição da pressão atmosférica.

Demais Especificações Técnicas

Especificações técnicas relativas a conversores, fontes de alimentação, placas de aquisição de dados, micocomputadores, softwares de aquisição encontram-se em ABRH/FURNAS (1997).
Conforme salientado anteriormente, os dados foram aquisitados a partir de dois sistemas de aquisição independentes, operando simultaneamente.

Instrumentação de Apoio

Como instrumentação de apoio foram utilizados:

- Multímetro digital Fluke de 5 ½ dígitos, modelo 45 (COPPE);
- Multímetro digital Minipa 4 ½ dígitos modelo ET2700 (FURNAS);
- Osciloscópio Tektronic duplo traço, 50 MHz, modelo 2205 (COPPE);
- Analisador de espectro HP, modelo 3582A (FCTH);
- Filtro ativo programável (FCTH);
- Barômetro Bruel & Kjaer, faixa de trabalho de 790 a 1041 mbar e sensibilidade de 5 mbar (FURNAS);
- Bomba manual F. Maskina P. Tube RP-60 (p = 120 kg/cm2, Q = 7,51 l/min.);
- Medidores de nível ("PIO" – fabricação FURNAS).

Instalação dos Transdutores, Sistemas de Apoio, Procedimentos de Calibração

Após a instalação, montagem e verificação de todo o sistema de apoio (microcomputadores, conversores, fontes, multímetro etc) os transdutores foram conectados aos módulos, realizando-se o primeiro ensaio de calibração. Para tanto, foram feitas oito marcações metro a metro nas mangueiras "poly-flo" , marcações estas que se constituiram em referência de profundidade a que os transdutores seriam submetidos mergulhando-os a partir da superfície. A cada metro realizou-se uma aquisição de 10 s, tanto na imersão, quanto na emersão.

Realizado o primeiro ensaio de calibração dos transdutores, partiu-se para a sua instalação nos pontos determinados. Este trabalho ficou a cargo da equipe de mergulhadores da CESP, já que toda a etapa de instalação propriamente dita dos sete transdutores, foi subaquática. A operação de instalação dos transdutores foi monitorada da superfície, através de filmagem subaquática.

Inicialmente fêz-se uma avaliação da quantidade de sedimentos depositados no fundo da bacia e da eventual necessidade de um vertimento de limpeza. Embora a quantidade de resíduos no interior das caixas metálicas fosse pequena, em alguns casos foi necessário usar-se uma bomba manual, para desobstruir a passagem da mangueira do transdutor. Concomitantemente foram retirados os plugs dos piezômetros e aplicada a mesma bomba para desobstruí-los. Os mergulhadores localizaram os pontos de instalação dos transdutores, verificando que os flanges cegos e parafusos que os fixavam estavam em bom estado de conservação. Em seguida tais flanges foram retirados e os transdutores instalados um a um. As presilhas dos bujões foram presas aos cabos-guia das mangueiras nervuradas correspondentes e na oportunidade, o mergulhador que executou a operação reforçou tal enlace com uma amarração de cordão. Todas as mangueiras com os cabos de extensão dos transdutores passaram livres através das mangueiras nervuradas.

Com as mangueiras já na superfície, foram retirados os bujões de vedação e emendados os cabos, para que chegassem até a cabine de medição. Tais emendas foram idênticas às que foram feitas entre os transdutores e os cabos de extensão.

Campanha de Medições

Calibração dos Transdutores

Durante a campanha de medição de pressões, foram realizados sete ensaios de calibração estática dos transdutores, distribuídos da seguinte forma:

- CAL01 - Ensaio inicial com todos os transdutores, antes de sua instalação;
- CAL02 - Ensaio com os transdutores: IK-122, IK-127, IK-133, JF-105, JF-103, JG-19, IK112, 1K121, IK116;
- CAL03 - Ensaio com o transdutor JF-105;
- CAL04, 05, 06, 07 - Ensaio final com todos os transdutores, exceto JF-103, JF-105.

Todos os dados foram aquisitados em Volts, tendo sido necessário, através das curvas de calibração dos tansdutores, transformá-los para m.c.a.

Procedimentos de Ensaios

As calibrações estáticas foram feitas para níveis de água médios na bacia de 8,3 m. Sendo assim, todos os transdutores foram imersos até a profundidade de 8 m, de metro em metro, e depois emersos até a superfície, de igual forma. Adotou-se intervalo de aquisição de 10 s e frequência de amostragem de 100 Hz como valores padrões para a calibração estática. A primeira aquisição era feita sempre com o sensor na atmosfera, depois a uma profundidade de 5 cm e, posteriormente, para cada metro imerso ou emerso.

Para os vários ensaios de calibração realizados foi verificada a pressão atmosférica local, como se segue:

- CAL01 - 973 mbar;

- CAL02 - 972 mbar;
- CAL04 até 07 - 973 mbar.

Como a dispersão máxima entre os valores de pressão foi de 1 mbar e a precisão do barômetro utilizado era de 5 mbar, adotou-se para todos os ensaios de calibração, a pressão atmosférica de 973 mbar. A curva do fabricante foi então ajustada para a nova pressão atmosférica de 973 mbar.

Maiores detalhes sobre o procedimento de calibração podem ser encontrados em ABRH/FURNAS (1997).

A tabela 1 apresenta, para cada um dos ensaios realizados, as equações médias, por transdutor, utilizadas na conversão volt/m.c.a.

Tabela 1 – Equações de conversão volts/m.c.a. para os ensaios realizados (m3/s)

TRANSDUTOR	500/3000	500	1000/2000/3000/4000
IK – 112	p = 14,652xT-19,907	p = 14,652xT-19,882	p = 14,652xT-19,892
IK – 121	p = 14,348xT-19,753	p = 14,348xT-19,728	p = 14,348xT-19,738
IK – 116	p = 14,556xT-19,510	p = 14,556xT-19,485	p = 14,556xT-19,495
JG – 19	p = 14,546xT-20,229	p = 14,546xT-20,204	p = 14,546xT-20,214
IK – 127	p = 14,761xT-19,603	p = 14,761xT-19,578	p = 14,761xT-19,588
IK – 122F	p = 14,451xT-19,177	p = 14,451xT-19,152	p = 14,451xT-19,162
IK – 133F	p = 14,399xT-20,074	p = 14,399xT-20,049	p = 14,399xT-20,059

Vertimento de Limpeza

Para avaliação das condições de trabalho, realizou-se no dia 17/05/96 uma inspeção subaquática da bacia. Tal inspeção teve como principal objetivo, além da verificação das condições de depósito de sedimentos na bacia como um todo, o reconhecimento dos locais de instalação dos transdutores e dos piezômetros.

Apesar da pequena espessura da camada de sedimento encontrada no fundo da bacia, essa inspeção indicou a necessidade de se promover um vertimento de limpeza da mesma, pois, se a camada de sedimento não chegava a impedir a realização dos serviços de instalação, prejudicava, enormemente, a visibilidade dentro d'água, dificultando o trabalho de monitoramento que se fazia da superfície das imagens das filmagens feitas pela equipe de mergulhadores.

Solicitou-se portanto, à Operação da Usina, para o dia 19/05, o vertimento das vazões de 500 e 3000 m^3/s, ambas por um período de aproximadamente uma hora.

Os transdutores relativos aos pontos DA, DB, DC, situados no vertedor foram instalados antes do vertimento (dia 18/05), já que praticamente não foram afetados pelo depósito de sedimentos.

Durante a operação de vertimento para limpeza, foi possível o estabelecimento da seguinte metodologia de ensaio:

- A equipe de operação da Usina anotou com intervalos de 10 em 10 minutos todas as condições de contorno dos ensaios;
- Antes e após o período total de vertimento, foram obtidos os valores das pressões estáticas nos piezômetros e aquisitados os mesmos valores através dos transdutores, para efeito de verificação da calibração dos mesmos;
- Durante o vertimento de cada uma das vazões ensaiadas, foram medidos de 5 em 5 minutos os níveis d'água nos dois postos limnimétricos instalados na ilha a jusante. Estes dados eram anotados e transmitidos, via rádio, para a equipe responsável pelas medições, que procedia a análise da tendência à estabilização da vazão em trânsito.
- Uma vez estabilizado o nível d'água de jusante, para a vazão vertida, os valores de pressões instantâneas foram aquisitados e, concomitantemente, mediram-se os valores das pressões médias em cada um dos pontos monitorados (DA,DB e DC).

  Após o vertimento de limpeza, foram concluídos os trabalhos de instalação dos demais transdutores.

Ensaios Realizados

Os ensaios completos foram realizados para as vazões vertidas de 500 m^3/s (no dia 20/05), de 1000 e 2000 m^3/s (no dia 21/05) e de 3000 e 4000 m^3/s (no dia 22/05).
Devido as condições operacionais da Usina não foi possível a realização do ensaio com a vazão vertida de 6000 m^3/s, conforme previsto na programação original.
As fotos 5 e 6 ilustram as condições de escoamento no interior da bacia de dissipação.

Análise dos Resultados do Protótipo

As figuras 3 a 7 mostram a variação no tempo das pressões instantâneas medidas nos sete transdutores de pressão instalados, para vazões de 500 m^3/s (figura 3) a 4000 m^3/s (figura 7). Observa-se claramente nestas figuras o processo de produção e de ampliação de turbulência, particularmente para as vazões mais altas. Para cada figura são apresentados valores de pressões instantâneas máxima, média e mínima, a diferença entre os valores máximo e mínima e a cota do transdutor. Os resultados destes gráficos conduzem aos valores da tabela 2 onde são apresentados, para cada vazão, resultados de amplitude de flutuações de pressão para os transdutores situados no vertedouro e no início da bacia (DA, DB, DC, D1).

Tabela 2 - Resultados de amplitude de flutuações de pressão nos transdutores DA, DB,DC,D1

Vazão (m3/s)	Transdutores de Pressão			
	DA (m)	DB (m)	DC (m)	D1 (m)
500	4,17	3,87	3,84	5,15
1000	7,32	5,53	4,98	5,06
2000	5,51	7,51	8,03	7,46
3000	6,22	6,62	9,03	10,10
4000	4,06	8,13	11,16	12,93

As figuras N°s 3 a 7 mostram um aumento gradativo da energia de turbulência na bacia com o aumento da vazão, com amplitudes de flutuações atingindo valores da ordem de 13 m na entrada do ressalto para a vazão de 4000 m^3/s. A análise destas figuras mostra ainda, através do registro simultâneo nos sete transdutores de pressão, o processo de formação de picos de flutuações de pressão que são convecionados para jusante, sendo atenuados no final da bacia (ver figuras 5, 6 e 7).
As figuras 8 a 14 mostram os resultados da análise espectral que evidenciam que o ressalto é um fenômeno hidráulico turbulento de baixa frequência. A figura 8 mostra que o transdutor DA (canal 1), instalado no vertedor não é afetado pela energia de turbulência do ressalto para a vazão máxima vertida de 4000 m^3/s, o que não acontece no transdutor DB (figura 9 - canal 2), que já mostra o efeito desta energia para a vazão mencionada. Os picos de energia de turbulência, para a vazão máxima ensaiada, ocorrem sobre os transdutores DC (canal 3) e D1 (canal 4), já localizados no início da bacia de dissipação (figuras 10 e 11), observando-se que a energia de turbulência das maiores escalas concentram-se na faixa de 0 a 5 Hz, como era de se esperar. As figuras 12, 13 e 14 (transdutores D3 - canal 5, D5 - canal 6 e D7 - canal 7) mostram a atenuação gradativa do pico de energia de turbulência.
As figuras 15, 16 e 17 mostram os resultados de flutuações de pressão no domínio do tempo que evidenciam que o ressalto é um fenômeno hidráulico que se caracteriza por grandes amplitudes de flutuações. A figura 15 apresenta os resultados de amplitude de pressão ($p_{máx}$ - $p_{mín}$) ao longo do ressalto para vazões variando entre 500 e 4000 m^3/s. Nota-se claramente nesta figura o aumento gradativo das amplitudes de flutuação de pressão com a vazão, atingindo-se valores da ordem de 20

m, notando-se ainda que a zona crítica do ressalto para a vazão máxima vertida se situa entre os transdutores DC (canal 3) e D1 (canal 4), como já observado na análise espectral. As figuras 16 e 17 apresentam as linhas de pressão máxima, média e mínima ao longo do ressalto para as vazões de 2000 e 4000 m^3/s, notando-se que para a vazão de 4000 m^3/s ocorrem pressões negativas da ordem de 4 m.c.a. na zona crítica do ressalto (região dos transdutores DC e D1).

Importância do Tema para o Desenvolvimento de Pesquisa

Pesquisa Aplicada em Engenharia Hidráulica

A literatura tem reportado a ocorrência de cavitação e erosão por vórtices ferradura em estruturas de dissipação para vazões operacionais bem abaixo das vazões de projeto dos vertedores (**BORSARI** & ORTIZ - 1987). No caso da UHE Porto Colômbia, que tinha uma bacia **tipo II** do **USBR**, erosões significativas foram observadas para descargas máximas inferiores a 36% (5700 m^3/s) da capacidade plena de vazão(16000 m^3/s). Isto está associado ao fato que para vazões mais baixas o vórtice ocorre próximo as fronteiras sólidas, acarretando danos as estruturas.

A decisão de engenharia, mencionada neste relatório, de se remover os blocos de queda da bacia de Porto Colômbia, praticamente elimina a possibilidade de cavitação nesta região, já que os vórtices ferradura não devem mais se formar, apesar de ainda ocorrerem pressões negativas, conforme mencionado no item anterior. Todavia, como as medições de flutuações de pressão no protótipo foram feitas após a eliminação dos blocos, os dados disponíveis não permitem um estudo direto da formação dos referidos vórtices.

Por outro lado, embora não exista a possibilidade de se estudar a cavitação no protótipo, os resultados permitirão estudar com detalhes os efeitos de escala em modelos em semelhança de Froude, já que são raras as possibilidades de instrumentação e medição em protótipo. A análise dos resultados dos estudos em modelos hidráulicos que estão sendo conduzidos nos laboratórios de hidráulica, assim como a interpretação dos efeitos de escala, não serão tratados no trabalho aqui apresentado. Todavia, é interessante frizar que a interpretação correta destes efeitos de escala nos estudos de semelhança de Froude deve permitir a utilização com segurança dos chamados "blocos supercavitantes" em estruturas de dissipação por ressalto.

O banco de dados disponível a partir das medições de Porto Colômbia será extremamente útil para os próximos projetos de estruturas de dissipação. Conforme salientado anteriormente, o ressalto é um fenômeno hidráulico de baixa frequência e de grande amplitude de flutuações, sendo que a análise de seu comportamento em protótipo, nos domínios do tempo e da frequência, permitirá a determinação, com segurança, das maiores escalas de turbulência e das solicitações hidrodinâmicas das estruturas.

É interessante salientar que as medições feitas com os sete transdutores permitirão uma análise criteriosa dos momentos de diversas ordens (média, desvio-padrão, variância, assimetria, curtose etc), das funções de autocorrelação, das correlações espaciais entre transdutores, dos espectros de potência, dos espectros cruzados entre transdutores etc. Todas estas informações devem permitir visualizar o caminhamento do " roller" na bacia, o desenvolvimento e amortecimento de picos, a duração e o tamanho das maiores escalas de turbilhões, a possível distribuição de probabilidade de pressões flutuantes, que supõe-se não gaussiana na zona crítica do ressalto, a velocidade de convecção do ressalto, que supõe-se menor que a velocidade média do escoamento etc. Estas informações estão sendo trabalhadas, através do banco de dados disponível, e serão motivo de uma outra publicação, devendo ser utilizadas para o aprimoramento dos critérios de projeto de bacias de dissipação.

Pesquisa Básica em Turbulência

A modelagem da turbulência é um assunto em franca evolução que depende, para o seu desenvolvimento, do convívio balanceado entre pesquisas experimentais em laboratório, utilização de instrumentação e técnicas modernas de medição, informações de campo e desenvolvimento de novas técnicas numéricas. Em publicação recente da revista da ABCM, Freire et alli (1998) apresentam a evolução do estado da arte na modelagem em turbulência no Brasil. A publicação embora bastante detalhada e extensa, é ainda parcial, pois se restringe apenas aos trabalhos publicados na referida revista, o que mostra a dificuldade do domínio do assunto com aplicações em diversas áreas do conhecimento científico.

Nos últimos dez anos o estudo da turbulência em escoamentos tem sido conduzido a partir de dois pontos de vista até certo ponto antagônicos. Por um lado, sustenta-se que a turbulência é um fenômeno esencialmente randômico, de forma que deve ser modelada a partir de ferramentas da estatística pesquisando-se os valores médios das quantidades turbulentas. Seguindo a linha estabelecida pela teoria de Kolmogorov de 1941 da cascata de turbilhões (apud Frisch, 1996), a turbulência se origina a partir da deformação do escoamento médio pelas instabilidades hidrodinâmicas e fronteiras dos escoamentos, gerando-se as maiores escalas de turbilhões (escalas integrais) que vão se decompondo em cascata até as menores escalas (escalas dissipativas).

Por outro lado há um outro ponto de vista que sustenta qua a turbulência é composta por estruturas de coerência de modo a poder ser tratada como um fenômeno determinístico.

Uma análise mais aprofundada do tema indica que cada um destes pontos de vista não pode ser tratado isoladamente. Conforme friza Lesieur (1990), deve-se considerar as estruturas de coerência como parte integrante do escoamento turbulento. Em outras palavras, quando se analisa um sinal turbulento de um escoamento qualquer e se identificam estruturas de coerência, observa-se que estas estruturas podem conservar a forma geométrica por algum tempo, mas são imprevisíveis em termos de posição no espaço e em tais situações, a análise randômica do sinal turbulento, utilizando as ferramentas da estatística, continua sendo fundamental para o estudo do fenômeno.

Dentro desta filosofia portanto a turbulência poderia ser interpretada como: " um processo de geração de ordem a partir da ação de instabilidades hidrodinâmicas caóticas no escoamento, sem no entanto perder sua característica de imprevisibilidade".

Nos escoamentos turbulentos as estruturas de coerência podem ser identificadas nas maiores escalas de turbilhões e no caso do ressalto hidráulico estão associadas ao caminhamento dos picos de flutuações de pressão, o que corresponde fisicamente ao caminhamento do " roller" ao longo da bacia de dissipação. Os maiores turbilhões no ressalto são essencialmente anisotrópicos e a questão como estes turbilhões trocam energia com os turbilhões menores até atingir as escalas dissipativas, em que os turbilhões são essencialmente isotrópicos, ainda é um problema teórico não claramente entendido. A análise dos dados de flutuações de pressão nos modelos e no protótipo da bacia de dissipação da Usina de Porto Colômbia, deve trazer subsídios importantes no sentido de se poder interpretar a estrutura da turbulência no ressalto hidráulico.

Com relação à distribuição de probabilidade, acredita-se que as flutuações de pressão no ressalto hidráulico não seguem uma distribuição gaussiana, pelo menos na zona crítica do ressalto. Para se determinar a real distribuição de probabilidade são necessários registros longos, sendo escassas estas informações na literatura. Uma tentativa neste sentido foi realizada por Toso & Bowers (1988) que utilizaram um registro de 24 horas de medição de flutuações de pressão em ressalto hidráulico em modelo. Embora seus resultados possam ser questionados quanto aos intevalos de confiança, já que os registros foram divididos em registros de 1 hora cada, fica claro que a distribuição se destaca da distribuição gaussiana na região crítica do ressalto para valores da ordem de 2 a 3 vezes o desvio-padrão das flutuações de pressão. Por outro lado, observa-se que os valores de pico de flutuações de pressão obtidos por Toso & Bowers (1988), baseados nos valores de cálculo de $C_p^+ = \frac{p_{max} - p_{min}}{\frac{1}{2}\rho U^2}$, são da ordem de dez vezes os valores de **RMS** de flutuações de pressão

baseados nos valores de cálculo de $C_p = \frac{\sqrt{\overline{p^2}}}{\frac{1}{2}\rho U^2}$. Os resultados mostram valores de $C_p^+ \rightarrow 1$ para registro longo, não sendo todavia conclusivos.

Os resultados disponíveis do protótipo de Porto Colômbia, onde foram feitos registros de flutuações de pressão através de dois sistemas de aquisição em paralelo, com intervalos de amostragem entre 5 minutos (sistema CTH) e 45 minutos (sistema FURNAS), além da possibilidade de se fazerem registros longos nos modelos, abrem a perspectiva de se conhecer a verdadeira distribuição de probabilidade de pressões no ressalto hidráulico, o que por si só seria um trabalho inédito.

Com relação a simulação numérica da turbulência, sabe-se que para a simulação direta de escoamentos turbulentos, a partir da equação de Navier-Stokes, há necessidade de se explicitar todas as escalas de turbulência, desde as maiores (escalas integrais) até as menores (escalas dissipativas de Kolmogorov). Considerando-se que a distância entre as maiores e as menores escalas aumenta com o número de Reynolds, torna-se impossível nos dias de hoje a simulação numérica direta dos escoamentos turbulentos encontrados na natureza com números de Reynolds superiores a 10^5, sendo que o ressalto se enquadra nesta situação. No sentido de se suprir esta dificuldade, a utilização dos chamados "LES - Large Eddy Simulation Turbulence Model" tem sido objeto de discussões em diversos simpósios internacionais e publicações recentes (ver Wilcox, 1993). Os "LES" tem como principal interesse descrever o comportamento das maiores escalas do escoamento, que normalmente, contém as informações desejadas sobre a estrutura de coerência da turbulência e os processos de transferência de energia para as menores escalas. Estes modelos requerem menos capacidade computacional, pois não tem o objetivo de simular as escalas dissipativas, que são introduzidas no cálculo a partir do estabelecimento de uma hipótese.

A simulação via "LES", em princípio, deve permitir a previsão das propriedades estatísticas do escoamento turbulento pesquisado (momentos de diversas ordens, distribuição espectral, coeficientes de transferência para as menores escalas etc), além de possibilitar a previsão da forma e da topologia da estrutura organizada das maiores escalas do escoamento, embora não tenha condição de reproduzir corretamente a fase destas estruturas, considerando-se que os escoamentos turbulentos são imprevisíveis no espaço. Considerando que a base de dados disponível consiste em dados de pressões instantâneas, isto traz uma certa limitação ao desenvolvimento da modelagem computacional. No entanto, Song & Zhou em trabalho recentemente concluído, apresentam resultados de flutuações de pressão de escoamento de superfície livre em vertedores, a partir da simulação via "LES", utilizando o supercomputador CRAY C90 da University of Minnesota/USA. Além disso, os valores de velocidades instantâneas sempre poderão ser medidos em modelo, deste que se disponha de medidores instantâneos de velocidade. .

Pretende-se portanto, a partir do banco de dados de Porto Colômbia estudar a possibilidade de aplicação dos chamados "LES" na simulação numérica do ressalto hidráulico em bacias de dissipação.Finalmente é importante enfatizar a contribuição à pesquisa na área de instrumentação aplicada a medição de fenômenos hidráulicos turbulentos. Na prática da Engenharia Hidráulica aplicada ao estudo das estruturas de dissipação tem sido mais comum a utilização de transdutores piezoresistivos para a medição de flutuações de pressão. Dois cuidados devem ser tomados quando da utilização destes transdutores. Em primeiro lugar, os transdutores devem ter uma membrana suficientemente pequena, de modo a registrar as menores escalas de turbulência. Em segundo lugar, preferencialmente, devem, ser instalados faceados aos pontos de medição, de modo a impedir a atenuação ou amplificação das respostas em frequência introduzidas por sistemas de mangueiras e adaptadores instalados entre o ponto da tomada de pressão e o ponto de instalação do transdutor (ver Ortiz & Barbosa - 1995). No caso de Porto Colômbia, estes cuidados foram tomados, faceando-se os transdutores, o que torna, mais uma vez, o trabalho inédito em termos de instrumentação de protótipo. Nos estudos em modelo, pesquisas poderão se conduzidas com transdutores faceados ou não, de modo a se estabelecer uma modelagem matemática de correção dos sinais de pressão, quando da necessidade de utilização de sistemas de mangueiras e adaptadores entre a tomada de pressão e o transdutor.

É interessante salientar que pelo fato dos números de Reynolds de protótipo e modelo serem diferentes, diferenças deverão ocorrer nos respectivos espectros de potência, mesmo no caso de utilização de transdutores faceados (tanto no protótipo, como no modelo). Sendo assim, os dados de Porto Colômbia permitirão contribuir com as pesquisas relativas aos estudos de resolução espacial e em frequência das escalas de turbulência, a partir de medições de flutuações de pressão com transdutores piezoresistivos.

Conclusões

Pelo exposto, conclue-se que o trabalho aquí apresentado sobre o tema "medições em protótipo de flutuações de pressão na bacia de dissipação da UHE de Porto Colômbia", ultrapassou todas as expectativas de sucesso e se reveste de uma importância muito grande, pois o banco de dados disponível contém informações que devem trazer benefícios não só à pesquisa aplicada a engenharia de projeto de estruturas hidráulicas, mas também à pesquisa básica do estudo da turbulência, que permanece ainda, neste final de século, como um dos tópicos não resolvidos da ciência.

Relação dos Participantes dos Ensaios no Protótipo

Coordenador Geral

Erton Carvalho - **FURNAS**

Participantes

FURNAS:	Fátima Moraes de Almeida Marcos da Rocha Botelho Rogério Sales Góz José Zanini Filho Edson Ricardo Holanda André Luiz Venâncio Cleober Michel Tosta Zanini Rosselini Ranieri Agostini Alcior Novaes de Faria
CTH/FCTH/EPUSP:	Jayme Pinto Ortiz Flávio Spinola Barbosa Cláudio Menegatte Filho
COPPE/UFRJ:	Fábio Nascimento de Carvalho Igor Afonso Fragoso
CEHPAR:	Sinildo Hermes Neidert Edie Roberto Taniguchi José Jungi Ota
CESP:	Mauro Hermógenes L. Cove Roberto Ferreira de Alvarenga Rogério de Oliveira Francisco Antônio A. Gouveia José Pereira da Silva

Referências Bibliográficas

ABRH/FURNAS (1997) " Relato do Trabalho da Subcomissão Desenvolvimento de Pesquisa - Estudo de Flutuação de Pressão em Bacia de Dissipação - Caso Usina de Porto Colômbia" - 64 págs., novembro, 1997.

Borsari, R.D. & Ortiz,J.P. (1985) "A Modelação de Fenômenos de Cavitação e sua Prevenção em Modelos Segundo Critério de Froude". Anais do VI Simpósio Brasileiro de Hidrologia e Recursos Hídricos, vol.2, pág.120-131

Carvalho,F.N.; Almeida,F.M. and Fragoso,I.A. (1997) "Aquisição de Dados no Protótipo da UHE de Porto Colômbia". Anais do XII Congresso da Associação Brasileira de Recursos Hídricos ABRH, vol. 1 , novembro, 1997.

Freire,A.P.S.; Avelino,M.R. and Santos,L.C.C. (1998) "The State of the Art in Turbulence Modelling in Brazil". Revista Brasileira de Ciências Mecânicas - ABCM, vol.XX, No.1,pp.1-38, march, 1998.

Frisch,U. (1996) "Turbulence". Cambridge University Press, Reprinted, 1996, 296 pages.

Lesieur,M. (1990) "Turbulence in Fluids". Kluwer Academic Publishers, second revision edition, 412 pag.

Ortiz,J.P. and Barbosa,F.S. (1995) "Critérios de Escolha de Transdutor Elétrico de Pressão como Padrão de Medida para Laboratórios de Hidráulica". Anais do Segundo Simpósio Brasileiro de Medição de Vazão, IPT/SP, p.415-424.

Toso,J.W. and Bowers,C.E. (1988) "Extreme Pressures in Hydraulic Jump Stilling Basins". Journal of Hydraulic Engineering, vol. 114, No.8, pp.829-843, august, 1988.

Wilcox,D.C. (1993) "Turbulence Modeling for CFD". DCW Industries, Inc. La Cañada, California, 460 pag.

Song,C.C.S. and Zhou,F. "Simulation of Free Surface Flow over a Spillway". 33 págs.

FIGURA 1 - PROJETO DOS EMBUTIDOS: POSICIONAMENTO DOS PONTOS DE MEDIÇÃO

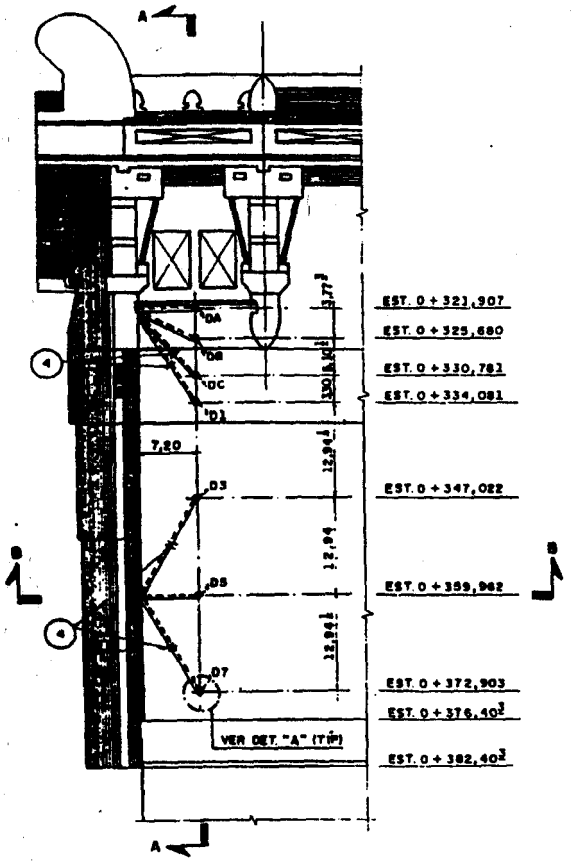

PONTOS DE MEDIÇÃO	ELEVAÇÕES	
	MEDIDOR DE PIEZ.	MEDIDOR DE PIEZ.
DA	437,500	437,498
DB	434,986	435,015
DC	434,013	434,014
D1	434,005	434,006
D3	434,012	434,011
D5	434,014	434,013
D7	433,988	434,000

PLANTA

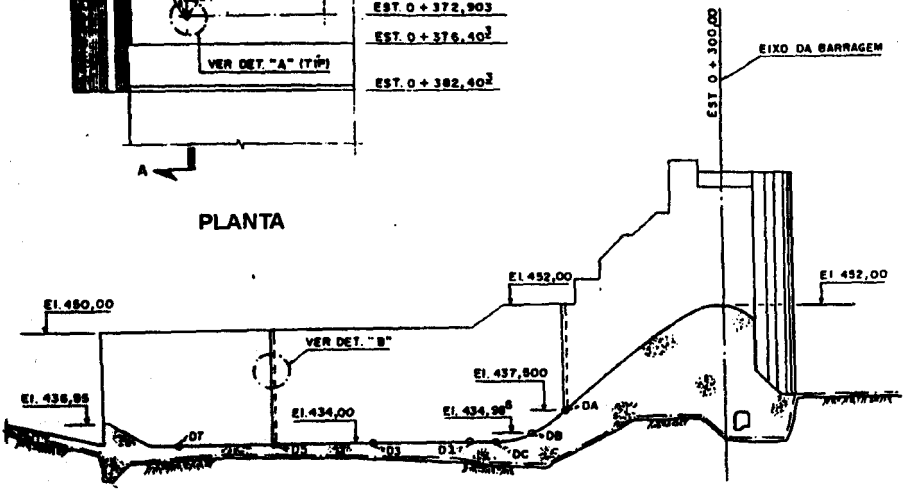

SEÇÃO AA

FIGURA 2 - PROJETO DOS EMBUTIDOS: SEÇÕES E DETALHES

DETALHE 2

Detalhe da extremidade do tubo de PVC rígido ϕ 3/4"

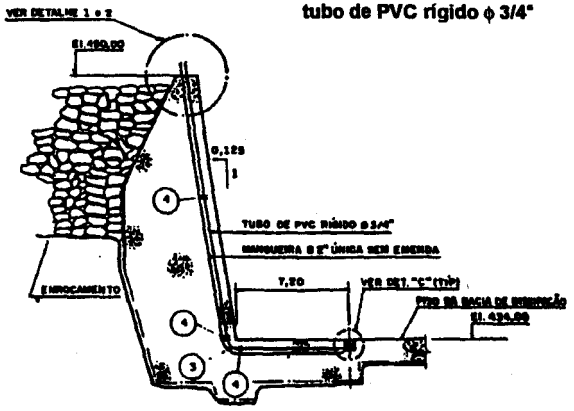

SEÇÃO BB

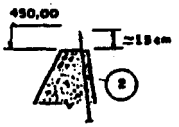

DETALHE 1

Detalhe da extremidade do tubo de PVC rígido ϕ 2"

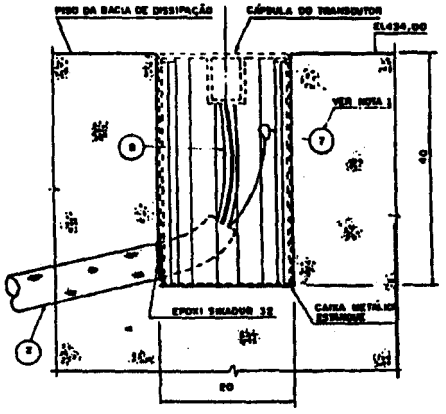

DETALHE C (típico)

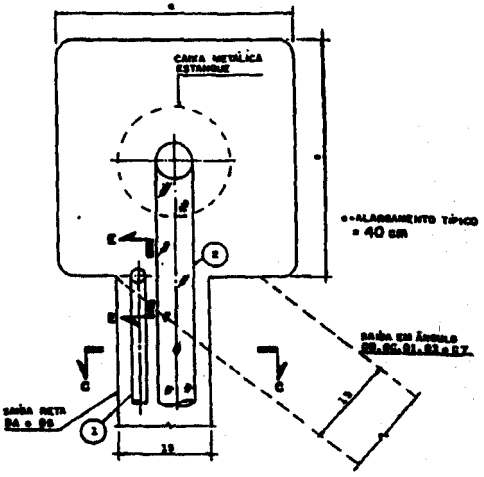

DETALHE A (típico)

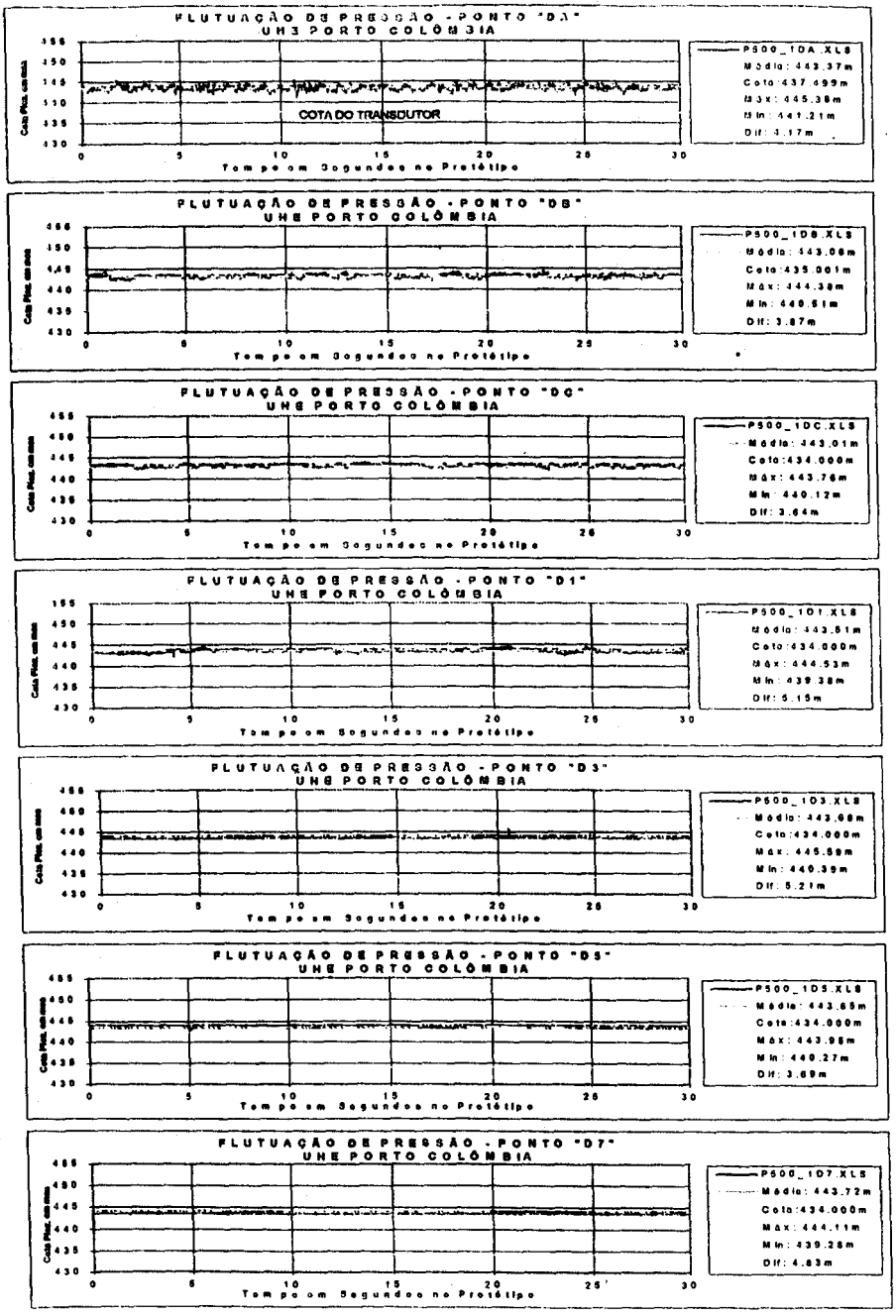

FIGURA 3- FLUTUAÇÃO DE PRESSÃO PARA A VAZÃO DE 500 m^3/s - AQUISIÇÃO 1
Resultados do protótipo

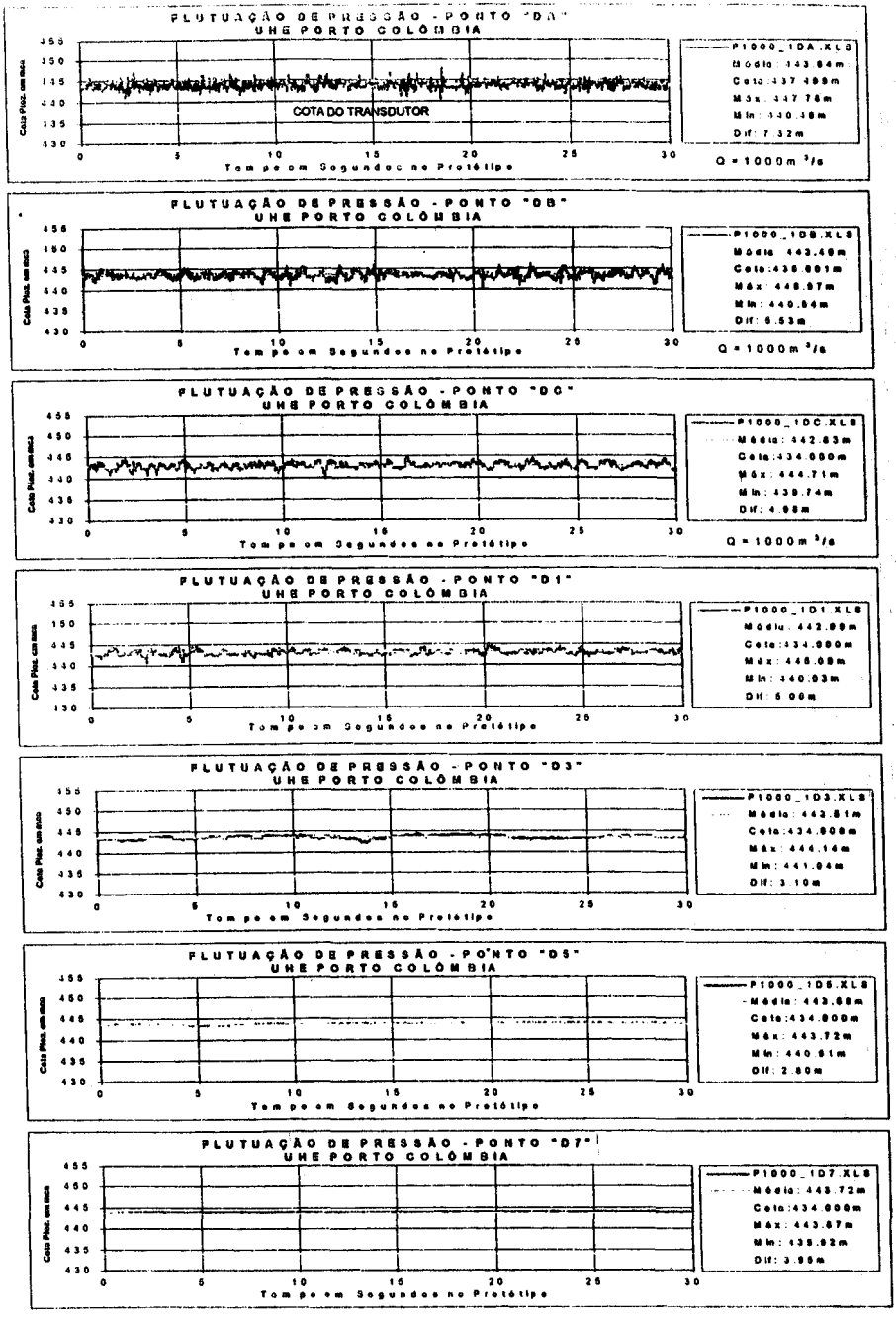

FIGURA 4- FLUTUAÇÃO DE PRESSÃO PARA A VAZÃO DE 1000 m^3/s - AQUISIÇÃO 1
Resultados do protótipo

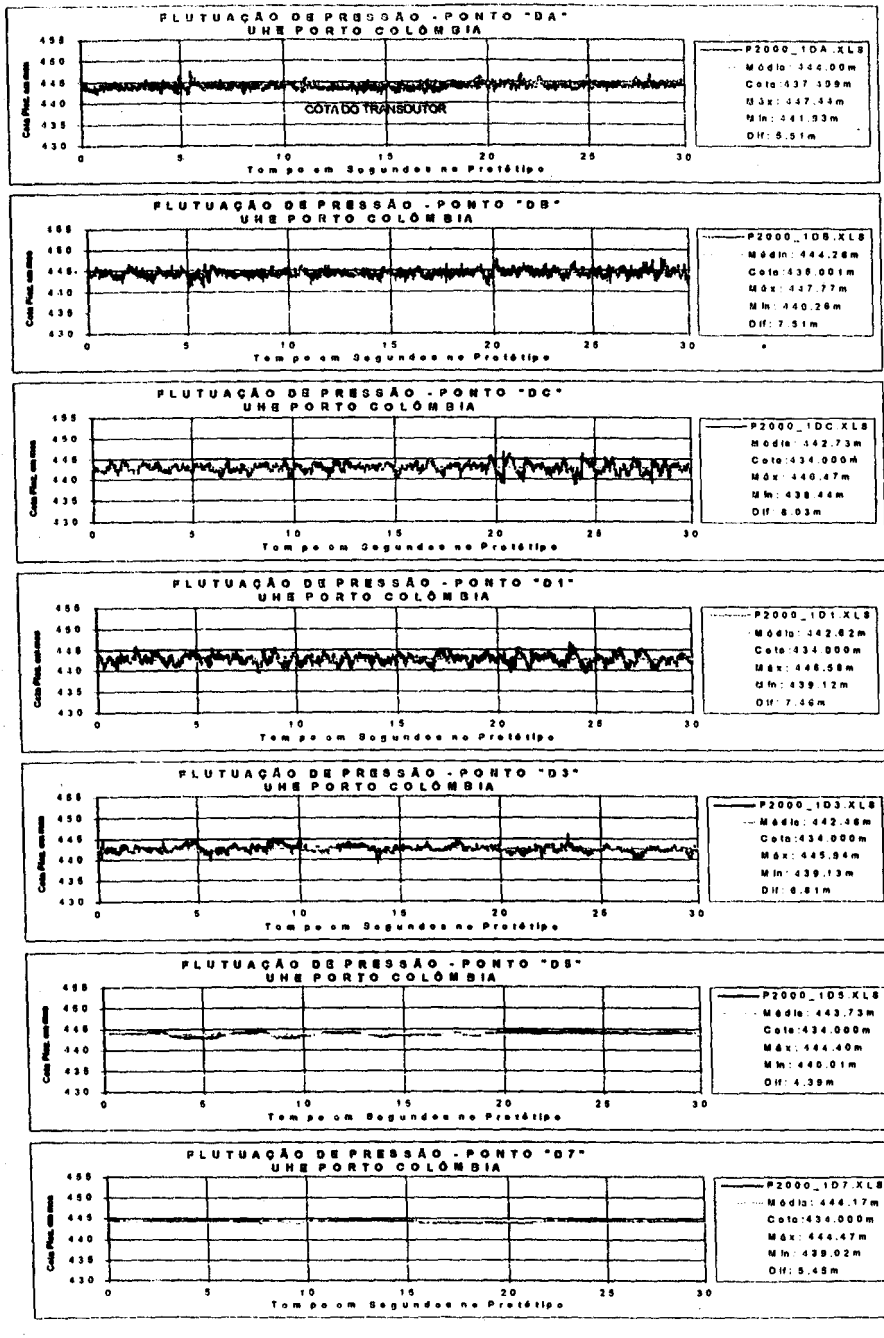

FIGURA 5- FLUTUAÇÃO DE PRESSÃO PARA A VAZÃO DE 2000 m^3/s - AQUISIÇÃO 1
Resultados do protótipo

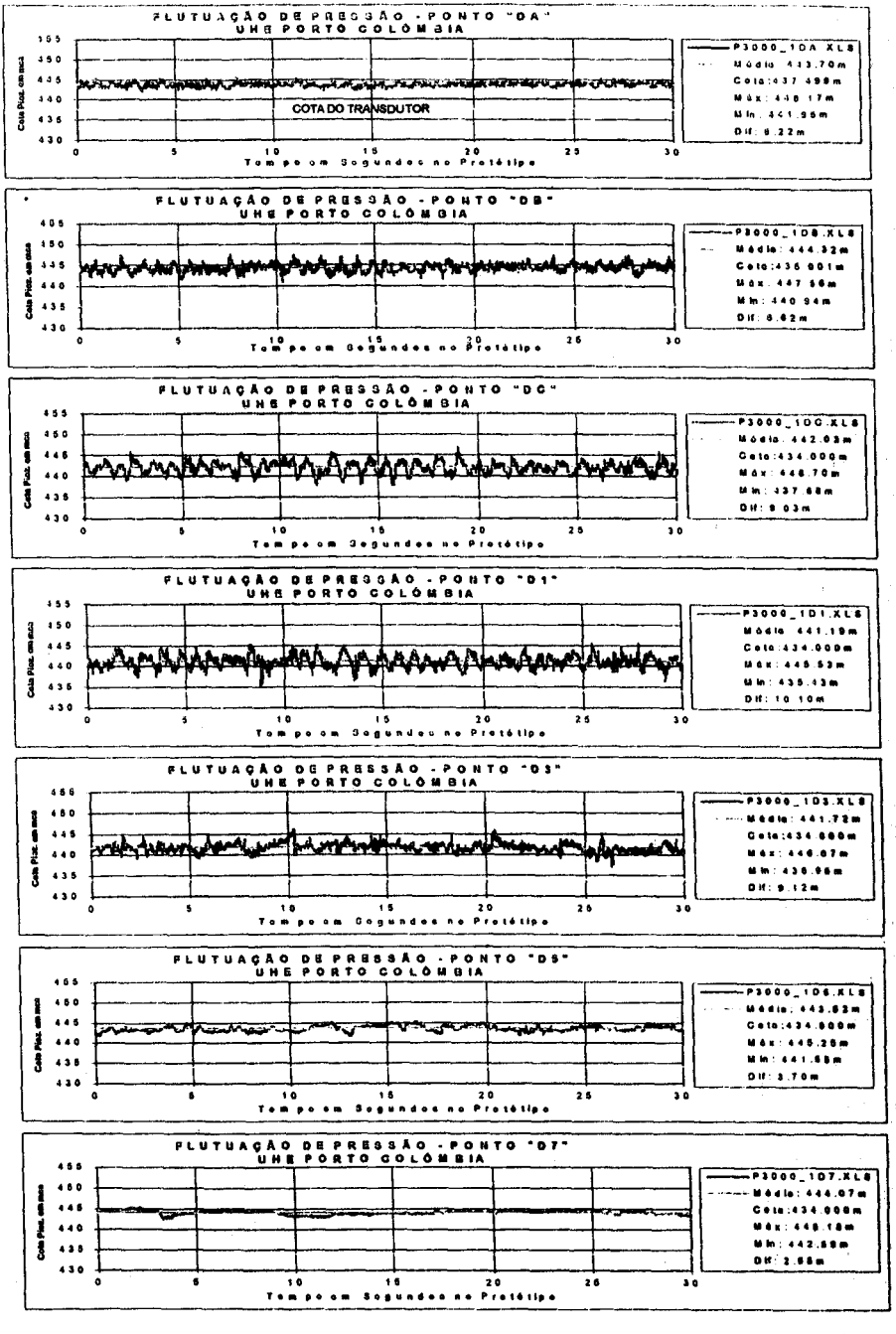

FIGURA 6 - FLUTUAÇÃO DE PRESSÃO PARA A VAZÃO DE 3000 m³/s - AQUISIÇÃO 1
Resultados do protótipo

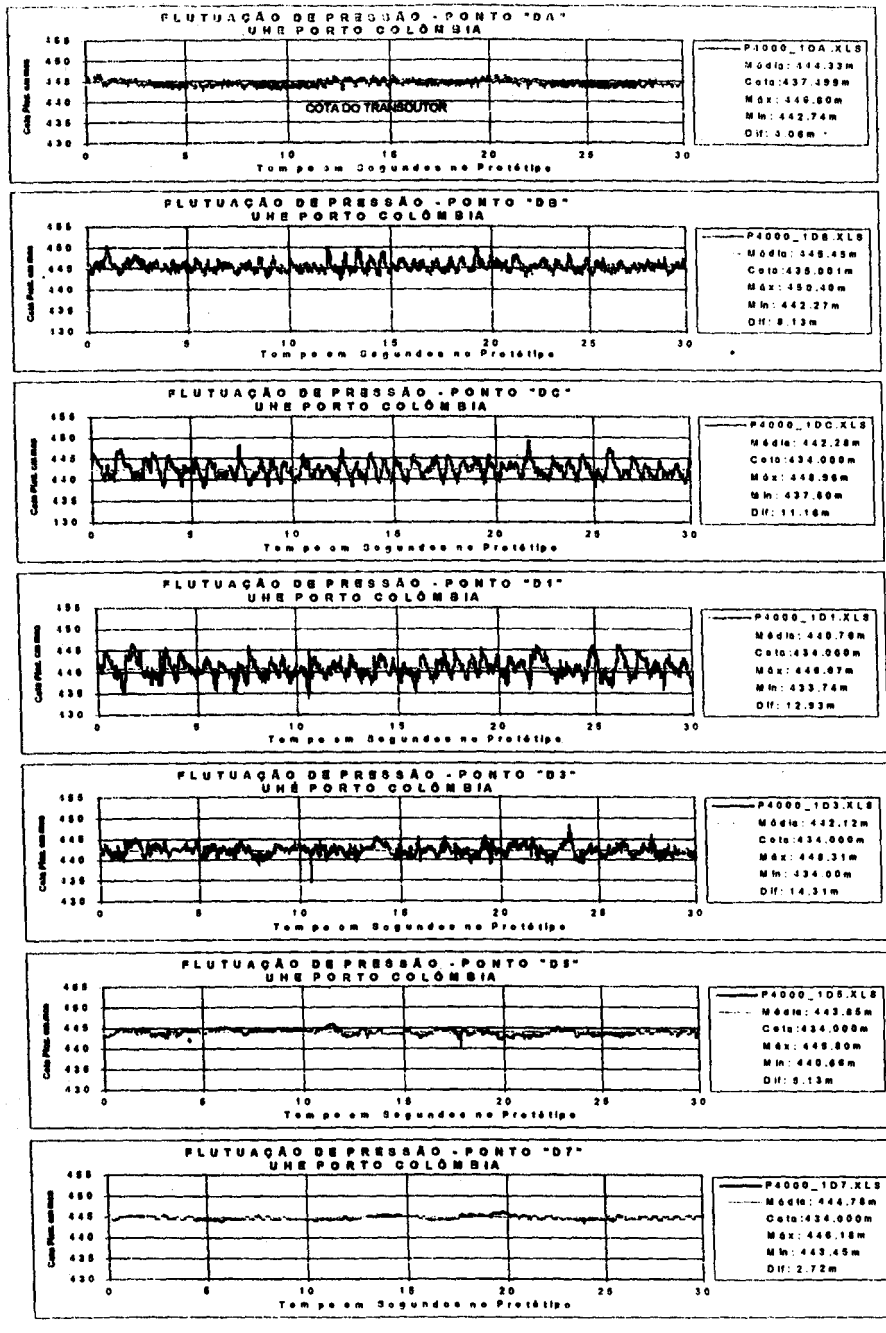

FIGURA 7- FLUTUAÇÃO DE PRESSÃO PARA A VAZÃO DE 4000 m³/s - AQUISIÇÃO 1
Resultados do protótipo

Figura 8 - Análise Espectral - canal 1 - Transdutor DA

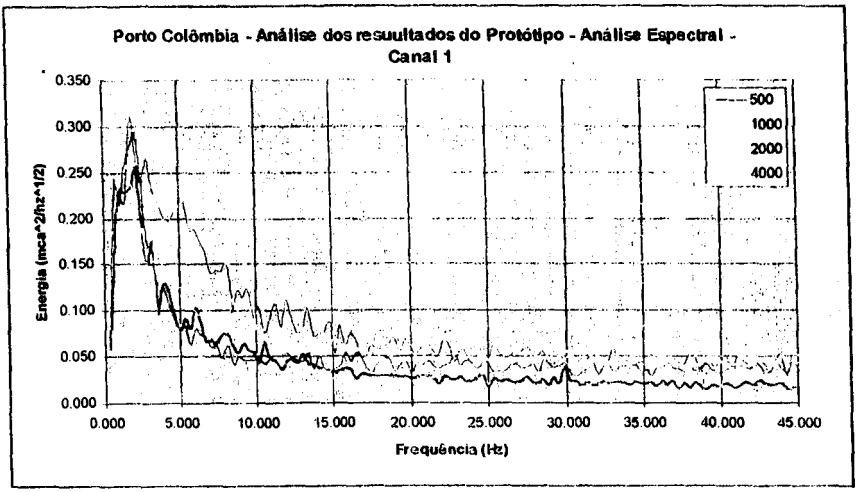

Figura 9- Análise Espectral - canal 2 - Transdutor DB

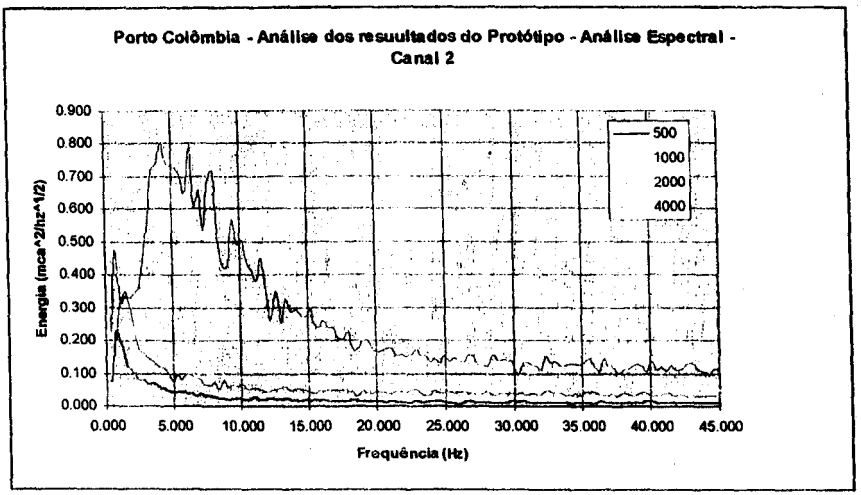

Figura 10- Análise Espectral - canal 3 - Transdutor DC

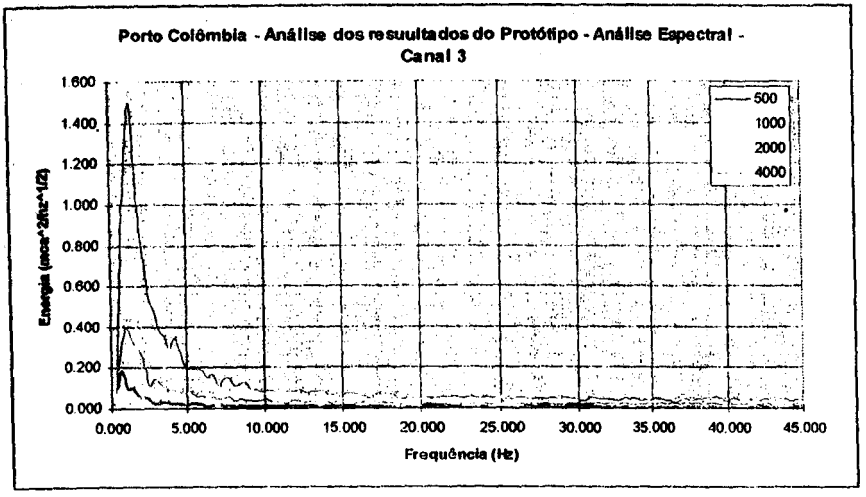

Figura 11- Análise Espectral - canal 4 - Transdutor D1

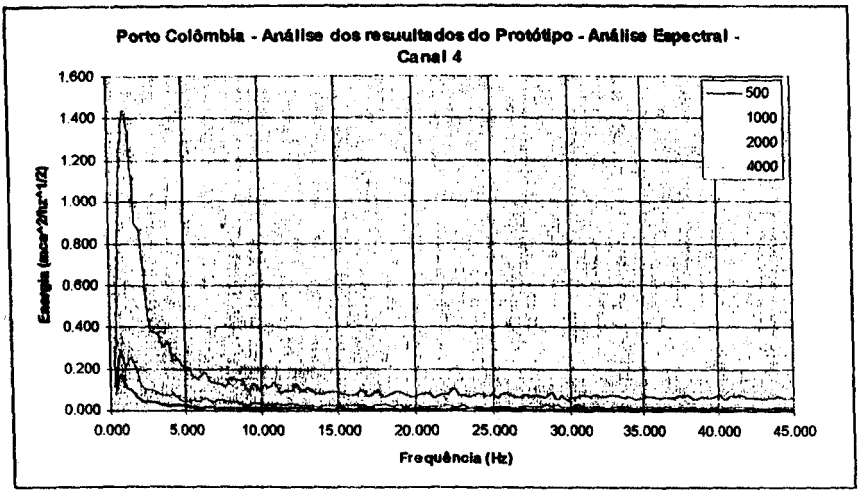

Figura12- Análise Espectral - canal 5 - Transdutor D3

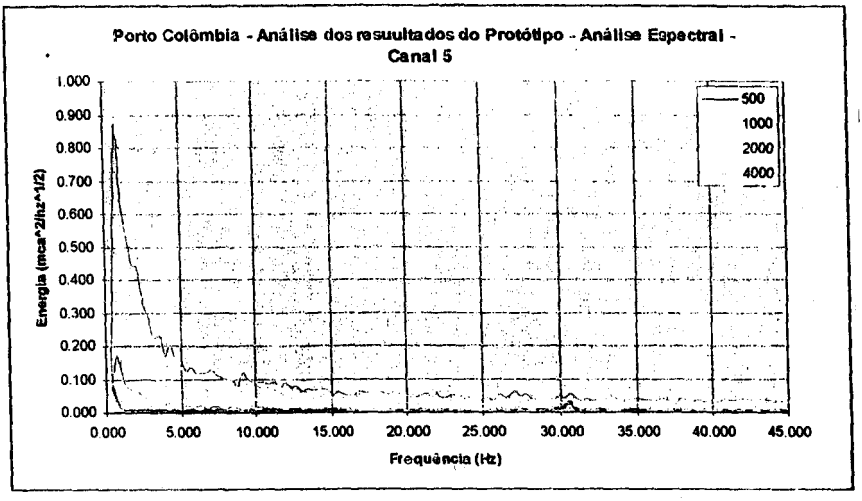

Figura 13- Análise Espectral - canal 6 - Transdutor D5

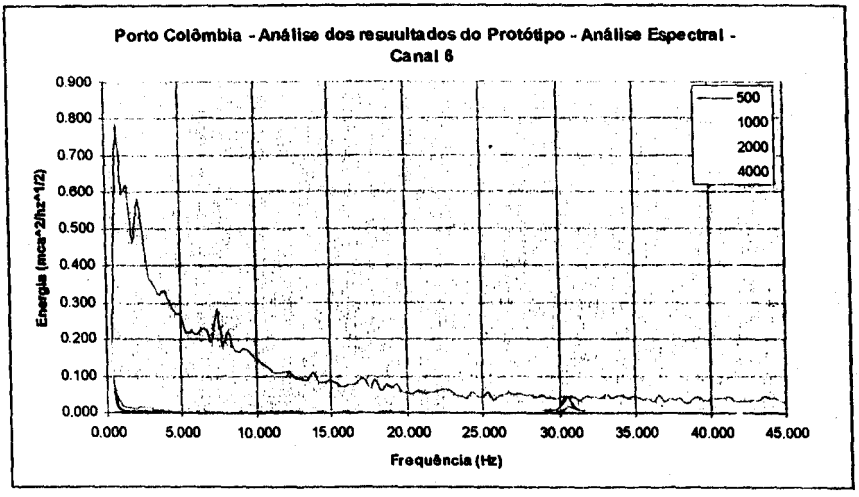

Figura 14- Análise Espectral - canal 7 - Transdutor D7

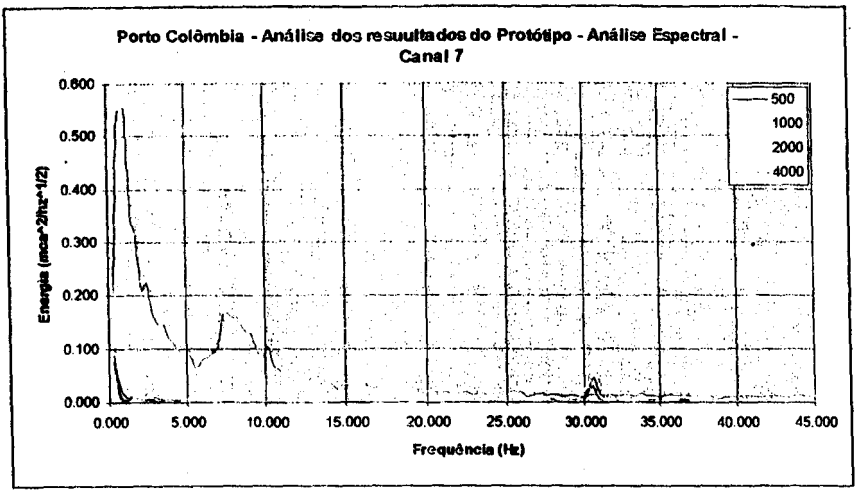

Figura 15 - Amplitudes de Flutuações de Pressão

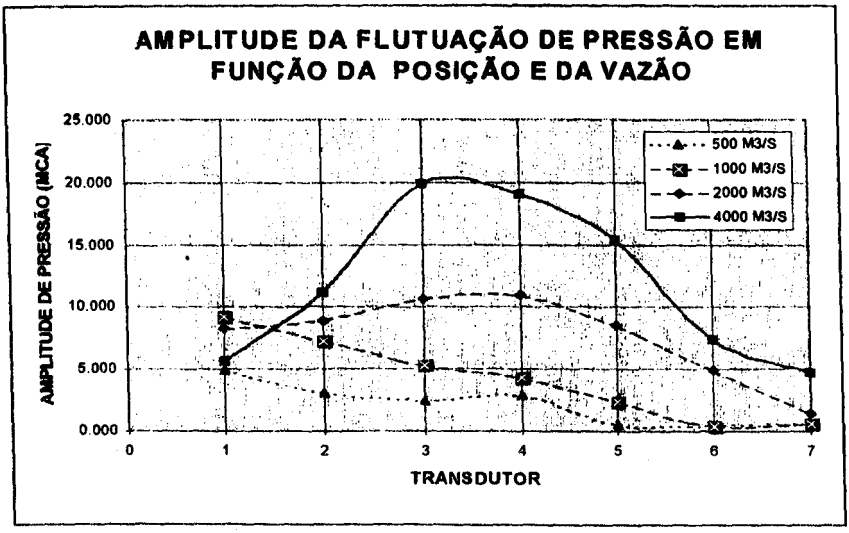

Figura 16 - PRESSÕES MÁXIMAS, MÉDIAS E MÍNIMAS, AO LONGO DO VERTEDOR Q = 2000 m3/s

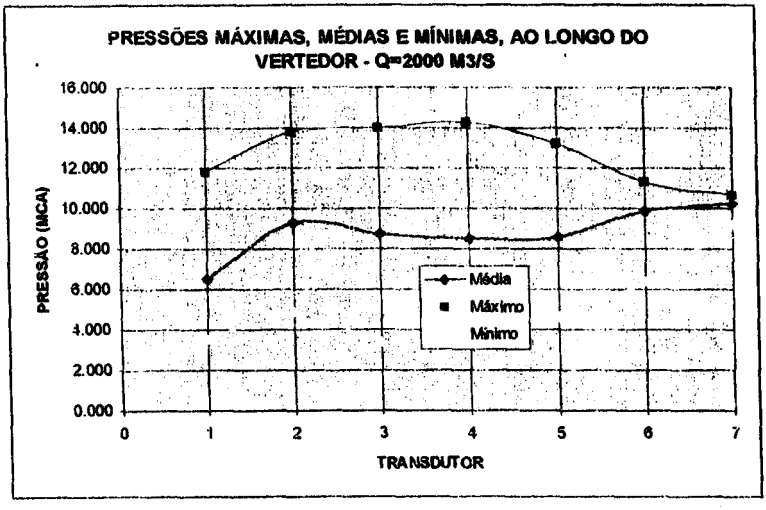

Figura 17 - PRESSÕES MÁXIMAS, MÉDIAS E MÍNIMAS, AO LONGO DOVERTEDOR Q = 4000 m3/s

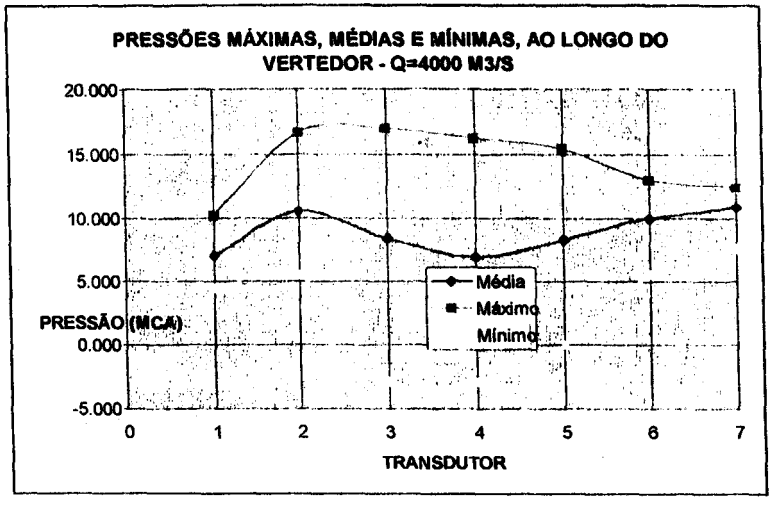

FOTO 1

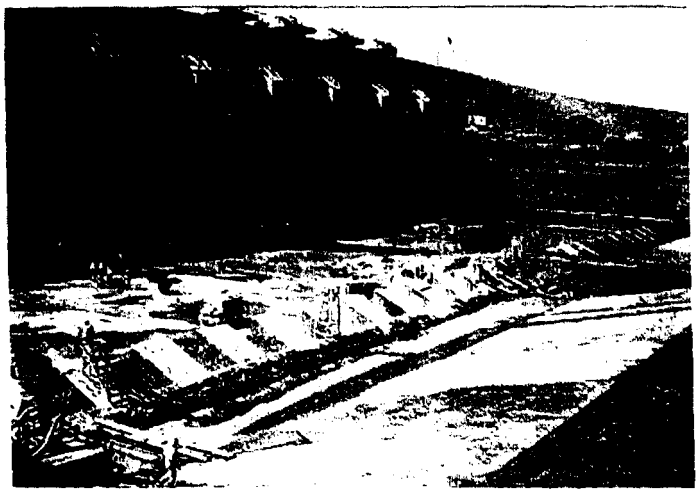

FOTO 2

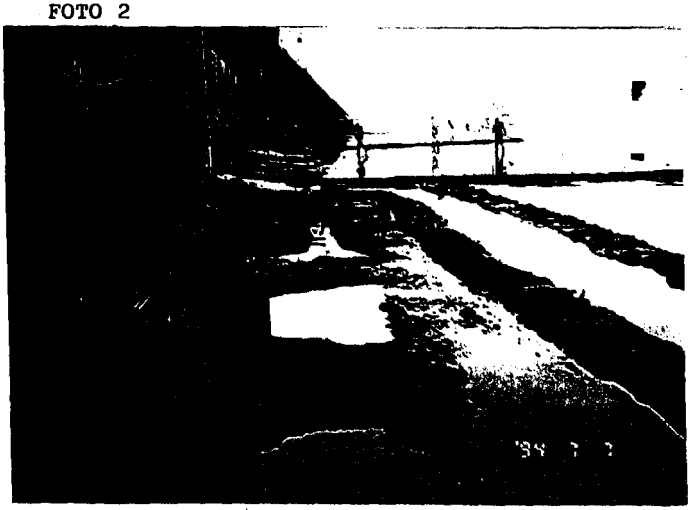

FOTO 3

FOTO 4

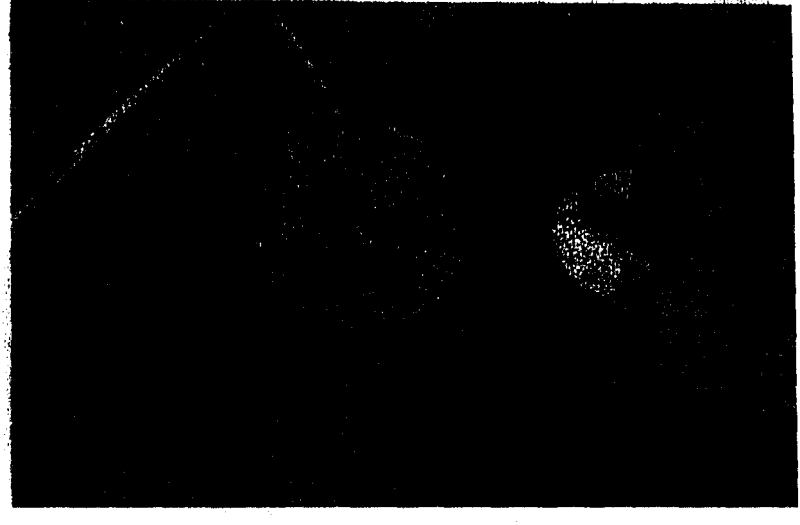

FOTO 5

FOTO 6

Laboratório de Mecânica da Turbulência, PEM/COPPE/UFRJ
C.P. 68503, 21945-970, Rio de Janeiro